

LONG-TERM BEHAVIOR OF BALLAST IN RAILWAY EMBANKMENT UNDER
HIGH-SPEED TRAIN AND FREIGHT TRAIN LOADING

A Dissertation

by

MOHAMMAD MAHDAVI KHARANAGHI

Submitted to the Office of Graduate and Professional Studies of
Texas A&M University
in partial fulfillment of the requirements for the degree of

DOCTOR OF PHILOSOPHY

Chair of Committee,	Jean-Louis Briaud
Committee Members,	Marcelo Sanchez
	Charles Aubeny
	David Allen
Head of Department,	Robin Autenrieth

August 2020

Major Subject: Civil Engineering

Copyright 2020 Mohammad Mahdavi Kharanaghi

ABSTRACT

The behavior of the railway ballast under the operation of high-speed trains and heavy freight trains is studied in this dissertation. For this purpose, a combination of laboratory testing and numerical simulations has been performed. This project can be categorized into three different phases: (1) behavior of the ballast under monotonic loading, (2) long-term behavior of the ballast under cyclic loading caused by train passage, and (3) stress and strain development in the track substructure under train loads.

The monotonic behavior of the railway ballast is investigated through extensive laboratory tests by using large-scale direct shear, direct simple shear, and triaxial tests. The outcomes of this phase of the study are the magnitude of the shear strength properties of the ballast, which directly uses in the railway substructure design and the maximum shear strength of the material, which is a key factor in the further cyclic investigations. Moreover, the stress-strain-strength of the large aggregate ballast material has been compared by the three abovementioned tests, and the appropriate empirical formulas for calculating the shear strength properties of the ballast based on all three tests are proposed.

To investigate the long-term behavior of the railway ballast under repeated loading, a series of large-scale cyclic direct simple shear and triaxial tests were conducted. The tests were performed under various normal/confining stress and cyclic stress conditions to be representative of the various railway geometry and trains. The long-term characteristics of the ballast represent in forms of permanent settlement, lateral spreading, and the resilient modulus. Finally, a series of empirical equations to predict the long-term

characteristics of the ballast based on the initial shear strength of the material, cyclic loading amplitude, and the number of cycles are provided.

For the third phase of this study, a four-dimensional (4-D) finite element model (FEM) of the ballasted railway by using LS-DYNA has been developed. This model, which validated by the field measurement in Sweden, was used to study the stress and strain development in the railway foundation under high-speed and heavy freight trains. Moreover, the impact of train characteristics, substructure geometry, and material properties on the track maximum deflection and dynamic stress distribution in the track substructure have been investigated.

ACKNOWLEDGMENT

My first sincere appreciation belongs to my committee chair, Professor Jean-Louis Briaud, for his continuous support, direction, patience, encouragement, and enthusiasm throughout the course of this research study. Without his valuable and essential advice, this work would not have been completed. He advised me beyond the border of the classroom and taught me to be a better person.

I would like to express my gratitude to my other committee members: Professor Charles Aubeny, Marcelo Sanchez, and David Allen, for their guidance and support.

Funding for this project was provided by the Spencer J. Buchanan Chair held by Professor Briaud. We would like to express our special gratitude to Mr. Anwar Akhtar, Mr. Jeff Locke, and Dr. Jisuk Yoon from Fugro Soil and Rocks Laboratory in Houston for performing the large-scale triaxial tests for this research project. Also, an extensive numerical study would not have been completed without computer resources provided by the Texas A&M Super Computer (SC) facilities.

Soheil Sohrabi, Mohammadreza Keshavarz, Bahman Torkamandi, Arman Rezaie, Farinoush Sharifi, Amin Bnihashem, Kamran Reihani and my other friends and colleagues in at Texas A&M University also deserve thanks for making my time at Texas A&M University such a great experience

Finally, I reserve my special thanks and appreciation for my parents and brothers for their unconditional love and supports. I would like to especially thank my brother, Dr. Mohsen Mahdavi Kharanaghi, for setting an example of excellence as a role model in my

whole life. I would also like to thank my beloved fiancé, Yasaman Shahbazi. Thank you for supporting me for everything, and especially I can't thank you enough for encouraging me throughout this experience.

CONTRIBUTORS AND FUNDING SOURCES

Contributors

This work was supervised by a dissertation committee consisting of Professors Jean-Louis Briaud, Marcelo Sanchez, and Charles Aubeny of the Department of Civil and Environmental Engineering and Professor David Allen of the Department of Ocean Engineering.

The part of data analyzed for Chapter 4 and 5 regarding a large-scale triaxial test was provided by Fugro Houston.

All other work conducted for the thesis (or) dissertation was completed by the student independently.

Funding Source

Graduate study was supported by Spencer J. Buchanan Chair held by Professor Briaud.

TABLE OF CONTENTS

	Page
ABSTRACT	ii
ACKNOWLEDGMENT	iv
TABLE OF CONTENTS	vii
LIST OF FIGURES	xi
LIST OF TABLES	xxii
1. INTRODUCTION.....	1
1.1. Overview	1
1.2. Problem Statement	2
1.3. Research Objectives and Scope.....	4
1.4. Dissertation Outline.....	5
2. LITERATURE REVIEW	7
2.1. Introduction	7
2.2. Railway Track Components	7
2.2.1. Track Superstructure	9
2.2.2. Track Substructure	9
2.3. Railway Track Loading.....	13
2.3.1. Vertical Forces	14
2.3.2. Lateral Forces	16
2.4. Laboratory Tests on Granular Material with Special Reference to Railway Ballast Material	17
2.4.1. Large-Scale Direct Shear Test (DST)	18
2.4.2. Large-Scale Direct Simple Shear Test (DSST).....	18
2.4.3. Large-Scale Triaxial Test (TT).....	19
2.4.4. Comparison of the Shear Properties of the large size aggregate Materials with DST, DSST, and TT	20
2.5. Behavior of Ballast Under Monotonic Loading	21
2.5.1. Influence of Grain Characteristics.....	22
2.5.2. Influence of Aggregate Characteristics	27
2.5.3. Influence of Loading Characteristics	31
2.6. Behavior of Ballast Under Cyclic Loading	38

2.6.1. Resilient Behavior of Ballast.....	39
2.6.2. Permanent Deformation and Cyclic Densification of Ballast	48
2.7. Empirical Models for Prediction of Long-Term Track Settlement.....	61
3. LABORATORY PROCEDURE.....	65
3.1. Introduction	65
3.2. Large-Scale Testing Facilities.....	65
3.2.1. Large-Scale Direct Shear (DST) Apparatus.....	65
3.2.2. Large-scale Direct Simple Shear (DSST) Apparatus	69
3.2.3. Large-Scale Triaxial Apparatus (TT)	72
3.3. Characteristics of the Testing Materials.....	75
3.4. Test Procedure and Plan.....	76
3.4.1. Large-Scale Direct Shear Test (DST)	76
3.4.2. Large-Scale Direct Simple Shear Test (DSST).....	84
3.4.3. Large-Scale Triaxial Test (TT).....	93
4. PRESENTATION AND DISCUSSION OF THE RESULTS OF MONOTONIC LOADING TESTS	102
4.1. Introduction	102
4.2. Monotonic Direct Shear Test (DST)	103
4.2.1. Test Repeatability.....	103
4.2.2. Shear Stress-Shear Displacement and Axial Displacement-Shear Displacement	104
4.2.3. Shear Strength Failure Envelope.....	106
4.2.4. Influence of Normal Stress on Friction Angle	108
4.2.5. Influence of Normal Stress on Dilation Angle.....	109
4.2.6. Influence of Ballast Maximum Particle Size.....	111
4.2.7. Influence of DST Gap on the Shear Behavior of Large Aggregate Materials.....	116
4.3. Monotonic Direct Simple Shear Test (DSST).....	122
4.3.1. Test Repeatability.....	122
4.3.2. Shear Stress- Shear Strain and Axial Strain-Shear Strain	124
4.3.3. Shear strength Failure Envelope.....	126
4.3.4. Shear Modulus.....	129
4.3.5. Influence of Normal Stress on the Friction Angle and the Dilatancy	132
4.3.6. Influence of Ballast Maximum Particle Size.....	135
4.4. Monotonic Triaxial Test (TT)	141
4.4.1. Deviatoric Stress-Axial Strain.....	141
4.4.2. Shear Strength Failure Envelop.....	144
4.4.3. Initial Triaxial Elastic Modulus.....	145
4.4.4. Influence of the Confining Stress on the Friction Angle.....	147

4.5. Comparison of the Shear Behavior of the Railway Ballast Based on DST, DSST, and TT Results.....	148
4.5.1. Shear Behavior	149
4.5.2. Shear Strength Failure Envelope.....	155
4.5.3. Friction Angle.....	158
4.5.4. Shear Modulus.....	160
5. PRESENTATION AND DISCUSSION OF THE RESULTS OF CYCLIC LOADING TESTS	163
5.1. Introduction	163
5.2. Cyclic Direct Simple Shear Test (DSST).....	164
5.2.1. Experimental Results.....	164
5.2.2. Parametric Study	177
5.2.3. Empirical Models to Predict the Long-Term Behavior of the Railroad Ballast Based on Cyclic DSST Results	204
5.3. Cyclic Triaxial Test (TT)	220
5.3.1. Experimental Results.....	221
5.3.2. Empirical Models to Predict the Long-Term Behavior of the Railroad Ballast Based on Cyclic TT Results	230
6. FINITE ELEMENT ANALYSIS OF BALLASTED RAILWAY TRACK.....	238
6.1. Introduction	238
6.2. Software Introduction (LS-DYNA)	239
6.3. Finite Element Modeling of Ballasted Railway Track.....	239
6.3.1. Railway Components Description.....	240
6.3.2. Material Model and Properties	244
6.3.3. Boundary Conditions.....	251
6.3.4. Train-Track Interaction	252
6.4. Model Verification	253
6.4.1. High-Speed Railway Track at Ledsgard, Sweden.....	254
6.4.2. Ballasted Railway Track at Bulli, Australia	260
6.5. Parametric Study	268
6.5.1. Influence of Train Weight	269
6.5.2. Influence of Train Speed	273
6.5.3. Influence of Sleeper's Width.....	279
6.5.4. Influence of Sleeper's Spacing.....	283
6.6. Bearing Capacity of the Ballast Layer	286
7. CONCLUSION AND RECOMMENDATIONS	288
7.1. Conclusion.....	288
7.1.1. Monotonic Behavior of the Railroad Ballast.....	290
7.1.2. Cyclic Behavior of the Railroad Ballast:.....	295

7.1.3. FEM Numerical Simulation of the Ballasted Railway Track:	301
7.2. Future Related Research.....	307
REFERENCES	308

LIST OF FIGURES

	Page
Figure 2.1. Components of ballasted railway track: (a) longitudinal cross-section; (b) transverse cross-section (after Selig and Waters (1994)).....	8
Figure 2.2. Trainload distribution to the track structure (after Selig and Waters (1994))	16
Figure 2.3. Influence of particle size on friction angle (after Marschi et al. (1972))	24
Figure 2.4. Friction angle variation with particle shape (after Holtz and Gibbs (1956))	25
Figure 2.5. Influence of particle size distribution on (a) friction angle, (b) dry density (after Thorn and Brown (1989)).....	28
Figure 2.6. Influence of relative density on the shear strength of sand using drained triaxial test (after Lee and Seed (1967))	29
Figure 2.7. Influence of void ratio on friction angle (after Roner (1985)).....	30
Figure 2.8. Influence of moisture content on the shear strength of fouled ballast (after Qian et al. (2016))	31
Figure 2.9. Non-linear failure envelope at low confining pressure (after Charles and Watts (1980))	33
Figure 2.10. Influence of confining pressure on the peak friction angle (after Indraratna et al. (1998))	34
Figure 2.11. Influence of confining pressure, particle breakage, and dilatancy on the friction angle (modified after Indraratna and Salim (2002))	35
Figure 2.12. Non-linear failure envelope from the direct shear test (after Estaire and Santana (2018))	36
Figure 2.13. Secant friction angle variation with relative normal stress from the direct shear test (after Estaire and Santana (2018))	36
Figure 2.14. Strains in granular materials under one cycle of load application (Lekarp et al. (2000)).....	39

Figure 2.15. Behavior of ballast under cyclic loading (after Selig and Waters (1994))	40
Figure 2.16. Influence of particle size on ballast resilient modulus (after Janardhanam and Desai (1983))	41
Figure 2.17. Resilient modulus of a well-graded crushed rock as a function of volume content of solid particles (after Kolisoja (1997)).....	44
Figure 2.18. Influence of confining pressure on the resilient modulus under various deviatoric stresses (after Lackenby et al. (2007))	46
Figure 2.19. Influence of deviatoric stress on the resilient modulus (a) After Lackenby et al. (2007); (b) After Zeghal (2004)	47
Figure 2.20. Ballast response regimes during cyclic loading (after Suiker and de Borst (2003)).....	50
Figure 2.21. Settlement of the ballast under cyclic loading (after Jeffs and Marich (1987))	51
Figure 2.22. Influence of aggregates gradation on the plastic strain of granular material; (a) modified after Thorn and Brown (1989); (b) after Raymond and Diyaljee (1979).....	54
Figure 2.23. Influence of density on the plastic strain of limestone ballast (from (Knutson, 1977)).....	55
Figure 2.24. Influence of confining pressure on the final axial strain (after Lackenby et al. (2007)).....	57
Figure 2.25. Influence of cyclic loading amplitude on the permanent strain (after Olowokere (1975)).....	58
Figure 2.26. Settlement of ballast under cyclic loading (after Ionescu et al. (1998))	59
Figure 2.27. Influence of train speed on the dynamic stress (after Kempfert and Hu (1999))	60
Figure 2.28. Influence of train speed on ballast settlement (after Luo et al. (1996))	61
Figure 2.29. Relative contributions of the substructure components to the long-term track settlement (after Selig and Waters (1994)).....	62

Figure 3.1. ShearTrac-III apparatus	66
Figure 3.2. Direct shear test (DST) setup.....	67
Figure 3.3. DST shear box	68
Figure 3.4. Direct simple shear test (DSST) setup (Zekkos et al. (2018))	70
Figure 3.5. DSST stacked rings.....	71
Figure 3.6. Crossbar and rollers configuration.....	72
Figure 3.7. Triaxial test apparatus.....	73
Figure 3.8. Triaxial test sample.....	74
Figure 3.9. Grain size distribution of the ballast materials	75
Figure 3.10. DST sample preparation. (a) Placement of the lower half of the shear box on the shear box stand; (b) Placement of the upper half of the shear box and alignment screws; (c) Final layer of the sample; (d) Top cap placement	78
Figure 3.11. DST test procedure. (a) Placement of shear box into the loading frame; (b) ShearTrac-III control panel system; (c) Lifting beams and crossbeam configuration	80
Figure 3.12. Large-scale direct shear calibration	83
Figure 3.13. DSST sample preparation. (a) Base plate components; (b) Membrane and O-ring placement; (c) Final DSST sample;	86
Figure 3.14. DSST test setup.....	87
Figure 3.15. Sitting load step	88
Figure 3.16. Typical cyclic load curve.....	89
Figure 3.17. Large-scale direct simple shear device calibration	92
Figure 3.18. TT sample preparation. (a) Vacuum of latex membrane inside the split mold; (b) Placement of the first layer; (c) Compaction of the material; (d) Complete specimen in latex membrane; (e) Placement of rubber membrane;.....	97

Figure 3.19. TT test set up. (a) Triaxial cell; (b) Placement of cell into the loading frame	99
Figure 4.1. DST repeatability. (a) Shear stress-shear displacement; (b) Axial displacement-shear displacement	104
Figure 4.2. Shear Behavior of Ballast#5 Based on DST. (a) Shear stress-shear displacement; (b) Axial displacement-shear displacement.....	105
Figure 4.3. Failure envelope of ballast#5 based on DST	107
Figure 4.4. Variation of friction angle with the normal stress of ballast#5 based on DST.....	109
Figure 4.5. Variation of secant dilation angle with the shear displacement for ballast#5 based on DST	110
Figure 4.6. Variation of maximum dilation angle with the normal stress of ballast#5 based on DST.	111
Figure 4.7. DST results for ballast#4. (a) Shear stress-shear displacement; (b) Axial displacement-shear displacement; (c) Failure envelope; (d) Variation of friction angle with the normal stress; (e) Variation of dilation angle with horizontal displacement; (f) Variation of maximum dilation angle with the normal stress	115
Figure 4.8. Gap in DST box	117
Figure 4.9. DST results for ballast#5 with the reduced gap. (a) Shear stress-shear displacement; (b) Axial displacement-shear displacement; (c) Failure envelope; (d) Variation of friction angle with the normal stress; (e) Variation of dilation angle with horizontal displacement; (f) Variation of maximum dilation angle with the normal stress.....	121
Figure 4.10. DSST repeatability. (a) Shear stress-shear strain; (b) Axial strain-shear strain	124
Figure 4.11. Shear Behavior of Ballast#5 Based on DSST. (a) Shear stress-shear strain; (b) Axial strain-shear strain	126
Figure 4.12. Interpretation of the stress states at failure for DSST results based on α and β methods (Zekkos and Fei (2017)).....	128
Figure 4.13. Failure envelope of ballast#5 based on DSST	129

Figure 4.14. Shear modulus variation with shear strain for ballast #5 based on DSST.....	130
Figure 4.15. Normalized Shear modulus variation with shear strain for ballast #5 based on DSST	131
Figure 4.16. Maximum Shear modulus variation with vertical stress for ballast #5 based on DSST	132
Figure 4.17. Variation of friction angle with the normal stress of ballast#5 based on DSST.....	133
Figure 4.18. Variation of dilation angle with the shear strain of ballast#5 based on DSST.....	134
Figure 4.19. Variation of maximum dilation angle with the normal stress of ballast#5 based on DSST.	134
Figure 4.20. DSST results for ballast#4. (a) Shear stress-shear strain; (b) Axial strain-shear strain; (c) Failure envelope; (d) Variation of friction angle with the normal stress; (e) Variation of dilation angle with the shear strain; (f) Variation of maximum dilation angle with the normal stress; (g) Shear modulus variation with the shear strain; (h) Normalized Shear modulus variation with shear strain; (i) Maximum Shear modulus variation with the vertical stress	140
Figure 4.21. Deviatoric stress-axial strain response of ballast #5 based on TT	142
Figure 4.22. Shear behavior of railroad ballast based on a triaxial test. (a) Deviatoric stress-axial strain; (b) volumetric-axial strain (data adopted from Indraratna et al. (1998))	144
Figure 4.23. Shear strength failure envelope of ballast #5 based on TT.....	145
Figure 4.24. Influence of the confining pressure on the initial triaxial elastic modulus.....	146
Figure 4.25. Variation of the friction angle with the confining stress for ballast #5 based on TT	147
Figure 4.26. Comparison of the stress-strain (or displacement) of the railroad ballast. (a) DST; (b) DSST; (c) TT	152

Figure 4.27. Comparison of the dilatancy response of ballast. (a) Axial displacement-shear displacement for DST; (b) Axial strain-shear strain for DSST	154
Figure 4.28. Comparison of the failure envelope of the railroad ballast based on DST, DSST, and TT results.....	156
Figure 4.29. Comparison of the variation of the friction angle of the railroad ballast based on DST, DSST, and TT results	159
Figure 4.30. Comparison of the variation of the shear modulus of the railroad ballast with the vertical stress on the plane of failure based on DSST and TT results	162
Figure 5.1. Cyclic DSST results of ballast material (first 100 cycles). (a) Horizontal stress vs. number of cycles; (b) Shear strain vs. number of cycles; (c) Shear strain vs. number of cycles.....	167
Figure 5.2. Cyclic shear stress-shear strain response of the ballast #4 based on the DSST for 50 kPa vertical stress	168
Figure 5.3. Development of the permanent strain based on DSST. (a) Permanent shear strain vs. number of cycles; (b) Permanent normal strain vs. number of cycles; (c) Permanent normal strain vs. permanent shear strain	170
Figure 5.4. Resilient shear modulus test results (Modified after Briaud (2013)).....	171
Figure 5.5. Resilient shear modulus of ballast based on DSST. (a) Resilient shear modulus vs. number of cycles; (b) Normalized resilient shear modulus vs. number of cycles	173
Figure 5.6. Cyclic secant shear modulus (modified after (Briaud (2013)))	174
Figure 5.7. Cyclic secant shear modulus of ballast based on DSST. (a) Secant shear modulus vs. number of cycles; (b) Normalized secant shear modulus vs. number of cycles; (c) Normalized secant shear modulus vs. shear strain	176
Figure 5.8. Influence of vertical stress on the shear stress-shear strain of ballast #4 by using cyclic DSST. (a) vertical stress of 40 kPa; (b) vertical stress of 50 kPa; (c) vertical stress of 60 kPa; (d) vertical stress of 70 kPa; (e) vertical stress of 90 kPa.....	181

Figure 5.9. Influence of the normal stress level on the response of ballast #4 under cyclic DSST. (a) Permanent shear strain vs. number of cycles; (b) Secant shear modulus vs. number of cycles; (c) Normalized secant shear modulus vs. number of cycles; (d) Resilient shear modulus vs. number of cycles; (e) Normalized resilient shear modulus vs. number of cycles	186
Figure 5.10. Influence of cyclic shear stress amplitude on the shear stress-shear strain of ballast #4 (10 kPa vertical stress). (a) 2.5 kPa cyclic shear stress; (b) 5 kPa cyclic shear stress; (c) 7 kPa cyclic shear stress	190
Figure 5.11. Influence of cyclic shear stress amplitude on the shear stress-shear strain of ballast #4 (50 kPa vertical stress). (a) 12.5 kPa cyclic shear stress; (b) 25 kPa cyclic shear stress; (c) 35 kPa cyclic shear stress	191
Figure 5.12. Influence of cyclic shear stress amplitude on the shear stress-shear strain of ballast #4 (90 kPa vertical stress). (a) 24 kPa cyclic shear stress; (b) 45 kPa cyclic shear stress	192
Figure 5.13. Influence of cyclic shear stress amplitude on the permanent shear strain of ballast #4 based on DSST. (a) 10 kPa vertical stress; (b) 50 kPa vertical stress; (c) 90 kPa vertical stress	195
Figure 5.14. Influence of cyclic shear stress amplitude on the secant shear modulus of ballast #4 based on DSST. (a) 10 kPa vertical stress; (b) 50 kPa vertical stress; (c) 90 kPa vertical stress	197
Figure 5.15. Influence of cyclic shear stress amplitude on the normalized secant shear modulus of ballast #4 based on DSST. (a) 10 kPa vertical stress; (b) 50 kPa vertical stress; (c) 90 kPa vertical stress	199
Figure 5.16. Influence of cyclic shear stress amplitude on the resilient shear modulus of ballast #4 based on DSST. (a) 10 kPa vertical stress; (b) 50 kPa vertical stress; (c) 90 kPa vertical stress	201
Figure 5.17. Influence of cyclic shear stress amplitude on the resilient shear modulus of ballast #4 based on DSST. (a) 10 kPa vertical stress; (b) 50 kPa vertical stress; (c) 90 kPa vertical stress	203
Figure 5.18. Variation of the plastic shear strain prediction equation (Equation (16)) constants with the cyclic stress ratio. (a) Parameter A; (b) Parameter B	206
Figure 5.19. Variation of the plastic shear strain with the cyclic stress ratio.....	207

Figure 5.20. Plastic shear strain model prediction with the experimental data. (a) Example of determination of the model parameters by fitting the experimental results; (b) Verification of the proposed model	209
Figure 5.21. Variation of the secant shear modulus at the first cycle with the cyclic stress ratio.....	210
Figure 5.22. Variation of the secant shear modulus equation (Equation (18)) constants with the cyclic stress ratio. (a) Parameter A; (b) Parameter B	212
Figure 5.23. Secant shear modulus Model Prediction with the experimental data. (a) Example of determination of the model parameters by fitting the experimental results; (b) Verification of the proposed model	214
Figure 5.24. Variation of the resilient shear modulus equation (Equation (19)) constants with the cyclic stress ratio. (a) Parameter A; (b) Parameter B	216
Figure 5.25. Variation of the resilient shear modulus at the first cycle with the cyclic stress ratio.....	218
Figure 5.26. Resilient shear modulus Model Prediction with the experimental data. (a) Example of determination of the model parameters by fitting the experimental results; (b) Verification of the proposed model	220
Figure 5.27. Cyclic deviatoric stress-axial strain response of railroad ballast based on TT results. (a) Deviatoric stress of 40 kPa; (c) Deviatoric stress of 80 kPa; (c) Deviatoric stress of 125 kPa	223
Figure 5.28. Development of the permanent axial strain of railroad ballast with the number of cycles	225
Figure 5.29. Permanent axial strain versus the number of cycles. (a) For the tests with the maximum cyclic magnitude of 240 (kPa); (b) For the tests with the maximum cyclic magnitude of 500 (kPa) (data adopted from Lackenby et al. (2007)).....	227
Figure 5.30. Development of the secant elastic modulus with the number of cycles based on cyclic TT results. (a) Secant elastic modulus; (b) Normalized secant elastic modulus	229
Figure 5.31. Variation of the permanent axial strain model (Equation (21)) constants with the cyclic stress ratio. (a) Parameter A; (b) Parameter B	232
Figure 5.32. Permanent axial strain prediction with the experimental data. ((a) Example of determination of the model parameters by fitting the	

experimental results; (b) Verification of the proposed model (Experimental data adopted from Lackenby et al. (2007)).....	234
Figure 5.33. Verification of the proposed model for the axial permanent strain on the cyclic TT results on crushed granite ballast.....	235
Figure 5.34. Comparison of the secant elastic modulus model prediction with the experimental data.....	236
Figure 5.35. Variation of the secant elastic modulus model (Equation (21)) constants with the cyclic stress ratio. (a) Parameter A; (b) Parameter B	237
Figure 6.1. Overview of the FEM model. (a) Cross-section; (b) Side view	241
Figure 6.2. Sleeper’s dimensions and spacing	242
Figure 6.3. Train specification used for model validation. (a) X2000 train (after Madshus and Kaynia (2000)); (b) Two wagons of a train (after Rezaei Tafti (2018)).....	243
Figure 6.4. The influence of the soil non-linearity on the track deflection. (a) Soft subgrade; (b) stiff subgrade (after Sayeed and Shahin (2016))	246
Figure 6.5. Comparison of the linear elastic and non-linear elastic behavior of ballast on the track deflection in different train speed (after Varandas et al. (2016))	247
Figure 6.6. Influence of soil non-linearity on the response of railway track at train speed equal to 108 kph. (a) Sleeper displacement; (b) vertical stress on top of the ballast; (c) vertical stress on top of the subgrade (after Banimahd (2008)).....	248
Figure 6.7. Influence of soil non-linearity on the response of railway track at train speed equal to 252 kph. (a) Sleeper displacement; (b) vertical stress on top of the ballast; (c) vertical stress on top of the subgrade (after Banimahd (2008)).....	249
Figure 6.8. Boundary Conditions. (a) Transverse view; (b) Longitudinal view	252
Figure 6.9. Wheel/rail contact surface (after Nicks (2009))	253
Figure 6.10. The geometry of the HST railway track at the Ledsgard site. (a) Field cross-section (after Madshus and Kaynia (2000)); (b) FEM model.....	256
Figure 6.11. Dynamic soil properties at the Ledsgard site (after Madshus and Kaynia (2000)).....	257

Figure 6.12. Comparison of the track vertical displacement (after Madshus and Kaynia (2000)) versus the FEM prediction. (a) train speed of 70 kph; (b) train speed of 185 kph.....	260
Figure 6.13. The geometry of the ballasted railway track at Bulli, Australia. (a) Cross-section (after Indraratna et al. (2010)); (b) FEM study	262
Figure 6.14. Schematic diagram of the location of the instrumentations. (a) Displacement transducers; (b) Pressure cells (after Indraratna et al. (2010))	263
Figure 6.15. Schematic of the train axles spacing used in the FEM study.....	264
Figure 6.16. Comparison of the field measurement of the maximum cyclic vertical and shear stress underneath the rail (after Indraratna et al. (2010)) with the FEM study	266
Figure 6.17. Comparison of the maximum cyclic vertical stress of the FEM study with the available measurement in the literature (data adopted from Indraratna et al. (2010))	268
Figure 6.18. Influence of the train wheel load on the distribution of the maximum cyclic stress generated by train with depth below the sleeper. (a) Maximum cyclic vertical stress; (b) Maximum cyclic shear stress	271
Figure 6.19. Relationship between the maximum cyclic stresses under the sleeper bottom with the train wheel load	272
Figure 6.20. Relationship between the maximum track downward displacement with the train wheel load.....	273
Figure 6.21. Influence of train speed on the vertical displacement of the track	276
Figure 6.22. Influence of train speed on the maximum cyclic stresses under the sleeper bottom.....	277
Figure 6.23. Influence of the train speed on the distribution of the maximum cyclic stress generated by train with depth below the sleeper. (a) Maximum cyclic vertical stress; (b) Maximum cyclic shear stress	278
Figure 6.24. Influence of sleeper's width on the maximum cyclic stresses under the sleeper bottom.....	280
Figure 6.25. Influence of sleeper's width on the maximum downward displacement of the track	281

Figure 6.26. Influence of the sleeper's width on the distribution of the maximum cyclic stress generated by train with depth below the sleeper. (a) Maximum cyclic vertical stress; (b) Maximum cyclic shear stress	282
Figure 6.27. Influence of sleeper's spacing on the maximum cyclic stresses under the sleeper bottom.....	284
Figure 6.28. Influence of sleeper's width on the maximum downward displacement of the track.....	285
Figure 6.29. Influence of the sleeper's spacing on the distribution of the maximum cyclic stress generated by train with depth below the sleeper. (a) Maximum cyclic vertical stress; (b) Maximum cyclic shear stress	286
Figure 7.1. Step by step procedure to predict the long-term response of ballast in the railway embankment.....	290

LIST OF TABLES

	Page
Table 2.1. Recommended limiting values of testing for ballast material (after AREMA (2008)).....	11
Table 2.2. Recommended ballast gradation (after AREMA (2008))	12
Table 2.3. Summary of Models for Calculating Dynamic Amplification Factor (DAF) (after Doyle (1980))	15
Table 2.4. Recommended range of normal and confining stresses for ballast based on FEM simulations (modified after Stark et al. (2018))	38
Table 3.1. Recommended duration of a consolidation phase (GeocompCo. (2015))	69
Table 3.2. Mechanical properties of the ballast materials.....	76
Table 3.3. DST test plan.....	82
Table 3.4. Monotonic DSST test plan.....	90
Table 3.5. Cyclic DSST test plan	91
Table 3.6. Monotonic TT test plan.....	101
Table 3.7. Cyclic TT test plan.....	101
Table 4.1. Strength parameters obtained from DST for ballast#5	107
Table 4.2. Strength parameters obtained from DST for ballast#4	116
Table 4.3. Strength parameters obtained from DST for ballast#5 (Reduced Gap)	122
Table 4.4. Summary of DSST results for ballast #5.....	128
Table 4.5. Shear modulus of ballast #5 at different shear strain and vertical stress.....	130
Table 4.6. Summary of DSST results for ballast #4.....	135
Table 4.7. Summary of monotonic TT results for ballast #5	145
Table 4.8. Shear strength model parameters for DST, DSST, and TT results	158

Table 4.9. Friction angle model parameters for DST, DSST, and TT results	160
Table 4.10. Summary of the maximum shear modulus of the railroad ballast based on the DSST and TT results	162
Table 5.1. Details of the influence of the normal stress level on the response of ballast #4 under cyclic DSST	178
Table 5.2. Details of the influence of the cyclic shear stress on the response of ballast #4 under cyclic DSST	187
Table 5.3. Calibration of the plastic shear strain model based on the experimental results	206
Table 5.4. Calibration of the secant shear modulus model based on the experimental results	213
Table 5.5. Calibration of the resilient shear modulus model based on the experimental results	217
Table 5.6. Details of the cyclic TT	224
Table 5.7. Summary of the cyclic triaxial testing program (data adopted from Lackenby et al. (2007))	226
Table 5.8. Details of the TT modules	228
Table 5.9. Calibration of the permanent axial strain model based on the experimental results (Experimental data adopted from Lackenby et al. (2007))	231
Table 6.1. Superstructure components constitutive model and material properties used in the FEM models	244
Table 6.2. Material properties of the Ledsgard site adopted in the FEM study (data adopted from Kaynia et al. (2000))	258
Table 6.3. Material properties of the Bulli site adopted in the FEM study (data adopted from Indraratna et al. (2012) and Jiang and Nimbalkar (2019))	262
Table 6.4. Rayleigh and shear wave velocity of the soil materials used in the parametric study	275

1. INTRODUCTION

1.1. Overview

Railway networks form a significant part of transportation infrastructure all over the world. It plays a crucial role in a successful and healthy economy, by accommodating the transportation of heavy bulk freights between the ports and major cities and also carrying the passengers. In order to compete with the other modes of transportation, the performance and operation quality of the railway should be increased while maintaining low operation and maintenance costs. Therefore, it demands a larger capacity (train speed and axle load), better safety, higher comfort, and lower maintenance costs.

The substantial amount of money spent on railway maintenance annually in all countries. According to Selig and Waters (1994), the remarkable portion of the maintenance costs is related to the railway substructure components, including ballast, subballast, and subgrade. The American railway industry has allocated millions of dollars annually for ballast maintenance costs (Chrismer (1986)). The Canadian railroad authorities reported the disbursement of one billion dollars on the maintenance of the ballast per year, which is approximately 40 percent of their track replacement yearly budget (Raymond (1983)). The state of New South Wales in Australia reported the cost of over 12 million dollars for ballast replacement during 1992-1993 (Indraratna et al. (1997)).

The emergence of high-speed trains and heavy freight trains even increase railway maintenance cost and frequency, and also brought new geotechnical challenges for the railway substructures. Increasing the train axle loads and speeds cause amplification of the dynamic train loading transmitted to the railway substructure. Therefore, the railway

ballast that is the first substructure layer capture the train loading experienced higher repeated stress, which causes a higher degree of degradation, densification, and settlement, which eventually increases the maintenance costs and intervals.

1.2. Problem Statement

The ballast is an essential component of the conventional ballasted railway track, and its significance has increased in high-speed trains and heavy haul freight trains. As it was mentioned by Selig (1998), in the presence of the proper and stable subgrade, the track settlement would mainly occur in the ballast. Thus, It is vital to investigate in detail the behavior of the ballast materials under the monotonic and cyclic loading conditions. It is also important to identify the impact of various conditions in the field that influence the behavior of the railway track.

The first step for design a stable and long-standing ballast is to understand the behavior of this large aggregate unbounded materials under monotonic loading conditions. Knowing the magnitude of the shear strength parameters is necessary for the design of the railway substructure, and the maximum shear strength of the materials is the key parameter for further investigation of the behavior of the ballast under train cyclic loading. Various laboratory apparatuses were used previously for understanding the shear behavior of the ballast under monotonic loading. On the one hand, there are limited studies reported in this area due to the need for large-scale laboratory facilities for testing such large aggregate materials. On the other hand, different laboratory tests such as direct shear, direct simple

shear, and triaxial tests have been utilized for the investigations of the shear strength of the ballast materials, without paying attention to the possible difference of the outcome.

Understanding the long-term behavior of the ballast under cyclic loading, especially for high-speed and heavy freight trains, can ultimately increase the operation safety and comfort and also decrease the maintenance costs of the railway remarkably. It is anticipated that the ballast aggregates rearrange and form a more stable configuration under the cyclic loading caused by train passage. This process leads to particle breakage, vertical settlement, lateral spreading, and changes the resilient behavior of the material in long-term cyclic loading. Therefore, it is vital to investigate the response of ballast under various cyclic loading and stress level conditions to study the long-term behavior of the material. The lack of quantitative relationships between the long-term characteristics of ballast such as the plastic vertical and lateral strain of the ballast and the in-situ stress condition and train loading characteristics are the other issue that needs to be further investigated.

The plastic deformation of the ballast, which forms the remarkable portion of the railway track long-term settlement, is highly dependent on the initial stress condition and cyclic stress amplitude during the train passage. The stress condition depends on the various components such as ballast initial stress states, track geometry, and train speed and axle loads. Therefore, a clear understanding of the mechanical behaviors (stress and strain) of the track substructure under high speed and heavy freight trains is crucial for the safe, comfortable, and economical railway design. Few field investigations (Indraratna et al. (2010) and Bowness et al. (2007)) and numerical simulations (Madshus et al. (2004),

Rezaei Tafti (2018), and Powrie et al. (2007)) on the stress changes during train passage in ballasted tracks are available in the literature. However, further numerical simulation analysis is needed to investigate the impact of the high-speed train, heavy freight train, track geometry, and other important factors on the mechanical behavior of the ballasted railway track during the train passage.

1.3. Research Objectives and Scope

The ultimate purpose of this project is to study the behavior of ballast in the railway embankment under the operation of high-speed trains and heavy freight trains. The specific objectives of this dissertation are summarized below:

1. Investigate the monotonic shear behavior of the crushed granite ballast material by using the large-scale direct shear, direct simple shear, and triaxial laboratory tests. Evaluate the effect of field stress state (i.e., confining/normal pressure) and the material maximum particle size (AREMA ballast #4 and #5) on the shear strength parameters of the ballast.
2. Compare the shear behavior of the railway ballast based on large-scale direct shear, direct simple shear, and triaxial tests. Provide the appropriate empirical formula to calculate the shear strength properties of the ballast.
3. Investigate the cyclic behavior of the crushed granite ballast material under large-scale cyclic direct simple shear and triaxial tests. Examine the effect of field stress states and various cyclic loading characteristics due to the train passage on the long-term behavior of the ballast.

4. Provide the appropriate empirical formulas for predicting the long-term cyclic permanent settlement, permanent shear strain, resilient shear modulus, secant shear modulus, and the secant elastic modulus of the ballast based on the laboratory data.
5. Develop a 4-D finite element model (FEM) representing the coupled train, track, and ballast dynamic responses under high-speed and heavy freight trains by using LS-DYNA (Livermore Software Technology Corporation (LSTC), 2006). The objectives of the numerical model are: (1) study the track deflection and the cyclic stresses development in the track substructure due to the high-speed passenger and heavy freight trains operation. (2) study the influence of train characteristics (weight and speed) on the dynamic response of the ballasted track (3) evaluate the influence of sleeper's characteristics (width and spacing) on reducing the magnitude of the cyclic stresses generated by the train.

1.4. Dissertation Outline

This dissertation is divided into seven chapters, including this introduction. A summary of the subsequent chapters is outlined in the following.

Chapter 2 provides a brief literature review of the railway components, track loading, most used laboratory tests of the large aggregate material with a focus to railway ballast, monotonic and cyclic behavior of the ballast materials, factors governing the behavior of the ballast, empirical models to predict long term behavior of the ballast, and FEM numerical simulations for a ballasted railway.

Chapter 3 explains the large scale testing facilities used in this study, including direct shear, direct simple shear, and triaxial apparatuses. The chapter also introduces the materials used for this investigation and the monotonic and cyclic testing procedures and plans.

Chapter 4 presents the finding of the large scale direct shear, direct simple shear, and triaxial on ballast materials under the monotonic condition. This chapter contains the investigation on the effect of the stress state and the maximum particle size on the shear strength parameters of the ballast. Then provided appropriate empirical equations for prediction of the shear strength parameters of the ballast based on the specific testing device. In the end, the comparison of the abovementioned tests was made.

Chapter 5 includes the results of cyclic tests on the ballast materials based on large scale direct simple shear and triaxial tests. It provides the effect of stress states and the cyclic loading characteristics on the long-term behavior of the ballast. This chapter includes the empirical equations for prediction of the long term plastic settlement, lateral spreading, and the resilient modulus of the ballast.

Chapter 6 introduces the 4-D FEM model using LS-DYNA of the coupled train, track, and embankment. This chapter includes the validation of the model based on two field investigations in the literature. The chapter also includes the study of the track deflection and the maximum cyclic shear and vertical stresses generated in the ballast layer caused by the train passage. Finally, the impact of train characteristics and the sleepers configuration on the dynamic response of the ballasted track was presented.

2. LITERATURE REVIEW

2.1. Introduction

Increasing the tendency of using a train as a primary source of transportation due to the traffic conjunction of highways, especially in big cities, raises new challenges in the railway industry. It increases the demands for faster and heavier trains, which means a higher load on the substructures and, consequently, higher material deterioration. Therefore high-speed and heavy haul trains would cause more settlement in track substructure as a result of stronger vibration. Previous researches showed that among the underlying layers, the largest portion of the settlement occurs in the ballast layer in comparison with the sub-ballast and subgrade.

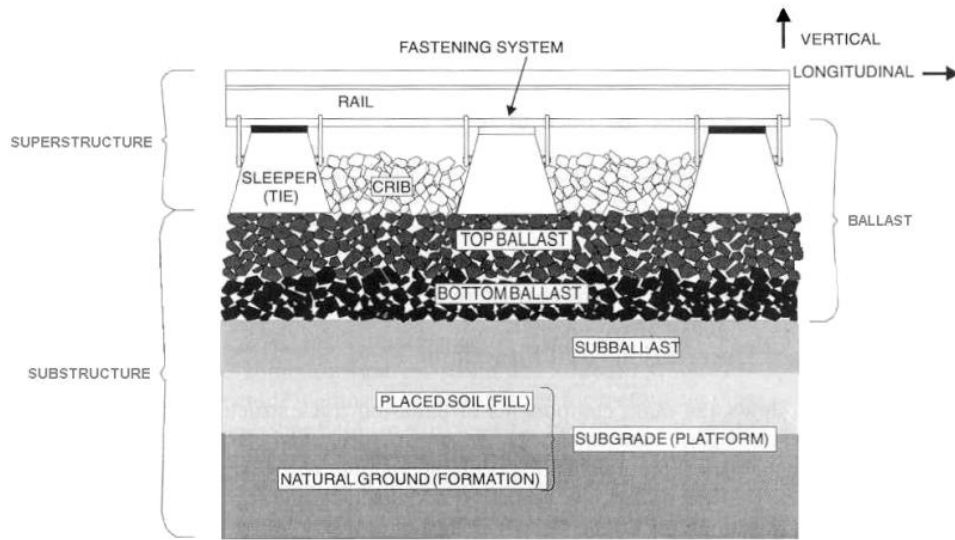
This chapter provides general information about railroad substructures with a special focus on the ballast layer. The sections of this chapter include:

- Railway track components and functions
- Stresses, stiffness, and settlement of the ballast layer under train passage
- Possible laboratory experiments on ballast
- The behavior of the granular material under monotonic and cyclic loading
- Empirical models to calculate the long-term settlement of the ballast

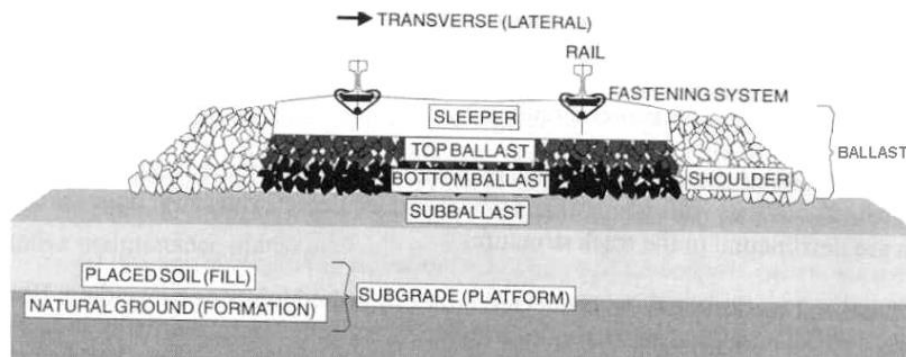
2.2. Railway Track Components

The railway track components can be categorized into two main parts named superstructure and substructure, as depicted in Figure 2.1. The superstructure includes rails, fastening systems, and sleepers, while substructure consists of ballast, subballast,

and subgrade. The main purpose of the railway system is to provide a stable foundation for safe and comfortable train transportation. For this purpose, each of the track components must perform its predefined role properly under various train axle loadings and speeds. It should reduce the train loading to the acceptable level and transfer it to the natural subgrade.



(a)



(b)

Figure 2.1. Components of ballasted railway track: (a) longitudinal cross-section; (b) transverse cross-section (after Selig and Waters (1994))

2.2.1. Track Superstructure

Rails are a pair of longitudinal steels placed along the length of the track to guide the train. Its main function is to provide support for the train wheel and transfer trainload to the sleepers. The rail is the only track component which is in direct contact with the train. Therefore, any defects can lower the passenger comfort, magnify the dynamic loading induced by train, and consequently accelerate the deterioration of the substructure. Fasteners are used to retain the rail on top of the sleeper and restrict any vertical, lateral, longitudinal rail movement. The sleepers are the last component of the superstructure, which is placed on top of the ballast layer. Its job is to provide a solid platform for the rail fastening system and distribute the wheel load to the substructure layers. Sleepers can be made of different materials such as concrete, wood, or pre stressed concrete. Dimensions and the distances between the sleepers vary depending on the site condition, loading traffic, and its material.

2.2.2. Track Substructure

2.2.2.1. Ballast

Ballast consists of coarse grain crushed granular material that serves as the upper layer of track substructure placed on top of the subballast or subgrade, and underneath and between the sleepers. According to Selig and Waters (1994), large size angular particles originated from hard parent rock with uniform gradation and free of dust, and any cementation between particles can be defined as a satisfactory ballast material. A variety of materials can be used for ballast depending on the availability, economy, and quality of

the rock. According to the AREMA manual for railway engineering, the most commonly used rock deposits in the United States for the ballast materials include granite, trap rock, quartzite, Carbonate rocks (limestone and dolomite), and slags (iron blast furnace slag and steel furnace slag).

Ballast main functions according to the various research performed by Selig and Waters (1994), Jeffs (1989), and Indraratna and Ngo (2018) are as follow:

- Provide a solid platform for the railway superstructure and the ability to resist any loading condition applied from the sleepers.
- Capture the induced train dynamic loading from the superstructure and distribute it to the subballast and subgrade layers.
- Provide resiliency for the track and reduce the train loading to the bearable magnitude for underlying layers.
- Provide an adequate drainage condition for the track.
- Accommodate the fouled materials in the ballast.
- Facilitate maintenance operation and reconstruction of the track.

The behavior of ballast material is directly influenced by its mechanical properties, which are related to the physical properties of the particles and the in-situ physical state. Physical properties of the particles can be categorized into the particle size, gradation, angularity, roughness, surface texture, strength, durability, and resistance to weathering while the physical state is related to the field density (Selig and Waters (1994)). In general, the ballast should consist of uniformly graded angular particles with high strength and

durability under cyclic loading. For this purpose, the AREMA manual for railway engineering defined some required ASTM standard tests for the ballast to characterize it as the good quality material. These tests are including ASTM methods of sampling (ASTM C 702), sieve analysis (ASTM C 136), material finer than No. 200 sieve (ASTM C 117), bulk specific gravity and percentage of absorption (ASTM C 127), percentage of clay lumps and friable particles (ASTM C 142), resistance to degradation (ASTM C 535 and C 131), sodium sulfate soundness (ASTM C 88), unit weight (ASTM C 29), and percent of flat or elongated particles (ASTM C 4791). Table 2.1 shows the limiting value for each designated test. It should be noted that All the stated values are maximum values except the values for unit weight and bulk density, which are minimum values.

Table 2.1. Recommended limiting values of testing for ballast material (after AREMA (2008))

Property	Granite	Trap rock	Quartzite	Limestone	Dolomitic Limestone	Blast Furnace Slag	Steel Furnace Slag
Percent Material Passing No. 200 Sieve	1.0%	1.0%	1.0%	1.0%	1.0%	1.0%	1.0%
Bulk Specific Gravity (See Note 2)	2.60	2.60	2.60	2.60	2.65	2.30	2.90
Absorption Percent	1.0	1.0	1.0	2.0	2.0	5.0	2.0
Clay Lumps and Friable Particles	0.5%	0.5%	0.5%	0.5%	0.5%	0.5%	0.5%
Degradation	35%	25%	30%	30%	30%	40%	30%
Soundness (Sodium Sulfate) 5 Cycles	5.0%	5.0%	5.0%	5.0%	5.0%	5.0%	5.0%
Flat and/or Elongated Particles	5.0%	5.0%	5.0%	5.0%	5.0%	5.0%	5.0%

Ballast particle size and gradation are also crucial factors to define the behavior of this material. Table 2.2 outlines the recommended ballast gradation according to the AREMA manual for railway engineering. Gradations Numbers 24, 25, 3, 4A, and 4 are recommended to be used for the mainline ballast, while 5 and 57 are suitable materials for yard ballast.

Table 2.2. Recommended ballast gradation (after AREMA (2008))

Size No.	Size Square Opening	Percent Passing									
		3"	2½"	2"	1½"	1"	¾"	½"	d"	No.4	No.8
24	2½" - ¾"	100	90-100		25-60		0-10	0-5	–	–	–
25	2½" - d"	100	80-100	60-85	50-70	25-50	–	5-20	0-10	0-3	–
3	2" - 1"	–	100	95-100	35-70	0-15	–	0-5	–	–	–
4A	2" - ¾"	–	100	90-100	60-90	10-35	0-10	–	0-3	–	–
4	1½" - ¾"	–	–	100	90-100	20-55	0-15	–	0-5	–	–
5	1" - d"	–	–	–	100	90-100	40-75	15-35	0-15	0-5	–
57	1" - No. 4	–	–	–	100	95-100	–	25-60	–	0-10	0-5

2.2.2.2. Subballast

The subballast defines as an intermediate layer of substructure placed between ballast and subgrade. It is normally made of broad-graded crushed natural material or sand/gravel mixture. According to Selig and Waters (1994), the primary roles of ballast are as follow:

- Decrease the trainload along with the ballast layer to bearable magnitude for the subgrade.
- Separate the ballast from the subgrade, prevent ballast penetration into the subgrade, and prevent the fine upward migration from subgrade into the ballast
- Facilitate the drainage of water flowing upward from the subgrade.

2.2.2.3. Subgrade

The subgrade is the lowest layer of substructure that provides a stable platform for the track structure. It may consist of natural ground or the filling material. The subgrade must be suitable for subballast and ballast construction and be stiff enough to be able to resist against existing stresses induced by train passage. Therefore, in the case of the existence of soft soil, it should be stabilized to prevent instability or any mode of failure. It should be mentioned that the quality of the subgrade has a great impact on track maintenance and performance.

2.3. Railway Track Loading

An important factor for railway track design is to understand the loading mechanism imposed on the track structure during its service life. According to Selig and Waters (1994), loading can be categorized as mechanical (static and dynamic) and thermal. For the current research project, the influence of only mechanical load would be taking into consideration. The track structure should be designed to resist any cyclic loading generated from train passage in vertical, lateral, and longitudinal directions.

2.3.1. Vertical Forces

By definition, forces acting perpendicular to the plane of the rail are considered as vertical forces. According to Esveld (1989), vertical forces are a combination of quasi-static forces and dynamic forces. The most complicated and unknown portion of train loading is the dynamic component and generally calculated by multiplying a dynamic amplification factor to the train static load, as shown in equation (1) ((Banimahd (2008)). Jeffs and Tew (1991) stated that the dynamic portion of the vertical loading is influenced by many factors, including train speed, train static load, track condition (joints, geometry, and modulus), vehicle condition (wheel diameter, unsprung mass).

$$F_{dynamic} = DAF \times F_{static} \quad (1)$$

Where $F_{dynamic}$ and F_{static} are the dynamic and static vertical forces, respectively. Several empirical equations were proposed in the literature, by different researchers, to calculate this dimensionless factor. Table 2.3 summarized the proposed equations for dynamic amplification factors by various researchers such as AREA (1996), Talbot (1980), Eisenmann (1970), Clark (1957), ORE (1965), Agarwal (1984), Jenkins et al. (1974), and Koffman and Fairweather (1975). It can be observed that the earlier formulas proposed for the calculation of DAF are relatively simpler and only contain the train parameters including speed and wheel diameter.

Table 2.3. Summary of Models for Calculating Dynamic Amplification Factor (DAF)
(after Doyle (1980))

No.	Name of Model	Year First Published	DAF Formula ¹
1	<i>AREA</i>	1984	$1 + 5.21 \frac{V_T (\frac{km}{h})}{D(mm)}$
2	<i>Talbot</i>	1918 1920	$1 + 0.0062(V_T - 8)$
3	<i>Eisenmann</i>	1972	$1 + t\phi$ ($V_T < 60$ km/h) $1 + t\phi \left(1 + \frac{V_T (\frac{km}{h}) - 60}{140}\right)$ ($60 \text{ km/h} \leq V_T \leq 200 \text{ km/h}$)
4	<i>Clarke</i>	1957	$1 + \frac{19.65 V_T}{D\sqrt{k}}$
5	<i>Agarwal</i> (<i>Indian formula</i>)	1974	$1 + \frac{V_T}{58.14\sqrt{k}}$
6	<i>Schramm</i> (<i>German Formula</i>)	1961	$1 + \frac{V_T^2}{3 \times 10^4}$ ($V_T \leq 100$ km/h) $1 + \frac{4.5V_T^2}{10^5} - \frac{1.5V_T^3}{10^7}$ ($V_T > 100$ km/h)
7	<i>Lombard</i> (<i>South African formula</i>)	1974	$1 + 4.92 \frac{V_T}{D}$
8	<i>Prause et al.</i> (<i>WMATA formula</i>)	1974	$(1 + 3.86 \times 10^{-5} V_T^2)^{0.67}$
9	<i>British Railway</i>	1970 1972 1974	$1 + \frac{8.784(\alpha_1 + \alpha_2)V_T}{F_{static}} \sqrt{\frac{D_j F_u}{g}}$

¹ where V_T = train speed (km/hr), k =track modulus (MPa), D =wheel diameter (mm), $(\alpha_1 + \alpha_2)$ =total rail joint dip angle (radius), F_{static} =static wheel load (kN), D_j =track stiffness at joint(Kn/mm), F_u =unsprung weight at one wheel (kN), and $g=9.8\text{m/s}^2$

Typical distribution of the trainload to the track structure is depicted in Figure 2.2. The vertical wheel load causes downward and uplift force on the rail. The vertical load generated by the wheel creates a downward force on the rail at the contact point. At the

same time, the rail tends to lift up away from the wheel location and causes uplift force. If the uplift force is not compensated by the rail and sleeper weight, the sleeper could move up and down (pumping action) during the train passage and cause deterioration of the substructure components.

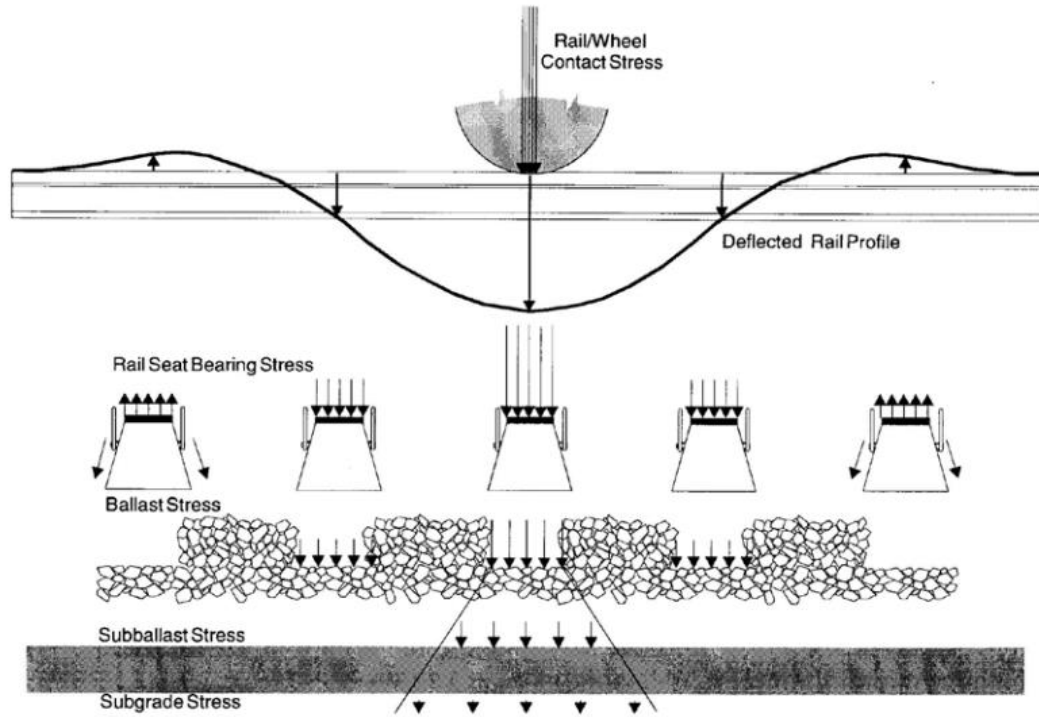


Figure 2.2. Trainload distribution to the track structure (after Selig and Waters (1994))

2.3.2. Lateral Forces

Lateral forces are defined as forces acting on the track structure parallel to the sleeper's long axis. According to Ionescu (2004), lateral forces have a significant contribution to passenger safety and comfort. Selig and Waters (1994) stated the possible sources of lateral loading on the track structure as follow:

- Lateral wheel force.

- Buckling reaction force.

Various attempts have been made in the past to assess the lateral forces acting on the railway track. ORE (1965) measured the lateral forces for the track with train speed up to 200 km/hr. The stated that the lateral forces happen only in curve lines, and it is only dependent on the radius of the curvature. However, the research performed by Key (1999) revealed that the magnitude of the lateral force is increasing with the traffic load.

2.4. Laboratory Tests on Granular Material with Special Reference to Railway Ballast Material

The primary objective of performing any geotechnical laboratory testing is to explore the behavior of soils, in a similar condition to that experienced in the field, to calculate the required parameters that represent the actual behavior of the material. In order to provide a suitable testing environment for large aggregate materials such as railroad ballast and retaining wall backfill material, there is a special need for large-scale testing devices to minimize the effects of particle size to equipment size ratio. Various apparatuses have been utilized to capture the shear strength parameters and stress-strain properties of large aggregate granular materials. The most widely used laboratory tests are the direct shear test, the triaxial test, and the direct simple shear test. However, due to the limited availability of such large scale laboratory equipment, the number of reported results on the behavior of this material is limited.

2.4.1. Large-Scale Direct Shear Test (DST)

The large-scale direct shear test (DST), which was first used by Coulomb in 1776 (Lambe and Whitman (1969)), is one possible candidate to obtain the shear strength parameters of large aggregate materials. Due to the simplicity of the test, it has been widely used for different applications of oversized particles. Understanding the shear behavior of railway substructures is a feasible application that has been studied by using large-scale DST. TolouKian et al. (2018), Liu et al. (2015), Wnek et al. (2013), Indraratna et al. (2016), and Kharanaghi and Briaud (2020) studied the shear behavior of ballast and subballast material by using a 300×300 mm shear box. Estaire and Santana (2018), Stark et al. (2014) employed a larger box up to 1×1 m for their investigations. Large-scale DST is also employed for the calculation of effective shear strength parameters of retaining wall large aggregate backfill (Bauer and Zhao (1993), Nakao and Fityus (2008), Asadzadeh and Soroush (2009), Goudarzi (2019)). Municipal solid waste material (Zekkos et al. (2010), Stark et al. (2009)), and reinforced large aggregate materials (Arulrajah et al. (2013), Indraratna et al. (2011a)) are other reported cases of using large-scale DST.

2.4.2. Large-Scale Direct Simple Shear Test (DSST)

The large-scale direct shear test (DST), which was first used by Coulomb in 1776 (Lambe and Whitman (1969)), is one possible candidate to obtain the shear strength parameters of large aggregate materials. Due to the simplicity of the test, it has been widely

used for different applications of oversized particles. Understanding the shear behavior of railway substructures is a feasible application that has been studied by using large-scale DST. TolouKian et al. (2018), Liu et al. (2015), Wnek et al. (2013), Indraratna et al. (2016) studied the shear behavior of ballast and subballast material by using a 300×300 mm shear box. Estaire and Santana (2018), Stark et al. (2014) employed a larger box up to 1×1 m for their investigations. Large-scale DST is also employed for the calculation of effective shear strength parameters of retaining wall large aggregate backfill (Bauer and Zhao (1993), Nakao and Fityus (2008), Asadzadeh and Soroush (2009)). Municipal solid waste material (Zekkos et al. (2010), Stark et al. (2009)), and reinforced large aggregate materials (Arulrajah et al. (2013), Indraratna et al. (2011a)) are other reported cases of using large-scale DST.

2.4.3. Large-Scale Triaxial Test (TT)

Large-scale triaxial test (TT) is the other common laboratory technique to investigate the shear behavior of large aggregate materials. Nålsund (2010), Sevi et al. (2009), Mishra et al. (2013), Lackenby et al. (2007), Dyvik and Kaynia (2018), Bian et al. (2016b) used the test to study the monotonic behavior of fresh ballast while Cui (2018), Tang et al. (2012), Ebrahimi et al. (2014), Cao et al. (2018) studied the impact of ballast fouling. The application of the triaxial test is also extended to different geotechnical projects such as testing rockfill dam materials (Charles and Watts (1980), Marsal (1967), Xiao et al. (2014), reinforcement impact on granular material (Bathurst and Karpurapu (1993), Moghaddas-Nejad and Small (2003), Abu-Farsakh et al. (2011)), and calculating

geotechnical properties of municipal solid waste material (Zekkos et al. (2008), Vilar and Carvalhod (2004)).

2.4.4. Comparison of the Shear Properties of the large size aggregate Materials with DST, DSST, and TT

The direct shear, direct simple shear, and triaxial tests have been used for many years to calculate the strength parameters of the soils (Saada and Townsend (1981)). These tests have been used interchangeably for testing large size aggregates. So, it is important to pay attention to the possible difference in the results. Attempts have been made in the literature to compare the results obtained from different tests. The results revealed that the difference in the calculated shear strength properties using different tests is highly dependent on the soil type. On the comparison of DST and TT, Skempton (1964), Casagrande and Poulos (1964) stated that the same effective stress parameters were obtained for lean clay. Castellanos and Brandon (2013) compared the results of a series of CD direct shear and CU triaxial tests on alluvial soils. Their results showed about a 2 to 5 degrees lower friction angle in a DST compared to the TT. Lini Dev et al. (2016) compare the results of DST and TT in drained conditions for sand. The friction angle obtained by DST was found to be 2 to 8 degrees higher compared to the TT results. The same difference was observed for sand by Cornforth (1964) and Lee (1970).

DST and DSST have also been compared for different geotechnical applications. Fei and Zekkos (2018) investigated the difference between the shear strength parameters obtained from large-scale DST and DSST on municipal waste material. According to their

results, the DST showed a higher friction angle and a lower cohesion than the DST. Dounias and Potts (1993) performed numerical analyses on idealized fully drained isotropic elastoplastic material. Their results showed that the DST overestimates the initial stiffness and peak strength by around 7.5%. The results of a comparative study on DST and DSST performed by Hanzawa et al. (2007), on clay samples showed a higher estimation of shear strength for the DST. The same trend was observed in FEM analyses performed by Tejchman and Bauer (2005).

As stated above, some comparisons between the results of these tests have been made for different materials. But, to the author's knowledge, there is no published study comparing the results of DST, DSST, and TT for samples with oversized particles.

2.5. Behavior of Ballast Under Monotonic Loading

The importance of the ballast layer is bringing attention to its stability and performance in the working environment. On the one hand, in order to have a high-quality ride, the track should be maintained at an accurate level, and when the settlement passes a certain limit, maintenance should be performed. Ballast settlement could happen as a result of various phenomenon such as particle movement and rearrangements, particle breakage and deterioration, ballast penetration into the layer underneath, and ballast contamination by fines. On the other hand, the stability of the ballast is governed by the shear strength properties of the material.

According to the research performed by Salim (2004), the behavior of ballast is influenced by the following factors:

- Particle characteristics such as size, parent rock shape, particle crushing strength, surface roughness, and resistance to weathering.
- Aggregates characteristics such as particle size distribution, density, and degree of saturation.
- Loading characteristics such as confining or normal pressure, loading history, Initial stress state, number of load cycles, frequency of loading, and amplitude of loading.

Therefore, a comprehensive understanding of the shear behavior of the ballast material is required to predict the track settlement and degradation growth of particles. If that can be accomplished, the maintenance frequency and costs may be minimized.

Various research on the cohesion less granular materials showed that shear strength characteristics of that given material govern the overall stability embankment (Bishop and Henkel (1962), Marsal (1967), and Charles and Watts (1980)). The shear strength of ballast material can be exposed by maximum shear stress, friction angle, dilation angle, and particle breakage. The factors that influenced the mechanical behavior of ballast under monotonic loading are discussed in the following.

2.5.1. Influence of Grain Characteristics

Single-particle characteristics affect the shear strength of the granular materials significantly. The influence of different characteristics, such as particle size, shape, roughness, strength, and resistance are discussed in the following.

Particle size is an important characteristic of the granular material that affects its shear strength. Several studies performed in the literature to investigate the influence of the particle size on the mechanical behavior of the coarse aggregate materials. However, there are some paradoxes among the findings. Charles and Watts (1980), Fumagalli (1969) stated that increasing the maximum particle size of the rockfill material would increase the overall shear strength. Kolbuszewski and Frederick (1963) mentioned that granular materials with larger particle sizes showed a higher friction angle. They concluded that increasing the particle size causes an increment in the dilatancy component of the friction angle. Dai et al. (2015) obtained that increasing the particle size would cause an increment of sample dilative behavior and shear strength.

In contrast, the results of Marschi et al. (1972) research on the properties of rockfill materials revealed that the shear strength decreases with increasing the maximum particle size (Figure 2.3). A similar conclusion was observed in the earlier research from Koerner (1970). Indraratna et al. (1998) revealed a similar relationship between the friction angle and the maximum particle size at the low range of confining pressure (<300 kPa). They also concluded that the effect of maximum particle size becomes negligible in higher confining pressure (>400 kPa).

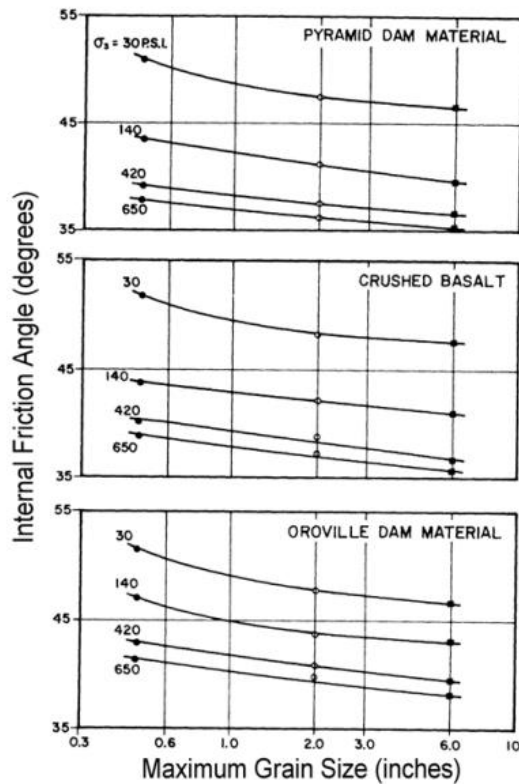


Figure 2.3. Influence of particle size on friction angle (after Marschi et al. (1972))

However, various research on the large aggregate materials reported that sample maximum particle size has a negligible impact on the shear strength properties of the material (Holtz and Gibbs (1956), Donaghe and Cohen (1978)). In conclusion, considering all the possible effects of particle size on the monotonic and the cyclic behavior of ballast, the 10 to 50 mm is recommended as an ideal range of material particle size (Selig (1985)).

Particle shape is the other characteristic of the particles that affect the shear strength of the ballast material. In general, the shear strength of the ballast material is increasing with the angularity of the particles (Salim (2004), Indraratna et al. (1998)). The results of the triaxial test performed by Holtz and Gibbs (1956) on granular material

showed that angular quarry materials have a higher friction angle in comparison with rounded riverbed materials (Figure 2.4). Chrismer (1986) stated that increasing the material angularity would increase the dilatancy, which causes higher shear strength for the material. Moreover, extensive research on the shear properties of sands has shown that higher angularity increases the degree of interlocking between the soil's grain and consequently increases the friction angle of the material (Koerner (1970), Pike (1973)). Discrete Element Method (DEM) simulations performed by Mishra and Mahmud (2017) and Boler et al. (2014) on ballast material also revealed that increasing the degree of annularity led to pronounce increase in shear strength of friction angle of the material.

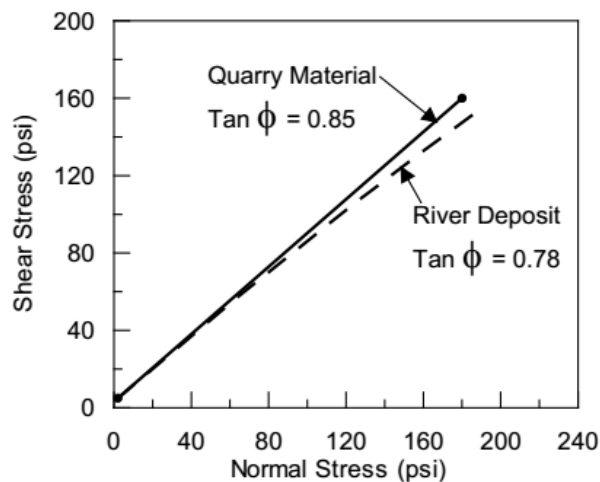


Figure 2.4. Friction angle variation with particle shape (after Holtz and Gibbs (1956))

Alongside with the particle angularity, surface roughness is considered to be another important factor that governs the shear behavior and friction angle of the granular materials. Raymond (1985) stated that particle shape and roughness are the two most important factors affecting railway track stability. Vallerga et al. (1957) conducted a series of triaxial tests on the glass beads with the range of surface roughness. The results showed

that increasing the surface roughness of the sample increases the internal friction angle by 8 degrees. Pike (1973) performed a shear box test on the materials with different sizes and roughness. The results showed that the dry density of the material with the same compaction efforts decreases by increasing the angularity and the roughness of the materials while the shear strength still increased.

Parent rock strength is another particle characteristics that influence the behavior of the material. It has a direct influence on the degradation potential of the ballast and indirect impact on the settlement and plastic deformation of the layer both in vertical and lateral directions. The results of Charles (1973) investigations revealed that there is a relationship between the unconfined compressive strength of the parent rock and the material compressibility. They concluded that the materials with higher parent rock strength show less compressibility.

Particle crushing strength is a usual method to evaluate the degradation potential of the aggregates which govern the shear strength of the ballast materials. By definition, particle crushing strength is dependent on the strength of the parent rock and particle geometry, loading point and direction (Salim (2004)). According to McDowell et al. (1996), particle fracture has a great impact on the behavior of crushable materials. Katzenbach and Festag (2004) classified the particle crushing into two categories of particle fracture or breakage and particle abrasion. Particle breakage is defined as the condition that particle divided into parts with approximately the same dimensions, and this case can happen at the high-stress level. However, particle abrasion refers to the case that

small pieces of the grain detached from the surface and it is independent of the stress condition.

2.5.2. Influence of Aggregate Characteristics

The particle assembly properties such as particle gradation, void ratio, density, and moisture content also affect the behavior of ballast material. The influence of all the abovementioned parameters is discussed in the following.

Grain size distribution is an important factor that governs the behavior of ballast under monotonic and cyclic loading conditions. Various researchers studied the role of grain size distribution on the performance cohesion less large aggregate materials. Thorn and Brown (1989) performed a series of triaxial tests on the granular material with the maximum particle size and various gradation from uniform to wide distributions. The results revealed that materials with the uniform particle size distribution show less friction angle and density while having better drainage and elastic shear stiffness (Figure 2.5). They also concluded that the grain size distribution has a negligible impact on the friction angle of materials in loose and uncompacted conditions.

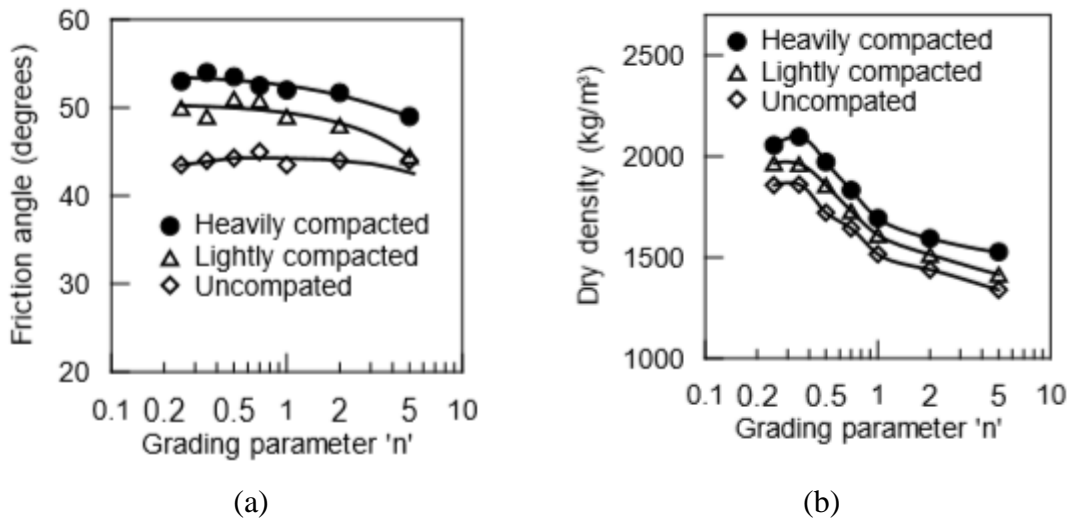


Figure 2.5. Influence of particle size distribution on (a) friction angle, (b) dry density (after Thorn and Brown (1989))

On the one hand, the Uniform gradation of the particles increases the void ration of the sample. Raymond (1985) mentioned that ballast with wider gradation contains less void ration, and therefore it is stronger. The same statements were observed from other researchers (Marsal (1967) and Jeffs and Tew (1991)). On the other hand, one of the ballast main function is to provide drainage for the track structure. Therefore according to Salim (2004), the optimum ballast grain size distribution should be between uniform and broadly graded conditions to be able to satisfy strength, settlement, and drainage requirement for the ballast layer.

Existent void ratio (or density) can be considered as the next aggregate characteristics that affect the monotonic behavior of the ballast. According to Terzaghi et al. (1996), the volume of voids in the porous materials has a great impact on the mechanical behavior of the material. The role of degree of compaction, which controls the

density and the void ratio of the ballast has been well recognized in the literature (Profillidis (2016) and Indraratna and Ionescu (2000)). Lee and Seed (1967) showed that increasing the degree of compaction, which leads to a lower void ratio at the same stress level would increase the shear strength properties of the granular material (Figure 2.6).

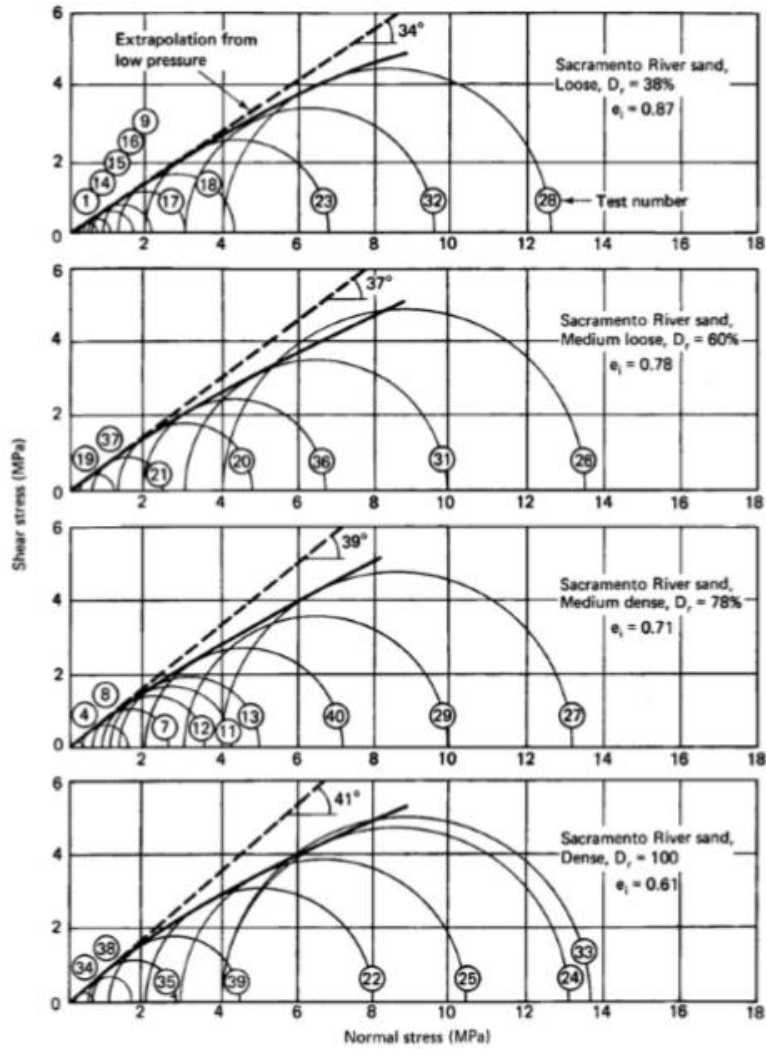


Figure 2.6. Influence of relative density on the shear strength of sand using drained triaxial test (after Lee and Seed (1967))

Research performed by Roner (1985) on the quartzite ballast materials revealed that increasing the density of the materials increases the shear strength properties, and this relationship is independent of the particle size and gradation (Figure 2.7).

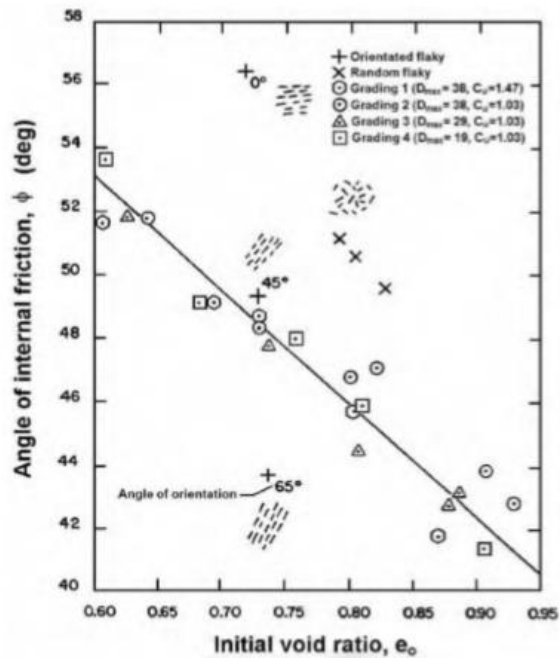


Figure 2.7. Influence of void ratio on friction angle (after Roner (1985))

Moisture content can be named as the other influence factor that govern the monotonic behavior of ballast material, especially in contaminated condition. Hardin (1985) explored the difference between the shear behavior of Antioch sand in saturated and dry conditions. Their results showed that increasing the moisture content would significantly increase the crushability potential of the material and therefore decreased the particle hardness. According to Sowers (1965), the same behavior was observed for crushed rock. Dombrow et al. (2009) studied the impact of moisture content on the shear strength of coal dust fouled ballast. The results showed that the presence of moisture in

the fouled ballast magnifies the negative impact of the fouling agent on the shear strength of the material. Qian et al. (2016) investigated the impact of moisture on the shear strength of fouled ballast by using a large-scale triaxial test. The results showed that moisture content has a significant effect on the shear strength. According to their results, adding 3% of water caused nearly 50% shear strength reduction in comparison to a fully dried fouled ballast (Figure 2.8). Light et al. (2014) results of triaxial compression tests clarified that the modulus values of wet fouled ballast decreased approximately 40 to 60 percent.

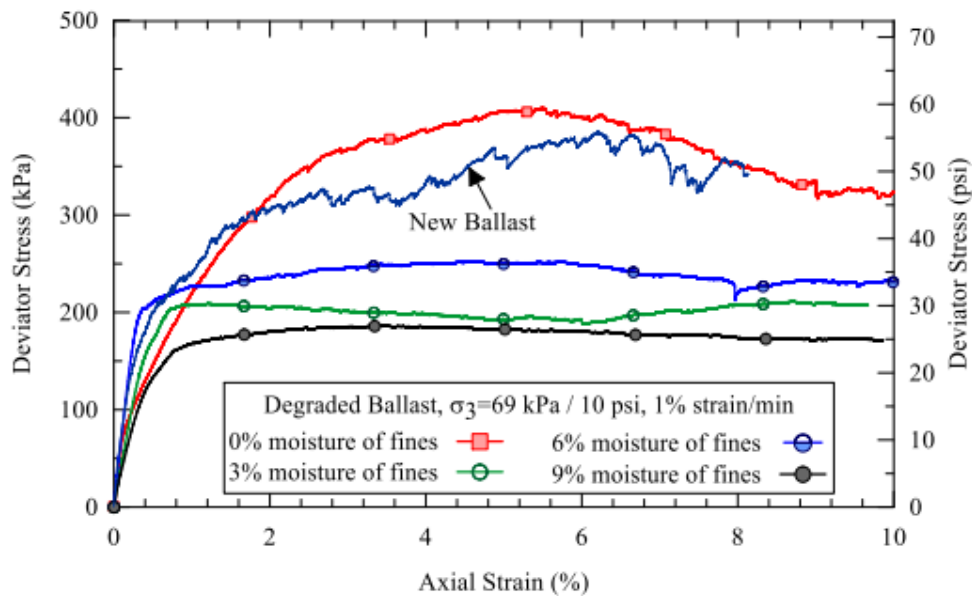


Figure 2.8. Influence of moisture content on the shear strength of fouled ballast (after Qian et al. (2016))

2.5.3. Influence of Loading Characteristics

The behavior of the ballast is highly dependent on the stress state and the loading characteristics. Therefore it is vital to understand the influence of field stress state and train loading on the behavior of the ballast. In situ stress state, which is defined as a stress

state in ballast before train loading can be simulated by confining stress or normal stress (Stark et al. (2018)). Moreover, train loading is consists of different components including cyclic loading amplitude, frequency, number of load cycles. This section explored the effect of loading on the monotonic behavior and shear strength parameters of the ballast layer.

The monotonic shear behavior of the ballast is directly influenced by field stress conditions. Two typical stress conditions are usually used for laboratory testing:

- Confining pressure applied to triaxial tests.
- Normal stress applied to direct shear and direct simple shear test.

The effect of field stress state in laboratory triaxial testing is simulating with confining pressure, which is representing the confining stress acting on the ballast layer before the train passage. Therefore it is important to have a clear understanding of the effect of confining stress on the shear behavior of ballast material. The significant role of confining stress on the shear strength of the granular materials has been recognized by various researchers in the literature (Terzaghi et al. (1996), Drucker (1957), Roscoe (1953), and Vesic and Clough (1968)). Charles and Watts (1980) attempt to examine the stability of highly compacted rockfill slopes using large scale drained triaxial tests on a wide range of confining pressures. They performed a series of tests on various rock types, including sandstone, slate, and basalt, with confining pressure up to 700 kPa. The results showed a strong dependence of shear strength of the material to the confining pressure and observed nonlinear failure envelope (Figure 2.9).

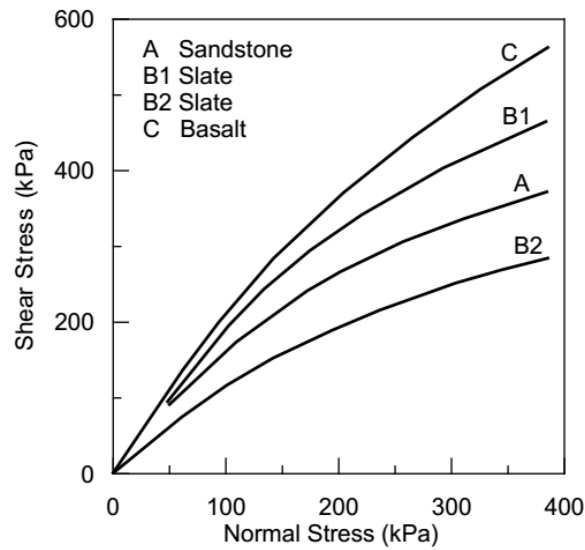


Figure 2.9. Non-linear failure envelope at low confining pressure (after Charles and Watts (1980))

Indraratna et al. (1998) investigated the behavior of ballast material at low level confining pressure using large scale monotonic triaxial tests. It is shown that shear behavior and deformation of the material at low level confining pressure are significantly different with a high level of pressure. The results showed a significant dependency relationship between internal friction angle and confining pressure (Figure 2.10). They concluded that in lower values of confining pressure because the stress state is less than particle crushing strength, the materials show a higher dilation angle, which leads to a higher friction angle. Therefore increasing the confining pressure causes more particle crushing and consequently decreases the friction angle. The same phenomenon was observed in the laboratory investigations performed by Marschi et al. (1972), Marsal (1967), and Charles and Watts (1980) on the other large aggregate granular materials.

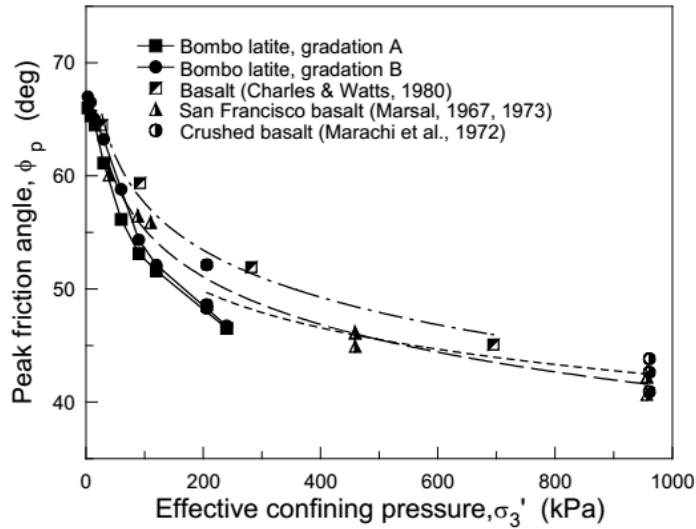
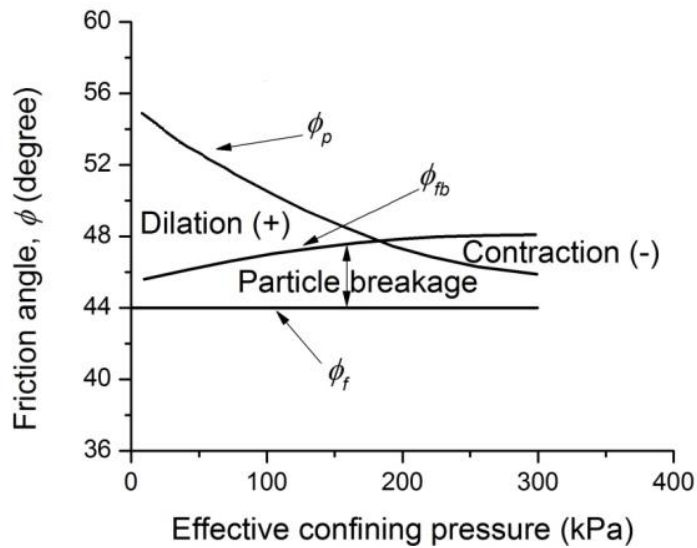


Figure 2.10. Influence of confining pressure on the peak friction angle (after Indraratna et al. (1998))

Indraratna and Salim (2002) performed a series of large scale triaxial tests to clarify the relationship between confining pressure, particle breakage, friction angle, and dilatancy under monotonic loading. Figure 2.11 shows the variation of different friction angles with increasing the applied confining stress. As can be observed at lower confining pressure the huge difference between ϕ_p and ϕ_{fb} shows a higher dilatancy, which is further decreased in higher confining pressure. The higher difference between ϕ_p and ϕ_{fb} shows the higher particle degradation at elevated confining pressure.



- * ϕ_p is friction angle of aggregate at peak deviator stress
- * ϕ_{fb} is apparent friction angle excluding dilatancy effect but including particle breakage effect
- * ϕ_f is basic friction angle of an aggregate excluding particle breakage and dilatancy effects

Figure 2.11. Influence of confining pressure, particle breakage, and dilatancy on the friction angle (modified after Indraratna and Salim (2002))

In the case that Laboratory direct shear or direct simple shear tests were selected to be used for investigating the shear behavior of the material, the normal stress should be used to represent the field stress condition. Normal stress is corresponding to vertical stress applied to the in situ vertical stress, which would be the weight of the superstructure and the ballast layer prior to train loading. Various researchers have been investigated the effect of normal stress on the shear behavior of the granular materials.

Estaire and Santana (2018) conducted a series of a 1 m by 1 m large-scale direct shear test on the mylonitic and andesitic material under a wide range of normal stress to study the influence of normal stress magnitude on the ballast shear strength. The results

showed the shear strength of the ballast is depended on the applied normal stress, and the parabolic failure envelope is the best representative of the failure envelope (Figure 2.12). They also showed that the secant friction angle is decreased nonlinearly with normal stress (Figure 2.13).

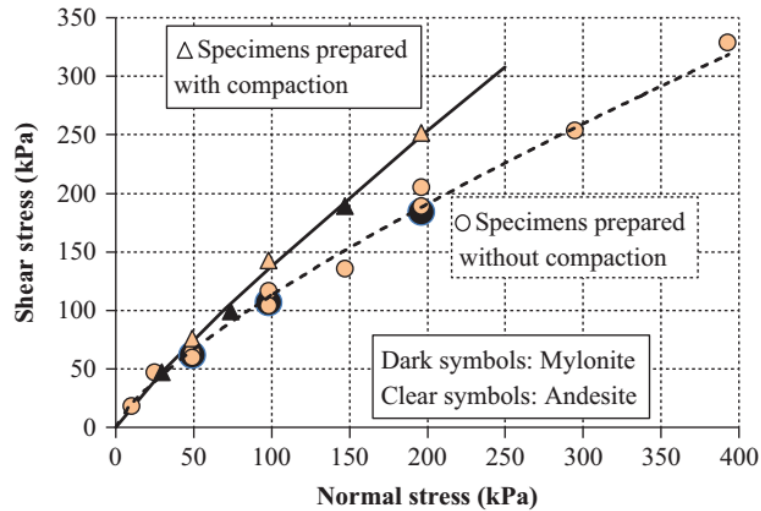


Figure 2.12. Non-linear failure envelope from the direct shear test (after Estaire and Santana (2018))

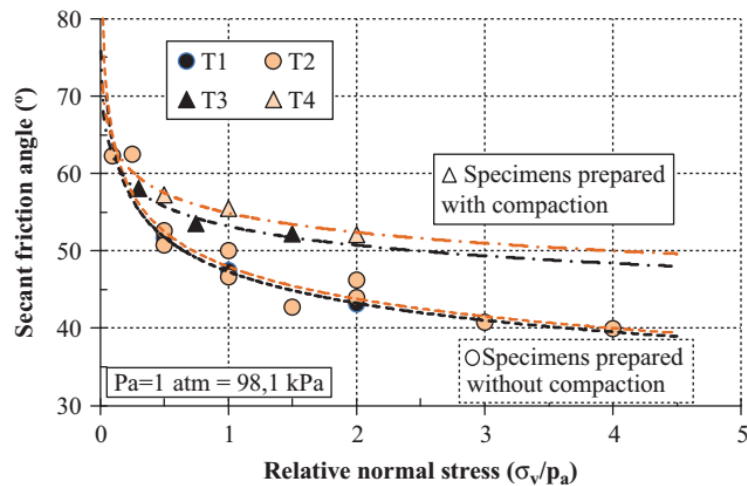


Figure 2.13. Secant friction angle variation with relative normal stress from the direct shear test (after Estaire and Santana (2018))

Asadzadeh and Soroush (2009) are also tried to investigate the impact of normal stress on the particle breakage and shear strength of rockfill material using a direct shear test. The results showed increasing the normal stress would increase the shear strength of the material nonlinearly. They also found that particle breakage of the material is increasing in higher normal stress. The same results were reported in Discrete Element (DEM) analysis of the direct shear test performed by Sitharam (1999) and Wang and Gutierrez (2010).

Confining stress applied in triaxial test and normal stress applied in direct shear or direct simple shear test should be representative of the vertical and confining stress conditions in the field, respectively. The range of values for these stresses were stated in the literature. Indraratna et al. (2010) reported that the average magnitude of the confining pressure for most of the tracks in Australia rarely exceeds 60 kPa. Suiker et al. (2005) stated the same value applied for the European track. According to their results, the range of confining pressure varies between 10 to 60 kPa in most of the sites. Moreover, Selig and Alva-Hurtado (1982) reported that the average confining pressure for the ballast layer is less than 40 kPa.

Stark et al. (2018) conducted the three-dimensional finite element modeling to verify the amount of confining pressure and normal stress to be used for laboratory tests. Table 2.4 provides the average value for the in situ stresses. It is important to mention that these values are prior to train passage and contain the weight of the track superstructures.

Table 2.4. Recommended range of normal and confining stresses for ballast based on FEM simulations (modified after Stark et al. (2018))

Stress Condition	SI (kPa)	Imperial (psf)
Normal Stress	0 to 24	0 to 500
Confining Stress	0 to 72	0 to 1,500

2.6. Behavior of Ballast Under Cyclic Loading

Railway substructure (ballast, subballast, and subgrade), which works as a railway foundation, is constantly subjected to the cyclic loading due to train passage. According to Selig and Waters (1994), the behavior of ballast under cyclic loading is nonlinear, stress-dependent, and completely different from the monotonic behavior of ballast. In the presence of the repeated loading, ballast particles are experiencing various mechanical processes, including sliding, slipping, rolling, and rotation, which causes deformation of the ballast (Ngo (2012)). In general, the ballast tends to densify under cyclic loading, and this tendency is independent of the cyclic amplitude stress level. Suiker et al. (2005) showed the densification tendency of the ballast under a wide range of cyclic loading amplitude, even the magnitude close to static failure of the material.

The deformation of the ballast under cyclic loading is being categorized to elastic (resilient) deformation and plastic (permanent) deformation. Figure 2.14 shows the stress-strain curve of unbounded granular aggregate during one load cycle (Lekarp et al. (2000)).

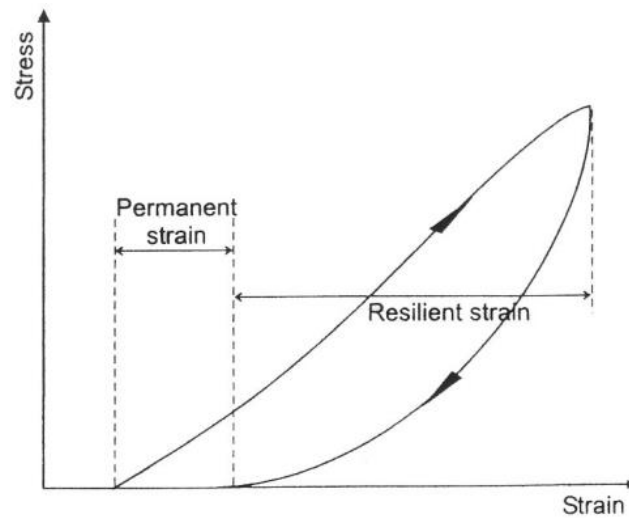


Figure 2.14. Strains in granular materials under one cycle of load application (Lekarp et al. (2000))

2.6.1. Resilient Behavior of Ballast

The resilient behavior of the granular materials is defined by resilient modulus and poisson's ratio (Lekarp et al. (2000)). The resilient modulus (M_R) is the ratio of cyclic loading amplitude and the recoverable portion of the strain. Due to the densification of the granular material, the resilient modulus increases with the number of cycles until it reaches the approximate constant value after a certain number of cycles (Figure 2.15) (Selig and Waters (1994)). Moreover, Aursudkij (2007) reported that under the cyclic loading with constant amplitude, the value of resilient modulus increases until it becomes constant after certain cycles.

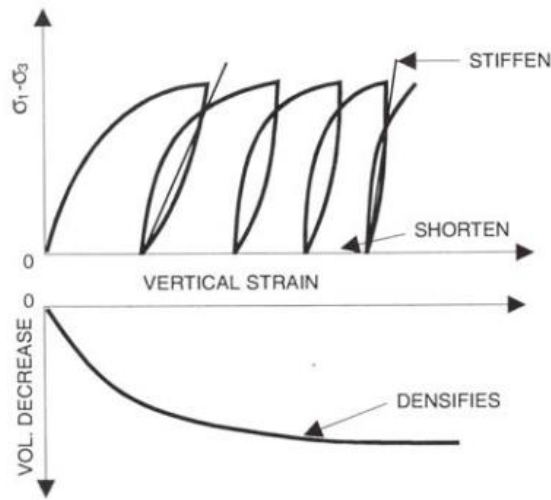


Figure 2.15. Behavior of ballast under cyclic loading (after Selig and Waters (1994))

The resilient behavior of the ballast is influenced by various factors that can be categorized as follow:

- Influence of single-particle characteristics such as maximum particle size, particle shape, and aggregate type.
- Influence of aggregate characteristics such as density, particle size distribution, and moisture content.
- Influence of loading characteristics such as stress level, loading frequency, number of cycles, and amplitude of cycles.

2.6.1.1. Influence of Grain Characteristics

Grain characteristics such as maximum particle size, particle shape, roughness, and aggregate type are among the important factors affecting the resilient behavior of the granular material. Janardhanam and Desai (1983) studied the effect of grain size on the

resilient behavior of the ballast by using a series of cyclic triaxial tests. They reported that although the ballast strain is independent of the grain size, the resilient modulus is significantly influenced by ballast particle size. Figure 2.16 shows the increment of the resilient modulus with the mean particle size at low confining pressure. The same relationship between the particle size and the resilient modulus was reported by Bosserman (1982) and Kolisoja (1997).

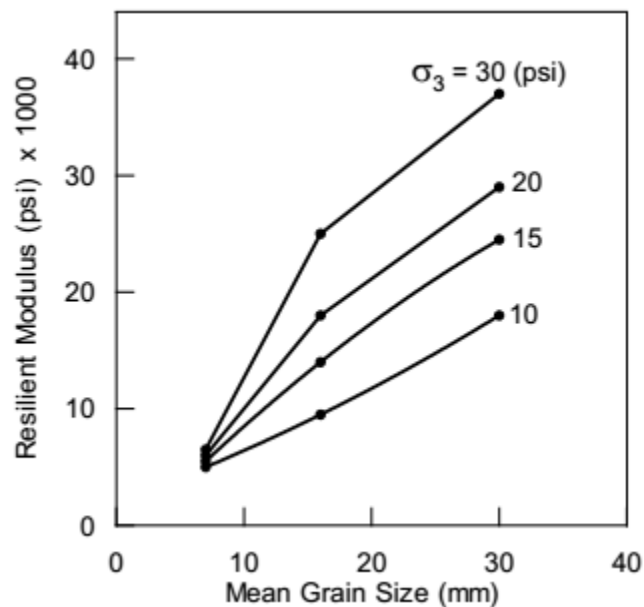


Figure 2.16. Influence of particle size on ballast resilient modulus (after Janardhanam and Desai (1983))

Particle shape and roughness are considered to be influencing factors on the resilient modulus of the ballast under cyclic loading. It is reported that the angular crushed aggregates showed higher resilient modulus because of the better load spreading potential (better aggregates interlocking) (Hicks and Monismith (1971) and Allen and Thompson (1974)). Barskale and Itani (1989) tried to investigate the effect of particle shape and

roughness on the resilient modulus of the granular material wide range of normal stress. According to their results, materials with angular and rough particles showed approximately 50% and 25% higher resilient modulus at low and high mean normal stress, respectively.

Various granular materials with the same particle characteristics show the different resilient modulus. Heydinger et al. (1996) reported that the resilient modulus of the gravel is higher than crushed limestone and slag. Furthermore, Zaman et al. (1994) result revealed that in the same testing condition and aggregate gradation, the resilient modulus varies with material type remarkably. Among the different material types they have tested, sandstone gravel shows the lowest, and limestone gravel shows the highest resilient modulus. Kolisoja (1997) declared the dominant role of rock type on the resilient modulus of the ballast.

2.6.1.2. Influence of Aggregate Characteristics

Besides the particle features, the resilient modulus of granular materials is governed by the aggregate characteristics, including gradation, density, fine contents, and moisture content. There are some contradictory results reported in the literature on the effect of material gradation on the resilient modulus of the ballast. Some studies stated that the particle size distribution has a slight impact on the resilient modulus. Among these studies, Thorn and Brown (1989) and Brown and Selig (1991) reported that the uniformly graded material has slightly higher resilient modulus, while Knutson (1977) reported that materials with broader gradation (well-graded) are moderately stiffer than the standard

No.4 and No.5 materials. On the other hand, Janardhanam and Desai (1983) and Sweere (1992) reported the significant dependency of the resilient modulus to the gradation. Heydinger et al. (1996) stated that the highest resilient modulus for limestone was observed for open-graded material.

Despite the clear understanding of the effect of density on the behavior of ballast under monotonic loading, there are some contrary statements on the impact of density on the cyclic behavior of the material. Various researchers (Hicks and Monismith (1971), Trollope et al. (1962), and Rada and Witzak (1981)) stated that increasing the degree of compaction, which increases the density would enhance the granular material behavior under cyclic loading and cause higher resilient modulus. Kolisoja (1997) laboratory investigations revealed that increasing the sample density (i.e., decrease porosity) greatly impacts the resilient modulus of the material. They concluded that increasing the aggregate density would increase the number of contacts in each grain, which decreases the contact stress which lead to the less deformation in particle contacts and consequently increase the resilient modulus. In contrary Brown and Selig (1991) and Thorn and Brown (1989) stated that the degree of compaction is an insignificant factor for the resilient behavior of granular materials under cyclic loading.

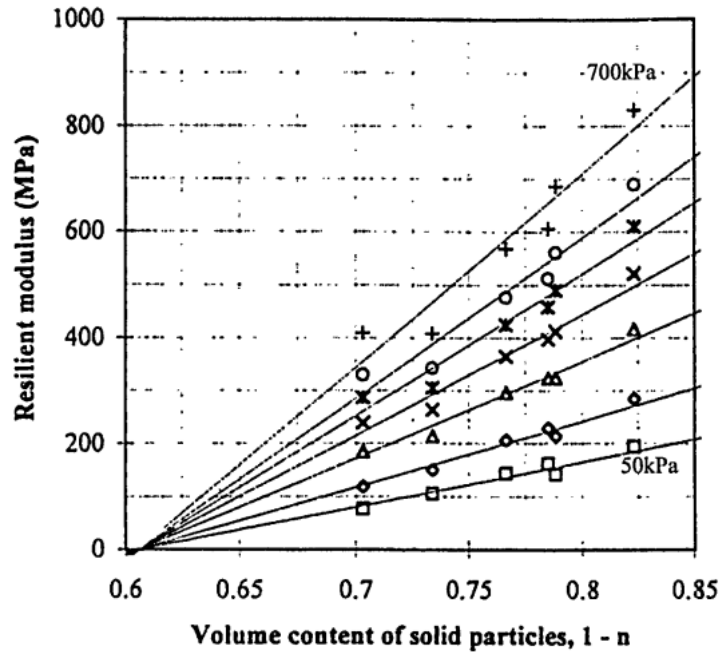


Figure 2.17. Resilient modulus of a well-graded crushed rock as a function of volume content of solid particles (after Kolisoja (1997))

The moisture content existent in the aggregate considered to be an effective factor in the resilient behavior of the material in most of the research found in the literature. Hicks and Monismith (1971), Khogali and Zeghal (2000), and Ping and Yang (1998) reported the high dependency of the resilient modulus to the moisture content. Lekarp et al. (2000) mentioned that the effect of moisture content in partially saturated conditions is negligible while increasing the water content to the saturation condition can significantly reduce the resilient modulus. Hicks and Monismith (1971) stated that the effect of moisture content is only significant for the values higher than optimum water content. The dependency of resilient modulus to the moisture content can be a reason for increasing the

suction (Dawson and Gomes Correia (1989)) and the lubrication effect of water between the grains (Thorn and Brown (1989)).

In contrast, the results of Kolisoja (1997) investigations revealed that for openly graded materials, the impact of water content on the resilient modulus of unbounded granular materials is negligible. The same finding was reported by Boyce (1976) for well-graded crushed rock. They concluded that if the full drainage is provided for the well-graded materials, the same resilient behavior would observe for the aggregates in the dry and saturation conditions.

2.6.1.3. Influence of Loading Characteristics

As it is mention previously, loading parameters can significantly alter the resilient behavior of the ballast under cyclic loading. The effect of stress state (i.e., confining pressure and normal stress) on the cyclic behavior of granular materials has been investigated extensively in the literature (Indraratna et al. (1998), Lackenby et al. (2007), and Selig and Waters (1994)). The results of all investigations consistently pointed out that increasing the state of stress increases the resilient modulus. Allen and Thompson (1974) showed that increasing the bulk stress from 69 to 552 kPa causes a 400% increment in the resilient modulus crushed limestone aggregates. Lackenby et al. (2007) tried to understand the relationship between the confining pressure, deviatoric stress, and resilient modulus by using a triaxial test. According to their results for any constant magnitude of deviatoric stress, resilient modulus increases in higher values of confining pressures (Figure 2.18).

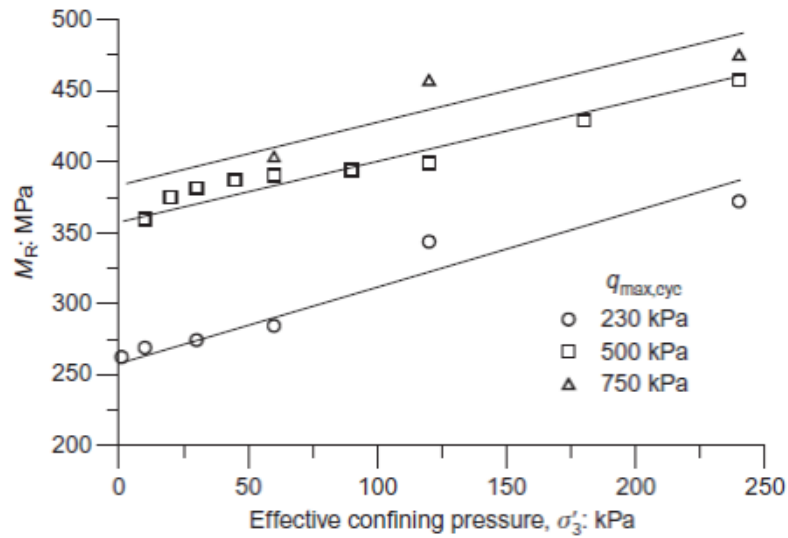
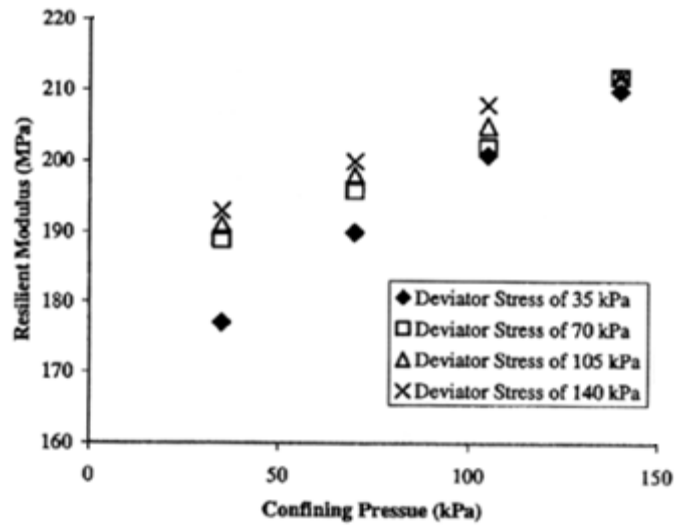
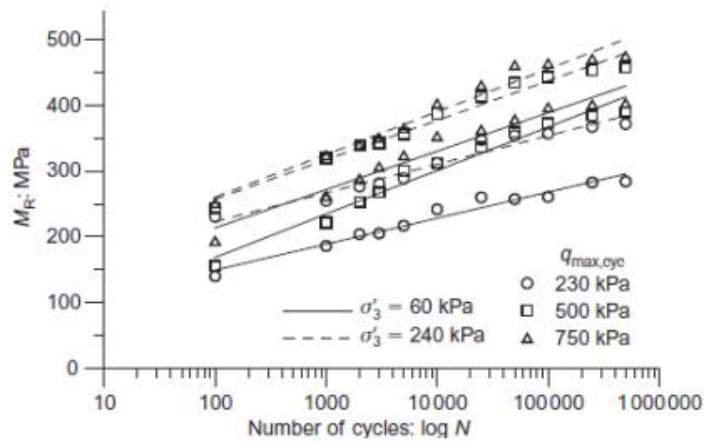


Figure 2.18. Influence of confining pressure on the resilient modulus under various deviatoric stresses (after Lackenby et al. (2007))

It is argued that the resilient modulus is less sensitive to loading amplitude in comparison with confining pressure (Lackenby et al. (2007)). Different statements about the influence of the loading amplitude on the resilient behavior of the granular material can be found in the literature. Allen and Thompson (1974), Hicks and Monismith (1971), and Seed et al. (1967) mentioned that the resilient modulus is independent of the magnitude of the cyclic loading. Various researchers concluded that increasing the loading amplitude increases the resilient modulus. As it is shown in Figure 2.19 (a), Zeghal (2004) showed that the impact of the loading amplitude is only remarkable in the low-stress level condition. However, the results of Lackenby et al. (2007) show an improvement on the resilient modulus of the material with increasing the loading amplitude in various confining pressure (Figure 2.19 (b)).



(a)



(b)

Figure 2.19. Influence of deviatoric stress on the resilient modulus (a) After Lackenby et al. (2007); (b) After Zeghal (2004)

The number of cycles is another loading characteristics that govern the behavior of the material under the cyclic loading. The majority of previous works on the cyclic behavior of the granular materials show that with increasing the load cycles the material gets more compacted and as a result shows more strength, stiffness and resilient modulus

(Moore et al. (1970), Key (1999), and Suiker et al. (2005)). However, this increment in the resilient modulus continues until a certain number of repeated load applications, and it becomes approximately constant. The laboratory investigation on the railroad ballast performed by Shenton (1974) revealed that the magnitude of resilient modulus increased rapidly in the first ten cycles and stabilized after approximately 100 cycles. Hicks and Monismith (1971) reported the same trend for the crushed rock and crushed gravel. They mentioned that the magnitude of resilient modulus becomes constant after 50 to 100 cycles.

Frequency is another cyclic loading characteristics that should be explored for the purpose of the railway substructure design. Previous research on the effect of loading frequency and duration shows its insignificant effect on the resilient behavior of the ballast (Thorn and Brown (1989), Boyce (1976), Selig and Waters (1994), and Seed et al. (1967)). Lekarp et al. (2000) stated that the frequency of the loading could be considered to be an influencing factor only when the material is nearly saturated. Seed et al. (1965) recorded the increment of resilient modulus from 160 to 190 MPa, while the loading duration decreased from 20 min to 0.3 sec.

2.6.2. Permanent Deformation and Cyclic Densification of Ballast

Railway substructure, which consisted of ballast, subballast, and subgrade, is consistently subjected to the cyclic loading due to train passage. During the cyclic loading, the aggregates going through various micromechanical processes, which lead to cyclic densification and eventually cause permanent deformation. Lambe and Whitman (1969)

stated that this phenomenon is mainly governed by particle rearrangement and settlement. According to Selig and Waters (1994), most of the railway track settlement is occurring at the ballast layer because it is the first layer that carries the train loading. Therefore, this section is mainly focused on the permanent deformation of the ballast materials.

Suiker and de Borst (2003) performed a series of large scale cyclic triaxial tests on ballast and subballast materials to investigate the mechanism of permanent deformation under repeated loading. They categorized the permanent deformation mechanism of the ballast based on the stress domain to four regimes (Figure 2.20):

- Shakedown: defined as a zone that the ballast response under cyclic loading is completely elastic and recoverable.
- Cyclic densification: defined as a zone that the ballast experiences the progressive plastic deformation under cyclic loading.
- Frictional failure: defined as a zone that the frictional collapse happens, and it is for the case that the cyclic loading amplitude is higher than ballast shear strength.
- Tensile failure: defined as a zone that the ballast takes apart due to ballast incapability to carry the tensile load.

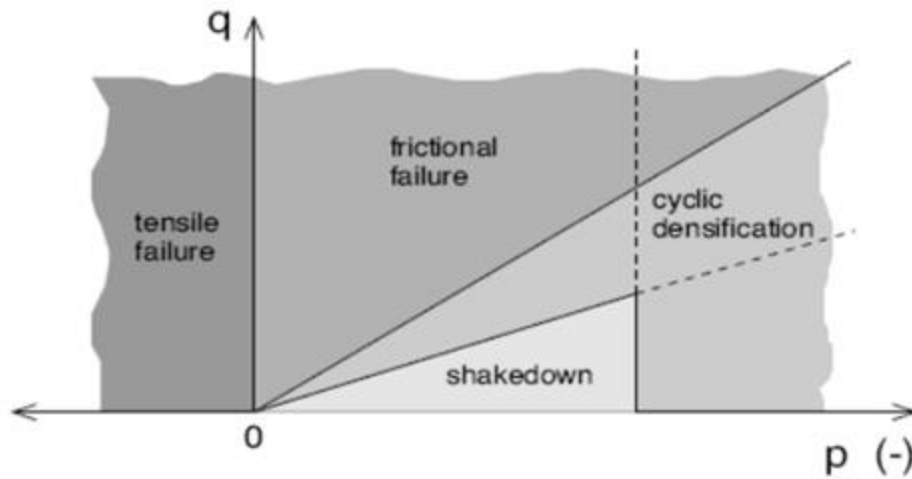


Figure 2.20. Ballast response regimes during cyclic loading (after Suiker and de Borst (2003))

Unlike resilient behavior, there are limited studies that can be found in the area of long term plastic settlement of the ballast mainly because it requires a long time to perform a large number of cycles. The results of cyclic tests performed by Selig and Waters (1994) displayed that the remarkable strain developed rapidly during the first cycle which some portion of it recovered after unloading. They mentioned that each cycle contributes an increment to the permanent strain and this contribution decreased with the number of cycles. Lekarp et al. (2000) concluded that the material is getting compacter and stiffer with increasing the number of cycles, and as a result, the rate of permanent strain growth is decreasing in the higher number of cycles.

The typical settlement of the granular materials is shown in Figure 2.21. Jeffs and Marich (1987) showed that the ballast tends to densify rapidly at the beginning (compaction phase). As can be observed, this phase is followed by a post compaction

phase in which material settlement is stabilized and growth nearly linear with the low rate with the number of cycles. The same permanent strain growth was reported later by Ionescu (2004).

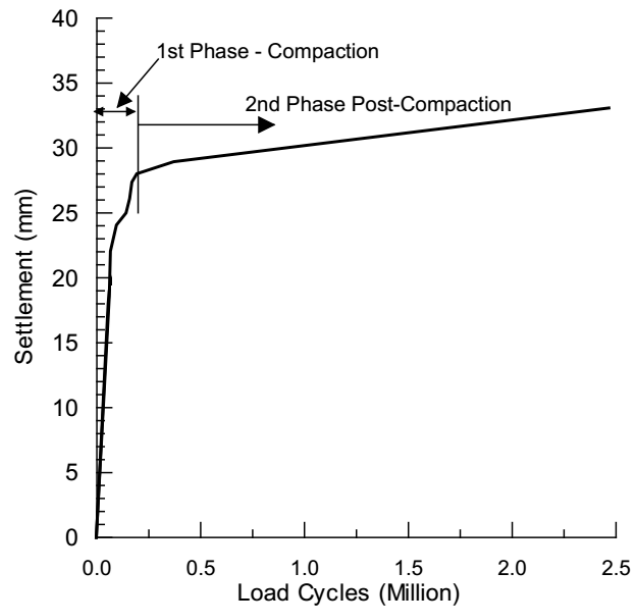


Figure 2.21. Settlement of the ballast under cyclic loading (after Jeffs and Marich (1987))

The permanent settlement and the aggregate densification of the ballast are governed by several factors. Similar to the resilient behavior, these factors can be categorized to particle, aggregate, loading characteristics. The influence of each dominant factor will be discussed in the following sections.

2.6.2.1. Influence of Grain Characteristics

As it was mentioned previously, single properties could have great impacts on the permanent settlement of the granular materials under repeated loading. The important

grain properties on the cyclic behavior of ballast are included maximum particle size, particle shape, aggregate type, and parent rock strength. However scarce studies are available in the literature on the influence of the particle characteristics on the permanent accumulated settlement of the ballast. The effect of each factor will be discussed in detail in the following.

Contrary statements on the effect of particle size on the permanent settlement of ballast can be found in the literature. The results of cyclic triaxial tests conducted by Janardhanam and Desai (1983) revealed that the ballast plastic strain is independent of its particle size in any range of stress levels. However, Raymond and Diyaljee (1979) stated that at lower cyclic loading amplitude, the uniform ballast with smaller particle size shows the less plastic strain. The same relationship between the average particle size and the settlement was further reported by Selig (1985).

The limited study can be found on the influence of particle shape on the permanent strain of the ballast. Jeffs and Marich (1987) described that the angular materials cause lower plastic strain in the same testing conditions than the rounded particles. Selig and Waters (1994) studied the impact of flakiness on the permanent accumulated settlement of the ballast under repeated loading. Based on that, they stated that increasing the particle flakiness causes decreasing stiffness and therefore increasing particle breakage and plastic settlement under cyclic loading.

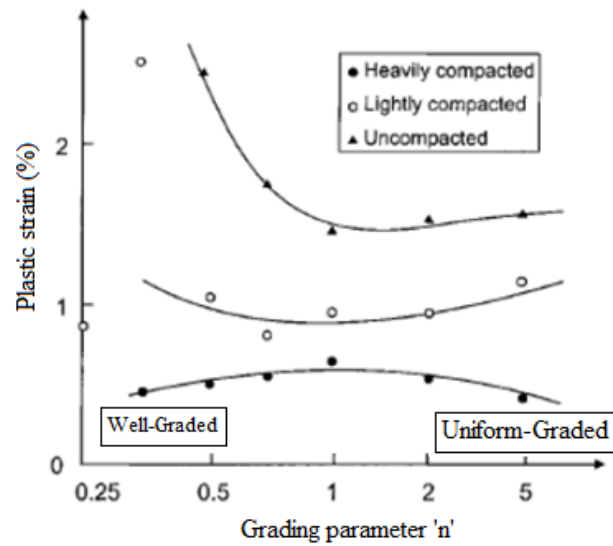
Parent rock strength is the other particle characteristics that can significantly alter the plastic deformation of large aggregate materials under the cyclic loading. According to Salim (2004) and Indraratna and Salim (2005), the parent rock strength is the most

important factor that is related to the particle breakage and degradation and consequently governs the long term plastic settlement. Jeffs (1989) studied the effect of different material types on the plastic settlement of the ballast under cyclic loading. They conducted 250,000 cycles on three different materials, including basalt, quartz, and limestone. The results showed the highest value for the plastic settlement is related to the limestone and quartz revealed the lowest strain.

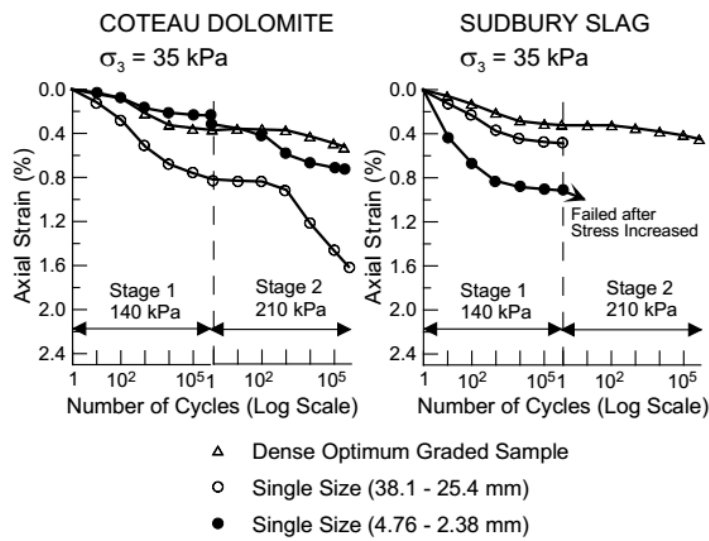
2.6.2.2. Influence of Aggregate Characteristics

The important factors regarding aggregate characteristics are including gradation, moisture content, and degree of compaction (density). These characteristics are discussed in the following.

Similar to the resilient behavior of large aggregate materials, the permanent deformation is affected by the sample particle size distribution under cyclic loading. Thorn and Brown (1989) reported that the permanent strain of unbounded granular materials could be changed with the sample density and the gradation. Their results showed that for highly compacted materials the particle gradation does not make any difference to the plastic strain. But, for uncompacted samples, the magnitude of plastic strain was highest for the well-graded materials (Figure 2.22 (a)). In contrast, Raymond and Diyaljee (1979) indicated that the accumulated plastic settlement is higher in single sized ballast (Figure 2.22 (b)). Moreover, Barksdale (1972) and Thorn and Brown (1989) also expressed that increasing the amount of fine in the sample may increase the plastic strain under cyclic loading.



(a)



(b)

Figure 2.22. Influence of aggregates gradation on the plastic strain of granular material; (a) modified after Thorn and Brown (1989); (b) after Raymond and Diyaljee (1979)

The density of the ballast has been found to be a dominant factor in the long term behavior of the ballast material under train cyclic loading. It has been well established among the previous research on the cyclic behavior of the unbounded granular materials

that compacted materials with lower void ratio acts stiffer and shows a lower plastic settlement in comparison with the uncompacted condition (Terzaghi et al. (1996), Selig and Waters (1994), Indraratna et al. (1998)). Lekarp et al. (2000) showed that increasing the density of the ballast can significantly decrease its long term plastic deformation. Figure 2.23 exemplified the influence of the degree of compaction on the plastic strain for limestone ballast under cyclic triaxial test ((Knutson, 1977)).

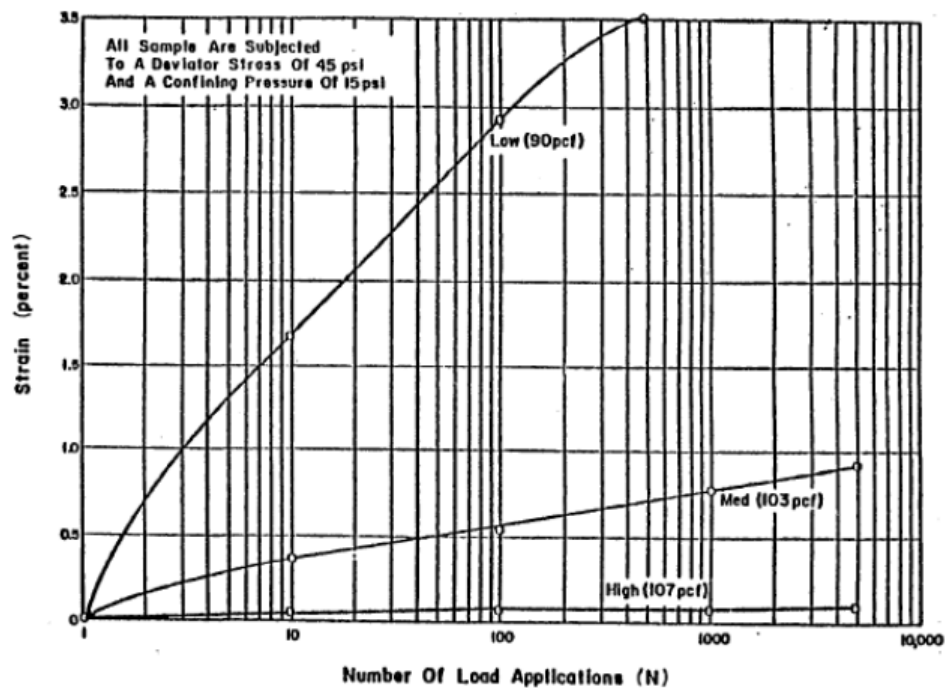


Figure 2.23. Influence of density on the plastic strain of limestone ballast (from (Knutson, 1977))

The studies on the effect of moisture content on the long term behavior of ballast are scarce. The majority of research in this area indicated that the coincidence of a high degree of water content and low drainage capability for the granular materials cause excess pore water pressure and consequently low stiffness and high plastic strain potential under

cyclic loading (Haynes and Yoder (1963), Barskale and Itani (1989), and Thakur (2011)). Thorn and Brown (1989) reported that the existence of a small amount of water could increase plastic settlement significantly.

2.6.2.3. Influence of Loading Characteristics

There is enough evidence to show that the cyclic behavior of the granular materials, including the resilient behavior and the permanent strain, are highly influenced by stress state and cyclic loading characteristics. (Selig and Waters (1994), Indraratna and Ngo (2018), Hicks and Monismith (1971), and Shenton (1974)). In this section, the influence of stress level, cyclic loading amplitude, number of cycles, and the loading frequency on the permanent settlement of ballast material is investigated.

Alongside the resilient modulus, it is previously shown that the confining pressure is one of the most important factors that control the permanent strain of the granular materials under repeated loading application (Barksdale (1972), Lackenby et al. (2007), and Brown and Selig (1991)). Barksdale (1972) reported the significant cumulative plastic settlement reduction with increasing the loading amplitude in the same testing conditions. Lackenby et al. (2007) tried to investigate the explore the impact of confining pressure on the permanent settlement of the railroad ballast by conducting a large scale cyclic triaxial test. They observe that increasing the confining stress causes enhancing the stability of the ballast and consequently lower accumulated plastic settlement (Figure 2.24).

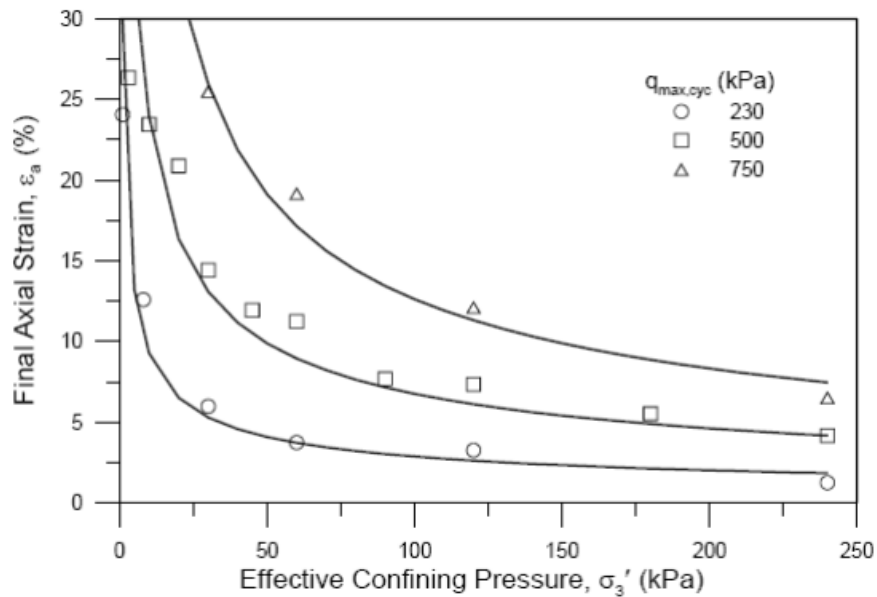


Figure 2.24. Influence of confining pressure on the final axial strain (after Lackenby et al. (2007))

The amplitude of cyclic loading is the other influencing factor on the permanent deformation of the ballast under cyclic loading. It is discussed that the rate of plastic strain accumulation is directly related to the ratio of the cyclic stress amplitude to the maximum shear strength from the monotonic loading (Olowokere (1975) and Raymond and Davies (1978)). Olowokere (1975) showed that in the same testing conditions (i.e., the degree of compaction and confining pressure) the plastic deformation is increased by increasing the cyclic stress amplitude to monotonic shear strength ratio (Figure 2.25). Moreover, Lekarp et al. (2000) concluded that the permanent strain is significantly dependent on the cyclic stress amplitude and confining pressure.

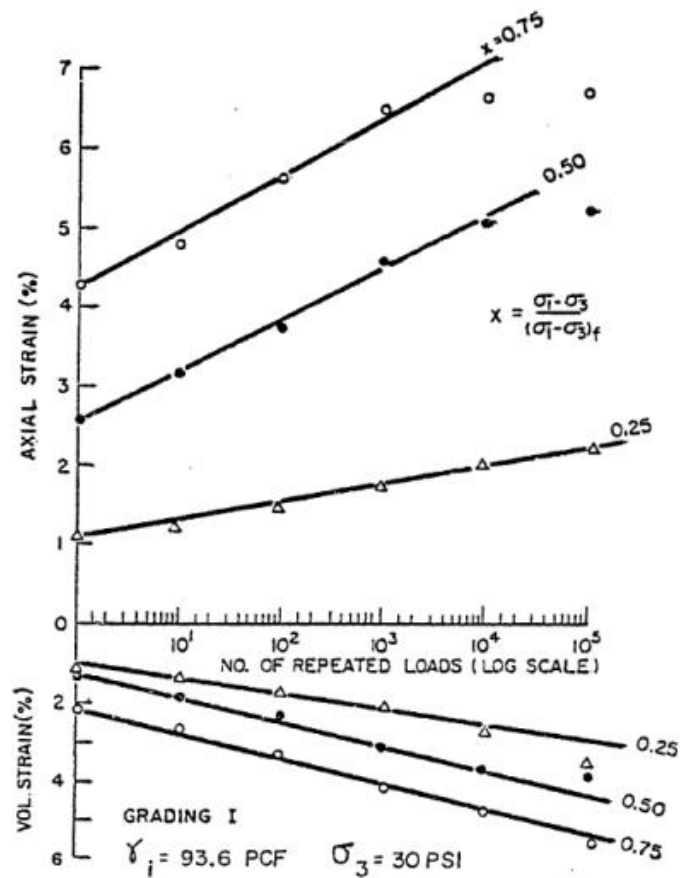


Figure 2.25. Influence of cyclic loading amplitude on the permanent strain (after Olowokere (1975))

It was shown previously that the permanent settlement of the granular materials under repeated loading is the gradual process, and each cycle contributes a small portion to the accumulated settlement (Lekarp et al. (2000)). In general with continuing the application of cyclic stress on the ballast, permanent settlement and the lateral deformation are accumulating. However, the rate of accumulation is decreasing with a number of cycles (Salim (2004)). The results of cyclic triaxial tests performed by (Suiker et al. (2005), Lackenby et al. (2007), and Raymond and Davies (1978)) revealed that the

maximum contribution of the plastic strain is corresponding to the first cycles, and the rate is decreasing until it stabilized after a certain number of cycles, which is known as a shakedown phase. Ionescu et al. (1998) conducted a series of cyclic triaxial tests on the Latite material to study the impact of loading characteristics on the cyclic behavior of the ballast. The results show the rapid growth of settlement during the first 20,000 cycles and stabilized after the application of approximately 100,000 cycles (Figure 2.26).

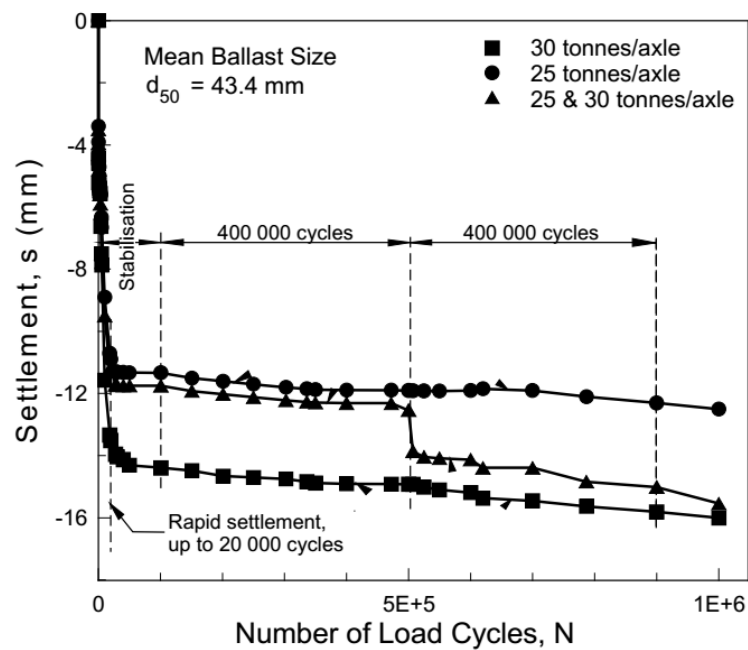


Figure 2.26. Settlement of ballast under cyclic loading (after Ionescu et al. (1998))

The frequency of the loading is the last loading characteristics that would be discussed in this section. Simulating the train speed in the laboratory tests can be done by changing the frequency of the loading. Therefore it is vital to see the effect train speed and loading frequency on the permanent settlement of the ballast. The results of some laboratory investigations on the cyclic behavior of the ballast materials indicated that

changing the loading frequency has an insignificant effect on the accumulated plastic strain of the granular materials (Shenton (1974) and Lee and Vernese (1978)). However, Shenton (1974) clarified that the results of laboratory investigations should not be confused by track behavior under the application of trains at different speeds. Because increasing the train speed causes increment of dynamic loading and consequently higher stresses on the ballast.

The results of field measurement of the dynamic vertical stresses on the ballast and subballast induced by various train speeds up to 400 km/hr are shown in Figure 2.27 (Kempfert and Hu (1999)). As can be observed, the influence of train speed on vertical stress is negligible until the speed of 150 km/hr. But, increasing the speed from 150 to 300 kph causes linear amplification of the vertical stresses induced by the train. They also mentioned that increasing the train speed from 300 to 400 kph again is insignificant on the induced dynamic vertical stress.

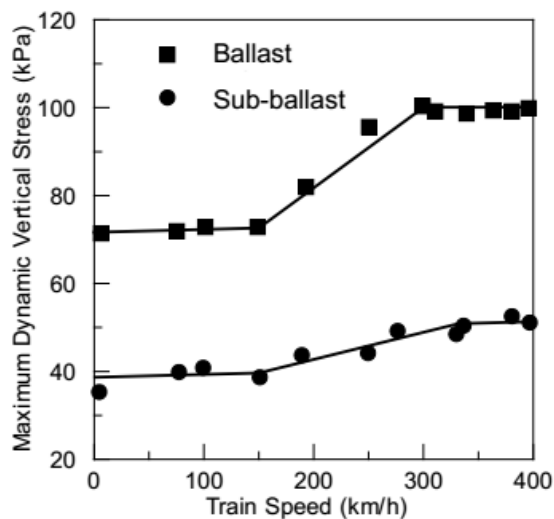


Figure 2.27. Influence of train speed on the dynamic stress (after Kempfert and Hu (1999))

Luo et al. (1996) performed Finite element modeling (FEM) simulations to investigate the impact of train speed on the dynamic behavior of the railroad ballast. They categorized the ballast settlement to three different phases based on the train speeds as follow (Figure 2.28):

- Low-speed zone (<180 km/hr): The train speed is an unimportant factor on the ballast settlement.
- Intermediate-speed zone (180-300 km/hr): Increasing the train speed increases the ballast settlement.
- High-speed zone (>300 km/hr): ballast settlement is less sensitive to the train speed.

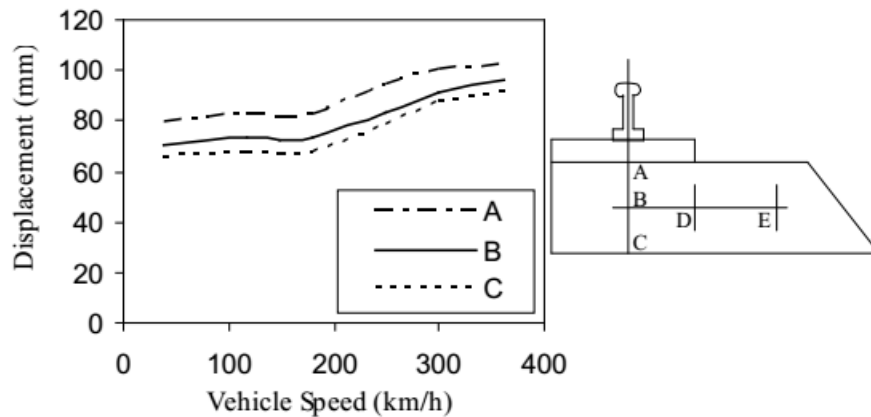


Figure 2.28. Influence of train speed on ballast settlement (after Luo et al. (1996))

2.7. Empirical Models for Prediction of Long-Term Track Settlement

Long-term accumulated plastic settlement of the railway track under train repeated loading is one of the important aspects of maintenance interval prediction. As it was mentioned by Selig and Waters (1994), for the regular track placed on a good subgrade,

the main portion of the settlement occurred in the ballast (Figure 2.29). The track settlement is generally divided into two phases. The compression or initial consolidation phase includes fast settlement after tamping, and it continues until complete consolidation. Followed by a slow settlement rate, which is in a nearly linear relationship with the number of repeated loads (Dahlberg (2001)).

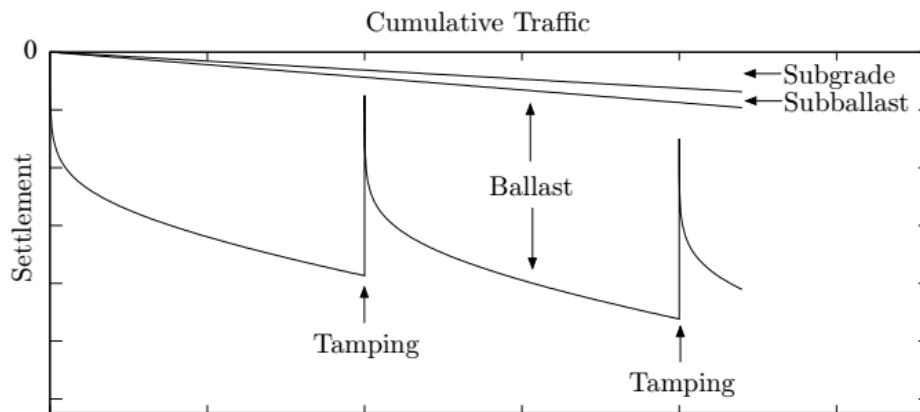


Figure 2.29. Relative contributions of the substructure components to the long-term track settlement (after Selig and Waters (1994))

This section provides some of the railway permanent settlement models available in the literature. Common assumptions for the majority of the proposed models are (Ferreira (2013)):

- Models are based on empirical investigations.
- The track settlement is divided into two parts: Initial rapid settlement followed by slow rate settlement, which proportional to the number of cycles.
- The loading conditions are constant.
- Loading of the track is shown by the number of cycles or passage tonnage.

Alva-Hurtado and Selig (1981), Raymond et al. (1978), and Ford (1995) proposed a logarithmic model to calculate the permanent strain in the ballast after a given number of cycles:

$$\varepsilon_N = \varepsilon_1(1 + C \log(N)) \quad (2)$$

where ε_1 and ε_N are the permanent strain after the number of cycles equal to 1 and N , respectively. C is the constant related to the material controlling the strain growth rate. The abovementioned model was derived from the triaxial laboratory test on the ballast. The corresponding permanent settlement can be calculated by applying the plastic settlement to the thickness of the ballast layer. Jeffs and Marich (1987) proposed a semi-log model for the permanent deformation of the ballast as follows:

$$S_v = g + h \log(N) + kN \quad \text{for } N \leq 200,000 \quad (3)$$

$$S_v = i + jN \quad \text{for } N > 200,000$$

where S_v is the total settlement, N is the number of cycles and g , h , k , i , and j are the material constants. Sato (1995) suggested that the accumulated settlement of the ballast can be defined as:

$$S_N = \gamma(1 - e^{-\alpha N}) + \beta N \quad (4)$$

where S_N is the total settlement, N is the number of cycles and α , β , and γ are the constants. Neidhart (2005) stated that the settlement change rate diminished after one million cycles. They proposed a model to calculate the long term settlement as follows:

$$S_v = S_{v1} + \frac{e \log N}{1 + f \log N} \quad (5)$$

where S_v and S_{v1} are the permanent settlement after the number of cycles equal to 1 and N, respectively, and e and f are two empirical constants. However, Indraratna and Nimbalkar (2013) mention that the abovementioned models are not representative of the response of ballast aggregates during large scale laboratory tests. Therefore, they proposed the model for calculation of the deformation of ballast during cyclic loading as follow:

$$S_v = S_{v1}(1 + a \ln(N) + 0.5b \ln(N^2)) \quad (6)$$

where a and b are the constants, N is the number of cycles and S_{v1} is the permanent settlement of the first cycle. In the above equation, the first term related to the deformation of the first cycle, the second term is representing unstable zone ($N < 10,000$), and the third term shows the stable zone settlement ($N > 10,000$).

3. LABORATORY PROCEDURE

3.1. Introduction

Laboratory testing is a standard procedure to simulate the field conditions to understand the behavior of soil materials. The testing of the coarse grain materials with small-scale conventional equipment can lead to unrealistic test results. Therefore, due to large size nature of the ballast particles, large-scale testing facilities are required. In this study, large-scale direct shear (DST), direct simple shear (DSST), and triaxial test (TT) were chosen to investigate the monotonic and cyclic behavior of the ballast material.

In this chapter, details about the large-scale testing facilities, device calibrations, testing materials, sample preparation, test procedures, and plans are presented.

3.2. Large-Scale Testing Facilities

3.2.1. Large-Scale Direct Shear (DST) Apparatus

A large-scale shearing device (ShearTrac-III) manufactured by Geocomp Corp. (Figure 3.1) was used for direct shear and direct simple shear testing in this study. ShearTrac-III can be used for different laboratory testing of the soil and aggregates, including:

- Monotonic direct shear test
- Monotonic direct simple shear test
- Cyclic direct simple shear test
- Interface shear test
- 1-D incremental consolidation up to 32 steps



Figure 3.1. ShearTrac-III apparatus

The ShearTrac-III is consisted of a load frame and a computer for test control, data acquisition, displaying the test results in real-time, and creating a report. As it is shown in Figure 3.2, the device contains two independent embedded control and data logging systems for the vertical and horizontal directions. The vertical movement is generated by the combination of the vertical-load stepper motor and a jack that moves the loading cap up and down to adjust the vertical load on the sample. The horizontal movement is generated by the horizontal-load stepper motor, which is connected to the worm gear that moves the shear box to apply a shear force to the sample. A pair of load transducer (load cell) and displacement transducer (LVDT) are placed in the horizontal and vertical direction.

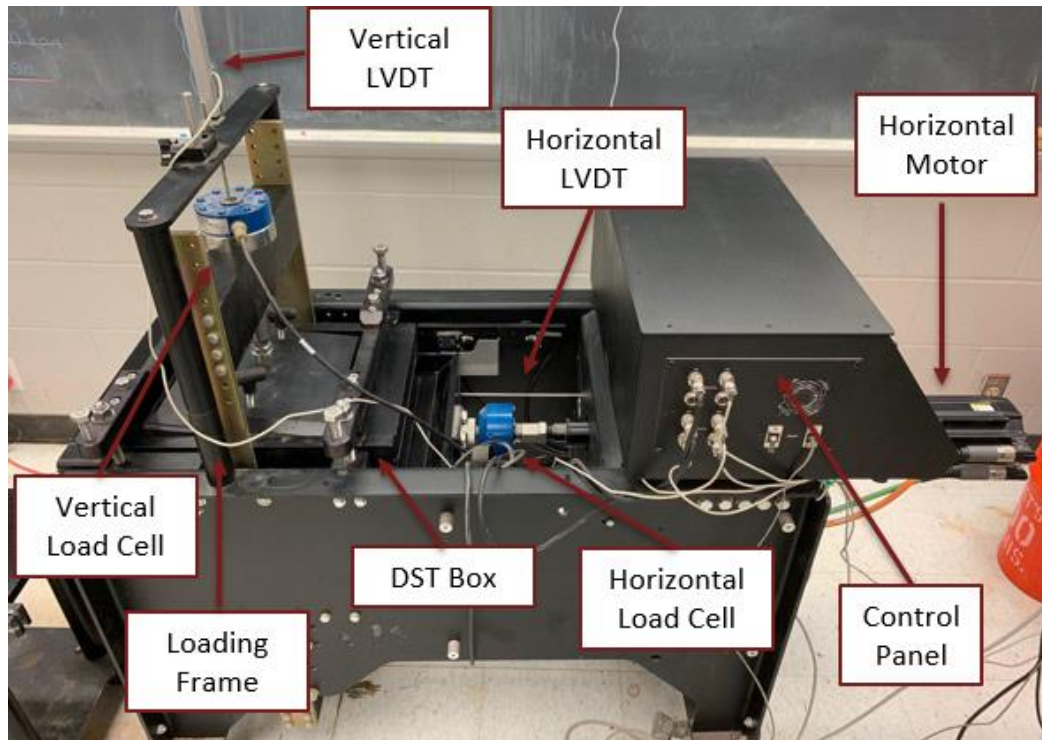


Figure 3.2. Direct shear test (DST) setup

The ShearTrac-III can accommodate a 305 mm x 305 mm (12 x 12 in.) by 200 mm (8.0 in.) height direct shear box, as shown in Figure 3.3. DST box is divided into two 100 mm high halves. After preparing a sample in the shear box, a rigid aluminum plate should be placed on top of the sample to transfer the vertical pressure to the specimen. During the test, the upper half of the shear box is fixed using the cross beam, and the lower half moves horizontally along the shearing axis. Before starting the test, a gap should be created between the two halves based on the sample particle size to create a shearing zone and to minimize the friction between the two halves. More details would be presented in the sample preparation section.

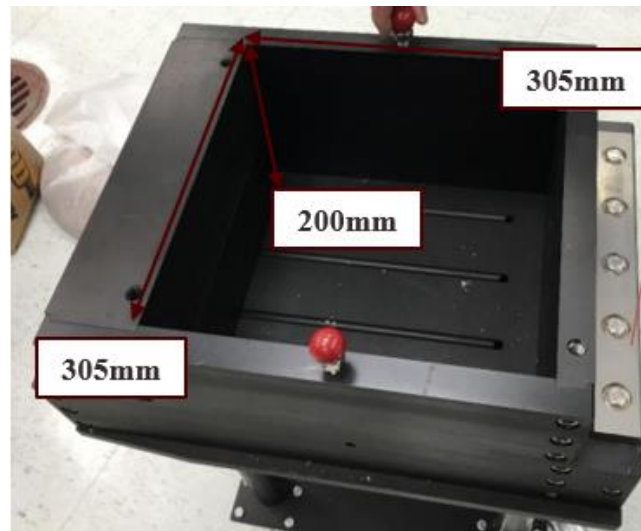


Figure 3.3. DST shear box

The direct shear test (DST) is performed in two separate phases named consolidation and shearing phase. In the consolidation phase, the magnitude and duration of applying normal pressure should be entered into the software. The device is capable of applying up to 32 loading steps with the various duration of loading based on the soil type. Table 3.1 represented the recommended duration of consolidation for different materials (GeocompCo. (2015)). The shear phase, which is performed after completion of the consolidation process, can be carried out in displacement or force control condition. The total range of horizontal and vertical movement of the device is 10 cm (4 in.) and 5 cm (2 in.), respectively. The device is capable of applying a maximum of 44.5 kN and 22.5 kN load in the vertical and horizontal directions, respectively.

Table 3.1. Recommended duration of a consolidation phase (GeocompCo. (2015))

Recommended Duration Settings for the Consolidation Phase		
Condition/Soil Type	Recommended Max. Duration	Recommended Min. Duration
Sandy Silt	1440 min (24 hr)	30 min
Silty Clay	1440 min (24 hr)	60 min
Plastic Clay	1440 min (24 hr)	120 min
Geotextile-Geotextile interface	15 min. (if creep is not significant)	
Geotextile-Geomembrane interface	15 min. (if creep is not significant)	
Geotextile-Clay interface	1 hr.	
Geomembrane-Sand Interface	15 min. (if creep is not significant)	
Geotextile-GCL Interface	24 hr.	
Geomembrane-Clay interface	Measure vertical displacement to get to end of consolidation/swelling	
Geomembrane-GCL interface		
GCL internal		

3.2.2. Large-scale Direct Simple Shear (DSST) Apparatus

The ShearTrac-III apparatus can also be utilized for performing monotonic and cyclic direct simple shear test. To perform a direct simple shear test, DSST set up, which is consisted of a round base plate and stack of shear rings, should replace the DST setup. Figure 3.4 shows the direct shear test device details ((Zekkos et al. (2018))). Similar to the DST, the DSST performs in two stages of consolidation and shearing. The lateral expansion in the consolidation phase is prevented by the stacked rings. During the shearing phase of the test, either constant vertical stress or constant height can be maintained. During the constant load test, the vertical pressure on the sample kept steady, and the specimen is able to dilate or contract. All the DSST experiments in the current research performed in constant load condition to be replicable of the ballast condition in the field.

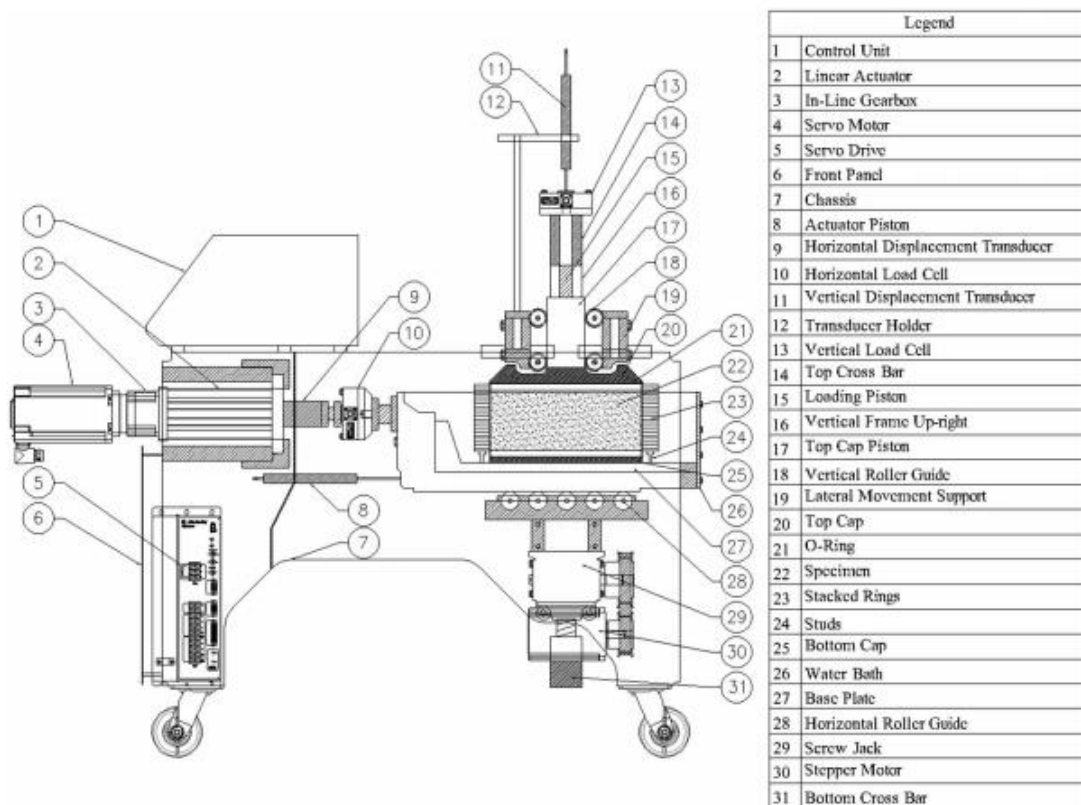


Figure 3.4. Direct simple shear test (DSST) setup (Zekkos et al. (2018))

For the cyclic phase, the cyclic loading can be chosen from four different control types (stress, strain, stress ratio record, and strain ratio record). For the first two options, the user defines up to 32 stress or strain ratio with a number of cycles and frequency. For the last two, a user-defined file containing amplitude values with the total duration time for the file is defined. According to the device manual, the maximum recommended cyclic stress frequency is 1 Hz.

The DSST apparatus can accommodate a cylindrical sample with a diameter of 300 mm, and a maximum height of 150mm. The specimen aspect ratio is $D/H = 300/150 = 2$. Figure 3.5 displays a prototype of the DSST sample. The specimen is created inside

the series of Teflon coated aluminum rings that have a thickness of 6.35 mm, the Teflon ensures minimum friction between the rings. A latex membrane is used to protect the shear rings from scratching by soil grains.

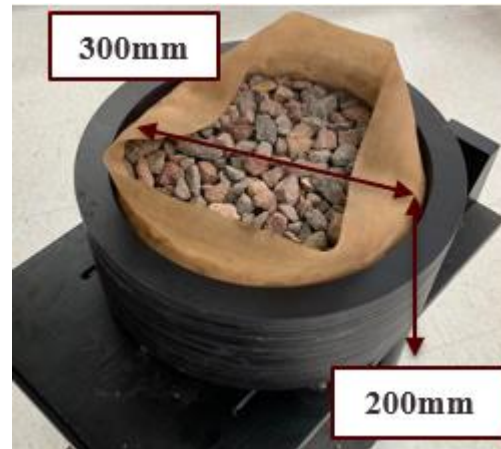


Figure 3.5. DSST stacked rings

The vertical pressures is applying on the top surface of the sample using a rigid round cap attached to the vertical piston. A steel piston is supported by four low friction steel rollers (Figure 3.6). The piston can freely move in vertical direction and its lateral movement is restricted by the rollers. The vertical displacement of the piston is measured by three displacement transducer with 0.002 mm resolution and 90cm capacity. Similar to DST, the maximum vertical and horizontal displacement of the test is limited to 5 cm and 10 cm, respectively.



Figure 3.6. Crossbar and rollers configuration

3.2.3. Large-Scale Triaxial Apparatus (TT)

A large-scale triaxial apparatus manufactured by GeoTac Inc. was used as a part of the testing program. The details about the triaxial apparatus are shown in Figure 3.7. The triaxial tests were performed in the Fugro Soil and Rocks Laboratory in Houston, Texas. The cell is capable of accommodating specimens up to 152 mm in diameter and 305 mm in height, for an aspect ratio of $H/D = 305/152 \sim 2$. Figure 2.1 shows a configuration of the triaxial sample. According to research conducted by Indraratna et al. (1998) and Marschi et al. (1972), the minimum sample size ratio of six (maximum particle size of 25 mm) was chosen for the triaxial test to minimize boundary effects. The triaxial apparatus contains five different parts, including triaxial cell, vertical loading unit capable of performing monotonic and cyclic loads, confining pressure system, pore pressure measurement, and axial change measurement system.

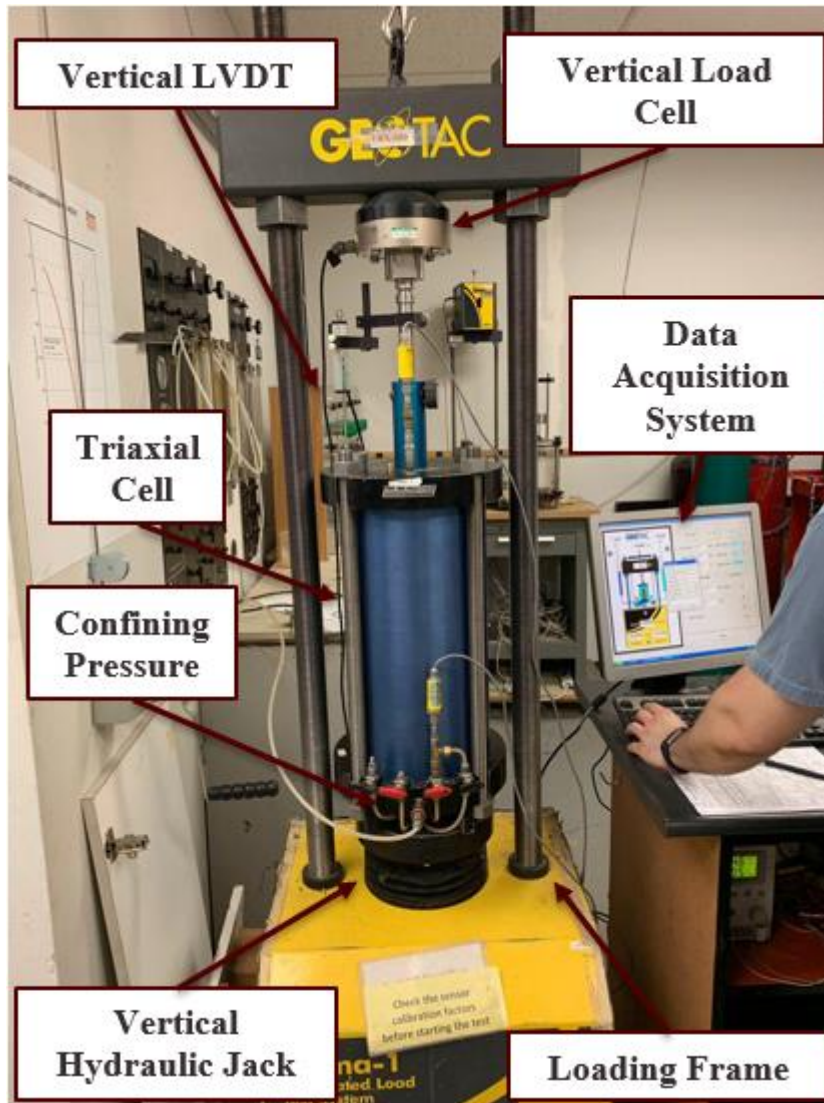


Figure 3.7. Triaxial test apparatus

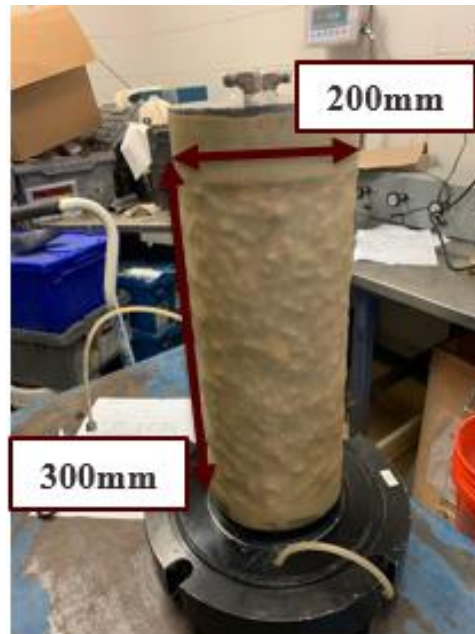


Figure 3.8. Triaxial test sample

A uniform all-around air pressure applies to the sample, while independent vertical stress applies to the sample by a piston. The maximum confining pressure capacity of the device is limited to 3.5 MPa. A vertical monotonic load up to 177 kN can be applied to the specimen with a bottom-up drive unit in a variety of modes, including deformation, load, or stress control. The axial displacement was measured with an external linear variable displacement transducer (LVDT) installed at the top of the specimen. The triaxial device is connected to the computer to control the test process and data measurement. The cyclic vertical loading can be precisely applied to the sample with the maximum recommended frequency of up to 1 Hz.

3.3. Characteristics of the Testing Materials

Crushed granite ballast material was obtained from the Martin Marietta quarry near Beaumont, Texas. Two different grain size distribution were used in this study that can be categorized as ballast #4 and #5 based on AREMA Manual for Railway Engineering. More details about Figure 3.9 shows the grain size distribution of ballast materials used in this study. For ballast #5, the maximum particle size of the particles is 25 mm, and the D_{50} is 16 mm. The maximum particle size and the D_{50} of ballast #4 are 38.1 and 25 mm, respectively. The minimum sample size ratio of 6 was satisfied with all the tests. More details about the mechanical characteristics of the materials are provided in Table 3.2. Due to particle breakage and deterioration during the tests, no materials were reused. All the tests were performed on the fresh crushed granite ballast materials.

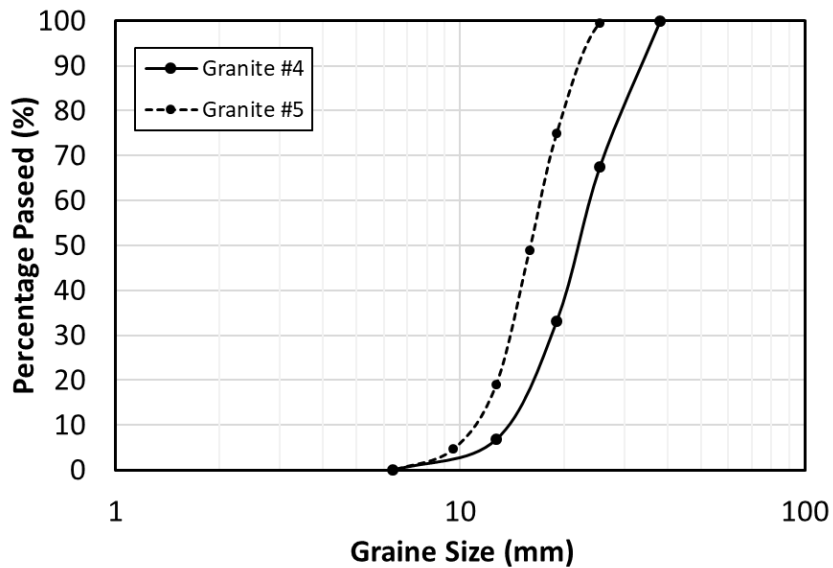


Figure 3.9. Grain size distribution of the ballast materials

Table 3.2. Mechanical properties of the ballast materials

Property	Granite #4	Granite #5
D₁₀ (mm)	14	11
D₃₀ (mm)	18.5	14
D₅₀ (mm)	22	16
D₆₀ (mm)	23.5	17
D_{max} (mm)	38	25
Coefficient of uniformity (C_u)	1.68	1.55
Coefficient of curvature (C_c)	1.04	1.05

3.4. Test Procedure and Plan

3.4.1. Large-Scale Direct Shear Test (DST)

3.4.1.1. Sample Preparation

Prior to sample preparation, the target dry density of the ballast samples has chosen in the range of 1550 to 1580 kg/m³. According to Indraratna et al. (1998), this range can replicate the field density of the ballast in a conventional track. The same range of density for the ballast material was later reported by Sun et al. (2014). There was no water added to the material, and the tests were performed with zero moisture content to reproduce the dry fresh ballast condition. All the samples were compacted to the same level of density to eliminate the effects of compaction on the results.

The required mass of the samples was calculated based on the dry density and the volume of the shear box. The materials were placed in three layers with equal high and compacted. For the first step, the lower half of the shear box was placed on the shear box stand, and the leftover of the material from the previous test was removed entirely (Figure

3.10(a)). Then, the first layer of the sample was placed and fully compacted with placing a wooden plate on top of each layer and compacting with the rubber hammer. The hammer strokes hit on the wooden plate that placed on the surface of the sample to reach the desired height and density for each layer. Then, the upper half of the box was placed on top of the lower half. Then the two halves were attached by placing two alignment screws for the purpose of sample preparation (Figure 3.10(b)). Then the next two layers were placed and compacted in the same way as the first layer to reach the final height of the sample (Figure 3.10(c)). After completion of the sample preparation, the top cap was placed carefully on top of the sample and aligned horizontally, as it is shown in Figure 3.10(d).



(a)



(b)



(c)



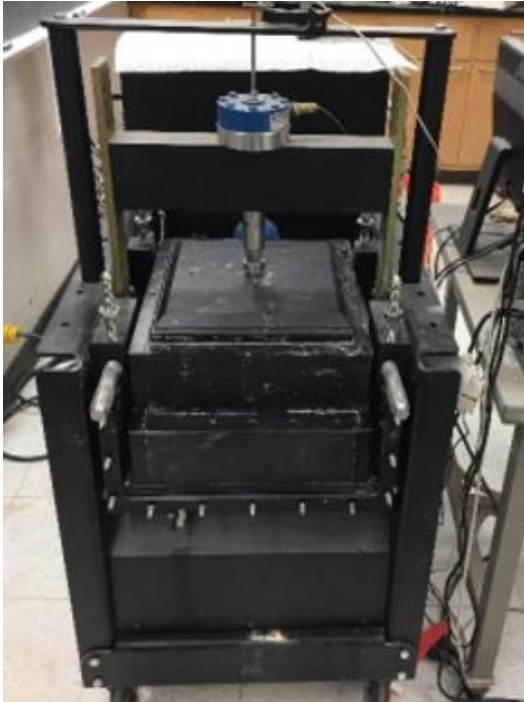
(d)

Figure 3.10. DST sample preparation. (a) Placement of the lower half of the shear box on the shear box stand; (b) Placement of the upper half of the shear box and alignment screws; (c) Final layer of the sample; (d) Top cap placement

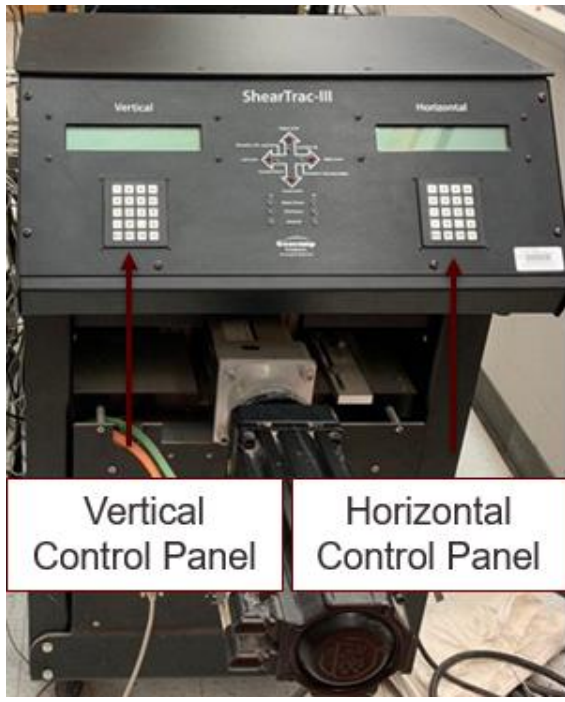
3.4.1.2. Test Procedure

After completion of the sample preparation, the shear box was placed into the DST loading frame, as shown in Figure 3.11(a). Then, the bottom of the shear box was connected to the device by using two bolts. After that, the loading piston was initialized to the appropriate location on the specimen top cap using the vertical and horizontal control panel. Figure 3.11(b) shows a ShearTrac-III control panel system. Next, the two alignment screws were removed, and a small amount of seating load was applied. Then, two lifting beams were connected to the upper half of the shear box to restrict the movement of the top part in every direction and also create an appropriate gap between the two halves (Figure 3.11(c)). In the end, the fix-end crossbeam was used to fix the shear

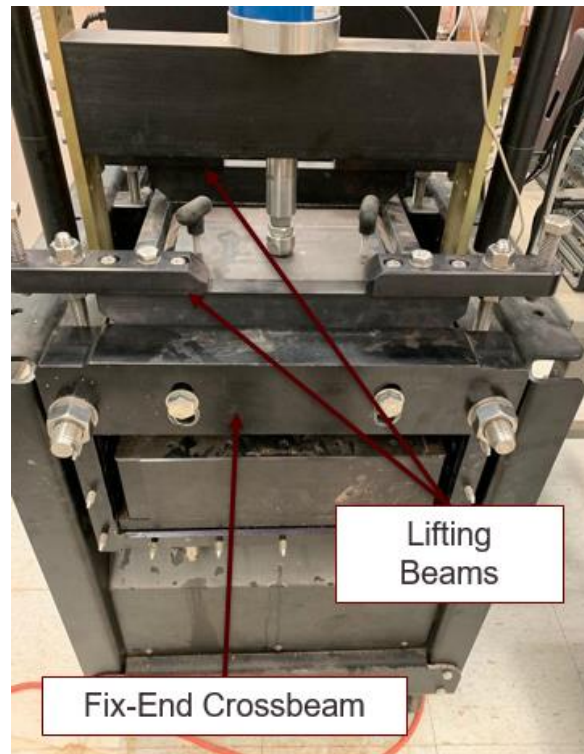
box and ensure that the upper part of the shear box is not sliding horizontally during the test.



(a)



(b)



(c)

Figure 3.11. DST test procedure. (a) Placement of shear box into the loading frame; (b) ShearTrac-III control panel system; (c) Lifting beams and crossbeam configuration

Direct shear test runs in two phases, including phase one (consolidation) and phase two (shearing). In the consolidation phase, constant vertical pressure is applied to the sample for simulating consolidation in the existence of water content. In our testing program, because of the dry condition of the ballast material, the consolidation phase causes compression of the sample. The consolidation phase follows by shearing of the sample. The shearing process can be performed in load control or displacement control condition. All the DST testing in the current research conducted in the displacement control condition with a constant shearing rate of 0.1016 mm/min. The tests were stopped

at either the horizontal displacement of 50.8 mm (2 in.) or the maximum horizontal load capacity of the device (22 kN).

Before starting the shear phase of the test, a gap should be created between the two halves of the shear box. The main reason for creating a gap for direct shear testing of the fine-grain materials is to reduce the metal to metal friction. According to the ASTM D3080, the maximum value of the gap is limited to 0.635 mm. The only deviation from the ASTM D3080 is the shear box gap size. According to ASTM D3521, the gap value between the two half of the shear box should be large enough to prevent the metal friction during the test and small enough to minimize falling the soil particles into the gap. Therefore, the gap size is considered equal to D_{85} of the material (i.e., the aggregate size that 85% is finer). This assumption is consistent with Nicks and Adams (2014) research.

3.4.1.3. Testing Plan

A series of large scale direct shear test (DST) was conducted on crushed granite ballast materials two different gradations equivalent to the AREMA ballast #4 and #5. ASTM D3080 procedure was followed for all direct shear testing in this research. These tests were performed in the different magnitude of vertical pressure from 10 kPa to 90 kPa. Because the shear strength parameters are stress-dependent, it is crucial to apply a stress level which approximates the field condition. Thus, the normal stress used in DST should be calculated based on the in situ stress condition in the ballast layer prior to train loading. The normal stress is assumed to be the weight of the rail, sleeper, and ballast material itself. So, the range of 10 to 90 kPa could be a good representation for the ballast

with a thickness of 0.5 to 5 m. The magnitude of the normal stresses used in this study covers the recommended range of stresses for ballast laboratory testing proposed by Stark et al. (2018). Table 3.3 provides more detail about the DST test plan on crushed granite material.

Table 3.3. DST test plan

Test No.	Test Type	Material Type	Normal Stress (kPa)	gap (mm)
1	DST	Granite #4	10	25
2	DST	Granite #4	30	25
3	DST	Granite #4	50	25
4	DST	Granite #4	70	25
5	DST	Granite #4	90	25
6	DST	Granite #5	10	21
8	DST	Granite #5	30	21
9	DST	Granite #5	50	21
10	DST	Granite #5	70	21
11	DST	Granite #5	90	21
12	DST	Granite #5	10	11
13	DST	Granite #5	10	11
14	DST	Granite #5	30	11
15	DST	Granite #5	50	11
16	DST	Granite #5	70	11

3.4.1.4. Device Calibration

The results of the large-scale DST were validated using a 63 mm diameter standard small-scale device. Ten tests were performed on sub-rounded dust-free play sand in the dense condition (dry density of 1685 kg/m^3) in both devices. Tests were performed with the normal stress of 10, 30, 50, 100, 150 kPa. Figure 3.12 shows the shear stress-shear displacement of the material. The dashed lines show the results of small-scale DST, while continuous lines correspond to large-scale DST. The close shear stress-shear displacement response from both devices can be observed. The nearly identical peak values of the maximum shear stress in each magnitude of the normal stress are observed from both devices. However, the residual shear stress value (i.e., the shear stress at 40 mm of shear displacement) large-scale DST is slightly higher than the other test.

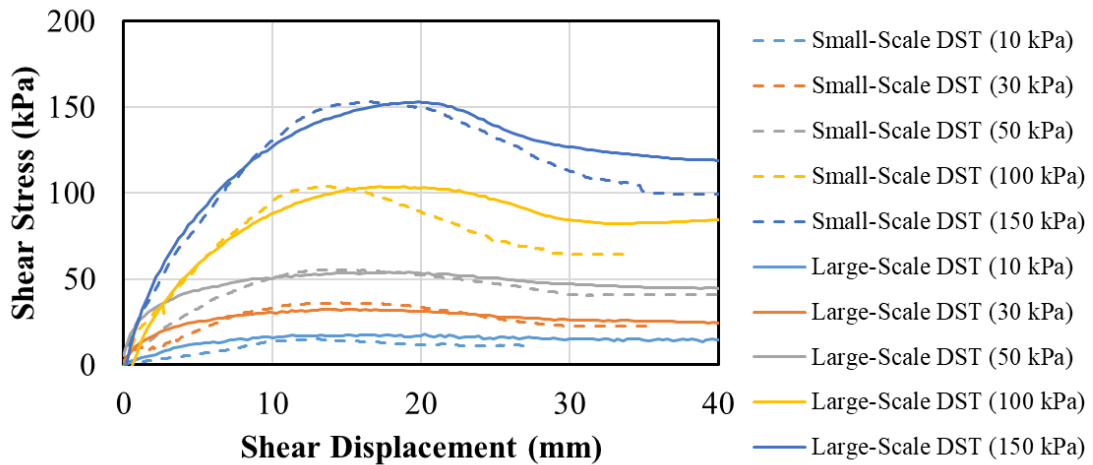


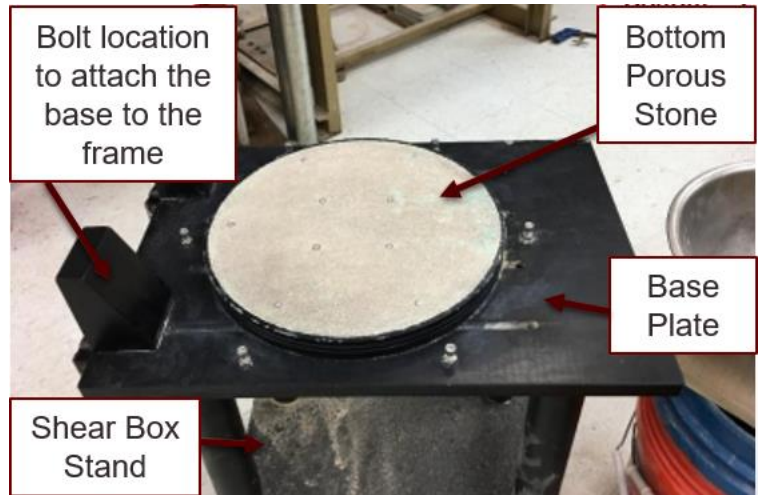
Figure 3.12. Large-scale direct shear calibration

3.4.2. Large-Scale Direct Simple Shear Test (DSST)

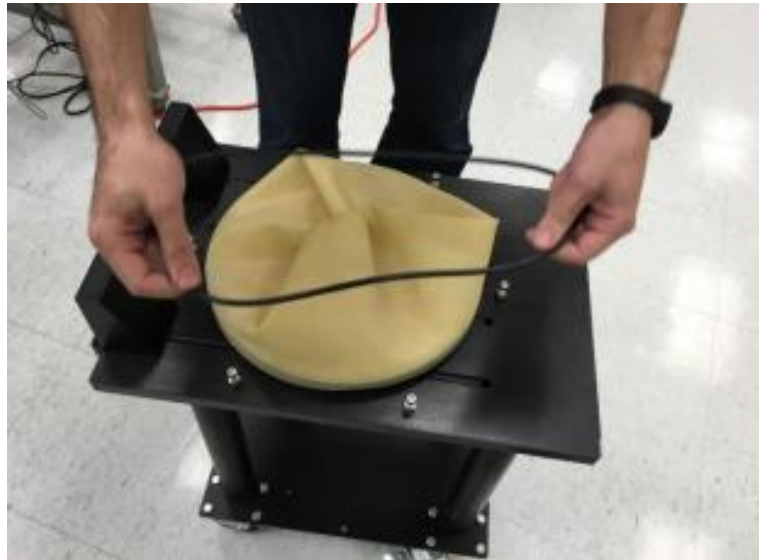
3.4.2.1. Sample Preparation

Sample preparation for DSST is quite similar to DST sample preparation, which is discussed before. The desired dry density of 1550 to 1580 kg/m³ was determined for the samples. The fresh angular crushed granite materials with gradation equivalent to AREMA ballast #4 and #5 were used in all the monotonic and cyclic DSST. The samples prepared in the absence of any fine materials or water content.

Firstly, the DSST base plate was placed on the shear box stand. Figure 3.13(a) shows the different components of the base plate. Then, the sample membrane was tightened around the bottom of the base plan by using an O-ring (Figure 3.13(b)). Then, the stacks of shear rings were placed on the base plate spacer. After that, similar to DST sample preparation based on the desired dry density and the volume inside the shear rings, the required mass of the specimen was calculated. The materials placed and compacted in three layers to reach the desired sample height. Figure 3.13(c) shows the final DSST sample.



(a)



(b)



(c)

Figure 3.13. DSST sample preparation. (a) Base plate components; (b) Membrane and O-ring placement; (c) Final DSST sample;

3.4.2.2. Test Procedure

DSST sample should be placed and fixed into the loading frame by using two bolts. Figure 3.14 illustrates the ShearTrac-III test set up for the DSST. As it can be observed in the picture, the vertical stress is applied to the sample by using a top cap which is connected to the shearing frame. The horizontal movement of the top cap is restricted, and it can only freely moves in a vertical direction. After the DSST sample is appropriately placed into the frame, the top cap should be lowered down to touch the surface of the sample gently. Next, the small amount of seating load should be applied to the sample to

make sure the top cap is in place and only touching the soil surface. As it is shown in Figure 3.15, after the seating load applied, the first few shear rings were moved to confirm the top cap is not seated on the shear rings.



Figure 3.14. DSST test setup



Figure 3.15. Sitting load step

DSST test consists of two different consolidation phase and shear phase similar to the DST. However, the horizontal force can be applied to the sample in both monotonic and cyclic conditions. The magnitude of vertical stress for all the monotonic and cyclic DSST was chosen in the range of 10 to 90 kPa to replicate the field stress level for the ballast layer in a conventional track. More details were provided in the DST test procedure section. It is noteworthy to mention that in DSST monotonic and cyclic testing program, the consolidation phase duration was very short and set to the time that the vertical stress is stabilized because the samples were tested in a fully dry condition. For the monotonic test, the shear phase of the test performed in displacement condition with the constant shear rate equal to 0.6 mm/min. Experiments were stopped at the maximum horizontal displacement of 25.4 mm (1 in.).

For the cyclic test, immediately after completion of the consolidation phase, a predefined horizontal cyclic loading was applied to the sample by a dynamic actuator with a maximum load of 22.5 kN. Four different characteristics for the cyclic loading including maximum cyclic stress amplitude (σ_{xmax}), minimum cyclic stress amplitude (σ_{xmin}), frequency, and the number of cycles should be defined for the tests. Figure 3.16 shows details of cyclic loading. According to Stark et al. (2018), the magnitude of cyclic loading should be representative of the stress generated by train passage. Therefore in this study the magnitude of minimum cyclic stress amplitude (σ_{xmin}) was set to zero. Moreover, the maximum cyclic stress amplitude (σ_{xmax}), which is defined as horizontal stress generated by train passage, was set as the percentage of the shear strength of the material that calculated from the monotonic test at the same normal stress. All the experiments were performed at a frequency of 1 Hz. For each test, the maximum number of cycles is defined. The test stops either at the maximum number of cycles or the predefined shear strain value.

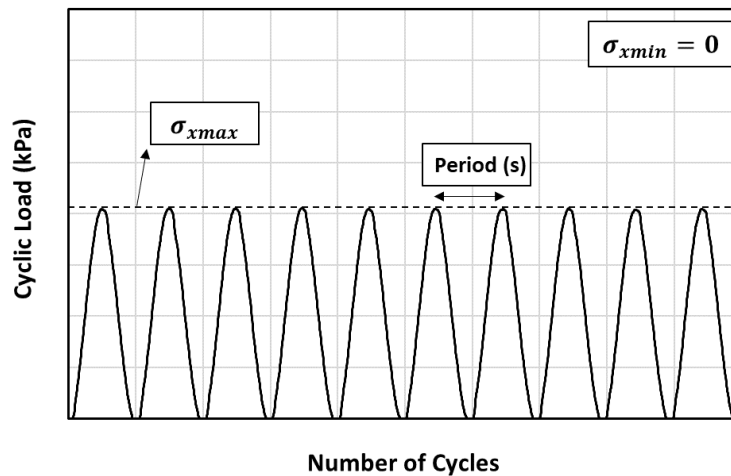


Figure 3.16. Typical cyclic load curve

3.4.2.3. Testing Plan

As a part of the investigation on the monotonic behavior of railroad ballast, a series of large-scale monotonic DSST has conducted. All the tests performed on crushed granite ballast material. Similar to DST, AREMA ballast #4 and #5 have been chosen for this study. The range of vertical stress applied to the tests was 10 to 90 kPa. More details about the testing plan are discussed in Table 3.4.

Table 3.4. Monotonic DSST test plan

Test No.	Test Type	Material Type	Normal Stress (kPa)
1	DSST	Granite #4	10
2	DSST	Granite #4	30
3	DSST	Granite #4	50
4	DSST	Granite #4	70
5	DSST	Granite #4	90
6	DSST	Granite #5	10
7	DSST	Granite #5	30
8	DSST	Granite #5	50
9	DSST	Granite #5	70
10	DSST	Granite #5	90
11	DSST	Granite #5	90

To study the behavior of ballast under cyclic loading, a series of cyclic testing performed at the Texas A&M laboratory. Table 3.5 illustrates the details of the cyclic DSST. All the tests performed on crushed granite ballast material with gradation equivalent to AREMA ballast #4. The sample preparation was the same as monotonic DSST.

Table 3.5. Cyclic DSST test plan

#	Normal Stress (kPa)	Shear Strength (kPa)	Cyclic Stress (kPa)	Cycles Amp	Number of Cycles	Frequency (Hz)
				τ_f		
1	10	10	2.5	25%	10,000	1
2	10	10	5	0.50%	100,000	1
3	40	30	23	0.77%	10,000	1
4	50	37	13	0.35%	20,000	1
5	50	37	25	0.68%	100,000	1
6	50	37	34	92%	100,000	1
7	60	42	24	0.57%	20,000	1
8	70	48	25	0.52%	20,000	1
9	90	63	24	0.38%	20,000	1
10	90	63	46	0.73%	50,000	1

3.4.2.4. Device Calibration

The large-scale direct simple shear device was calibrated using results published by Kim (2009). They performed a series of small scale direct simple shear tests on Ottawa sand in constant load conditions. For the purpose of calibration, sand with nearly close gradation and characteristics was chosen for further investigation. All the tests conducted in loose conditions. Three magnitudes of normal stress, including 50, 100, and 200 kPa, were tested for the purpose of comparison. Figure 3.17, the comparison of the tests results performed by Kim (2009) and Texas A&M University. As it can be observed in Figure 3.17, the nearly identical response was observed from both tests that shows the accurate results of large-scale DSST.

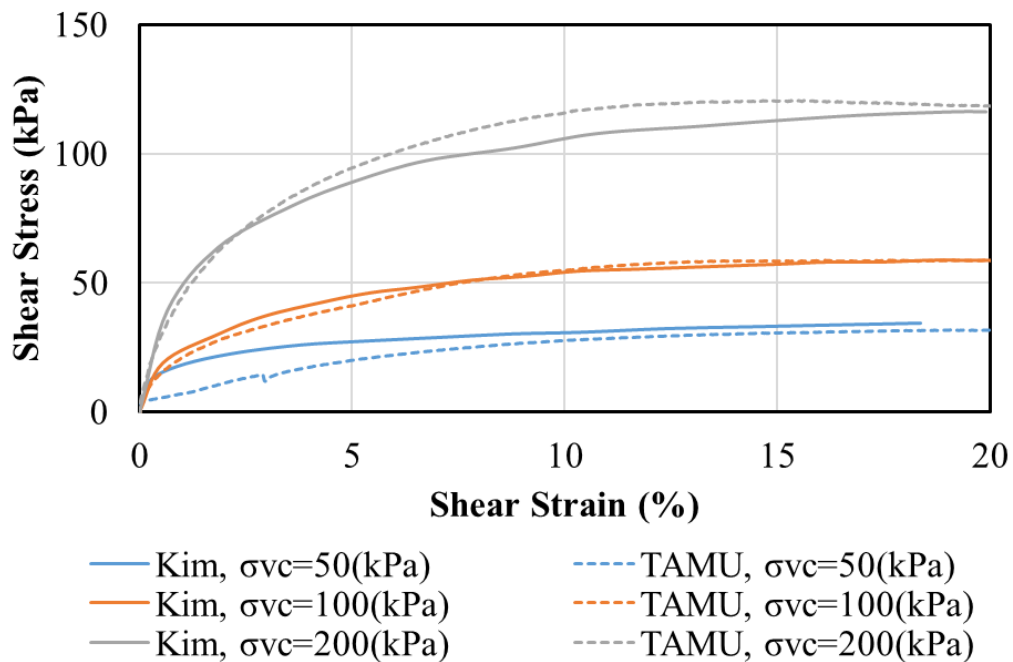


Figure 3.17. Large-scale direct simple shear device calibration

3.4.3. Large-Scale Triaxial Test (TT)

3.4.3.1. Sample Preparation

The triaxial cell dimensions used in this study are 152 mm diameter and 305 mm in height. Therefore due to the limitation of the size of the device, all the TT investigations were performed on AREMA ballast #5 with a maximum particle size of 28 mm. Based on the material particle size, the specimen diameter to grain size ratio of the sample is $D/d = 152/25 \sim 6$.

Specimens were prepared inside a split mold to prevent the puncturing of a latex membrane used to hold the ballast sample. After assembling the split mold and placing the latex membrane inside it, a vacuum was applied to suck the membrane to the sides of the mold (Figure 3.18(a)). Similar to DST and DSST desired dry density of the sample was chosen in the range of 1550 to 1580 kg/m³. The ballast material was placed inside the mold in three equal layers. The weight and the thickness of the layers were calculated based on the desired density of the samples. Figure 3.18(b) shows the placement of the first layer into the mold. Each layer was compacted using a steel hammer with the close area of the mold (Figure 3.18(c)) to reach the desired height of the layer. After compaction of all the layers, a loading cap was placed on top of the sample, and the vacuum was removed. The sample in the latex membrane is shown in Figure 3.18(d). Another rubber membrane with a thickness of 3.63 mm was used to confine the cylindrical sample during the testing (Figure 3.18(e)). Previous research had shown that using a thick rubber membrane would create extra confinement to the sample and affect the results (Bishop and Henkel (1962)). Thus, the stress measurements were corrected to eliminate the

influence of using a thick rubber membrane on the confining pressure. Yet the thicker rubber membrane was needed to avoid puncture during testing.



(a)



(b)



(c)



(d)



(e)

Figure 3.18. TT sample preparation. (a) Vacuum of latex membrane inside the split mold; (b) Placement of the first layer; (c) Compaction of the material; (d) Complete specimen in latex membrane; (e) Placement of rubber membrane;

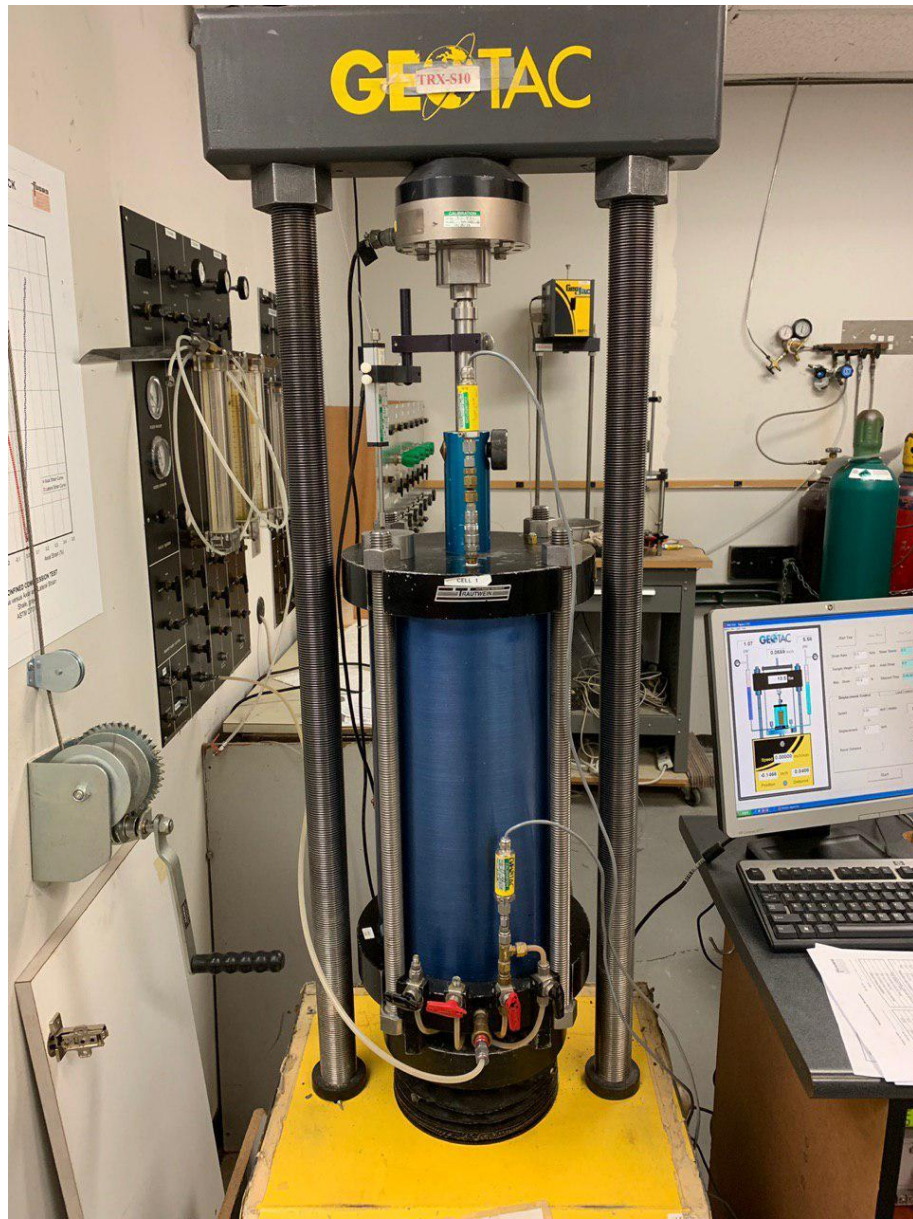
3.4.3.2. Test Procedure

Once the specimen is prepared, it was placed inside the triaxial cell (Figure 3.19(a)) and gently assembled in the loading frame. Figure 3.19(b) displayed the assembly of the triaxial cell in the loading frame. Then, the required cell pressure was applied to the sample inside the chamber. The monotonic tests were performed in a drain condition because the samples were prepared in a fully dry condition. The deviatoric stress with a

constant rate of 1% strain/hour was chosen to apply to the specimen during the shearing process. All the tests stopped at 15% axial strain and based on the applied shearing rate, each test completed in 15 hours. Axial load and strain were measured during the tests.



(a)



(b)

Figure 3.19. TT test set up. (a) Triaxial cell; (b) Placement of cell into the loading frame

3.4.3.3. Testing plan

To further investigate the behavior of the ballast, a series of the monotonic and cyclic triaxial tests have been conducted. All the tests performed on ballast#5 with the maximum particle size of 25 mm because of the size limitation of the triaxial cell. Table 3.6 summarized the details about the monotonic triaxial testing plans. The monotonic tests conducted at confining stresses of 40, 80, 140 kPa. The stress state of the triaxial tests should be representative of the confining or lateral stress that the ballast layer experienced before the train passage. It is difficult to measure this value from the field and can be calculated from the vertical component of stress indirectly. Selig (1987) stated that due to significant locked-in lateral stresses existed in the ballast, the magnitude of earth pressure coefficient (K) could reach the Rankine passive earth pressure coefficient (K_P). Therefore, by assuming the ballast friction angle equal to 45 degrees, the magnitude of confining stress can be as high as six times the vertical stress. Indraratna et al. (1998) mentioned that the magnitude of confining pressure for most of the Australian tracks is less than 70 kPa. Moreover, Stark et al. (2018) stated the upper bound of confining pressure in the ballast sleeper interface could be as high as 140 kPa. The range of confining pressures selected in this study would satisfy the abovementioned statements.

Table 3.6. Monotonic TT test plan

Test No.	Test Type	Material Type	Confining Pressure (kPa)
1	TT	Granite #5	40
2	TT	Granite #5	80
3	TT	Granite #5	140

Details about the triaxial cyclic testing program are stated in Table 3.7. Tests were performed at 80 kPa confining pressure and cyclic stress amplitudes between 40 to 120 kPa. The magnitude of cyclic stress is corresponding to the loading generated underneath the sleepers during the train passage. The cyclic loading applied at the frequency of 1 Hz.

Table 3.7. Cyclic TT test plan

#	Confining Stress (kPa)	Shear Strength (kPa)	Cyclic Stress (kPa)	$\frac{\text{Cycles Amp}}{\tau_f}$	Number of Cycles	Frequency (Hz)
1	80	210	40	19%	1,000	1
2	80	210	80	38%	1,000	1
3	80	210	120	57%	1,000	1

4. PRESENTATION AND DISCUSSION OF THE RESULTS OF MONOTONIC LOADING TESTS

4.1. Introduction

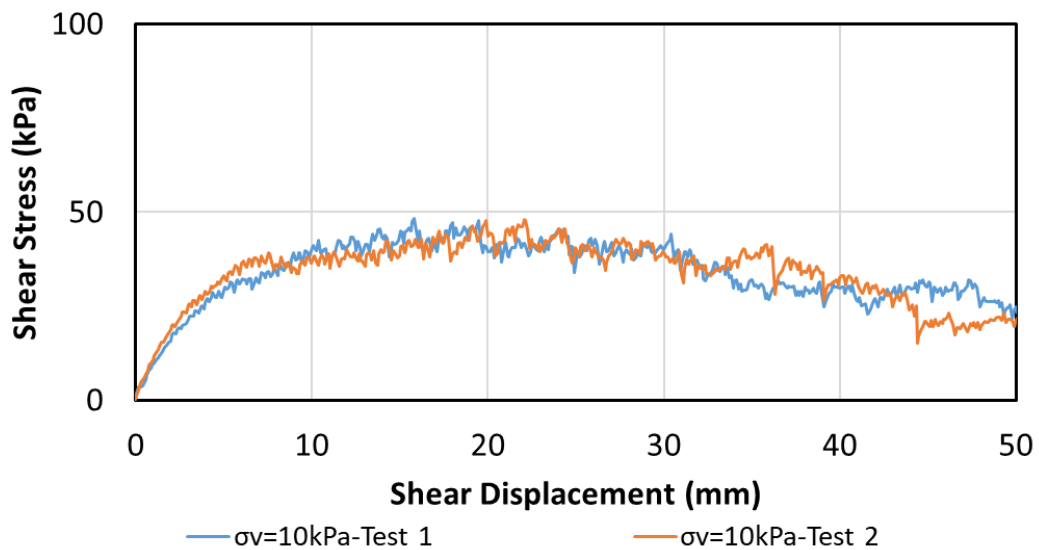
This chapter describes the experimental results of the shear behavior of the fresh railroad ballast under monotonic loading based on a large-scale direct shear test (DST), direct simple shear test (DSST), and triaxial test (TT). This chapter begins with the experimental results of DST and DSST on crushed granite ballast material with two different gradations equivalent to AREMA ballast no.4 and no.5. The non-linear failure envelope, the influence of normal stress on friction angle, and the dilative response of the materials are discussed. Moreover, the influence of ballast maximum particle size is studied based on DST and DSST results. As a part of DST investigations, the impact of the gap on the shear behavior of the materials is studied. Then the results of TT on ballast#5 are presented.

The chapter concludes with a comparison of the monotonic shear behavior of ballast material based on all three abovementioned tests. Crushed granite ballast material, the maximum particle size equal to 25 mm, was chosen for the comparison. All the samples were prepared with the same technique and were compacted to the same density. The details of the results of these experiments and the discussion of the results are presented in the following sections.

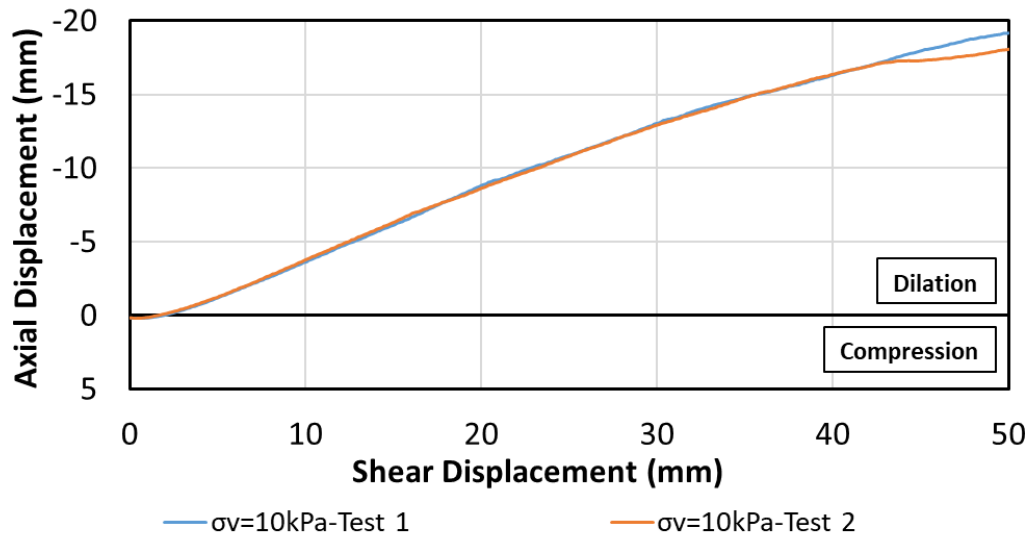
4.2. Monotonic Direct Shear Test (DST)

4.2.1. Test Repeatability

The initial goal for monotonic DST investigation was to check the consistency and repeatability of the results. For this purpose, the test under 10kPa vertical stress was duplicated. Shear stress-shear displacement and the axial displacement-shear displacement of the two tests were compared. Figure 4.1 shows the good repeatability of the direct shear experiment. Both tests were conducted on ballast#5 with an 11 mm gap.



(a)



(b)

Figure 4.1. DST repeatability. (a) Shear stress-shear displacement; (b) Axial displacement-shear displacement

4.2.2. Shear Stress-Shear Displacement and Axial Displacement-Shear Displacement

The shear behavior response of five ballast#5 samples with the same sample preparation under various normal stresses (10, 30, 50, 70, and 90 kPa) is presented in Figure 4.2. As is shown in Figure 4.2 (a), the shear stress of the material reaches a peak value in about 20-30 mm horizontal displacement and then decreases slightly to the residual value. The fluctuation in the stress-displacement diagram can be attributed to the particle relocation or the breakage of the sharp edges of the fresh ballast. It can be observed from the curve that the post-peak reduction in shear stress tends to increase in higher normal stress. The same behavior was reported for rockfill (Marsal (1967) and Marschi et al. (1972)) and ballast materials (Dissanayake et al. (2016)).

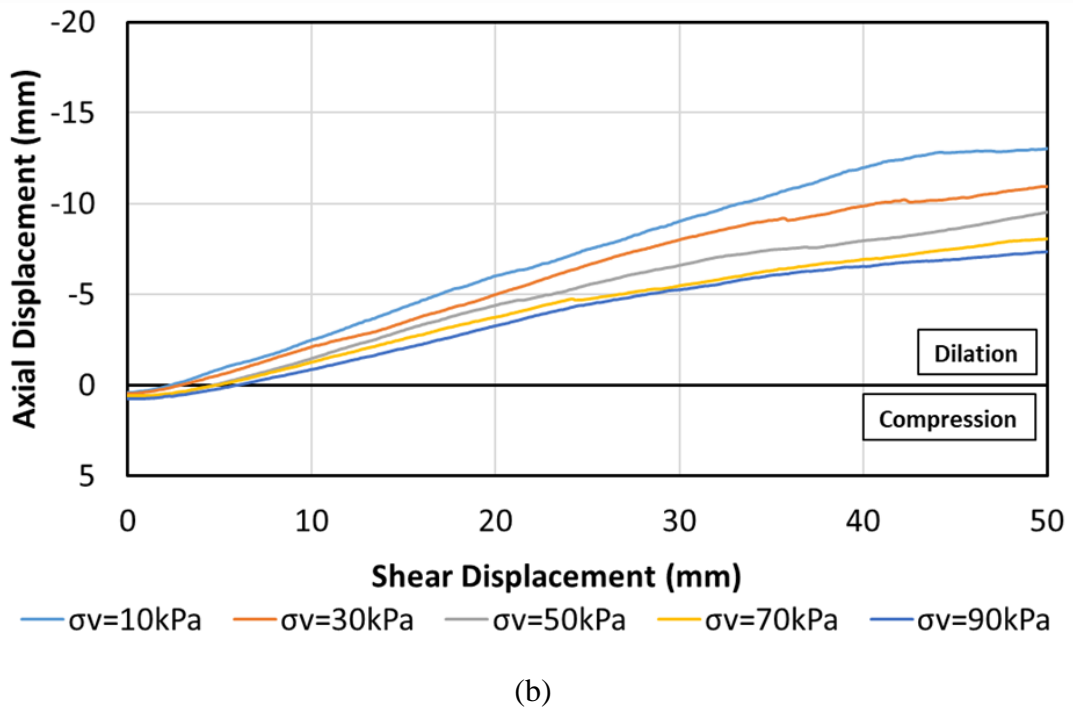
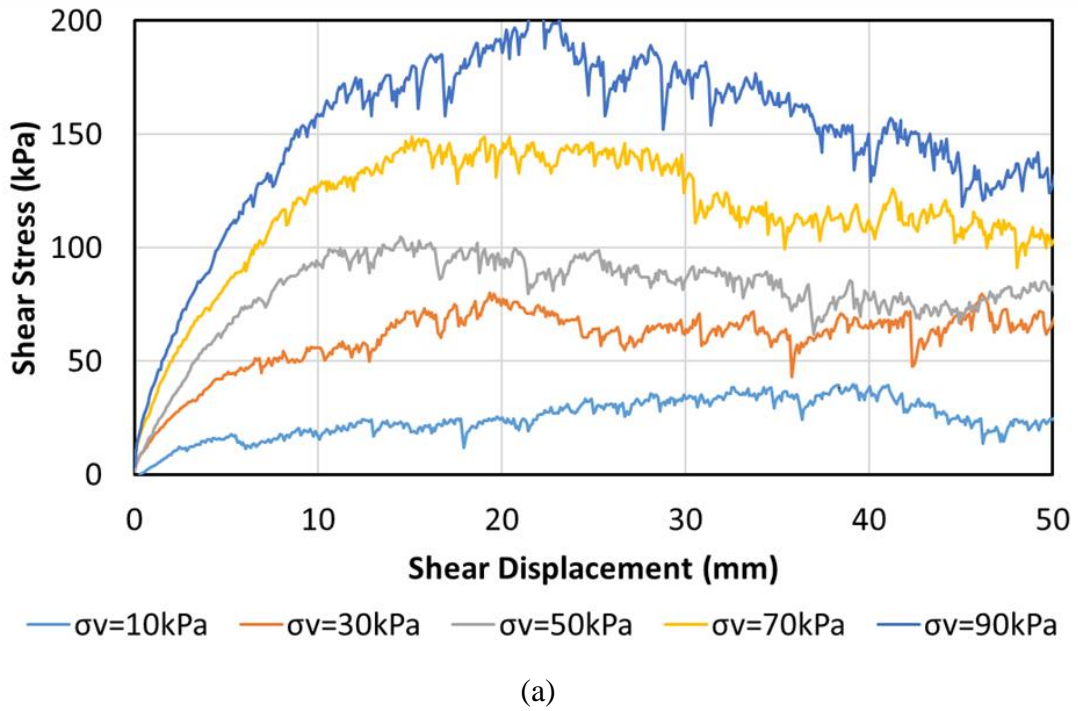


Figure 4.2. Shear Behavior of Ballast#5 Based on DST. (a) Shear stress-shear displacement; (b) Axial displacement-shear displacement

Figure 4.2 (b) illustrates the axial displacement-shear displacement behavior of the materials. As it can be observed in the figure, there is a small amount of compression at the beginning of the test followed by dilation with increasing the horizontal displacement. Also, with increasing normal stress, the amount of dilatancy decreases. This phenomenon is typical of dense granular materials with no cohesion (Lee and Seed (1967), Raymond and Davies (1978), and Suiker et al. (2005)).

4.2.3. Shear Strength Failure Envelope

Figure 4.3 shows the nonlinear failure envelopes for the crushed granite ballast#5 at peak and residual stresses. The peak stress is defined as the maximum recorded shear stress measured during the shearing, and the residual stress is defined as the average recorded stresses between 40 and 50 mm horizontal displacement during the shearing. The main reason for determining residual stress as an average value is to minimize the effects of stress fluctuation on the results of the shear strength parameters. Table 4.1 presents more details about ballast#5 DST results. The friction and dilation angle will be discussed in the following sections.

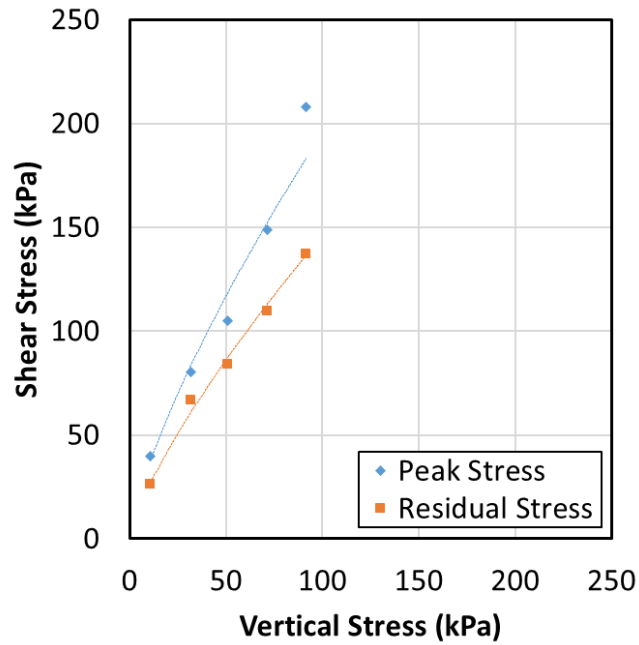


Figure 4.3. Failure envelope of ballast#5 based on DST

Table 4.1. Strength parameters obtained from DST for ballast#5

Test No.	Material	Normal Stress (kPa)	Max Shear Stress (kPa)	Residual Shear Stress (kPa)	φ_{Peak}	$\varphi_{Residual}$	ψ_{Peak}
1	Ballast #5	11	40	26.1	74.6	67.1	16.7
2	Ballast #5	31.7	80.1	67.0	68.4	64.7	14.9
3	Ballast #5	51.1	105	84.0	64.0	58.7	12.4
4	Ballast #5	71.4	149	109.8	64.4	57.0	10.3
5	Ballast #5	91.7	208	137.3	66.2	56.3	10.0

The non-linearity in the failure envelope of the large aggregate material occurs because of the reduction of dilation angle with increasing normal stress that will be discussed later. Therefore, the linear Mohr-Coulomb criteria cannot be used to define the shear strength characteristics of large aggregate materials. Similar behavior is observed in the literature for rockfill materials (Gharavy (1996), Asadzadeh and Soroush (2009), Douglas (2002)). However, as reported by Marsal (1967) and Marschi et al. (1972), at higher stress levels, the dilation is restricted, the failure envelope becomes more linear, and the linear Mohr-Coulomb envelope is a good representation of the material behavior at failure. Details about the equation that can capture the nonlinear failure of the ballast will be provided later in the chapter.

4.2.4. Influence of Normal Stress on Friction Angle

Figure 4.4 illustrates the variation of peak and residual internal friction angles with normal stress for crushed granite ballast. As can be seen in the figure, the friction angle decreases nonlinearly with stress level. With increasing normal stress from 10 to 90 kPa, the peak friction angle drops from 74.6 to 66.2 degrees. While the residual friction angle also decreases from 67.1 to 56.3 degrees for the same increment in normal stress. The friction angle is calculated based on the formula below while considering zero cohesion for the ballast:

$$\varphi = \tan^{-1} \left(\frac{\tau}{\sigma_v} \right) \quad (7)$$

where τ is the peak or residual shear stress, and σ_v is the normal stress.

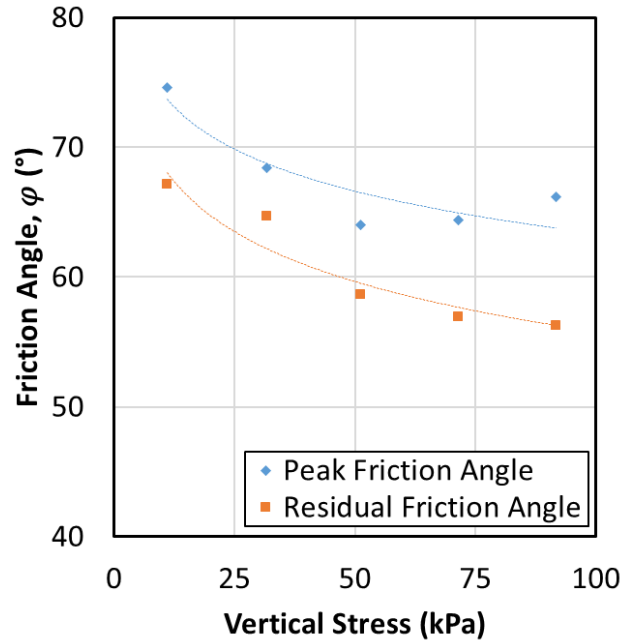


Figure 4.4. Variation of friction angle with the normal stress of ballast#5 based on DST

4.2.5. Influence of Normal Stress on Dilation Angle

A second important parameter that can be used to interpret the shear behavior of the ballast is the dilation angle. The dilation angle (ψ) is calculated according to the following equation (Ladd (1978)):

$$\psi = \tan^{-1} \left(\frac{\Delta\delta_v}{\Delta\delta_h} \right) \quad (8)$$

where $\Delta\delta_v$ is the vertical displacement increment, and $\Delta\delta_h$ is the horizontal displacement increment. Figure 4.5 shows the variation of the dilation with horizontal displacement for each test with applied vertical stress equal to 10, 30, 50, 70, and 90 kPa. It is observed that the magnitude of the dilation angle increases to the maximum value in about 30 mm of

shear displacement and decreases afterward. The same trend was seen in all the applied stresses. The peak of the dilation angle diagram is corresponding to the peak shear stress value for each test (Figure 4.2(a)).

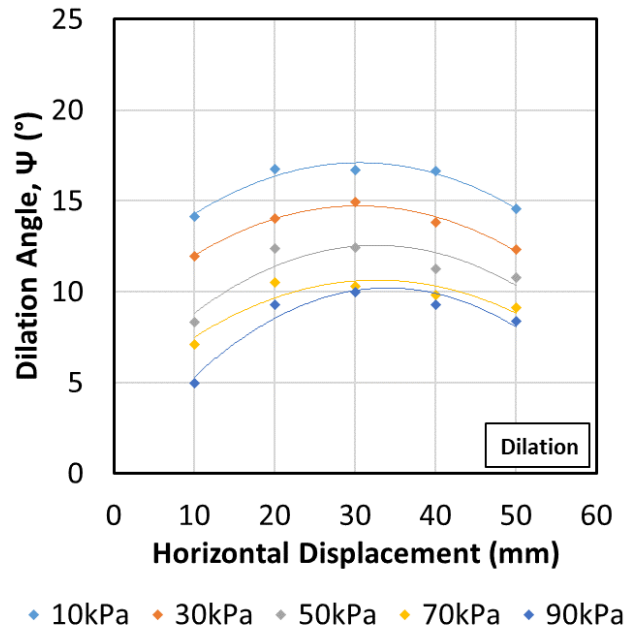


Figure 4.5. Variation of secant dilation angle with the shear displacement for ballast#5 based on DST

The results of secant dilation angle variation illustrated that increasing the magnitude of the normal stress compresses the dilatancy of the ballast material. Figure 4.6 shows the variation of maximum dilation angle with normal stress. The maximum dilation angle decreases non-linearly with increasing normal stress. When the normal stress increases from 10 to 90 kPa, the dilation angle decreases from 16.7 to 10 degrees.

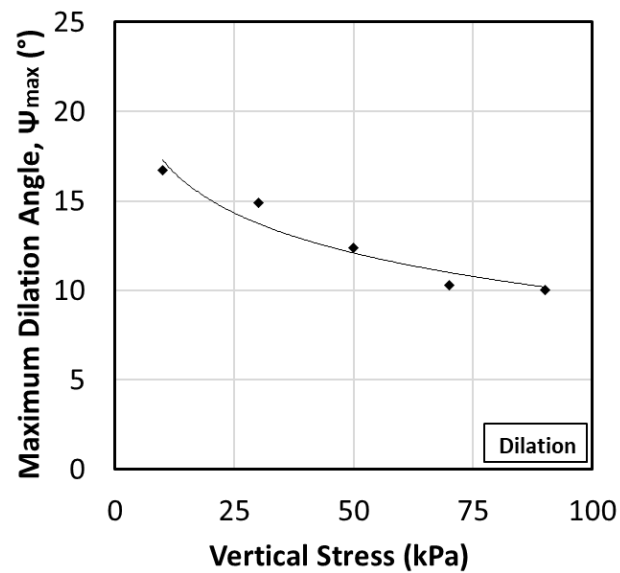
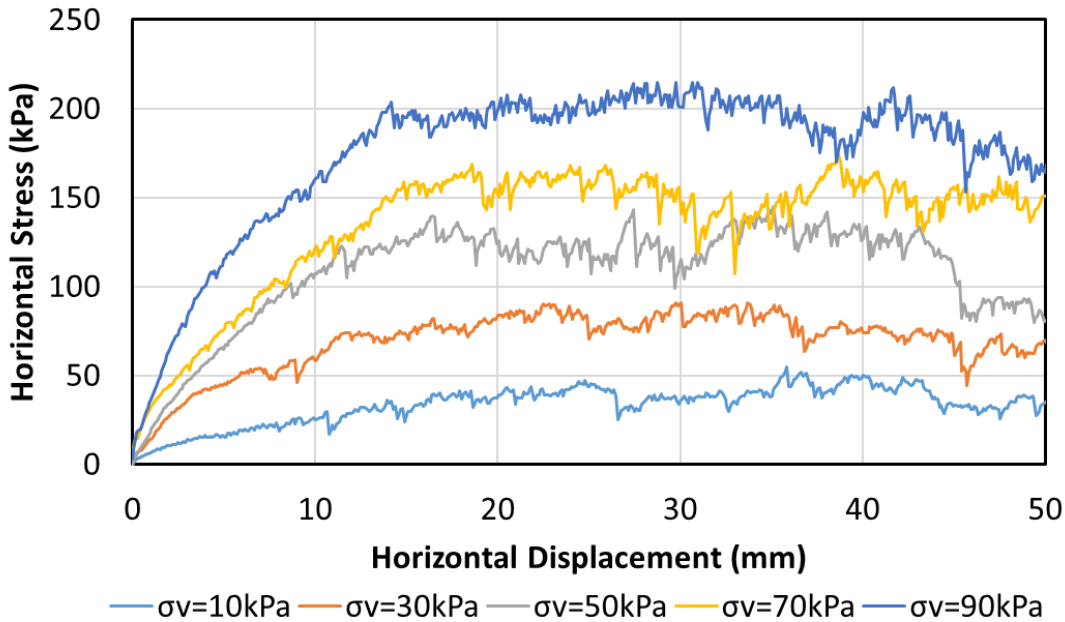


Figure 4.6. Variation of maximum dilation angle with the normal stress of ballast#5 based on DST.

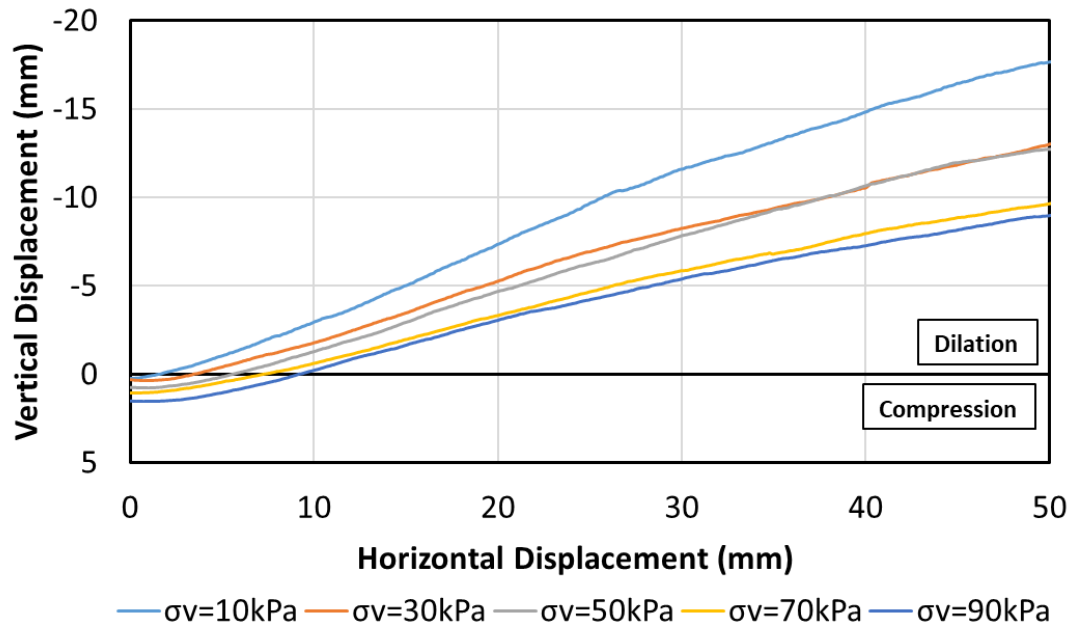
4.2.6. Influence of Ballast Maximum Particle Size

The ballast gradation and maximum particle size are among the critical factors that can govern the mechanical properties of the coarse aggregate materials. Contradictory statements can be found in the literature about the role of sample particle size on the shear strength properties of the material. Some researchers stated that shear strength increases with increasing the maximum particle size (Charles and Watts (1980), Fumagalli (1969), and Kolbuszewski and Frederick (1963)). On the other hand, some others believe that maximum particle size lowers the shear strength (Marschi et al. (1972) and Koerner (1970)). Moreover, Holtz and Gibbs (1956) and Donaghe and Cohen (1978) concluded that strength properties are independent of the particle size.

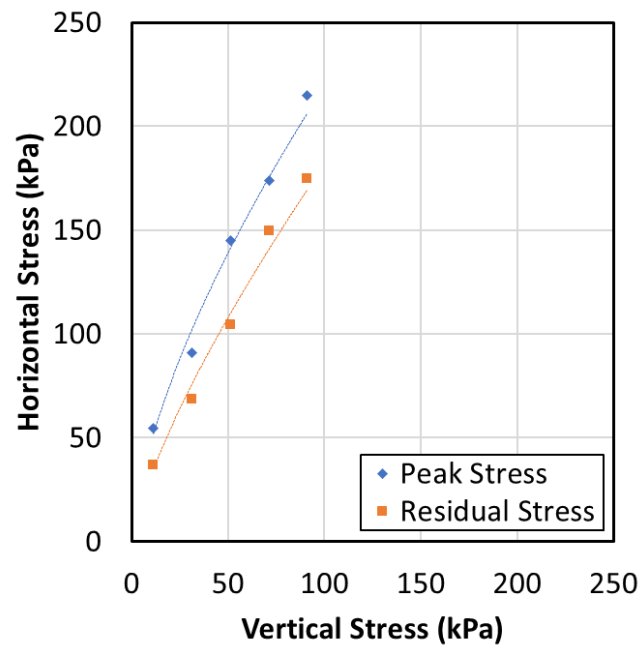
Therefore, the impact of ballast maximum particle size on the shear behavior of the material has been investigated as a part of the DST testing program. Crushed granite ballast material with the gradation similar to AREMA ballast #4 and #5 was chosen for the purpose of comparison. The maximum particle size for ballast #4 and #5 are 38 and 25 mm, respectively. The gradation curves of both materials were shown in Figure 3.9 in chapter 3. All the samples were prepared with the same procedure and compacted to the same level of density. Figure 4.7 shows the DST results for ballast #4.



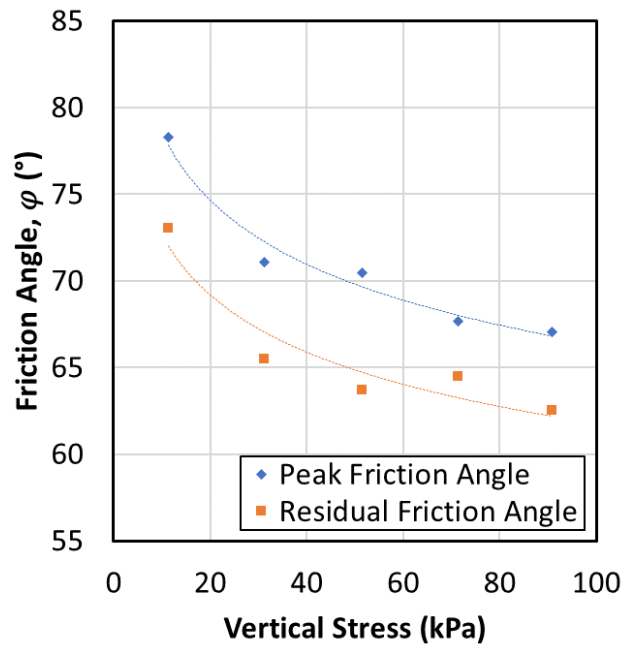
(a)



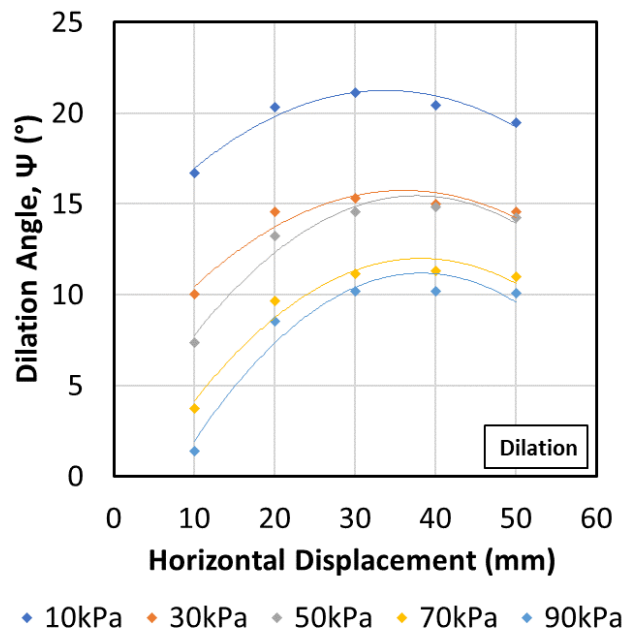
(b)



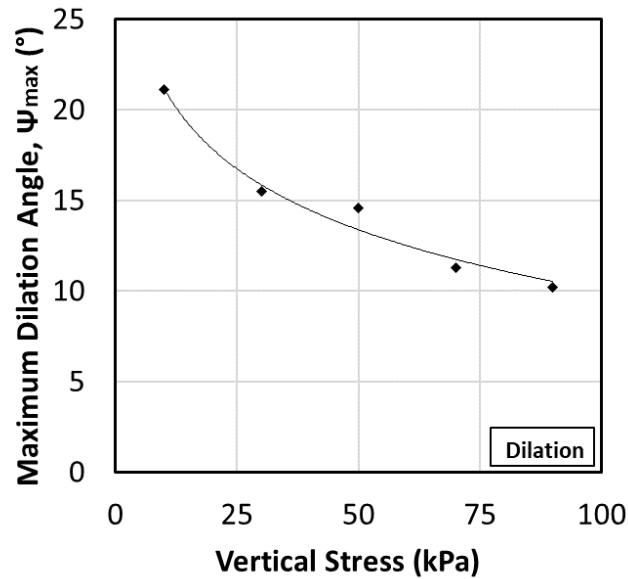
(c)



(d)



(e)



(f)

Figure 4.7. DST results for ballast#4. (a) Shear stress-shear displacement; (b) Axial displacement-shear displacement; (c) Failure envelope; (d) Variation of friction angle with the normal stress; (e) Variation of dilation angle with horizontal displacement; (f) Variation of maximum dilation angle with the normal stress

Details about the shear strength properties of ballast #4 based on DST are presented in Table 4.2. By comparing the results of ballast #4 with ballast#5 that introduced previously, differences between the shear strength properties are as follow:

- Increasing the maximum particle size increases the shear strength of the ballast. Ballast #4 shows up to 40% higher maximum and residual shear strength in comparison with ballast #5. For example, in 10kPa vertical stress, the maximum and residual shear strength of ballast #5 are 40 and 26 kPa, while these values are increased to 54 and 37 kPa for ballast #5, respectively.

- Samples with coarser particles show higher friction angle as well. Ballast #4 shows a higher peak and residual friction angle than ballast #5. For instance, in 10 kPa, normal stress, peak, and residual friction angle for ballast #4 are 78 and 73 degrees. However, for the same stress level, these values are 74 and 67 degrees, respectively.
- The existence of larger grain in the ballast produces more dilation than the samples with smaller particles. For example, in 10 kPa vertical stress, ballast #4 shows a 26% higher dilation angle. This difference is less pronounced at the higher magnitude of vertical stress.

Table 4.2. Strength parameters obtained from DST for ballast#4

Test No.	Material	Normal Stress (kPa)	Max Shear Stress (kPa)	Residual Shear Stress (kPa)	φ_{Peak}	$\varphi_{Residual}$	Ψ_{Peak}
1	Ballast #4	11.3	54.6	37.1	78.3	73.1	21.1
2	Ballast #4	31.2	91.1	68.4	71.1	65.5	15.5
3	Ballast #4	51.5	145	104.3	70.4	63.7	14.6
4	Ballast #4	71.4	174	149.6	67.7	64.5	11.3
5	Ballast #4	90.9	215	175.0	67.1	62.6	10.2

4.2.7. Influence of DST Gap on the Shear Behavior of Large Aggregate Materials

It is an accepted fact that the shear strength of large aggregate materials such as ballast is dependent on the particle rolling and resistance against sliding between particles. Therefore, in a direct shear test, particle and gap size can significantly influence the

strength properties of the material. If the DST gap is too small in comparison with the specimen particle size, rock particles within the shear band forced to fractured and cause overestimation of the shear strength properties of the coarse-grain soil. Figure 4.8 displays the configuration of the gap in the direct shear box. There is no precise specification to determine the gap size based on particle size distribution. In this study, the DST gap size is considered to be equal to D_{85} of the material (i.e., the aggregate size that 85% is finer) (Nicks and Adams (2014)).

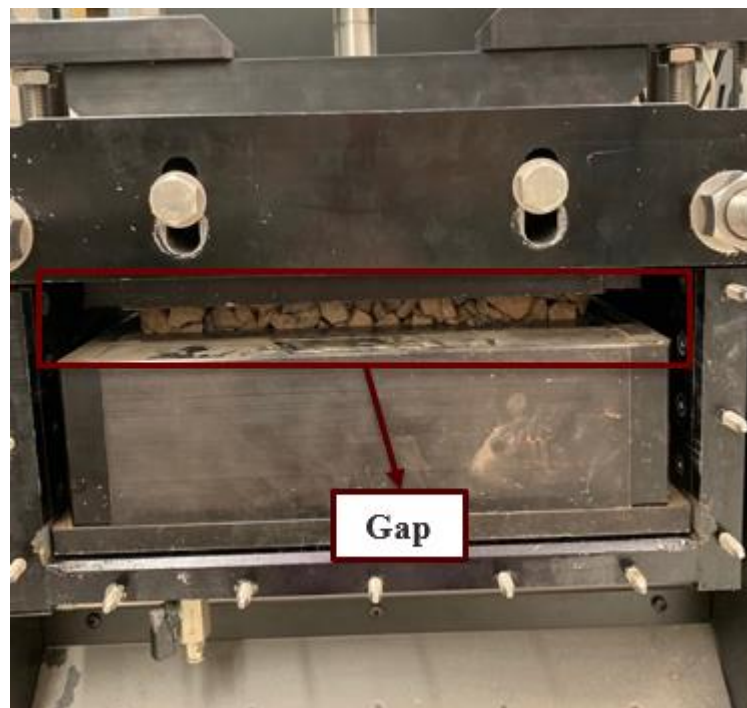
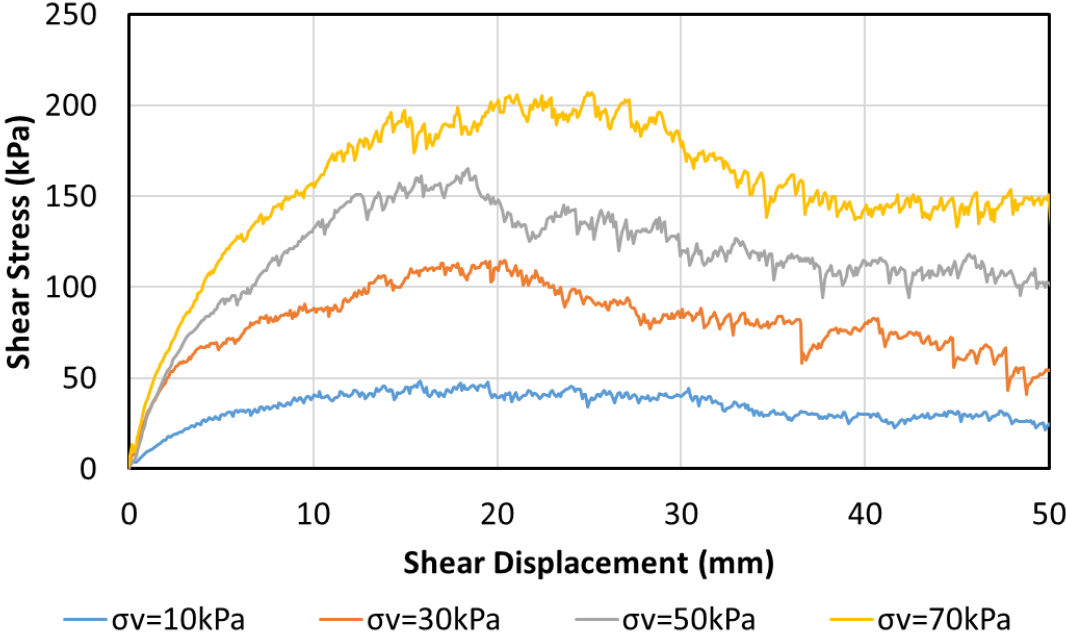


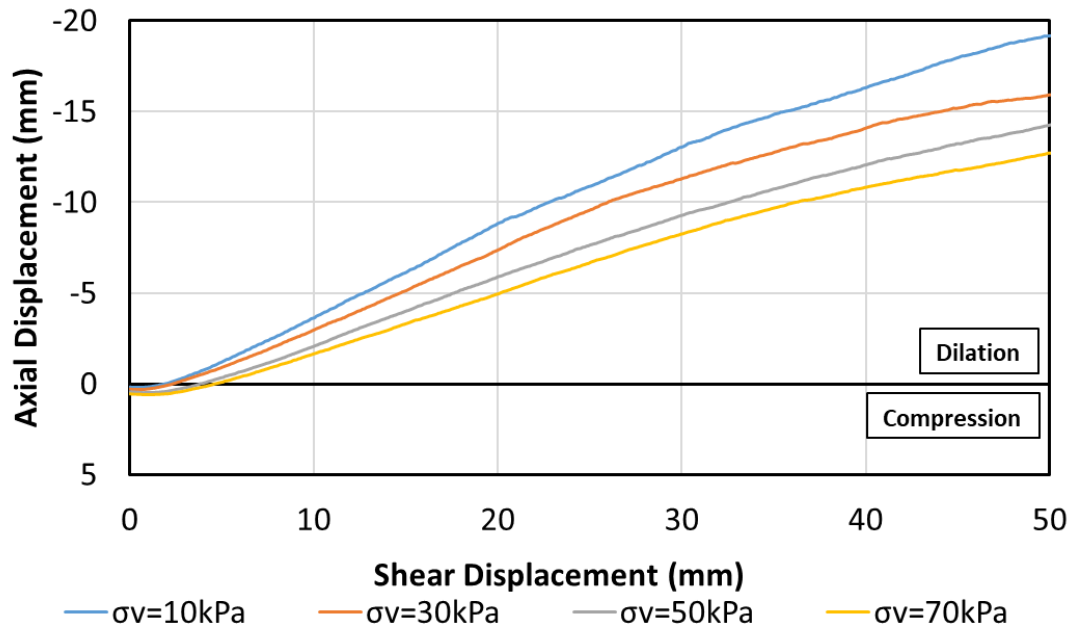
Figure 4.8. Gap in DST box

In this section, the role of the gap between two halves of the DST box is investigated. For this purpose, a series of DST test on ballast #5 crushed granite material with 10, 30, 50, and 70 kPa vertical stresses were duplicated with two constant gap size.

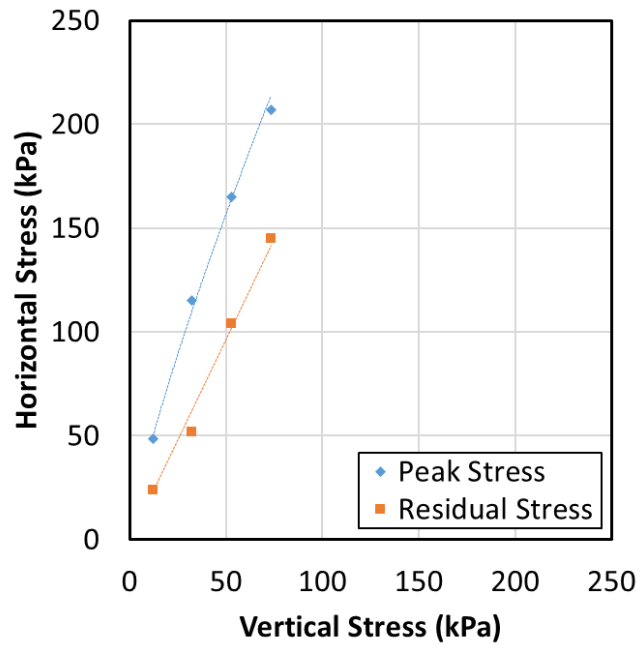
The first series was performed with a regular gap (the gap dimension equal to D_{85} of the material, which is 21 mm). On the other hand, another series was conducted with the gap dimension equal to D_{10} of the material (11 mm). All the sample preparation and the testing condition were the same to eliminate the influence of other factors. Figure 4.9 shows the DST results of ballast #5 with a reduced gap (11 mm).



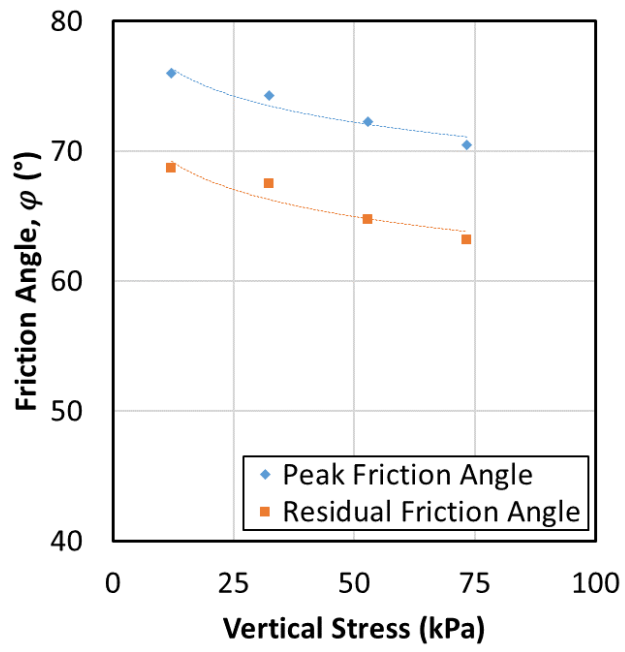
(a)



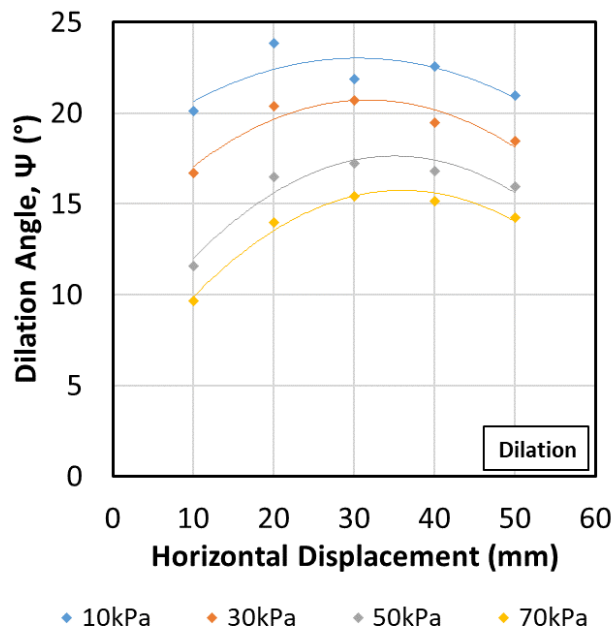
(b)



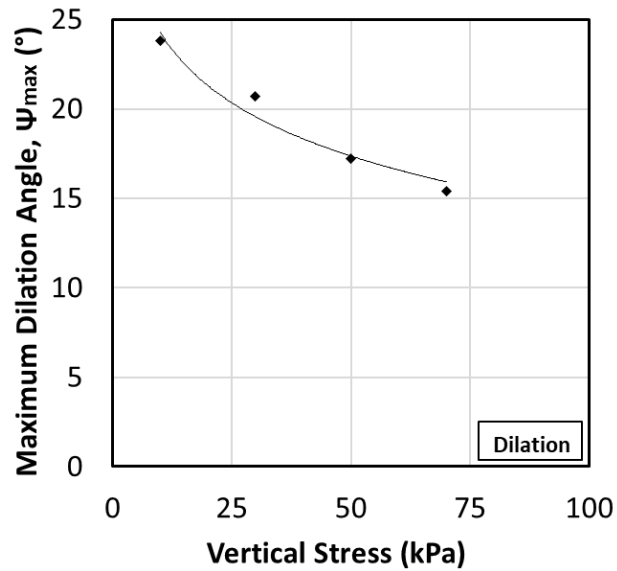
(c)



(d)



(e)



(f)

Figure 4.9. DST results for ballast#5 with the reduced gap. (a) Shear stress-shear displacement; (b) Axial displacement-shear displacement; (c) Failure envelope; (d) Variation of friction angle with the normal stress; (e) Variation of dilation angle with horizontal displacement; (f) Variation of maximum dilation angle with the normal stress

Table 4.3 summarized the shear strength properties of ballast #5 with a reduced gap (11 mm gap). The results revealed that lowering the gap can significantly enhance the shear resistance of the material. The shear strength for the test with a reduced gap (11 mm) is up to 57% higher than the tests with the regular gap (21 mm). Moreover, the peak friction angle of the tests with a reduced gap is 2 to 8 degrees higher than the tests with a regular gap. The same conclusion was made previously by Fu et al. (2015) for the influence of the gap.

Decreasing the gap in the direct shear test would also cause higher dilatancy for the sample. Comparing the results of two series of experiments with 11 mm and 21 mm gap revealed that the tests with a lower gap show 5 to 8 degrees higher maximum dilation angle.

Table 4.3. Strength parameters obtained from DST for ballast#5 (Reduced Gap)

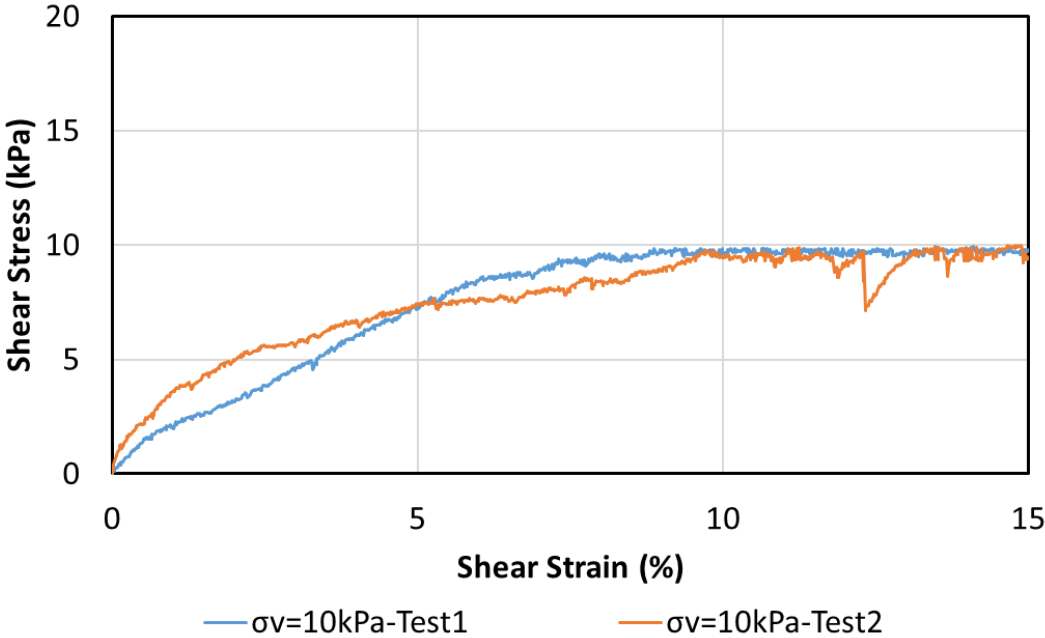
Test No.	Material	Normal Stress (kPa)	Max Shear Stress (kPa)	Residual Shear Stress (kPa)	φ_{Peak}	$\varphi_{Residual}$	ψ_{Peak}
1	Ballast #5	12.1	48.4	27.8	76.0	66.5	23.8
2	Ballast #5	32.3	115	64.3	74.3	63.3	20.7
3	Ballast #5	52.8	165	108.1	72.3	64.0	17.2
4	Ballast #5	73.3	207	144.5	70.5	63.1	15.4

4.3. Monotonic Direct Simple Shear Test (DSST)

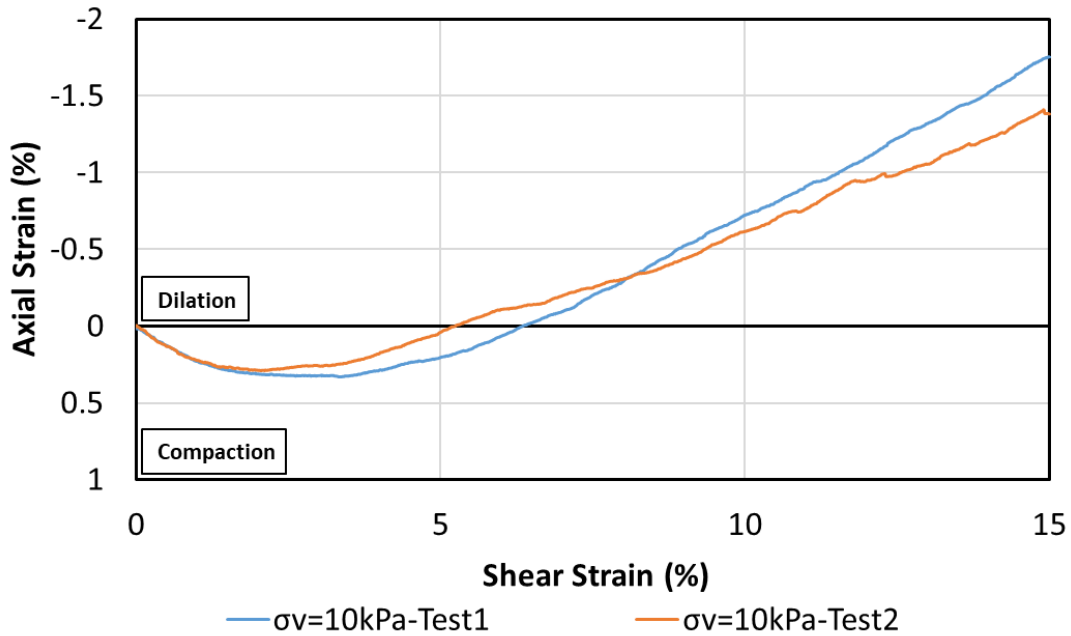
4.3.1. Test Repeatability

The repeatability and consistency of the direct simple shear apparatus was checked by performing two identical tests with the constant normal stress of 10 kPa on crushed granite ballast material. Figure 4.10 shows the shear stress-shear strain and axial strain-shear strain response of the tests. Comparing the stress-strain response of the ballast revealed approximately the same shear strength for both tests. A comparison of the dilatancy behavior of both tests shows a minor difference between the two experiments, which happens as a result of particle arrangement in the sample. In general, the close

response of the shear behavior of both tests displays the reproducibility of the DSST apparatus and the test procedure.



(a)



(b)

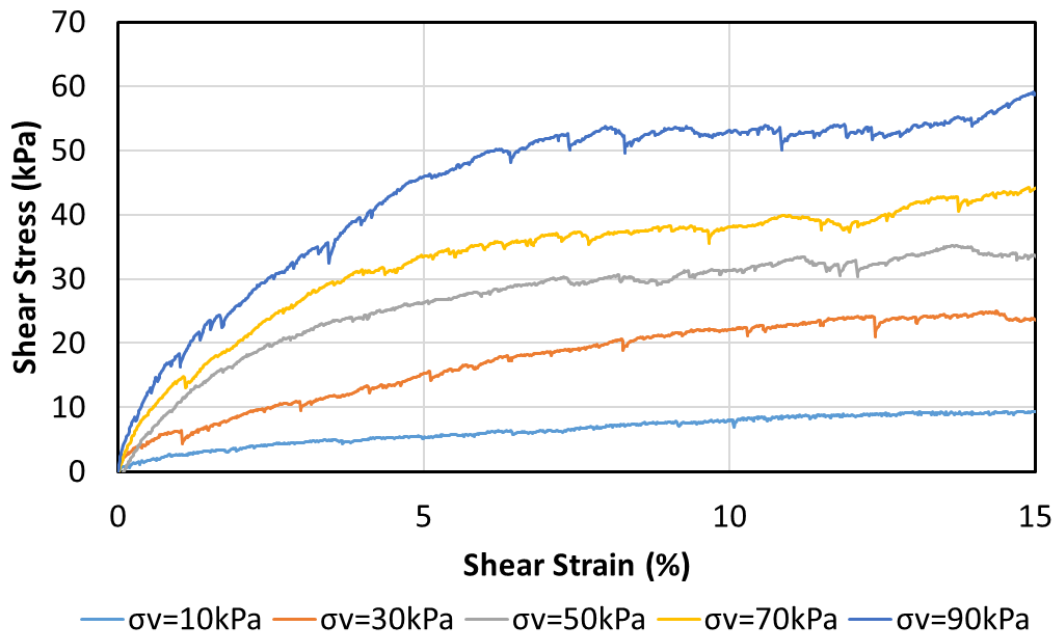
Figure 4.10. DSST repeatability. (a) Shear stress-shear strain; (b) Axial strain-shear strain

4.3.2. Shear Stress- Shear Strain and Axial Strain-Shear Strain

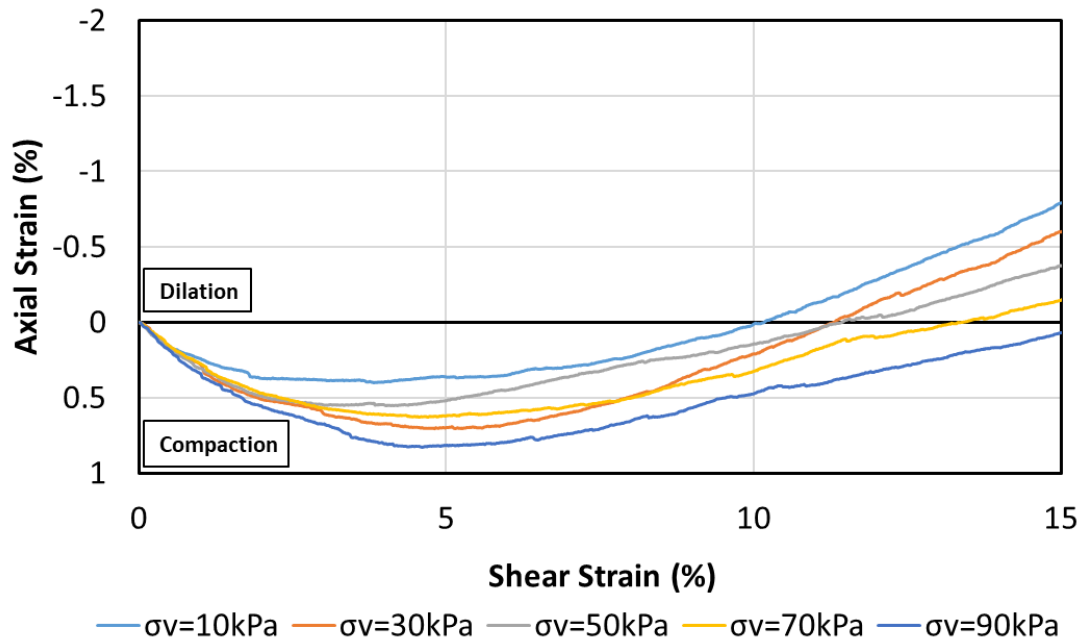
Figure 4.11 displays the shear response of ballast #5 based on DSST. Five tests were performed in constant load conditions with vertical stresses of 10, 30, 50, 70, and 90kPa. The range of applied vertical stresses is compatible with DST and represents the vertical stress that ballast experience in the field before train passage. The shear stress-shear strain diagram is shown in Figure 4.11(a). The shear stress for all the tests was increasing with shear strain and became approximately constant. Unlike the DST, there is no post-peak softening effect observed in DSST. It can be observed from the diagram that the shear strength of the material is remarkably dependent on the applied vertical stress. Increasing the magnitude of vertical stress from 10 to 90 kPa causes an increment of the

shear strength from 9.4 to 58.8 kPa. There are some noises found on the stress-strain diagram, which are due to particle breakage and rearrangement.

The dilatancy response of ballast #5 is shown in Figure 4.11(b). In this study, dilation (increase in volume) is considered to be negative upward while compression is positive downward. DSST results show significant compression at the beginning of the test, and after a specific shear strain (approximately 3 to 5%), the behavior changes to dilation. Most of the tests showed overall dilation in large shear strain. The dilation of the materials is compressed by increasing the test stress level. Therefore, increasing the applied normal stress causes more compression at the beginning of the test and less dilatancy afterward. It can be seen from the results of the test with a 90 kPa stress level that in the higher magnitude of the vertical level, the material can stay in the compression zone for all the shearing zone.



(a)



(b)

Figure 4.11. Shear Behavior of Ballast#5 Based on DSST. (a) Shear stress-shear strain; (b) Axial strain-shear strain

4.3.3. Shear strength Failure Envelope

The results of the direct simple shear test are presented in shear stress versus shear strain, and the maximum mobilized shear stress is defined as the shear strength of the material. Consequently, only a single stress point (vertical stress and maximum shear stress) is measured from the test. Therefore, the interpretation of the results of the DST and DSST can only be achieved by making an assumption on the stress state in the specimen at failure. There are various assumptions available in the literature (DeGroot et al. (1992)), and the two most common assumptions will be presented here.

The first theory (β method) assumes that the specimen fails along the horizontal plane. Thus, the maximum horizontal stress and the vertical stress that were obtained from

the test would be the shear and normal stress on the failure plane. In this circumstance, the friction angle is calculated as follow:

$$\varphi_{\beta\text{-method}} = \tan^{-1}\left(\frac{\tau_{hf}}{\sigma_{vf}}\right) \quad (9)$$

where τ_{hf} is the mobilized shear stress at failure and σ_{hf} is the vertical stress at failure. This assumption is reasonable for the direct shear test because the sample is forced to fail in the narrow horizontal failure plane. Therefore, the β method is used for the DST calculation in this study. However, this assumption is considered to be incorrect (Roscoe (1953), Airey (1985), and DeGroot et al. (1992)) for DSST and leads to conservative and low shear strength properties.

Another theory (α method) proposed by Roscoe (1953) is used for defining the failure envelope and calculating the friction angle from the DSST results. In this theory, it is assumed that the horizontal plane corresponds to the plane with the maximum shear stress but not to the failure plane. In this case, the friction angle is calculated by using the following equation:

$$\varphi_{\alpha\text{-method}} = \sin^{-1}\left(\frac{\tau_{hf}}{\sigma_{vf}}\right) \quad (10)$$

where τ_{hf} is the mobilized shear stress at failure and σ_{hf} is the vertical stress at failure. α method is used for interpretation of the DSST results in this study. Figure 4.12 depicts the difference between the α and β methods, which can be used for the interpretation of the results of DSST.

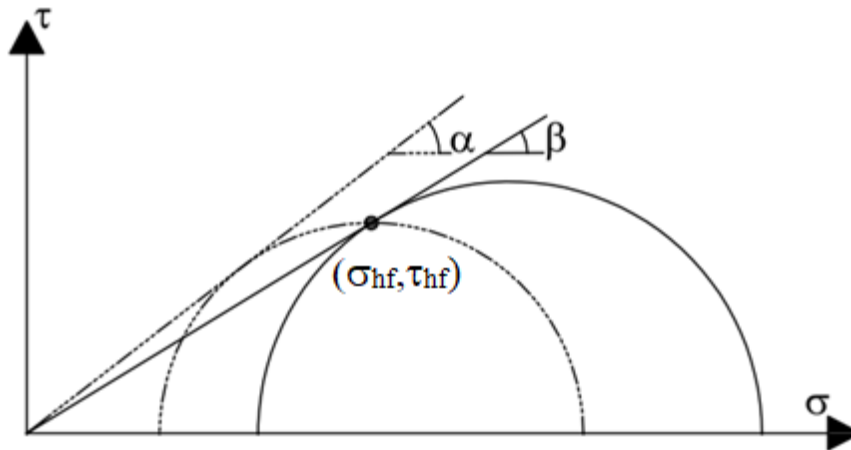


Figure 4.12. Interpretation of the stress states at failure for DSST results based on α and β methods (Zekkos and Fei (2017))

Figure 4.13 shows the failure envelope of ballast #5 based on DSST by using both α and β methods. It can be observed how the β method yields a lower failure envelop. The failure envelope for DSST is nonlinear, and the curvature is more pronounced in the lower stress level. Table 4.4 summarized the shear strength properties of ballast #5 based on DSST.

Table 4.4. Summary of DSST results for ballast #5

Test No.	Material	Normal Stress (kPa)	Max Shear Stress (kPa)	φ (°)	Ψ_{Peak}	G_{max} (MPa)
1	Ballast #5	10.5	9.4	64.0	3	2.37
2	Ballast #5	30.1	25.1	56.4	2.3	5.8
3	Ballast #5	50.2	36.8	47.1	1.4	7.35
4	Ballast #5	70.0	49.2	44.6	0.6	9.87
5	Ballast #5	90.1	58.8	40.7	-0.3	11.3

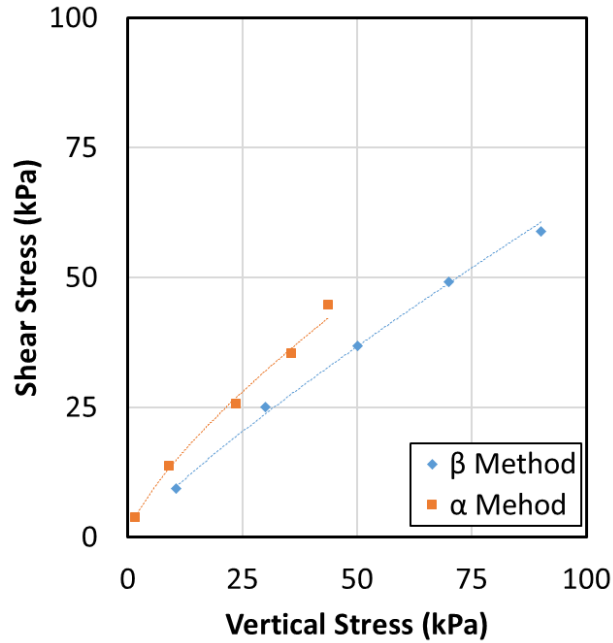


Figure 4.13. Failure envelope of ballast#5 based on DSST

4.3.4. Shear Modulus

The variation of the ballast shear modulus with the shear strain for five DSST with vertical stresses of 10, 30, 50, 70, and 90 kPa is presented in Figure 4.14. In DSST performed in this study, the shear modulus variation is captured for the shear strain range of 0.01% to 15%. The shear modulus is defined as a slope of the shear stress-shear strain curve, and it is given by the following equation:

$$G = \frac{\tau}{\gamma} \quad (11)$$

where τ is the shear stress and γ is the shear strain. As it can be observed in Figure 4.14, the shear modulus is decreasing in higher shear strain. Table 4.5 summarized the magnitude of ballast #5 shear modulus at different shear strain and vertical stress.

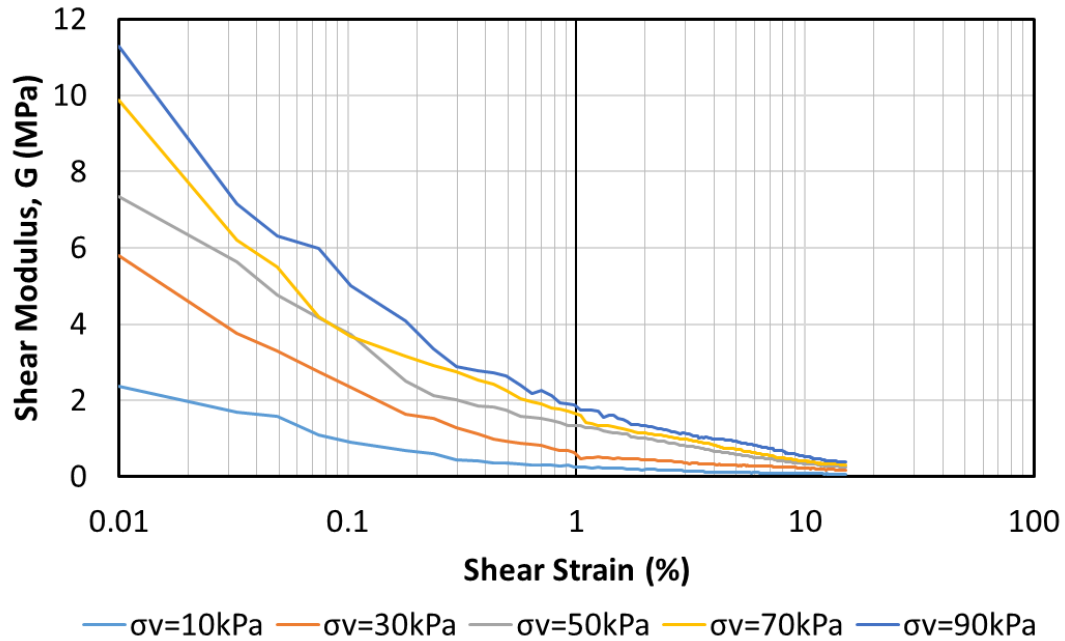


Figure 4.14. Shear modulus variation with shear strain for ballast #5 based on DSST

Table 4.5. Shear modulus of ballast #5 at different shear strain and vertical stress

Normal Stress (kPa)	$G_{\gamma=0.01\%}$ (MPa)	$G_{\gamma=0.1\%}$ (MPa)	$G_{\gamma=1\%}$ (MPa)	$G_{\gamma=10\%}$ (MPa)
10	2.37	0.9	0.27	0.09
30	5.8	2.34	0.43	0.22
50	7.35	3.74	1.34	0.34
70	9.87	3.66	1.62	0.4
90	11.3	4.99	1.67	0.53

The highest value of the shear modulus, which is corresponding to the lowest shear strain (i.e. $\gamma=0.01\%$ in this study), is defined as the maximum shear modulus (G_{max}). The variation of the normalized shear modulus ($\frac{G}{G_{max}}$) is shown in Figure 4.15. The normalized

shear modulus is adopted to clarify the shear modulus degradation of the ballast. The close shear modulus degradation response of all the tests revealed that although the magnitude of the shear modulus highly depends on the stress level, the normalized shear modulus trend is independent of the vertical stress level. In other words, the shear modulus degradation is independent of stress level. The results also revealed that the significant reduction in shear modulus happens in a low amount of the shear strain. For example, the ballast shear modulus in all the tests reduced to approximately 7 to 18% of their maximum shear modulus (i.e., at 0.01%) at shear strain equal to 1%.

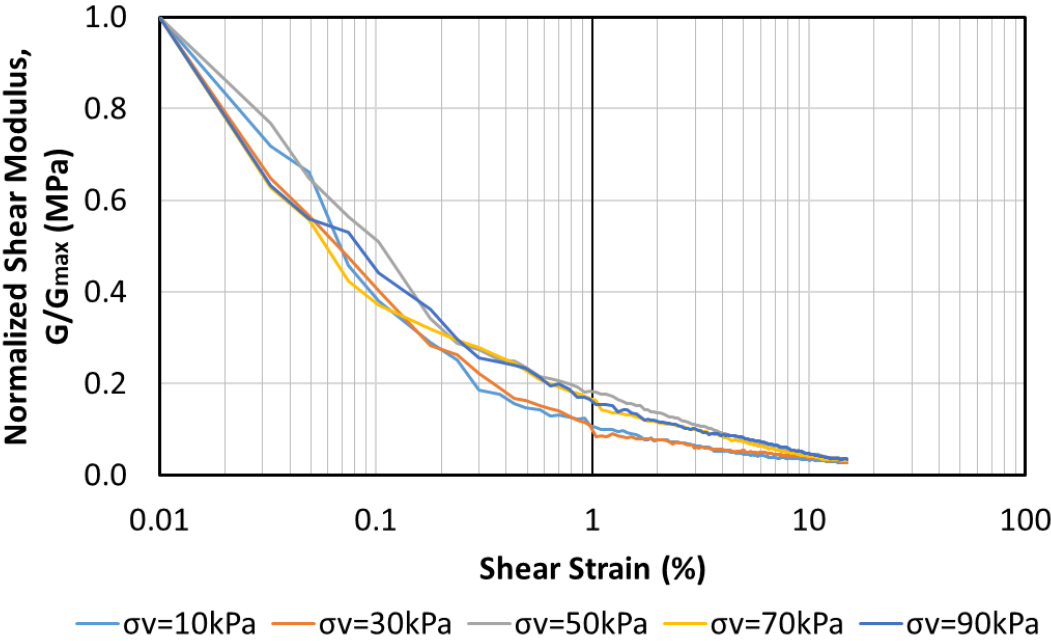


Figure 4.15. Normalized Shear modulus variation with shear strain for ballast #5 based on DSST

Figure 4.16 shows the variation of maximum shear modulus (G_{max}) with vertical stress. The shear modulus of the material is significantly influenced by the magnitude of

the vertical stress. The results revealed that the maximum shear modulus of ballast #5 increased from 2.4 to 11.3 MPa by increasing the vertical stress from 10 to 90 kPa. The same behavior for different soil materials was reported in the literature (Briaud (2013)).

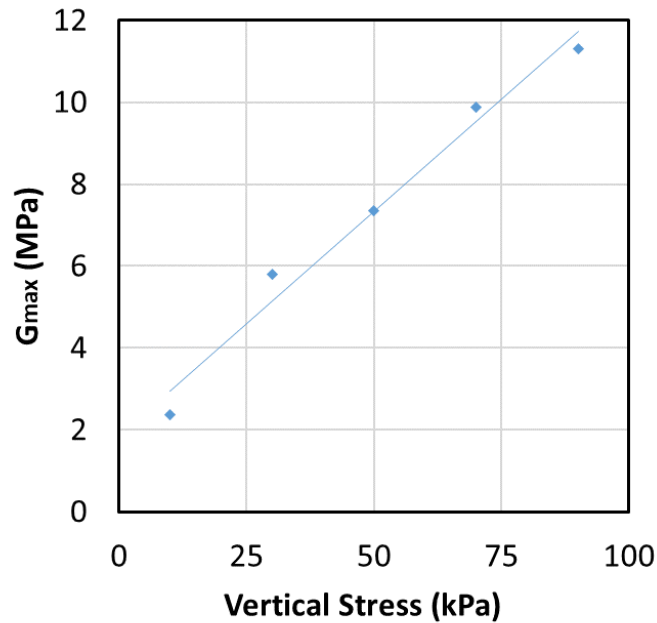


Figure 4.16. Maximum Shear modulus variation with vertical stress for ballast #5 based on DSST

4.3.5. Influence of Normal Stress on the Friction Angle and the Dilatancy

The friction angle is stress-dependent and decreases nonlinearly with the applied vertical stress. Figure 4.17 shows the variation of friction angle with normal stress for ballast #5 based on DSST. Increasing the normal stress from 10 to 90 kPa causes an increment of the friction angle from 40.7 to 64 degrees. More details about the equation that can show the nonlinear dependency of the friction angle to applied stress will be presented later in this chapter.

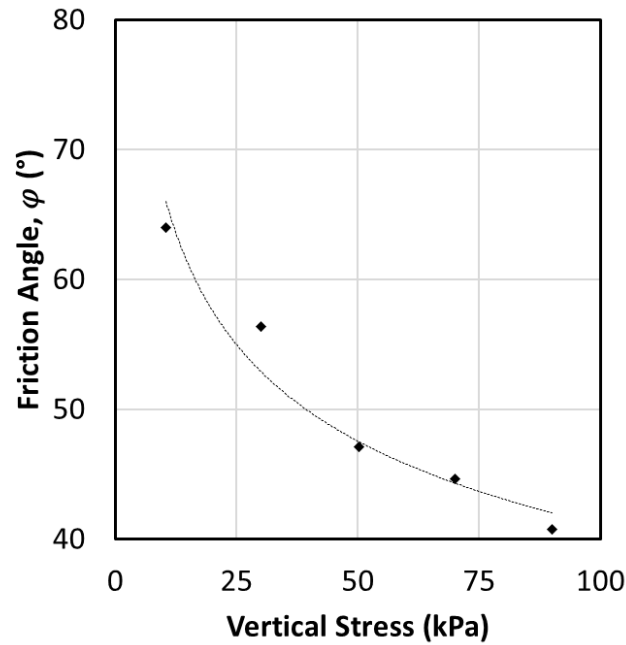


Figure 4.17. Variation of friction angle with the normal stress of ballast#5 based on DSST

Figure 4.18 illustrates the relationship between the dilation angle and the shear strain for five DSST with 10, 30, 50, 70, and 90 kPa vertical stress. As it was mentioned previously, in this study, the dilation angle defines a positive value, while compression is negative. The axial strain-shear strain relationship (Figure 4.10(b)) of the materials showed the tendency of compression at the beginning of the test (approximately 3 to 5%) followed by dilation. Therefore, at 5% shear strain, all the tests showed negative dilatancy (compression) ranging from approximately -4 to -9 degrees. After 5% shear strain, positive dilatancy starts, and as it can be observed in Figure 4.18 at 15% of shear strain, most of the tests showed a positive dilation angle. Figure 4.19 depicts the variation of maximum dilation angle with the vertical stress.

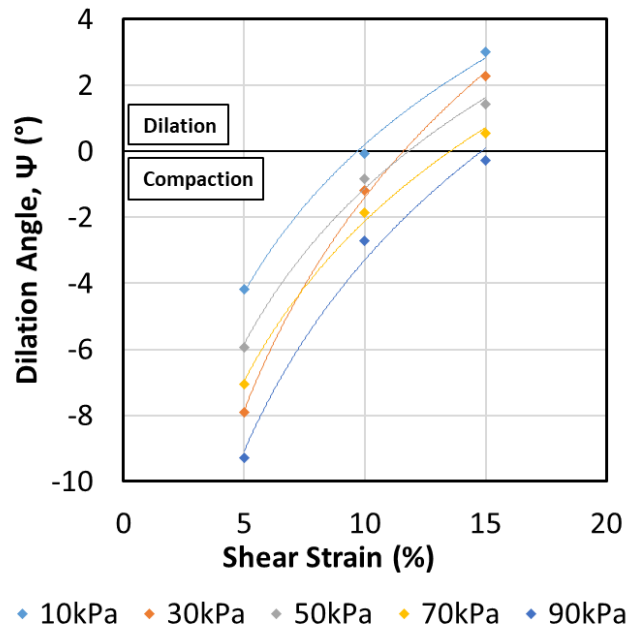


Figure 4.18. Variation of dilation angle with the shear strain of ballast#5 based on DSST

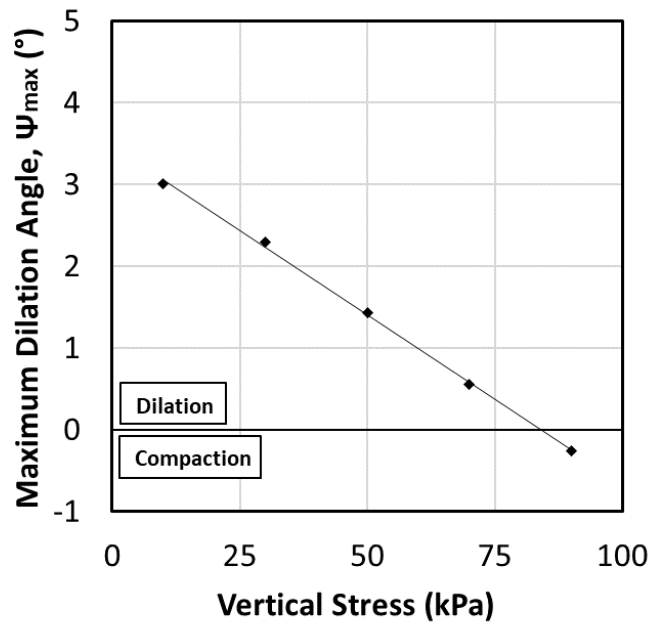


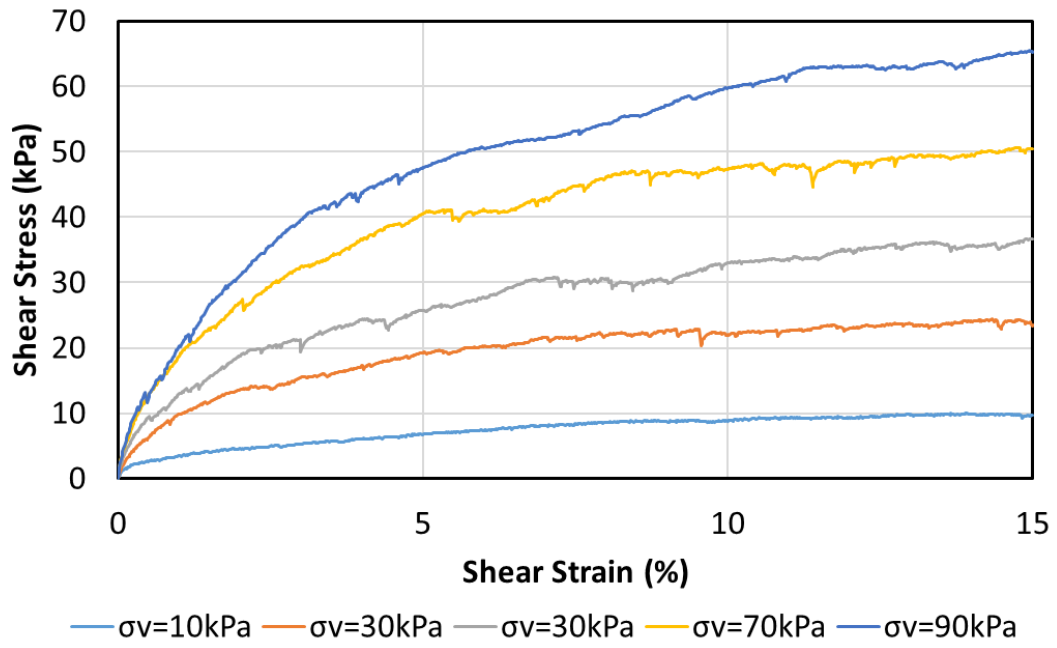
Figure 4.19. Variation of maximum dilation angle with the normal stress of ballast#5 based on DSST.

4.3.6. Influence of Ballast Maximum Particle Size

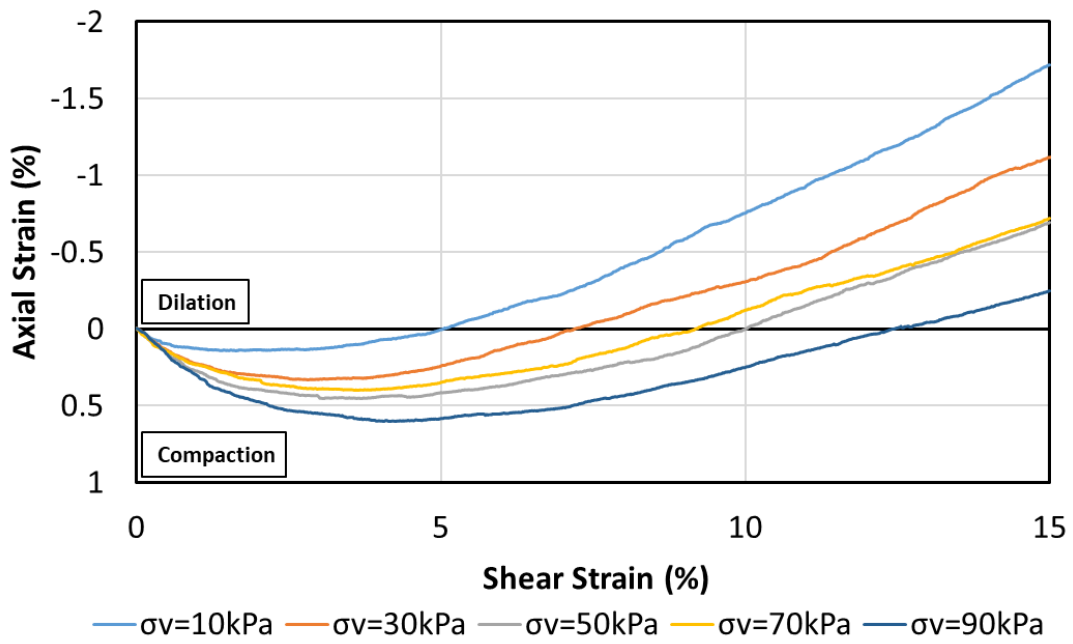
Similar to DST investigation, the impact of ballast maximum particle size is explored in DSST. For this purpose, two series of DSST in an identical testing environment and sample preparation with normal stresses of 10, 30, 50, 70, 90 kPa were performed on ballast #4 and #5. The maximum particle size for ballast #4 and #5 are 38.1 and 25 mm, respectively. Figure 4.20 and Table 4.6 show the complete sets of DSST results on ballast #4. The results of DSST on ballast #5 were presented previously in the chapter.

Table 4.6. Summary of DSST results for ballast #4

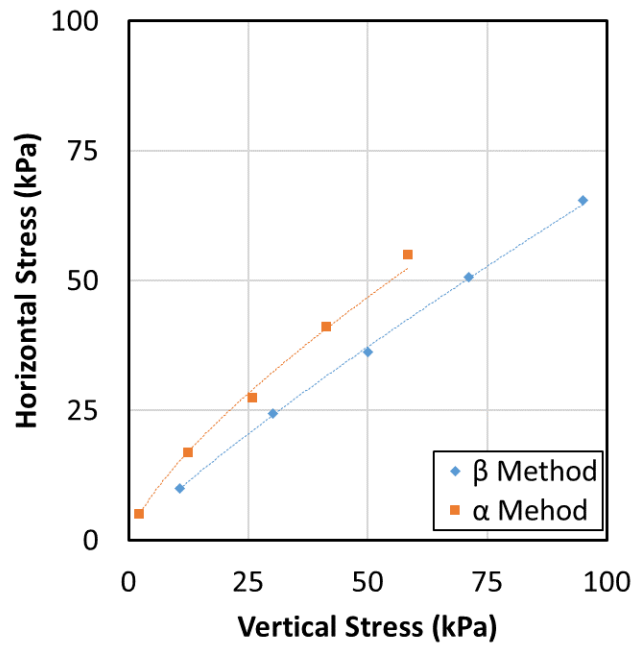
Test No.	Material	Normal Stress (kPa)	Max Shear Stress (kPa)	φ (°)	Ψ_{Peak}	G_{max} (MPa)
1	Ballast #4	10.8	10.0	67.5	6.5	4.1
2	Ballast #4	30.1	24.4	54.0	4.3	7.2
3	Ballast #4	50.1	36.2	46.2	2.7	9.4
4	Ballast #4	71.2	50.7	45.4	2.7	12.1
5	Ballast #4	95.1	65.5	43.5	0.9	13.4



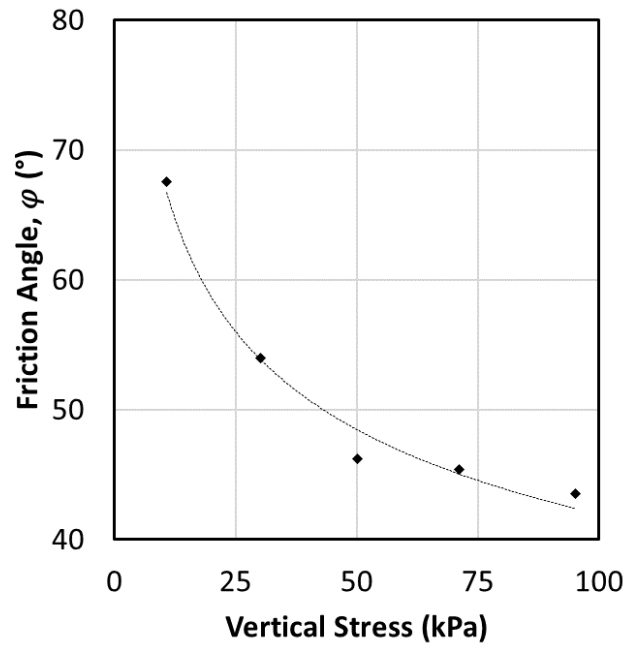
(a)



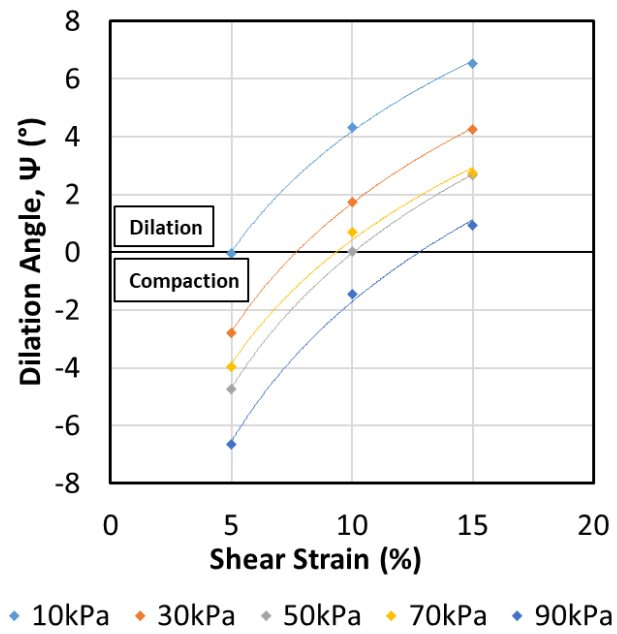
(b)



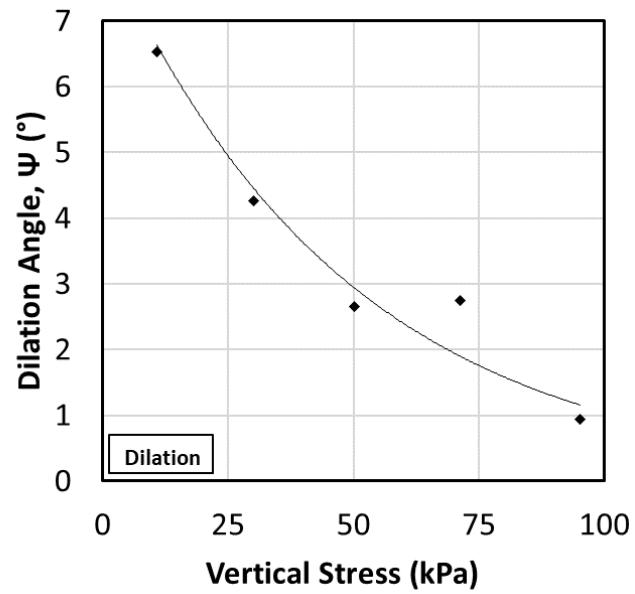
(c)



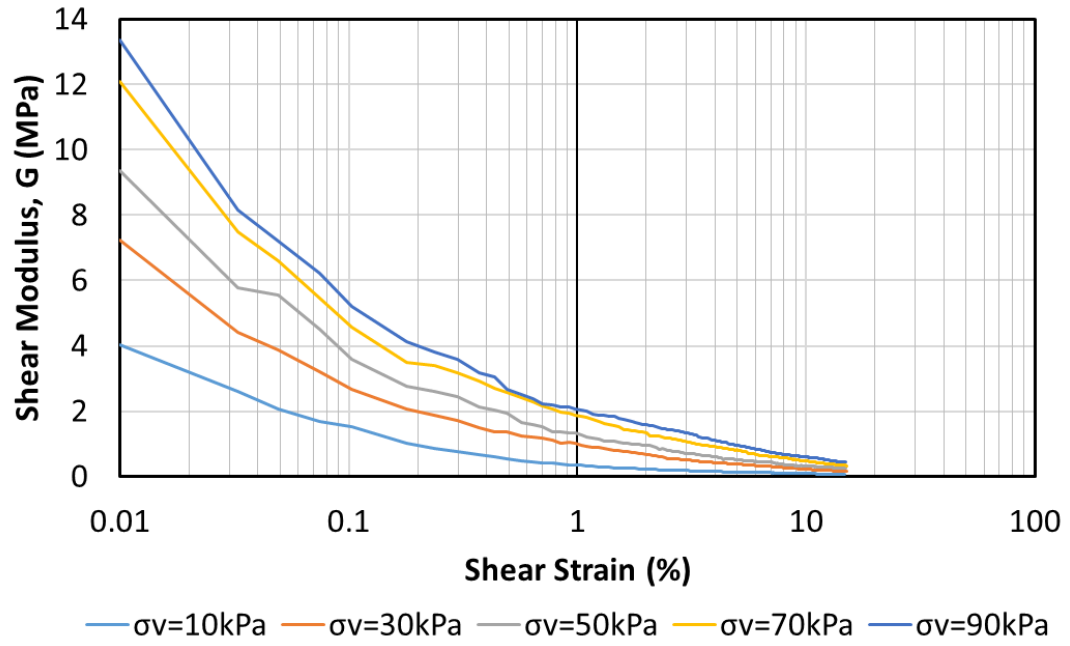
(d)



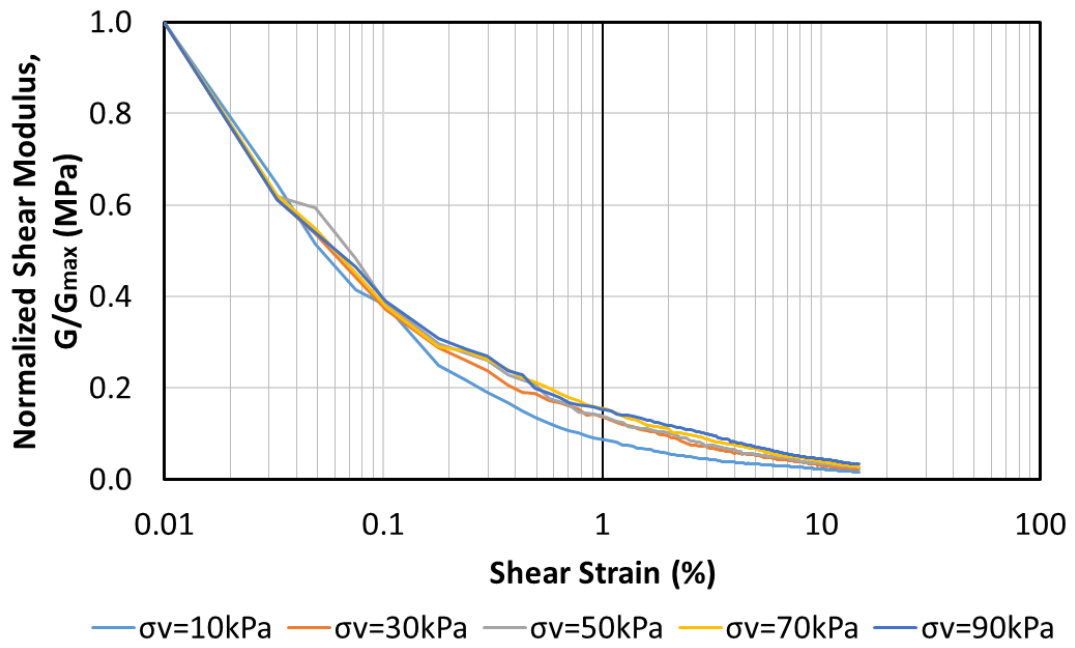
(e)



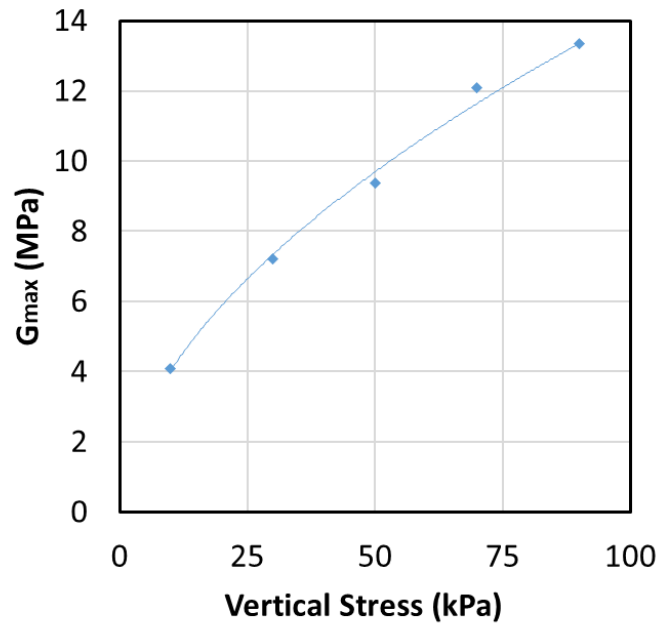
(f)



(g)



(h)



(i)

Figure 4.20. DSST results for ballast#4. (a) Shear stress-shear strain; (b) Axial strain-shear strain; (c) Failure envelope; (d) Variation of friction angle with the normal stress; (e) Variation of dilation angle with the shear strain; (f) Variation of maximum dilation angle with the normal stress; (g) Shear modulus variation with the shear strain; (h) Normalized Shear modulus variation with shear strain; (i) Maximum Shear modulus variation with the vertical stress

The differences between the shear behavior of ballast #4 and #5 are summarized in the following:

- Increasing the maximum particle size enhances the shear strength of the ballast. The range of shear strength of ballast #5 is 9.4 to 58.8 kPa while it is 10.0 to 65.5 kPa for ballast #4 with increasing the vertical stress from 10 to 90 kPa.

- The friction angle is increased with the sample maximum particle size. For example, in 10 kPa of vertical stress, the friction angle of ballast #4 and #5 are 67.5 and 64.0 degrees, respectively.
- Samples with larger particle size showed higher dilatancy. The dilation angle in 10 kPa vertical stress for ballast #4 is 6.5 degrees, while this number for ballast #5 is 3 degrees.
- Comparing the maximum shear modulus of the tests revealed that the maximum shear modulus is influenced by the specimen particle size. For example, the maximum shear modulus of ballast #4 and #5 at the vertical stress equal to 90 kPa are 13.4 and 11.3 MPa, respectively.

4.4. Monotonic Triaxial Test (TT)

4.4.1. Deviatoric Stress-Axial Strain

The results of three monotonic triaxial tests on railroad ballast with the confining pressure of 40, 80, 140 kPa are presented in this section. Figure 4.21 shows the deviatoric stress-axial strain of the monotonic TT performed on ballast#5. Similar to DST and DSST, the diagram is not smooth; as a consequence of breakage of the ballast particle's angular edge or particle relocation. The peak deviatoric stress is increased with confining pressure. The tests showed very slight or negligible post-peak strain softening. Unfortunately, there was no measurement of radial strain during the tests. Therefore, there is no information about the volumetric strain and the dilatancy of the material.

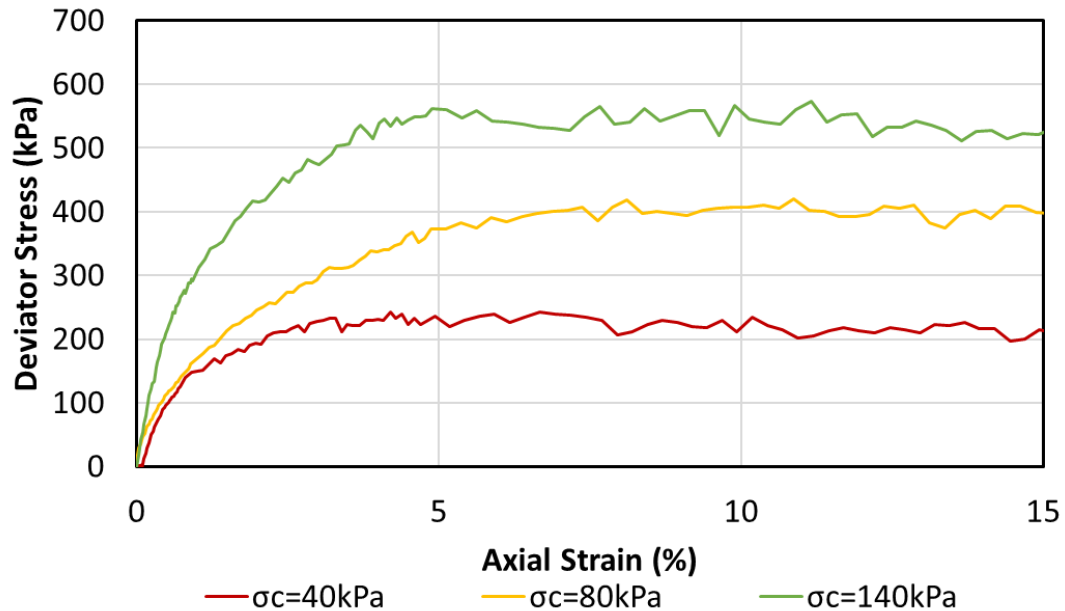


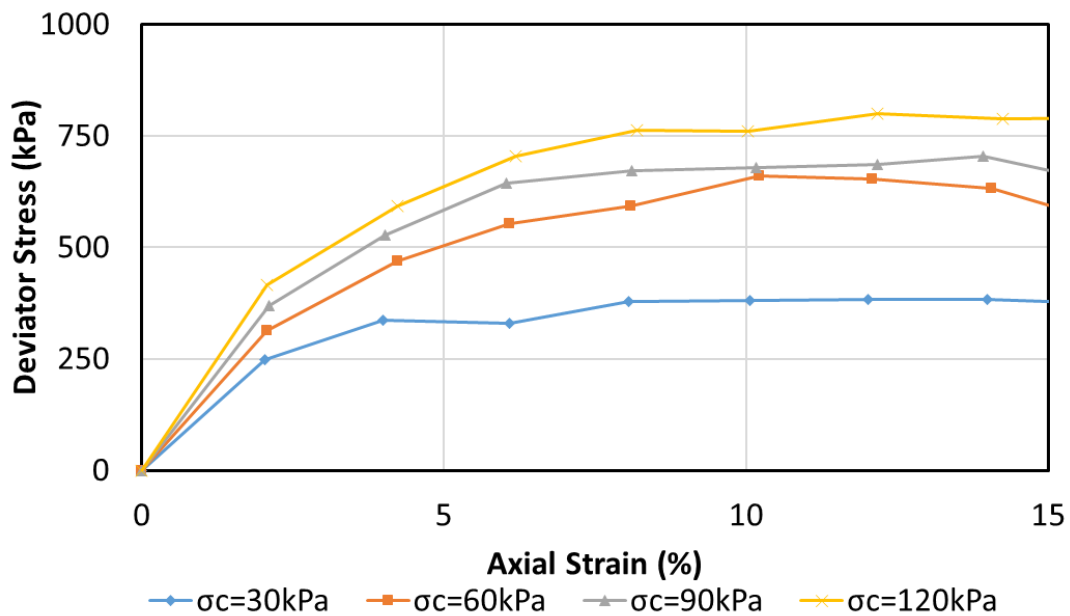
Figure 4.21. Deviatoric stress-axial strain response of ballast #5 based on TT

To illustrate the TT volumetric response of the railroad ballast, the results of large-scale triaxial tests performed by Indraratna et al. (1998) on railroad ballast will be discussed here. They used large-scale triaxial apparatus (300 mm diameter \times 600 mm height) to investigate the shear behavior of Latite ballast. The material was highly angular Latite stone with d_{\max} and d_{50} equal to 53 and 38.9 mm, respectively. The samples were compacted to reach the 15.3 kN/m^3 bulk unit weight. The ballast material used in their study is not similar to the current research performed at Texas A&M University. However, the primary purpose of presenting their results here is to exemplify the volumetric response of the railroad ballast.

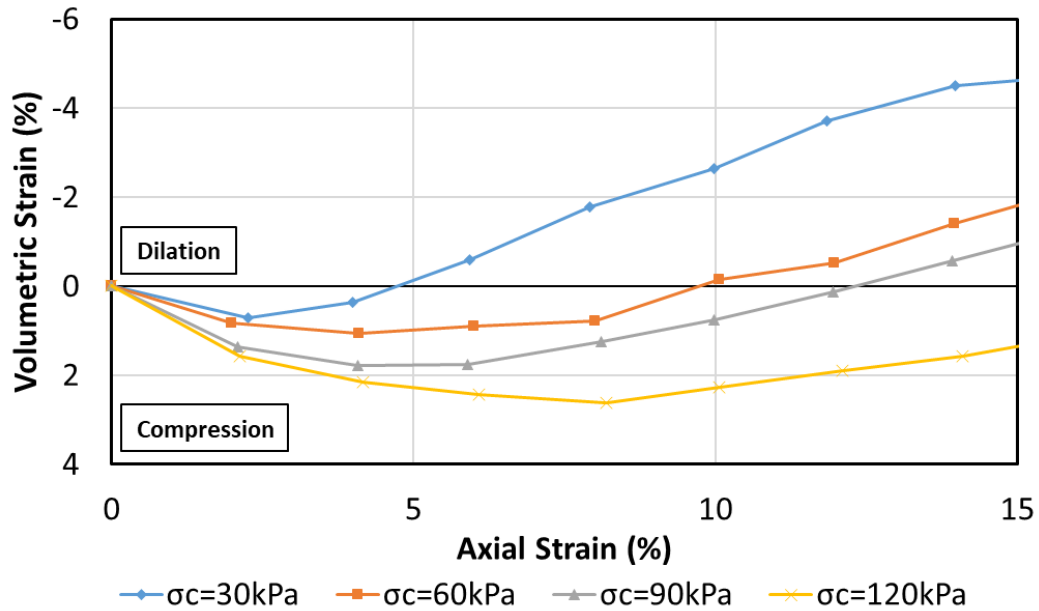
The results of four triaxial tests with confining pressure equal to 30, 60, 90, 120 kPa are presented in Figure 4.22 (Indraratna et al. (1998)). The deviatoric stress-axial

strain response is given in Figure 4.22(a). The overall behavior is similar to the TT results of the current study. However, the higher deviatoric stress is due to the larger tested particle size. The smoother diagram is a result of fewer data points available from their tests. The influence of particle size on the shear behavior of the large aggregate materials was presented previously in this chapter based on DST and DSST.

Figure 4.22(b) shows the volumetric-axial strain response of the material. The materials tend to compress at the low axial strain following by dilation. Increasing the confining pressure compresses the dilatancy of the materials. For example, the test at 30 kPa confining pressure showed a lower compression at the beginning and ended up with approximately 5% volumetric dilation at 15% axial strain. However, the test at 120 kPa confining pressure stayed at the compression zone for all the axial strain range.



(a)



(b)

Figure 4.22. Shear behavior of railroad ballast based on a triaxial test. (a) Deviatoric stress-axial strain; (b) volumetric-axial strain (data adopted from Indraratna et al. (1998))

4.4.2. Shear Strength Failure Envelop

The shear strength failure of ballast #5 based on the TT results is shown in Figure 4.23. The failure envelope is nonlinear and passes through the origin, which represents the zero value for the cohesion. The same behavior was expected and is in agreement with the DST and DSST findings. The non-linearity of the failure envelope is due to the dilatancy of the rock material at low-stress states. The same phenomenon is reported in the literature (Indraratna et al. (1998) and Charles and Watts (1980)). Table 4.7 provides a summary of the TT results on ballast #5.

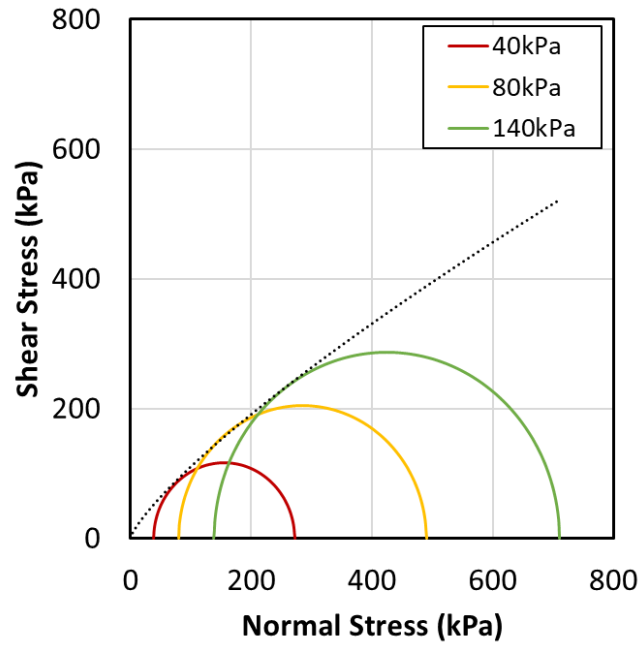


Figure 4.23. Shear strength failure envelope of ballast #5 based on TT

Table 4.7. Summary of monotonic TT results for ballast #5

Test No.	Confining Stress (kPa)	Vertical Stress at Plane of Failure (kPa)	Deviatoric Stress (kPa)	φ (°)	E_i (MPa)
1	38.3	75.0	243.0	50.5	49.1
2	79.9	165.0	420.0	46.5	99.9
3	137.9	260.0	573.0	42.5	169.9

4.4.3. Initial Triaxial Elastic Modulus

The initial triaxial elastic modulus (Young's modulus) is the other crucial properties of the ballast material that is studied in the triaxial test. The following equation expresses the initial triaxial elastic modulus:

$$E_i = \frac{\sigma_1' - 2\nu\sigma_3'}{\varepsilon_a} \quad (12)$$

where σ_1' is the effective vertical stress, σ_3' is the effective confining stress, ε_a is the axial strain, and ν is the Poisson's ratio. The abovementioned formula should be used at the initial linear section of the stress-strain curve. Figure 4.24 illustrates the relationship between the initial triaxial elastic modulus of ballast #5 and the confining stress level based on TT results. The Poisson's ratio of the material was assumed to be 0.35. The initial value for the elastic triaxial modulus was determined for an axial strain equal to approximately 0.01%. As was expected, this parameter is increasing with confining stress.

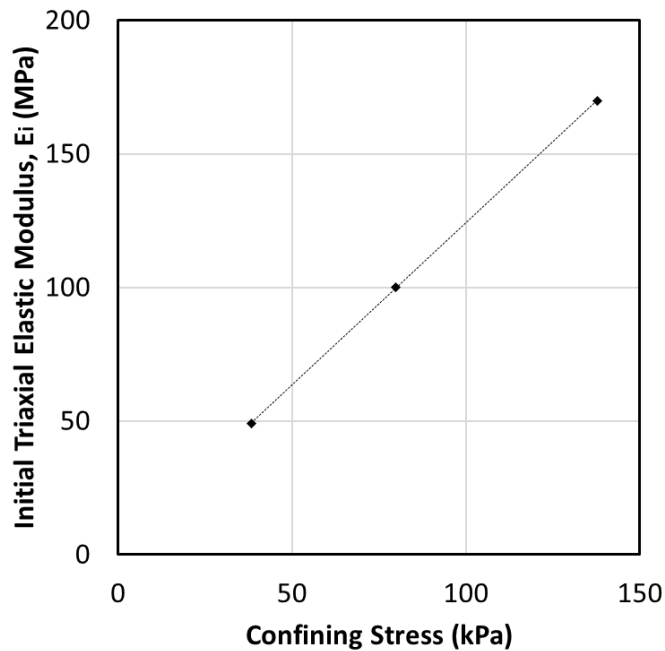


Figure 4.24. Influence of the confining pressure on the initial triaxial elastic modulus

4.4.4. Influence of the Confining Stress on the Friction Angle

The variation of the friction angle of ballast #5 with confining pressure is presented in Figure 4.25. The friction angle decreased nonlinearly with the confining pressure. Similar to DST and DSST results, the reduction in friction angle is more pronounced in lower stress levels. The large magnitude of the friction angle at low confining pressure occurs because at this stress level, the inter particle contact forces are below the parent rock crushing strength. As a consequence, particle degradation is small, and the materials are able to dilate. The same observations were made previously for the Latite ballast materials (Indraratna et al. (1998)) and rockfill materials (Marsal (1967) and Charles and Watts (1980)).

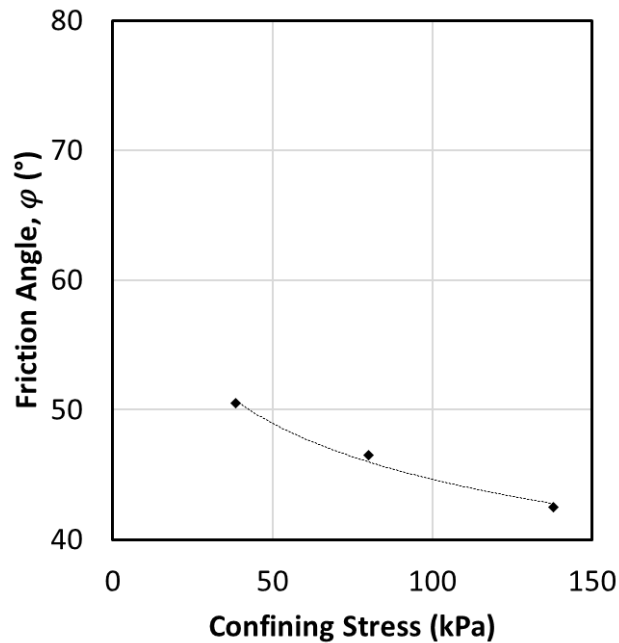


Figure 4.25. Variation of the friction angle with the confining stress for ballast #5 based on TT

4.5. Comparison of the Shear Behavior of the Railway Ballast Based on DST, DSST, and TT Results

The direct shear, direct simple shear, and triaxial tests have been used for many years to calculate the strength parameters of the soils (Saada and Townsend (1981)). These tests have been used interchangeably for testing large size aggregates. So, it is essential to pay attention to the possible difference in the results. Attempts have been made in the literature to compare the results obtained from different tests. The results revealed that the difference in the calculated shear strength properties using various tests is highly dependent on the soil type.

On the comparison of DST and TT, Skempton (1964), Casagrande and Poulos (1964) stated that the same effective stress parameters were obtained for lean clay. Castellanos and Brandon (2013) compared the results of a series of CD direct shear and CU triaxial tests on alluvial soils. Their results showed about a 2 to 5 degrees lower friction angle in a DST compared to the TT. Lini Dev et al. (2016) compare the results of DST and TT in drained conditions for sand. The friction angle obtained by DST was found to be 2 to 8 degrees higher compared to the TT results. The same difference was observed for sand by Cornforth (1964) and Lee (1970).

DST and DSST have also been compared for different geotechnical applications. Fei and Zekkos (2018) investigated the difference between the shear strength parameters obtained from large-scale DST and DSST on municipal waste material. According to their results, the DST showed a higher friction angle and a lower cohesion than the DST. Dounias and Potts (1993) performed numerical analyses on idealized fully drained

isotropic elastoplastic material. Their results showed that the DST overestimates the initial stiffness and peak strength by around 7.5%. The results of a comparative study on DST and DSST performed by Hanzawa et al. (2007), on clay samples showed a higher estimation of shear strength for the DST. The same trend was observed in FEM analyses performed by Tejchman and Bauer (2005).

As stated above, some comparisons between the results of these tests have been made for different materials. But, to the author's knowledge, there is no published study comparing the results of DST, DSST, and TT for samples with oversized particles. Therefore, the shear behavior of the ballast in all three tests will be discussed and compared in the following sections.

4.5.1. Shear Behavior

The shear behavior results of the large-scale DST, DSST, and TT on crushed granite ballast #5 are presented in Figure 4.26. For the purpose of consistency, the results of the triaxial tests are presented in terms of the maximum shear stress on the Mohr circle (i.e., half of the deviatoric stress). By comparing the results of shear stress vs. shear strain or shear displacement of the DST (Figure 4.26(a)), DSST (Figure 4.26(b)), and TT (Figure 4.26(c)), the following observations can be made.

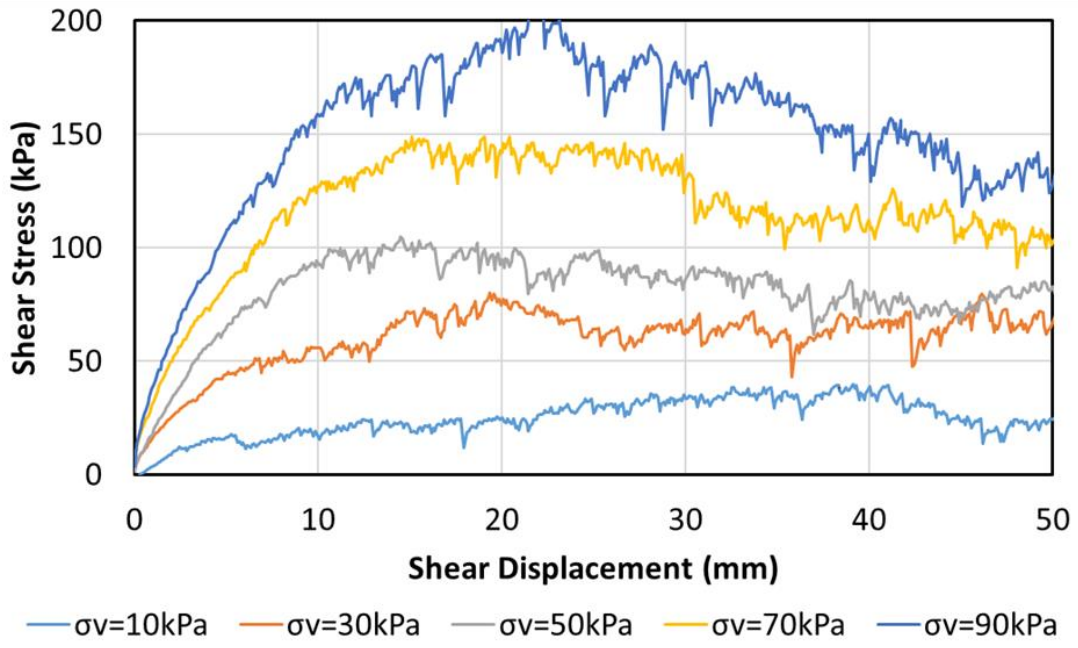
First, in all tests, the shear stress increases when the shear strain/displacement axial strain (in TT) increases until the peak shear stress is reached. However, there is a difference observed in the post-peak softening behavior of the material. The DST shear stress-shear displacement results show considerable strain-softening for the material while

the DSST and the TT results show no or negligible post-peak strain-softening. The same observation for the strain-softening behavior of large aggregate materials has been reported for the direct shear test (Dai et al. (2015)), and the triaxial test (Indraratna et al. (1998)).

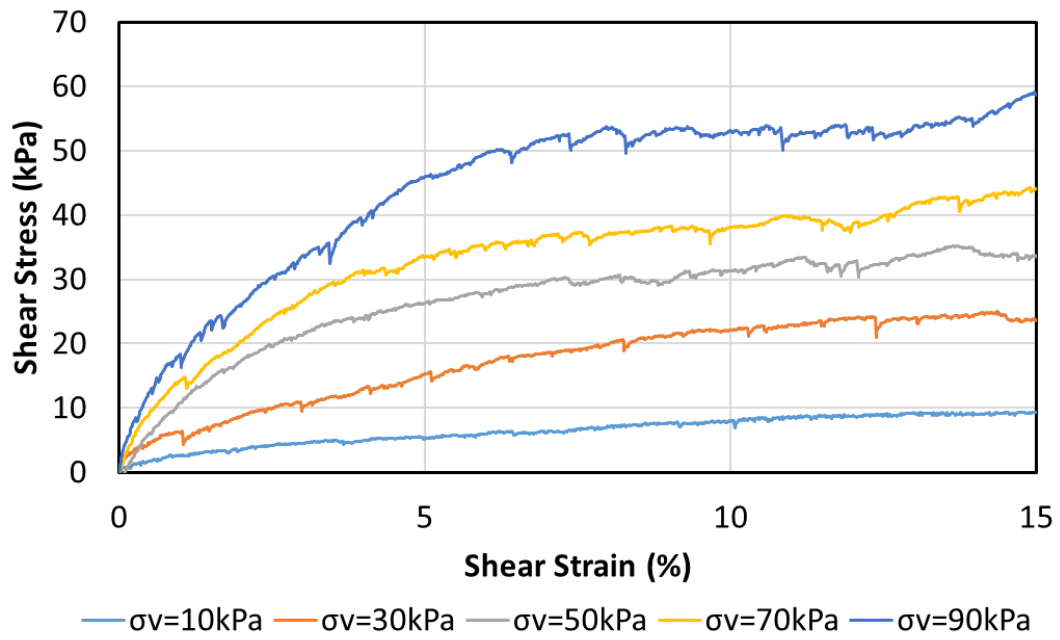
Second, all the tests revealed a fluctuating response of the stress-strain (displacement). This phenomenon is common for large aggregate angular materials and happened due to the deterioration of the particle edges, particle breakage, relocation, and rearrangement. However, DST shows more noise than DSST and TT because it forces the sample to fail in the narrow horizontal shear band.

Third, all the tests showed the dependency of the shear strength to the stress level. The peak shear strength increases with increasing normal/confining stress. But, the maximum shear strength measured in each test is different. For DST, the peak shear strength increased from 40 to 208 kPa for increasing the vertical stress from 10 to 90 kPa. The same range of normal stress causes a shear strength increment from 10 to 59 kPa for DSST. The TT results revealed 121 and 286 kPa shear strength for the confining stresses of 40 and 140 kPa, respectively.

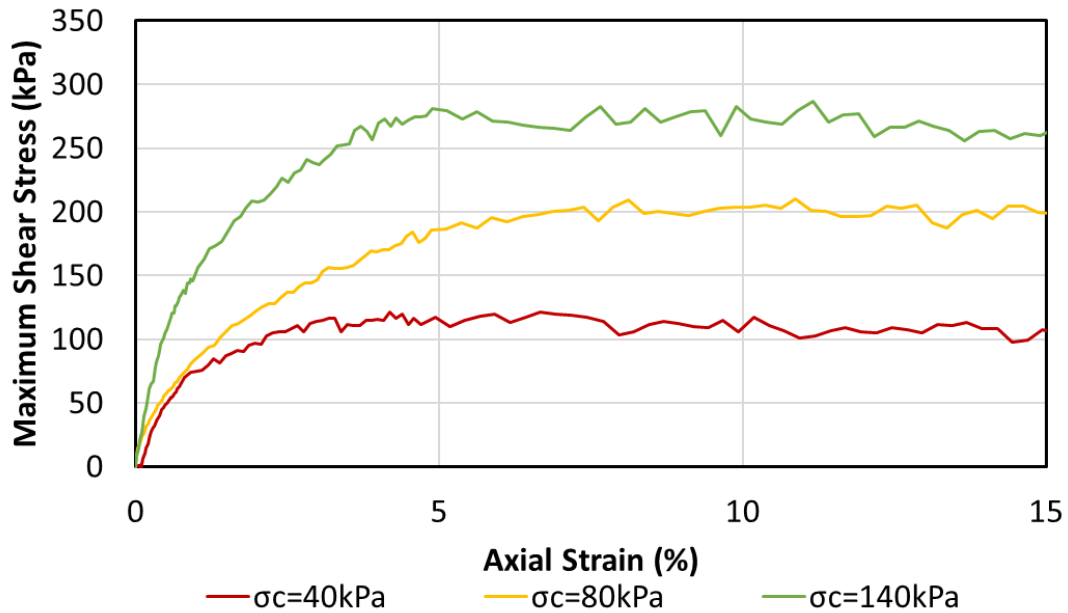
Forth, the results of DSST and TT showed that the initial tangent modulus of the material increased with increasing normal/confining stress. DSST results showed that the maximum shear modulus increased from 2.4 to 11.3 MPa for increasing the normal stress from 10 to 90 kPa. Moreover, the initial triaxial elastic modulus was risen from 49.1 to 169.9 MPa for increasing the confining pressure from 40 to 140 kPa.



(a)



(b)



(c)

Figure 4.26. Comparison of the stress-strain (or displacement) of the railroad ballast.

(a) DST; (b) DSST; (c) TT

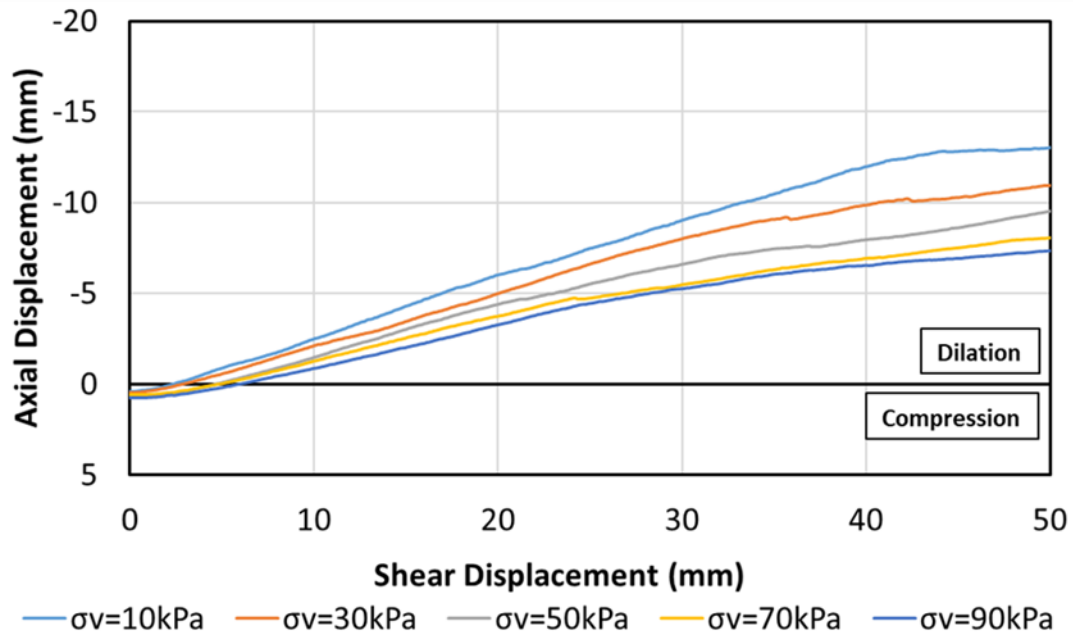
The dilatancy response of the ballast based on DST and DSST is presented in Figure 4.27. Because there were no measurements of the radial strain in the triaxial tests, the results of the triaxial tests only show the shear stress vs. axial strain. As it was mentioned previously, dilation (increase in volume) is considered to be negative upward while compression is positive downward. Comparing the results of the DST and DSST reveals a different volumetric response of the ballast material for each test.

The DST results show a slight initial compression followed by significant dilation with increasing shear displacement. The results also showed that increasing the applied normal stress causes a reduction in dilatancy. The maximum dilation angle calculated from the DST results for the crushed granite material decreased from 16.7 to 10 degrees when

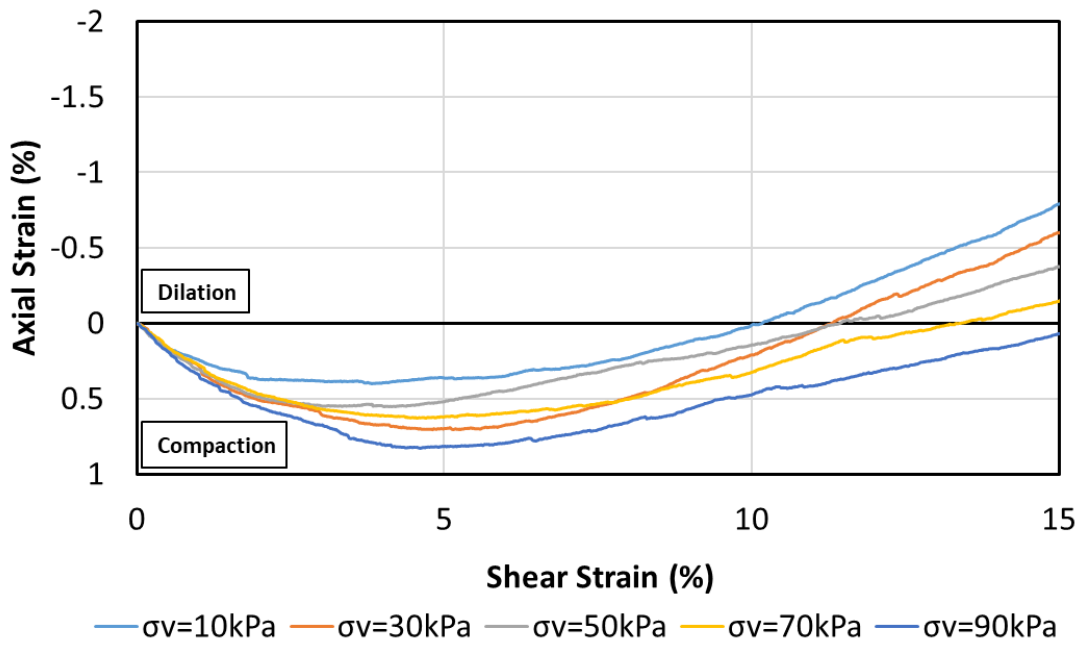
increasing the normal stress from 10 to 90 kPa. Similar behavior was observed in previous direct shear tests performed by Indraratna et al. (2011b) and Dai et al. (2015). As can be seen in Figure 4.27(a), the dilation rate decreases at large shear displacement. The reduction in the dilation angle seems to be associated with the post-peak strain-softening.

On the other hand, as it is shown in Figure 4.27(b), the DSST results show significant compression at the beginning of the test. The behavior changed to dilation after a certain shear strain (approximately 3 to 5%). Most of the tests showed overall dilatancy at 15% shear strain. Similar to the DST results, increasing the applied normal stress in the DSST causes more compression at the beginning of the test and less dilatancy afterward. The results revealed that with increasing normal stress, the maximum compression angle increases from 10.5 to 15.6 degrees, and the maximum dilation angle decreases from 4.2 to 0.8 degrees. Although the volumetric behavior trend is similar to the DST results, the DSST shows higher compression at the beginning of the test, less overall dilation, and stays in the compression zone for a broad range of shear strain.

Because there was no measurement of radial strain in the triaxial tests, results of Indraratna et al. (1998) triaxial investigation on ballast materials were used (Figure 4.22(b)). According to their findings, the ballast showed dilatancy at very low confining pressure and showed more compression in higher stress levels. They concluded that for confining pressure greater than 60 kPa, the overall behavior of the material is compressive. Their finding is in line with other triaxial results reported by Tang et al. (2012). Thus, the volumetric behavior in the triaxial test seems to be closer to the DSST results.



(a)



(b)

Figure 4.27. Comparison of the dilatancy response of ballast. (a) Axial displacement-shear displacement for DST; (b) Axial strain-shear strain for DSST

4.5.2. Shear Strength Failure Envelope

The failure envelopes of the crushed granite ballast material derived from the DST, DSST, and TT results are depicted in Figure 4.28. It should be noted that each data point represents the shear stress and vertical stress at the plane of failure. DST data is related to the residual value discussed in section 4.2.3. DSST data is representing the α -method described in section 4.3.3.

The results of all three tests show a non-linear shear strength envelope, which is more pronounced in the lower normal/confining stresses. The same phenomenon is reported in the literature for different kinds of granular materials (Ponce and Bell (1971), Lee and Seed (1967)). This behavior can be attributed to the greater particle interlocking, more dilative behavior, and less particle breakage of the granular materials at lower stress levels. Moreover, as reported by Marsal (1967) and Marschi et al. (1972), at higher stress levels, the dilation is restricted, the failure envelope becomes more linear, and the linear Mohr-Coulomb envelope is a good representation of the material behavior at failure.

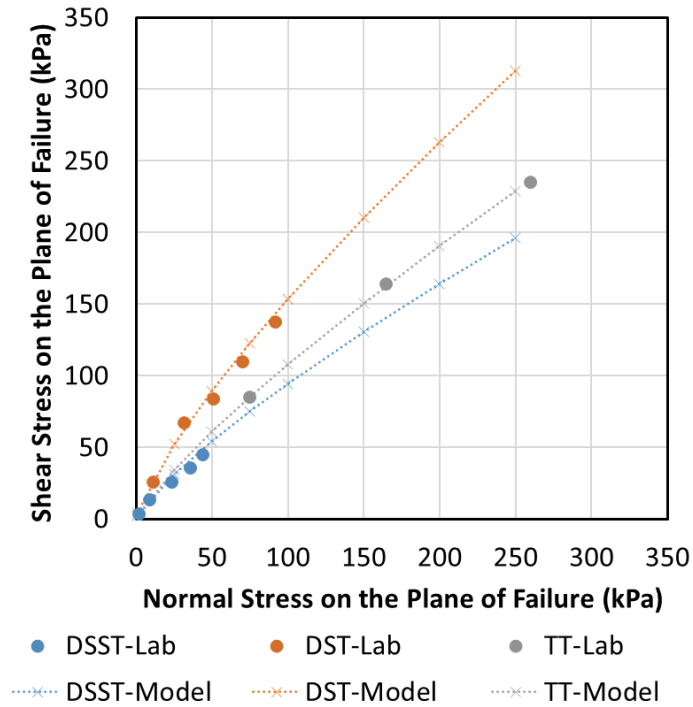


Figure 4.28. Comparison of the failure envelope of the railroad ballast based on DST, DSST, and TT results

Different equations have been proposed to describe the non-linear failure envelope. Based on the DST, DSST, and TT results obtained in this study, the model proposed by De Mello (1977) can be the best representative of the failure envelope of the ballast material as described by the following equation:

$$\tau = a\sigma_n^b \quad (13)$$

where σ_n is the normal stress on the plane of failure, a, and b are the constants related to the physical characteristics of the material. Parameter “a” is equivalent to $\tan(\varphi_1)$, which is the tangent of the friction angle for the vertical stress on the plane of failure equal to 1 kPa. Parameter “b” is related to the stress level and controls the non-linearity of the failure

envelope. According to Indraratna et al. (1993), the value of b in low stresses (less than 100 kPa) is less than 0.8 and can be greater than 0.9 in high stress value (more than 1.5 MPa).

The dashed lines in Figure 4.28 shows the validation of the proposed model with the experimental data from DST, DSST, and TT results. It can be observed that the model can successfully simulate the failure envelopes of all three tests. The failure envelopes were extended for the vertical stress on the plane of failure from 1 to 250 kPa for the purpose of comparison. The results showed that each test gives a unique failure envelope for the ballast material. Among the three tests, DST shows the highest failure envelope, and the DSST show the lowest. However, for the application of the railroad ballast, which experiences a low stress level at the field, the TT and DSST show nearly close failure envelopes.

Table 4.8 summarized the values of “ a ” and “ b ” in Equation (13) based on the results of the three tests. Comparing the “ a ” values reveals that the DST shows a higher value for the parameter a , which means higher friction angle. On the other hand, the DSST and the TT show nearly the same values for the parameter a , which correspond to friction angles of 67.3 and 68 degrees, respectively. The value of b is approximately the same for the DST and the DSST. The magnitude of the parameter b , which is related to the material characteristics, is approximately the same (in the range of 0.78 to 0.82) for all three tests.

Table 4.8. Shear strength model parameters for DST, DSST, and TT results

Test Type	φ_1	b
DST	76.8	0.80
DSST	67.3	0.78
TT	68	0.82

4.5.3. Friction Angle

The variation of the friction angle with the vertical stress on the plane of failure for the DST, DSST, and TT are presented in Figure 4.29. It should be noted that the DST friction angle is related to residual stress, as described in section 4.2.3. In addition, the DSST friction angle is based on the α -method (section 4.3.3). All three tests indicate that the friction angle of the ballast decreases nonlinearly with increasing stress levels. A comparison of the friction angle range for the tests shows that DST shows the highest magnitude of the friction angle while DSST shows the lowest. This finding is entirely in line with the failure envelope of the railroad ballast based on the three tests, as shown in Figure 4.28.

The high friction angle at low stress level occurs as a result of a high dilation angle of the material in that confinement. As discussed by Indraratna et al. (1998), at low confining pressure, the magnitude of the particles contact forces is less than the parent rock crushing strength. Thus, the interlocking particles cause more dilation at a low stress level, and consequently, a higher value of friction angle is measured. According to Charles

and Watts (1980), materials with higher crushing strength show higher dilatancy and higher friction angle.

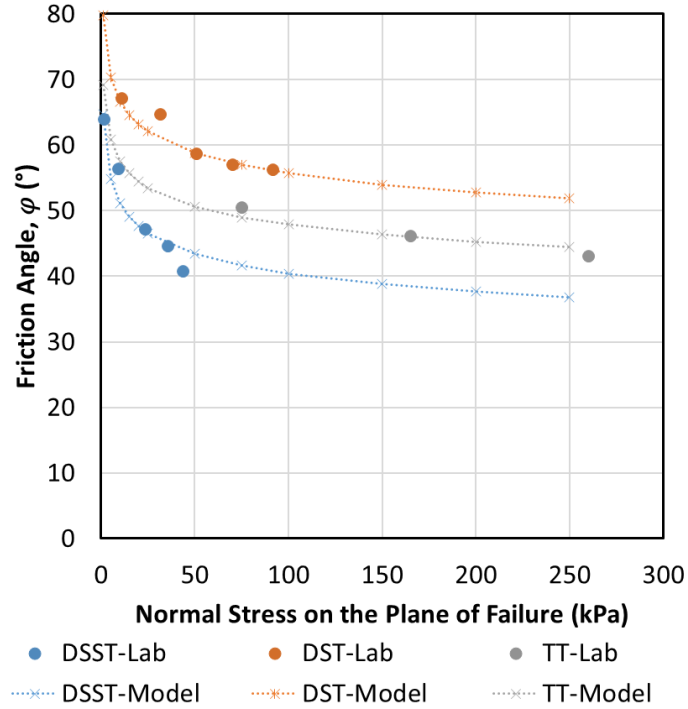


Figure 4.29. Comparison of the variation of the friction angle of the railroad ballast based on DST, DSST, and TT results

The variation of the friction angle with the applied stress can be presented by using the parabolic equation proposed by Gharavy (1996) for rockfill materials as follow:

$$\varphi_{\sigma} = \varphi_{p_a} \left(\frac{\sigma_n}{p_a} \right)^{-A} \quad (14)$$

where σ_n is the magnitude of the vertical stress on the plane of failure, φ_{p_a} is the friction angle of the material at one atmospheric pressure (98.1 kPa), and the parameter A is related to the characteristics of the material and controls the diagram nonlinearity. The dashed lines in Figure 4.29 shows the comparison of the proposed model prediction with the

experimental laboratory data. As can be observed, there is an acceptable agreement between the laboratory data and the model prediction. The range of the vertical stress on the plane of failure for all the three tests was extended from 1 to 250 kPa to cover all the measured experimental results.

Table 4.9 summarized the constant of the Equations (14) constants based on the calibration of the proposed model with the DST, DSST, and TT experimental data. The parameter b value, which is related to the tested material characteristics, is approximately constant for all three tests. Comparing the magnitude of the φ_{p_a} shows a higher prediction of the friction angle at the failure plane vertical stress equal to atmospheric pressure for DST than TT than DSST.

Table 4.9. Friction angle model parameters for DST, DSST, and TT results

Test Type	φ_{p_a}	A
DST	55.8	0.08
DSST	40.5	0.10
TT	47.9	0.08

4.5.4. Shear Modulus

The elastic and shear modulus is one of the most important shear properties of the ballast material that needs to be evaluated to have a safe and long-lasting railway design. The shear modulus of the ballast material in the DSST and the influence of the applied normal stress on the sample were previously discussed in section 4.3.4. Besides, the initial

elastic modulus of the TT and the influence of the confining pressure applied to the triaxial cells on the initial elastic modulus were explored in section 4.4.3.

In order to compare the modulus from DSST and TT, the vertical stress on the plane of failure was chosen to have a consistent stress definition for both tests. It should be noted that the TT elastic modulus was converted to the shear modulus by assuming the Poisson's ratio of the ballast material equal to 0.35. Figure 4.30 shows the variation of the maximum shear modulus of the ballast #5 with the magnitude of the vertical stress on the plane of failure based on DSST and TT experimental results. The maximum shear and elastic modulus in the DSST and TT are related to 0.01% of the shear and axial strain, respectively. As shown, the DSST results are corresponding to the lower stress level, while TT results are covering a higher range of the vertical stresses on the plane of failure. The details of the shear modulus of both tests are summarized in Table 4.10.

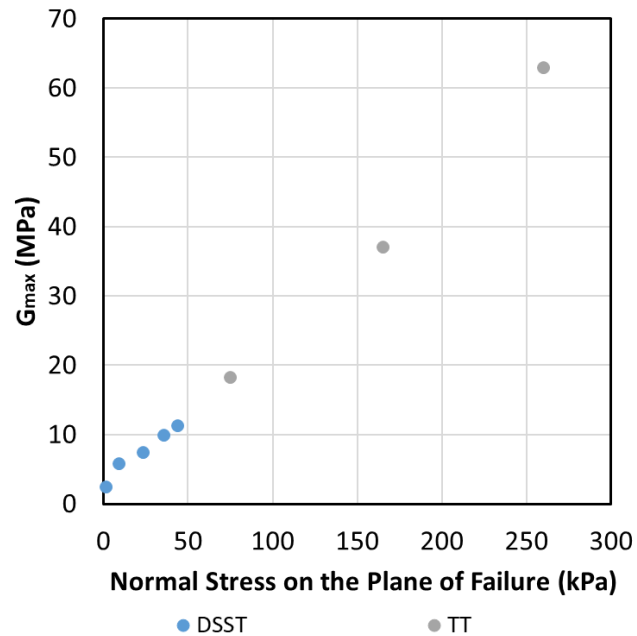


Figure 4.30. Comparison of the variation of the shear modulus of the railroad ballast with the vertical stress on the plane of failure based on DSST and TT results

Table 4.10. Summary of the maximum shear modulus of the railroad ballast based on the DSST and TT results

Test No.	Lab Test	Normal Stress (kPa)	Confining Stress (kPa)	Vertical Stress on the Plane of Failure (kPa)	G _{max} (MPa)
1	TT	-	40	75	18.2
2	TT	-	80	165	37.0
3	TT	-	140	260	62.9
4	DSST	10	-	2	2.4
5	DSST	30	-	9	5.8
6	DSST	50	-	24	7.4
7	DSST	70	-	36	9.9
8	DSST	90	-	44	11.3

5. PRESENTATION AND DISCUSSION OF THE RESULTS OF CYCLIC LOADING TESTS

5.1. Introduction

A comprehensive understanding of the ballast response under cyclic loading generated by train passage will help to enhance the performance of the ballasted track and reduced the maintenance cost. Therefore, this chapter summarized the results of the cyclic simple shear test (DSST) and triaxial test (TT) on the ballast material. Details regarding the large-scale test equipment, materials, and the test procedure were presented in Chapter 3, thus, not repeated here.

In the first section of this chapter, the results of the cyclic shear stress-strain, permanent shear strain, secant shear modulus, and resilient shear modulus of the ballast based on cyclic DSST are presented. Afterward, a series of empirical equations are provided to predict the permanent shear strain, cyclic secant shear modulus, and resilient shear modulus as a function of the number of cycles. Moreover, the results of the parametric study on the cyclic behavior of the ballast by using the DSST is presented. The primary objective of the parametric study is to evaluate the influence of the field stress state (normal stress) and cyclic stress amplitude on the cyclic behavior of the ballast material.

In the second part, the results of the cyclic triaxial test (TT) are presented and discussed. The TT results were used to predict the long-term permanent settlement and the resilient and secant elastic modulus of the ballast under the cyclic loading. Consequently,

a series of empirical formulas are presented to quantify the long-term plastic settlement and the secant elastic modulus of the ballast. Finally, the results of sensitivity analysis on the impact of the cyclic stress amplitude on the response of the material based on TT is described.

5.2. Cyclic Direct Simple Shear Test (DSST)

5.2.1. Experimental Results

5.2.1.1. Results of First 100 Cycles

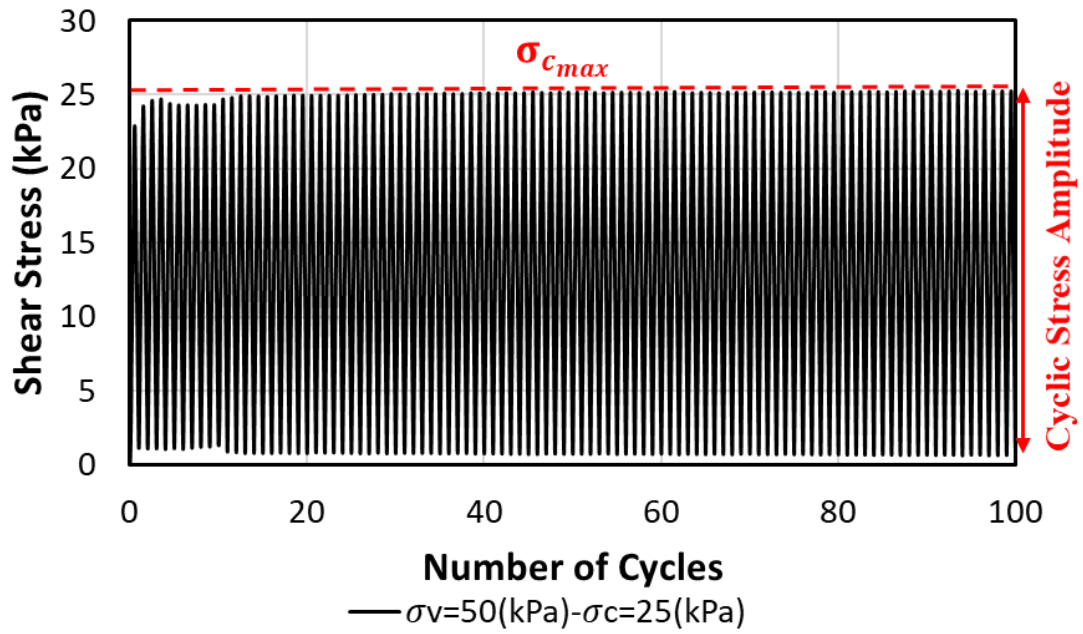
A series of large-scale cyclic DSST performed on ballast #4 material under normal stress varying from 10 to 90 kPa. Details about the testing procedure were presented in Table 3.5. All the samples were prepared and compacted in the same manner, as explained in Chapter 3. Figure 5.1 illustrates the cyclic DSST results (first 100 cycles) of the ballast #4 material with vertical and cyclic stress amplitude equal to 50 kPa and 25 kPa, respectively. Due to a large number of data points (128 per cycle) generated from the cyclic DSST, the plots of all the data points cannot be made for a test with a large number of cycles. Therefore, the results of the tests will be presented for specific points, as will be discussed later. In addition, the plots of all the data points for the first 100 cycles of one sample test will be shown in this section for the purpose of clarification.

Figure 5.1(a) shows the cyclic shear stress applied in the DSST versus the number of cycles. As can be observed, the magnitude of the maximum and the minimum horizontal stress are constant during the same. This condition is the same for all the cyclic tests performed in this study. The magnitude of the cyclic horizontal stress is corresponding to

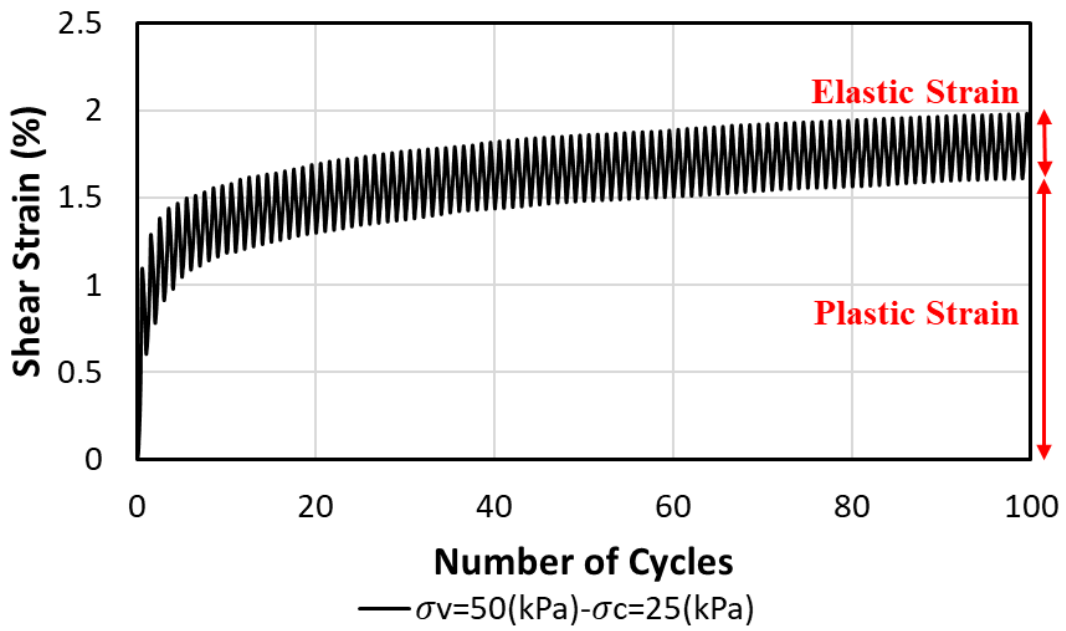
the cyclic horizontal stress generated by the train passage in the field. As a part of this study, a comprehensive numerical simulation was performed on the stresses generated by train passage, which will be discussed in Chapter 6. The minimum horizontal stress was considered equal to zero for all the cyclic tests to show the complete unloading process after the train passage. The small amount of minimum horizontal stress (less than one kPa for all the tests) was observed because of the apparatus limitation for applying the oneway high-frequency cyclic loading. A wide range of the cyclic stress amplitude was tested, even the magnitude close to the static failure of the material.

The growth of shear strain with the number of cycles is shown in Figure 5.1(b). Due to the applied cyclic loading, the shear strain grows accordingly in a cyclic manner. As it is marked in the figure, the shear strain in the cyclic test consists of two distinct parts, including the recoverable strain (elastic) and the unrecoverable strain (plastic). The plastic strain is occurring as a result of sliding between the particles or fracturing of the grains (Lambe and Whitman (1969)). The elastic portion of the shear strain seems to become constant after a few cycles, while the plastic strain is growing nonlinearly with the number of cycles.

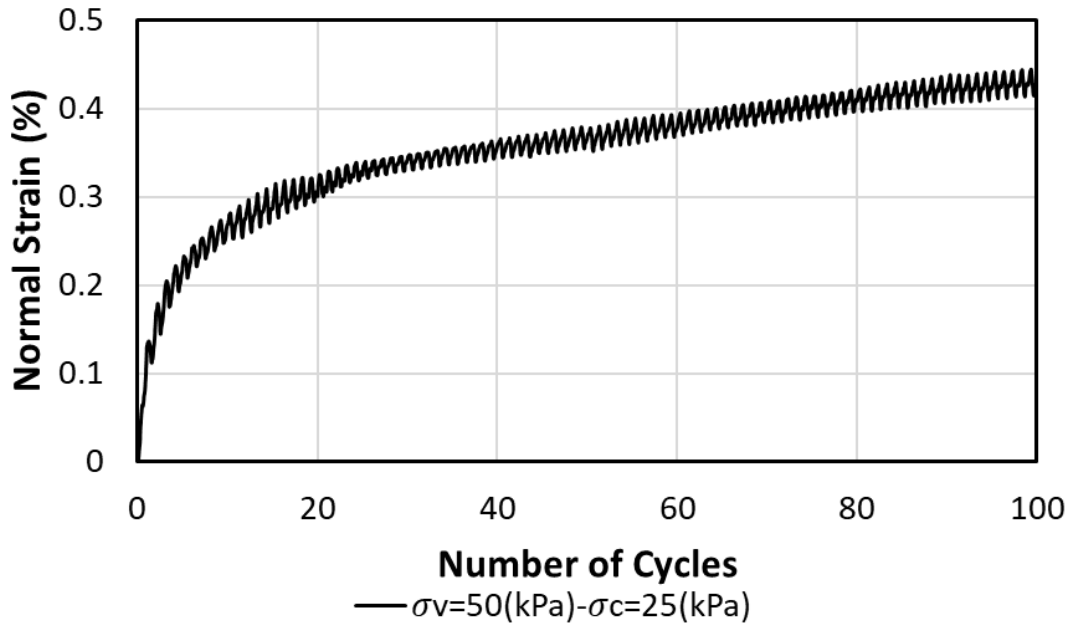
The elastic shear strain is used in the calculation of resilient shear modulus, which will be discussed later in this section. More importantly, the plastic shear strain would be used to predict the long-term permanent shear strain of the ballast. Figure 5.1(c) illustrates the advancement of the normal strain in the DSST under the cyclic loading. It should be noted that the axial strain follows the same pattern as the shear strain. However, the magnitude of normal plastic and elastic strain is lower than the shear strain.



(a)



(b)



(c)

Figure 5.1. Cyclic DSST results of ballast material (first 100 cycles). (a) Horizontal stress vs. number of cycles; (b) Shear strain vs. number of cycles; (c) Shear strain vs. number of cycles

5.2.1.2. Cyclic Shear Stress-Shear Strain Response

Figure 5.2 shows the shear stress-shear strain response of ballast #4 under cyclic loading based on the DSST. The magnitude of the vertical stress and cyclic shear stress are 50 and 25 kPa, respectively. To illustrate the details of the shear strain growth with the number of cycles, the results of 1-100; 1,000; 10,000; and the 100,000 were plotted. It can be observed that the unrecoverable shear strain is developed rapidly at the beginning of the test, and the growth rate decreases with the number of cycles. The magnitude of the cyclic shear stress for the first few cycles does not reach the predefined value. This happens as a result of possibly the small stiffness of the specimens at the beginning of the

test. However, the cyclic shear stress reaches the maximum predefined value successfully after about ten cycles. The same phenomenon was reported in the triaxial cyclic testing of the ballast performed by Bian et al. (2016b).

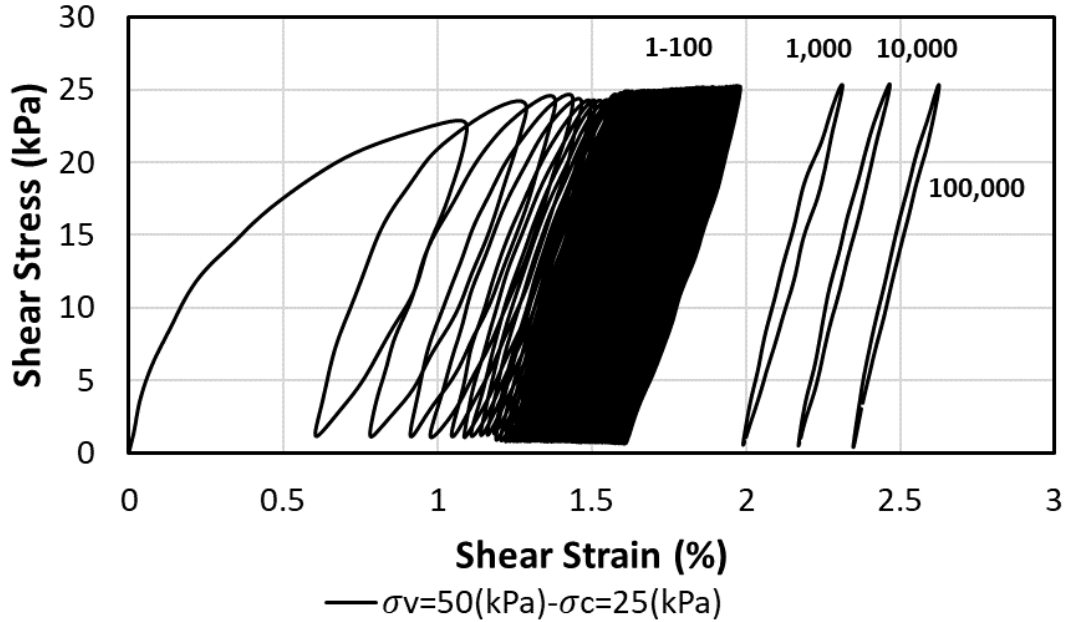


Figure 5.2. Cyclic shear stress-shear strain response of the ballast #4 based on the DSST for 50 kPa vertical stress

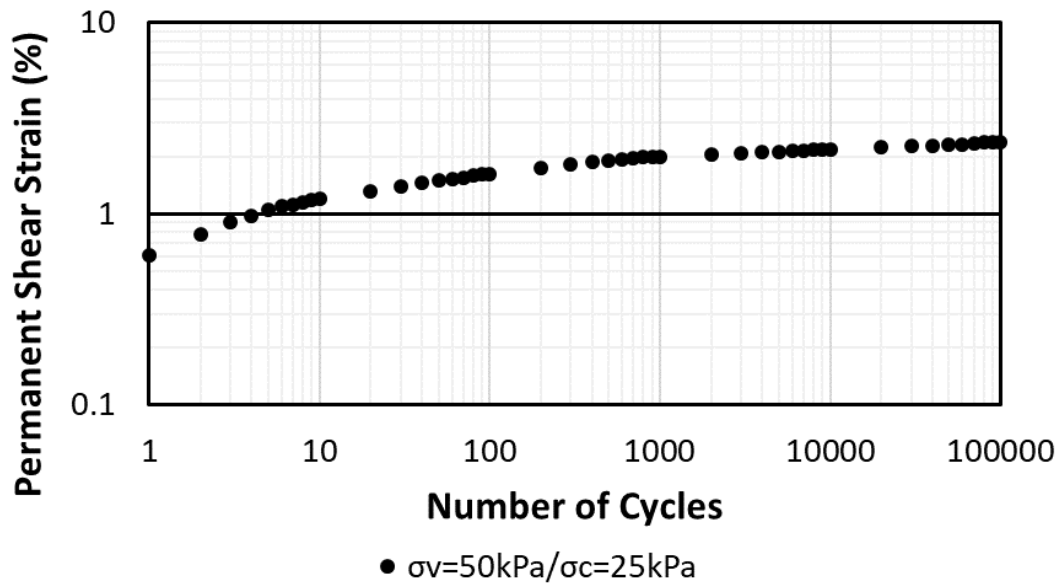
5.2.1.3. Permanent Shear and Normal Strain under Cyclic Loading

The plastic shear and normal strain development for ballast #4 based on cyclic DSST is depicted in Figure 5.3. These results are related to the tests performed at the vertical stress of 50 kPa and the cyclic shear stress amplitude equal to 25 kPa. It should be noted that the cyclic loading frequency was equal to $f=1$ Hz, and the test stopped at 100,000 cycles. In order to show the development of the permanent strain more clearly, only the results of specific cycles were plotted. It should be noted that the results of all the cycles were followed the same trend. Thus, in all the cyclic DSST permanent strain

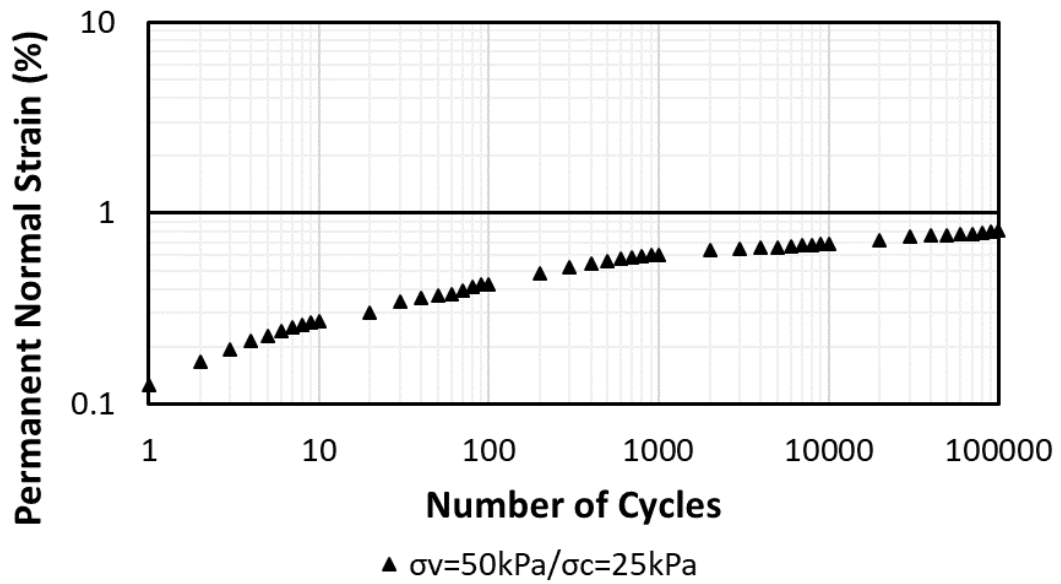
diagrams in this study the results of cycles (1, 2, 3, ..., and 10), (10, 20, 30, ..., and 100), (100, 200, 300, ..., 1000), (1000, 2000, 3000, ..., 10000), and (10000, 20000, 30000, ..., and 100000) were plotted.

Figure 5.3(a) shows the accumulated shear strain developed during the test against the number of loading cycles. The results showed the rapid growth of the plastic strain in the early stage of the test and then became stable. Although most portion of the plastic shear strain occurred within the first 1,000 cycles, the increasing trend continued with the lower rate up to 100,000 load cycles. The same pattern was observed for the accumulated axial strain of the ballast material in the cyclic triaxial test (Anderson and Fair (2008).

The accumulation of the normal strain with the number of cycles is shown in Figure 5.3(b). The permanent normal strain follows the same pattern as the shear strain, which is discussed before. There is no dilation observed in all the cyclic loading tests. This issue happened because the shear strain range in all the tests was below the strain level that dilatancy appeared in the monotonic tests. It is essential to mention that the DSST normal strain was not used for the prediction of the long-term settlement of the ballast. Instead, the cyclic triaxial test was performed to demonstrate the permanent settlement of the ballast layer.



(a)



(b)

Figure 5.3. Development of the permanent strain based on DSST. (a) Permanent shear strain vs. number of cycles; (b) Permanent normal strain vs. number of cycles; (c) Permanent normal strain vs. permanent shear strain

5.2.1.4. Resilient Shear Modulus

The cyclic shear stress-shear strain relationships (Figure 5.2) can be employed to study the resilient shear modulus of the ballast. The resilient shear modulus (M_R) is the ratio of cyclic loading amplitude and the recoverable portion of the shear strain defined by the following equation:

$$M_R = \frac{\Delta\sigma}{\varepsilon_r} \quad (15)$$

where $\Delta\sigma$ is the amplitude of cyclic loading and ε_r is the recoverable strain. Furthermore, Key (1999) defined resilient shear modulus as the slope of the load-unload curve. To better understand the definition, the schematic of the resilient shear modulus is shown in Figure 5.4 (Briaud (2013)).

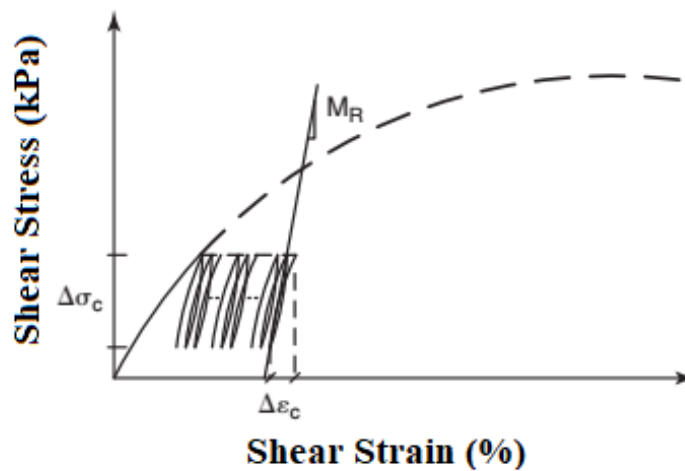
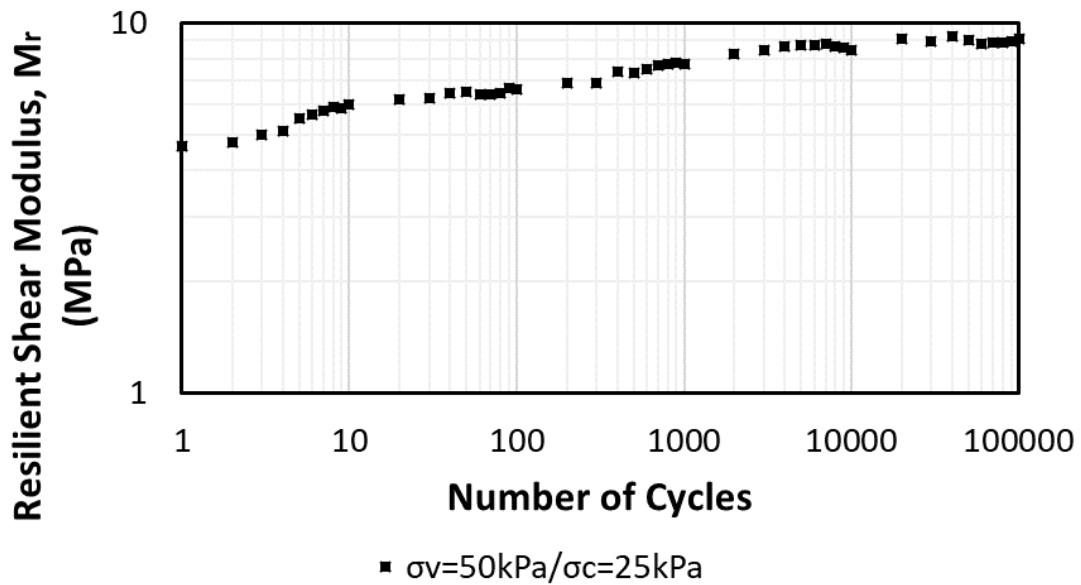


Figure 5.4. Resilient shear modulus test results (Modified after Briaud (2013))

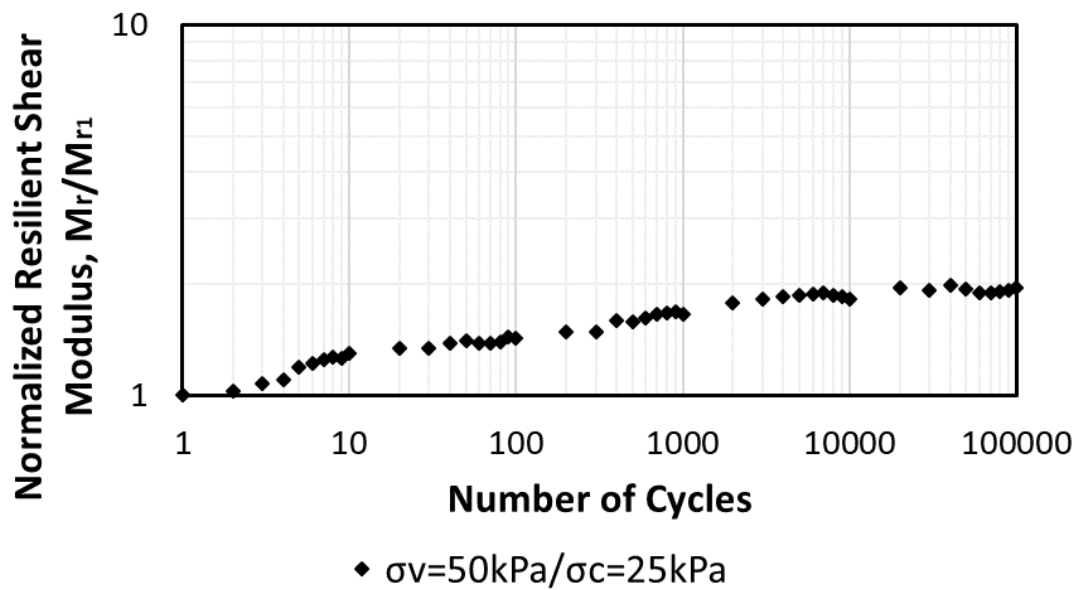
Figure 5.5 shows the progression of the resilient shear modulus with the number of cycles based on cyclic DSST results. According to the results, the resilient shear modulus of the ballast #4 tested at the vertical stress of 50 kPa and the cyclic shear stress

of 25 kPa, increased from 4.6 to 9 MPa after 100,000 cycles (Figure 5.5(a)). Some previous research (Allen and Thompson (1974) and Khedr (1985)) reported that the resilient shear modulus reaches its maximum value after a small number of cycles (less than 100 cycles) and becomes independent of the number of cycles afterward. In contrast, the results of this research revealed that M_r is dependent on the number of the cycle, but the rate of increment is lower in a larger amount of cycles. The same trend of the resilient behavior of the granular material reported by Lackenby et al. (2007).

The increasing of the resilient shear modulus of the ballast can be explained by increasing the specimen stiffness, which happens as a result of specimen compaction during the cyclic loading. Figure 5.5(b) shows the normalized resilient shear modulus development with the number of cycles. In this figure, the resilient shear modulus of each cycle normalized by the magnitude of the resilient shear modulus of the first cycle. The equation that can predict this behavior would be presented later in this chapter.



(a)



(b)

Figure 5.5. Resilient shear modulus of ballast based on DSST. (a) Resilient shear modulus vs. number of cycles; (b) Normalized resilient shear modulus vs. number of cycles

5.2.1.5. Secant Shear Modulus

The secant shear modulus is another way to investigate the behavior of ballast under cyclic loading. The cyclic secant shear modulus generally defines the slope of a straight line drawn from the origin to the maximum shear stress in a given cycle. Figure 5.6 illustrates the definition of the secant shear modulus in a one-way cyclic loading (Briaud (2013)). As can be observed in the figure, the secant modulus decreases in a larger number of cycles.

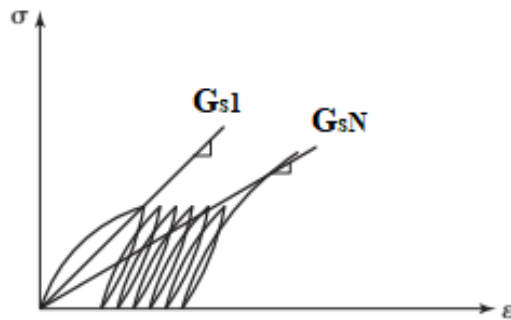
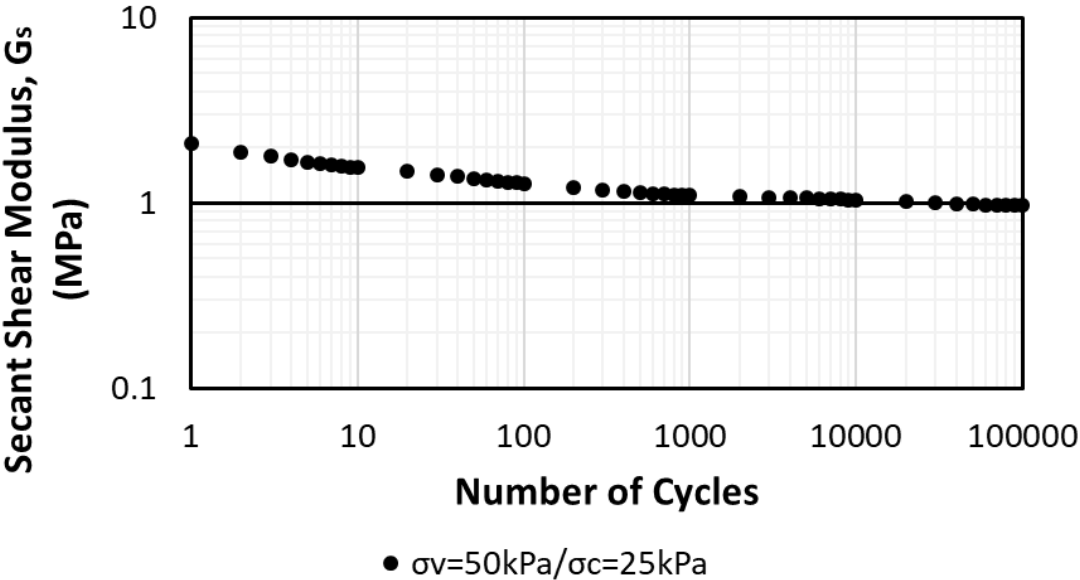


Figure 5.6. Cyclic secant shear modulus (modified after (Briaud (2013)))

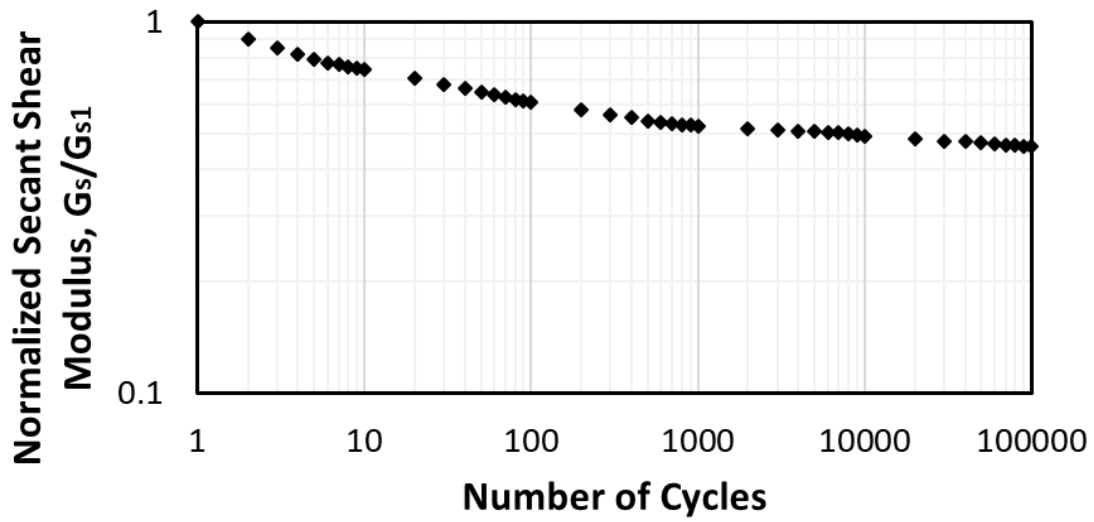
The secant shear modulus progression of the ballast in cyclic DSST is shown in Figure 5.7. As was expected, the secant shear modulus decreased with the number of cycles while the rate of the changes is lower in higher cycles. According to the results of the test with vertical stress of 50 kPa and the cyclic shear stress of 25 kPa (Figure 5.7(a)), the secant shear modulus reduced from 2.1 to 0.97 MPa after 100,000 cycles. Figure 5.7(b) shows the variation of the normalized secant shear modulus (G_S/G_{S1}) with the number of the cycles. It should be noted that G_{S1} is defined as the secant shear modulus of the first

cycle and different from the initial tangent shear modulus (G_{max}). According to Briaud (2013), the initial shear modulus is equal to secant shear modulus at for shear strain equal to zero. The value of the initial shear modulus (G_{max}) at the shear strain of 0.01% is equal to 13.3 MPa for this test.

Figure 5.7(c) depicts the variation of the normalized secant shear modulus (G_s/G_{S1}) with the shear strain. The normalized secant shear modulus decreased with increasing the shear strain. The value of G_{S1} is corresponding to the shear strain of 0.6%, which is related to the maximum shear stress of the first cycle. The data points are available until the shear strain of 2.4% that belongs to the 100,000 cycles.

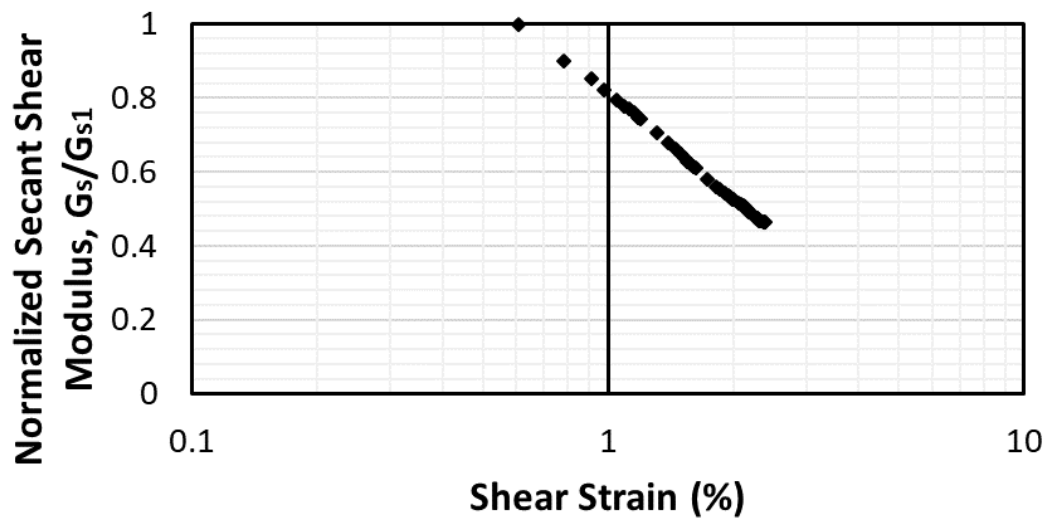


(a)



◆ $\sigma_v=50\text{kPa}/\sigma_c=25\text{kPa}$

(b)



◆ $\sigma_v=50\text{kPa}/\sigma_c=25\text{kPa}$

(c)

Figure 5.7. Cyclic secant shear modulus of ballast based on DSST. (a) Secant shear modulus vs. number of cycles; (b) Normalized secant shear modulus vs. number of cycles; (c) Normalized secant shear modulus vs. shear strain

5.2.2. Parametric Study

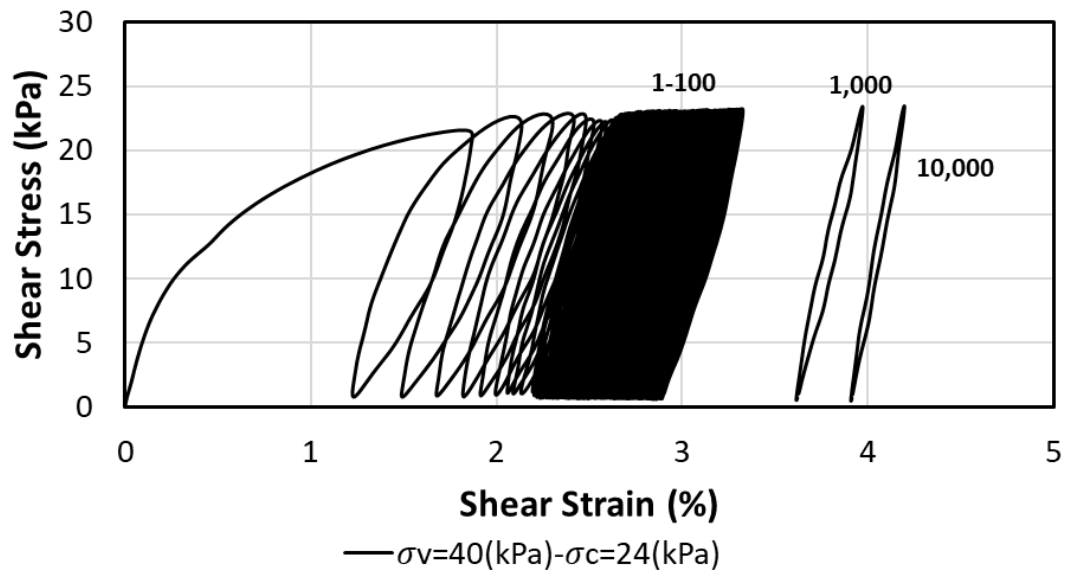
5.2.2.1. Influence of Normal Stress Level

The applied stress level in laboratory testing is an essential factor that has a significant impact on the cyclic behavior of the material. The influence of the normal stress on the cyclic behavior of the ballast by using the DSST has been studied in this section. It is important to note that the stress level that is applied in the laboratory test should be representative of the field stress state. For this purpose, five identical cyclic DSST with the cyclic shear stress of approximately 22 to 25 kPa were performed with the vertical stress of 40, 50, 60, 70, and 90 kPa. Details of these tests are provided in Table 5.1.

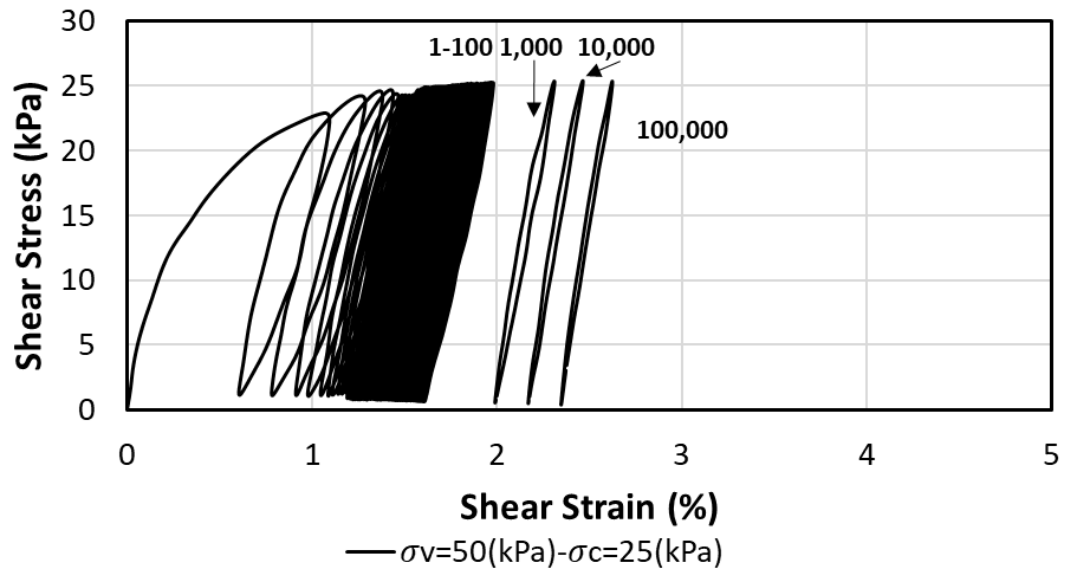
The cyclic behavior of the material is highly influenced by the cyclic stress ratio (i.e., the ratio of the cyclic shear stress over the monotonic shear strength). By increasing the vertical stress, the monotonic shear strength of the ballast is increasing (see Chapter 4 for more details). Therefore, with the same cyclic shear stress magnitude, the cyclic stress ratio is decreasing by increasing the vertical stress. As it is indicated in Table 5.1, the cyclic stress ratio decreased from 74% to 36% for increasing the vertical stress from 40 to 90 kPa. Figure 5.8 shows the influence of the vertical stress on the shear stress-shear strain response of ballast #4 based on cyclic DSST results.

Table 5.1. Details of the influence of the normal stress level on the response of ballast #4 under cyclic DSST

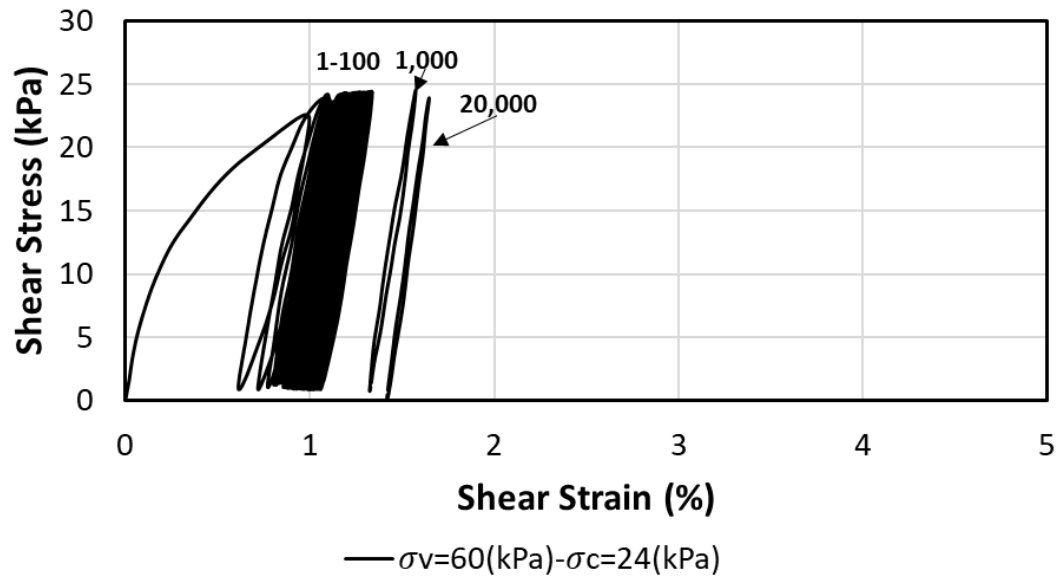
Test No.	1	2	3	4	5
Vertical Stress (kPa)	40	50	60	70	90
Shear Strength (kPa)	31.6	36.2	44.5	50.7	65.5
Cyclic Shear Stress (kPa)	23.4	25.3	24	25.2	23.7
$\frac{\sigma_c}{\tau_f}$ (%)	74.1	69.9	53.9	49.7	36.2
γ_{p1} (%)	1.24	0.608	0.62	0.43	0.19
$\gamma_{p10,000}$ (%)	3.92	2.17	1.36	1.26	0.48
G_{S1} (MPa)	1.15	2.09	2.27	3.05	5.43
$G_{S10,000}$ (MPa)	0.56	1.03	1.45	1.7	3.47
$G_{S10,000}/G_{S1}$	0.48	0.49	0.64	0.56	0.64
M_{r1} (MPa)	3.34	4.64	5.87	6.86	10.16
$M_{r10,000}$ (MPa)	7.99	8.41	10.42	10.45	11.5
$M_{r10,000}/M_{r1}$	2.39	1.81	1.77	1.51	1.13



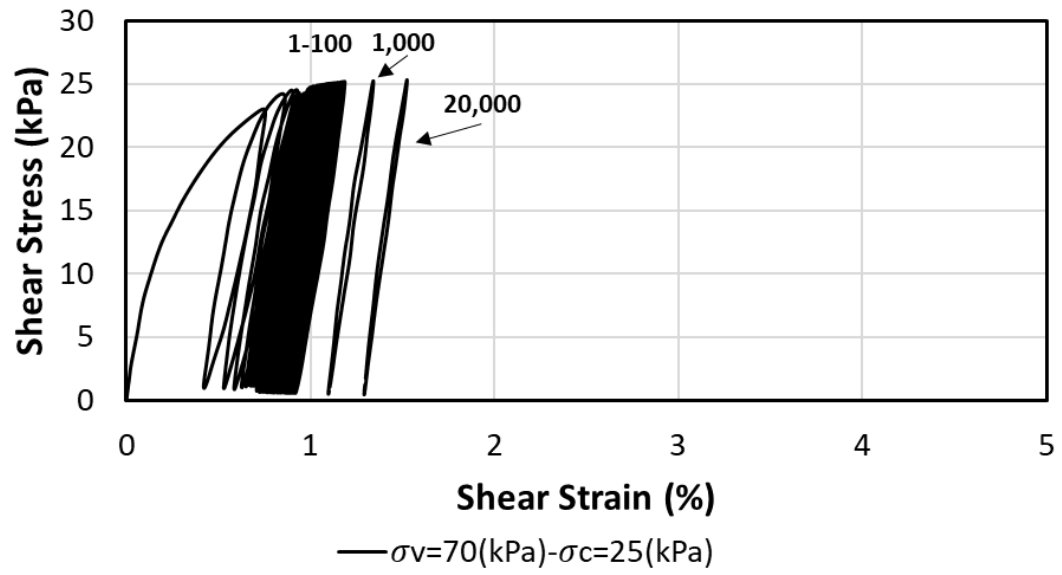
(a)



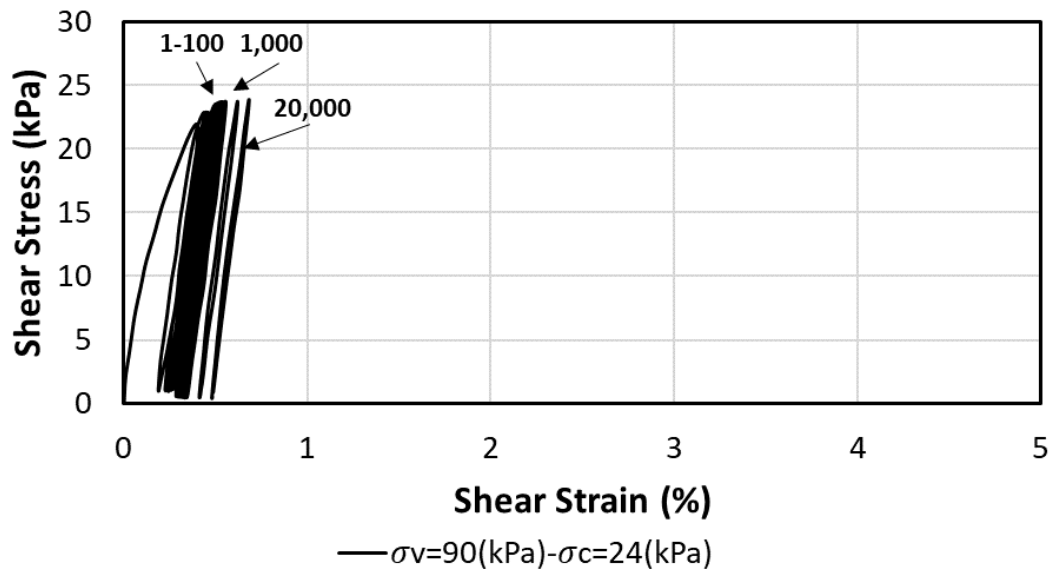
(b)



(c)



(d)



(e)

Figure 5.8. Influence of vertical stress on the shear stress-shear strain of ballast #4 by using cyclic DSST. (a) vertical stress of 40 kPa; (b) vertical stress of 50 kPa; (c) vertical stress of 60 kPa; (d) vertical stress of 70 kPa; (e) vertical stress of 90 kPa

The influence of the normal stress level on the response of ballast #4 under cyclic DSST is shown in (Figure 5.9). Figure 5.9(a) shows the variation of the permanent shear strain with the number of cycles. The first observation is the plastic shear strain is increasing with increasing the number of cycles for all the tests. For example, after 10,000 cycles, the shear strain increased from 1.2% to 3.9% for 40 kPa vertical stress, while this increment is 0.2% to 0.5 for 90 kPa vertical stress. Second, Increasing the vertical stress level is beneficial to minimize the permanent shear strain of the ballast. By increasing the vertical stress from 40 to 90 kPa, the plastic shear strain at the first cycle is decreased from 1.2 to 0.2% and at 10,000 cycles decreased from 3.9% to 0.5%. The same behavior reported in the literature on the influence of confining pressure on the plastic axial strain

of the ballast in the cyclic triaxial test (Lackenby et al. (2007) and Brown and Selig (1991)).

Moreover, a comparison of the results revealed that the rate of plastic shear strain accumulation is higher when the cyclic shear stress is closer to the monotonic shear strength value (i.e., lower vertical stress). For example, the plastic shear strain after 10,000 cycles increased by 320% and 250% for the vertical stress of 40 and 90 kPa, respectively. Therefore, increasing the ballast thickness (i.e., more vertical stress state in the ballast) causes a reduction in the permanent shear strain for the same cyclic stress generated by the train passage.

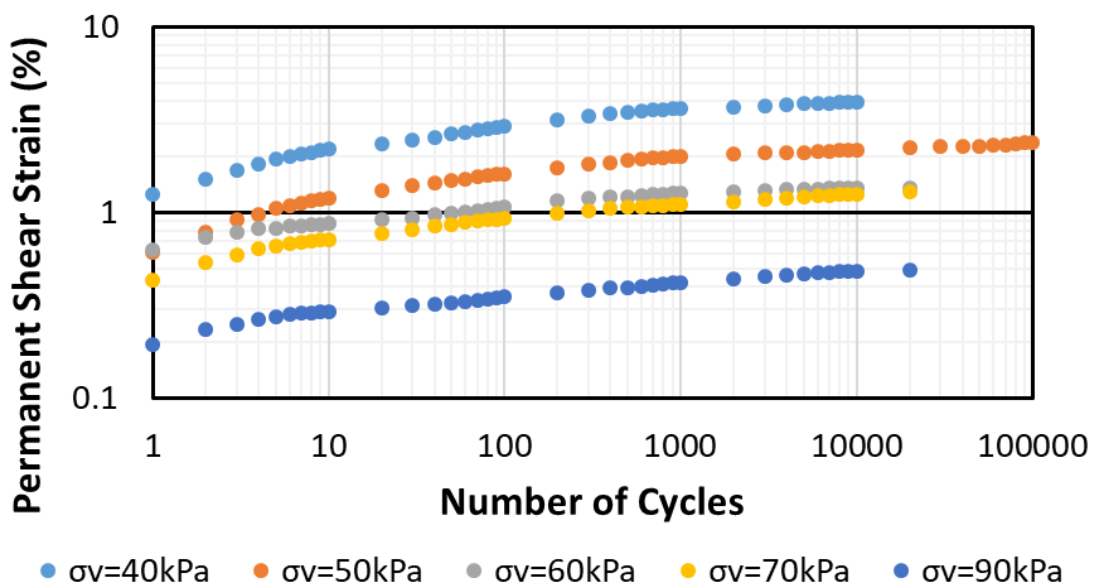
Figure 5.9(b) shows the variation of the secant shear modulus with the number of cycles under various vertical stress. The results of all tests showed that despite the applied stress state, the magnitude of secant shear modulus is decreasing with the number of cycles. Because the permanent shear strain is increasing with the number of cycles. Moreover, it is shown that increasing the vertical stress state increases the secant shear modulus. This behavior shows the dependency of the secant shear modulus to the strain level. For instance, the ballast secant shear modulus in the first cycle at 40 and 90 kPa vertical stress is 1.1 and 5.4 MPa, respectively.

Figure 5.9(c) illustrates the progression of the normalized secant shear modulus (G_s/G_{s1}) against the number of cycles. Comparison of the results of tests with different vertical stress revealed that increasing the stress level reduce the deterioration rate of the G_s/G_{s1} . The secant shear modulus at 10,000 cycles is 48% at 40kPa and 64% at 90kPa vertical stress of the secant shear modulus at the first cycle. This phenomenon happens

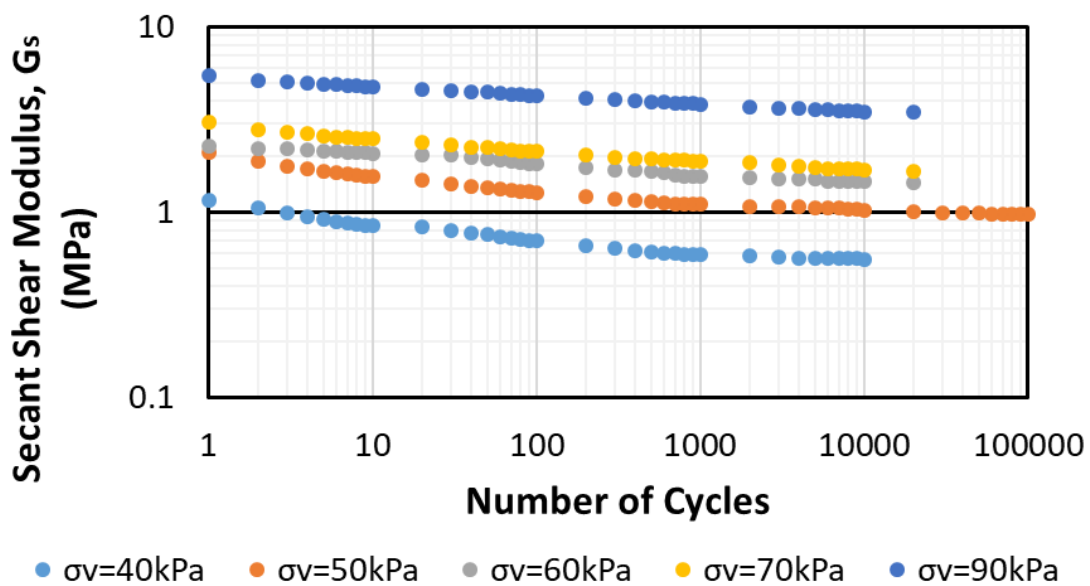
because, in the higher cyclic shear stress ratio (for example, 40 kPa), the rate of accumulated shear strain is higher. Consequently, the degradation in the secant shear modulus is more pronounced.

Figure 5.9(d) shows the development of the resilient shear modulus with the number of cycles. The resilient shear modulus is influenced by the stress state, and it is increasing in higher vertical stress. For example, the magnitude of the resilient shear modulus is increased from 3.3 to 10.2 MPa for increasing the vertical stress from 40 to 90 kPa. This behavior can be explained by more densification of the ballast at higher stress levels. The results also showed the rate of resilient shear modulus increasing is decreased with the number of cycles. This finding is in contrast with the early research performed by Allen and Thompson (1974) and Khedr (1985) to evaluate the resilient shear modulus development under cyclic loading. They reported that the resilient shear modulus is independent of the number of cycles after a few successfully applied cycles. However, in the later research, Lackenby et al. (2007) reported the increasing tendency of resilient shear modulus with the number of cycles while the increment is lower in the larger amount of cycles.

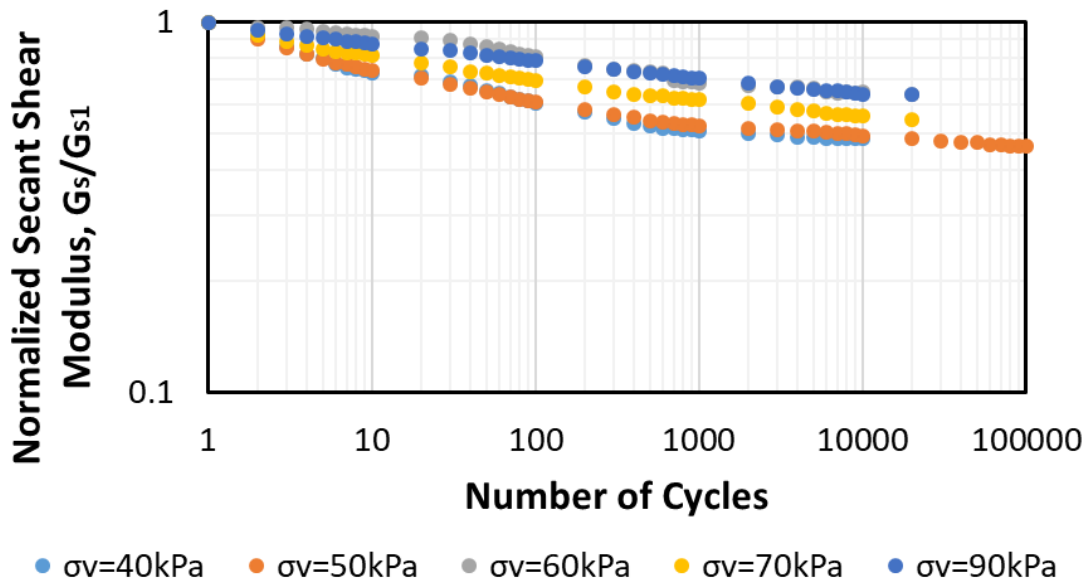
Figure 5.9(e) shows the normalized resilient shear modulus (M_r/M_{r1}) growth against the number of cycles. It is shown that the rate of resilient shear modulus increasing is enhanced in lower stress state (i.e., higher cyclic stress ratio). According to the results, the ratio of the resilient shear modulus at 10,000th cycles over the 1st cycle is 2.4 for the test with 40 kPa vertical stress while this value is 1.1 for the vertical stress equal to 90 kPa.



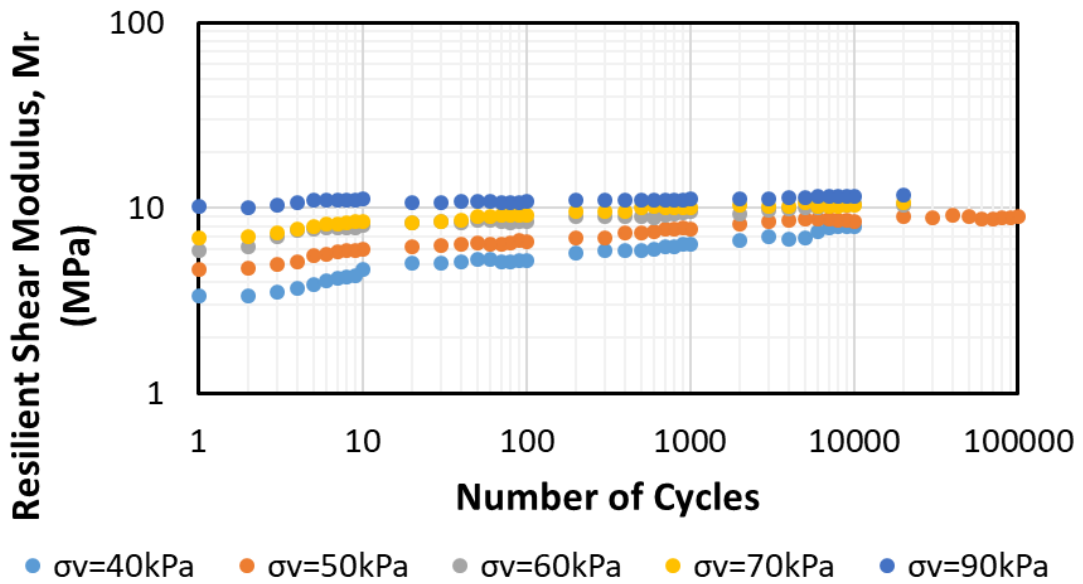
(a)



(b)



(c)



(d)

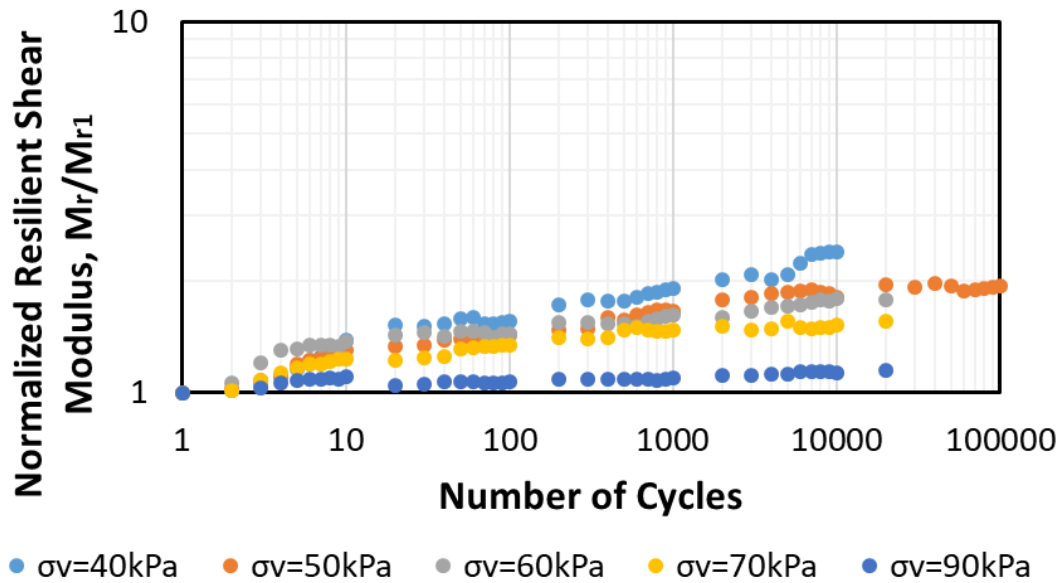


Figure 5.9. Influence of the normal stress level on the response of ballast #4 under cyclic DSST. (a) Permanent shear strain vs. number of cycles; (b) Secant shear modulus vs. number of cycles; (c) Normalized secant shear modulus vs. number of cycles; (d) Resilient shear modulus vs. number of cycles; (e) Normalized resilient shear modulus vs. number of cycles

5.2.2.2. Influence of Cyclic Stress Amplitude

The influence of cyclic shear stress amplitude on the cyclic behavior of the ballast is evaluated in this section by using cyclic DDST. The magnitude of the cyclic stress applied in laboratory test should be representative of the corresponding value generated in the ballast layer by train passage. In order to understand the influence of cyclic loading amplitude, three sets of cyclic DSST have been conducted as a part of this study. It should be noted that all the tests in each series have been performed in identical conditions except the magnitude of the cyclic shear stress.

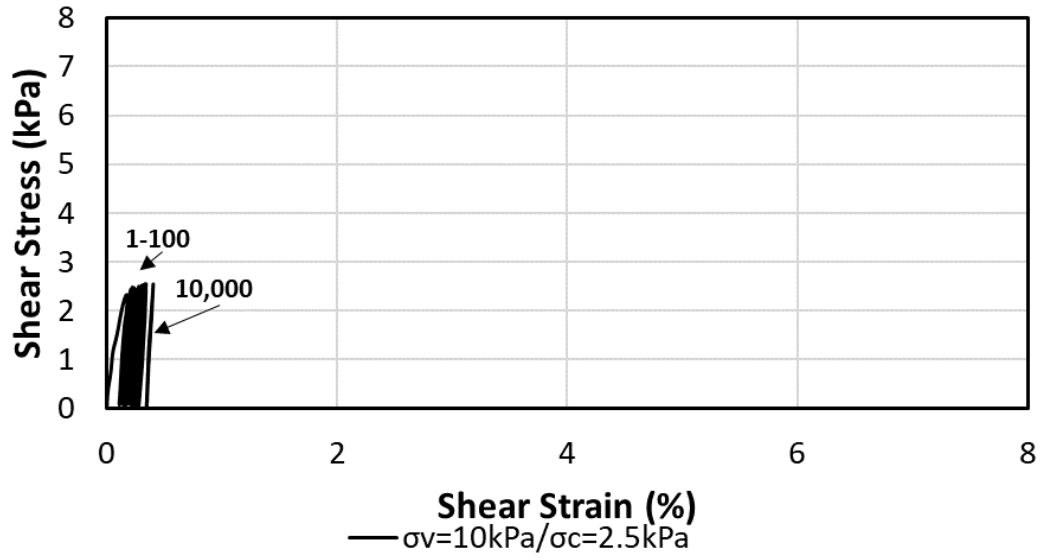
Series A contains three tests with the constant vertical stress of 10 kPa and cyclic shear stress of 2.5, 5, and 7.5 kPa. Series B has also consisted of three experiments with the vertical stress of 50 kPa and cyclic shear stress amplitude of 12.5, 25, and 35 kPa. Series C includes two tests with the normal stress of 90 kPa and cyclic shear stress of 24 and 45 kPa. More details about all the tests are provided in Table 5.2.

Table 5.2. Details of the influence of the cyclic shear stress on the response of ballast #4 under cyclic DSST

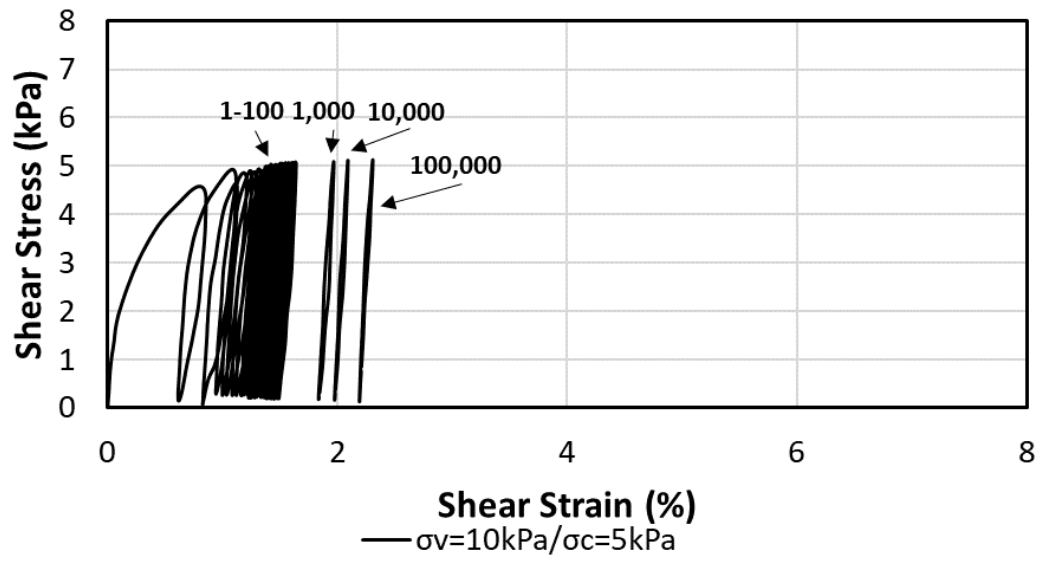
Test Series	A			B			C	
Test No.	1	2	3	4	5	6	7	8
Vertical Stress (kPa)	10	10	10	50	50	50	90	90
Shear Strength (kPa)	9.2	9.2	9.2	36.2	36.2	36.2	65.5	65.5
Cyclic Shear Stress (kPa)	2.6	5.1	7.2	13.2	25.3	34	23.7	45.5
$\frac{\sigma_c}{\tau_f}$ (%)	28.3	55.4	78.3	36.5	69.9	93.9	36.2	69.5
γ_{p1} (%)	0.11	0.62	0.834	0.12	0.608	0.826	0.19	0.84
$\gamma_{p10,000}$ (%)	0.413	1.98	7.57	0.39	2.17	5.69	0.48	2.44
G_{S1} (MPa)	1.36	0.54	0.54	4.3	2.09	2.2	5.43	2.97
$G_{S10,000}$ (MPa)	0.57	0.24	0.09	2.5	1.03	0.56	3.47	1.66
$G_{S10,000}/G_{S1}$	0.42	0.45	0.16	0.56	0.49	0.25	0.64	0.56
M_{r1} (MPa)	3.37	1.88	2	7.05	4.64	5	10.16	6.87
$M_{r10,000}$ (MPa)	4.65	4.23	4.22	8.79	8.41	8.82	11.52	12.89
$M_{r10,000}/M_{r1}$	1.35	2.25	2.1	1.25	1.81	1.76	1.13	1.87

The influence of the cyclic shear stress amplitude on the shear stress-shear strain response of DSST series A (10 kPa vertical stress), series B (50 kPa vertical stress), and series C (90 kPa vertical stress) is shown in Figure 5.10, Figure 5.11, and Figure 5.12, respectively. These tests have been conducted with a different number of cycles from 10,000 to 100,000. But, for consistency, the cyclic properties of the ballast have been compared for the 10,000th cycle in Table 2.1. The results of all the tests revealed that increasing the magnitude of cyclic shear stress (higher cyclic stress ratio) causes more unrecoverable shear strain regardless of the applied vertical stress.

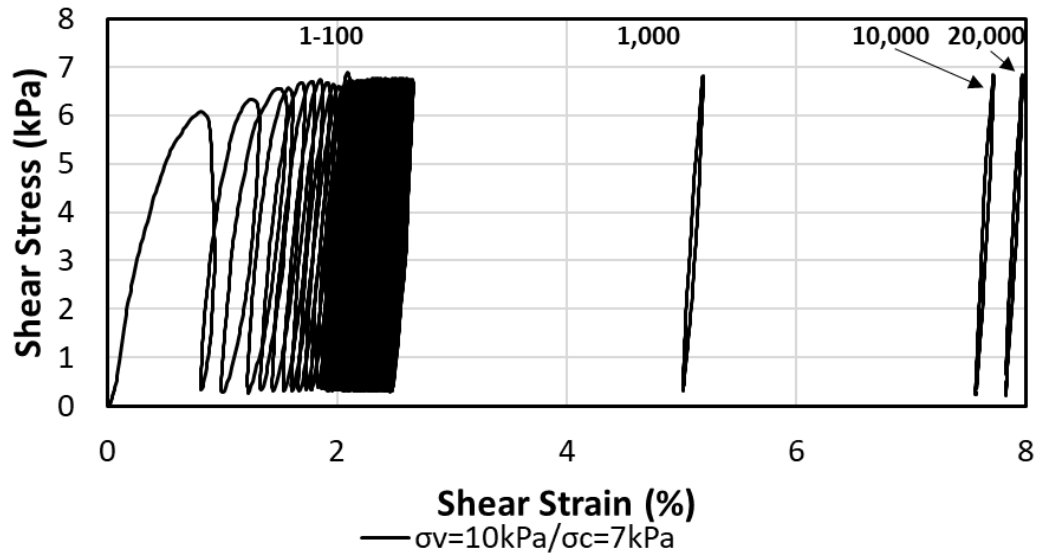
The results of two tests with the cyclic stress ratio of 78% (vertical stress of 10 kPa and cyclic shear stress of 7 kPa) and 94% (vertical stress of 50 kPa and cyclic shear stress of 34 kPa) show a remarkably higher plastic strain in comparison with other tests. The higher plastic deformation happens as a result of a higher cyclic stress ratio. The same observation reported by Lackenby et al. (2007) for the development of the permanent axial strain in the cyclic triaxial test.



(a)

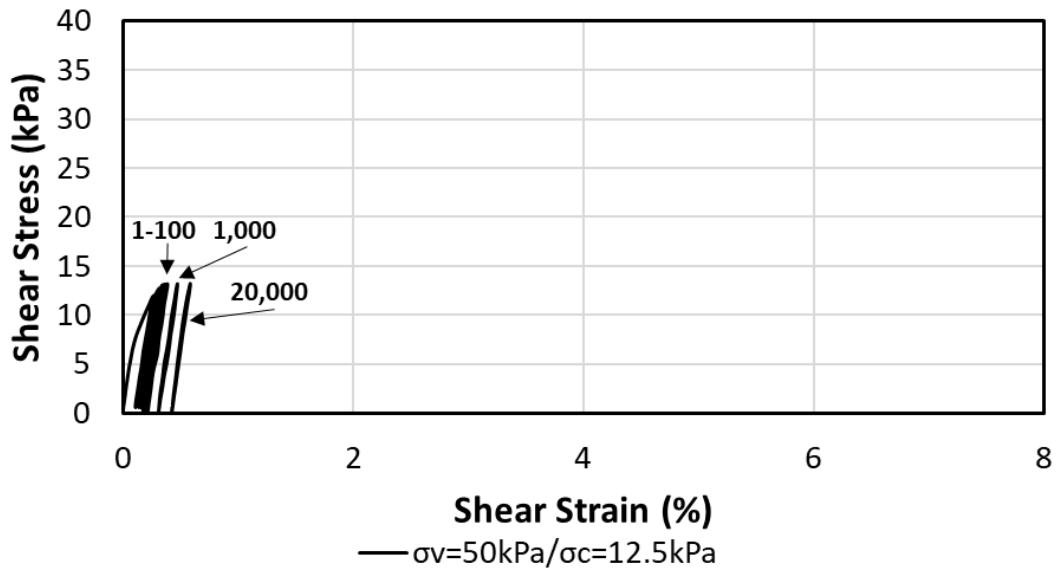


(b)

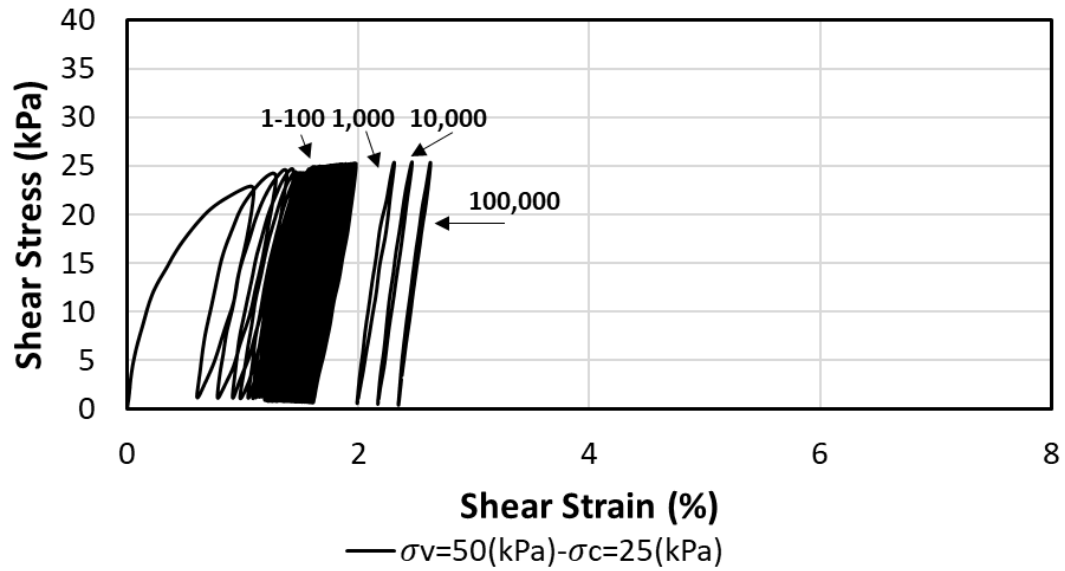


(c)

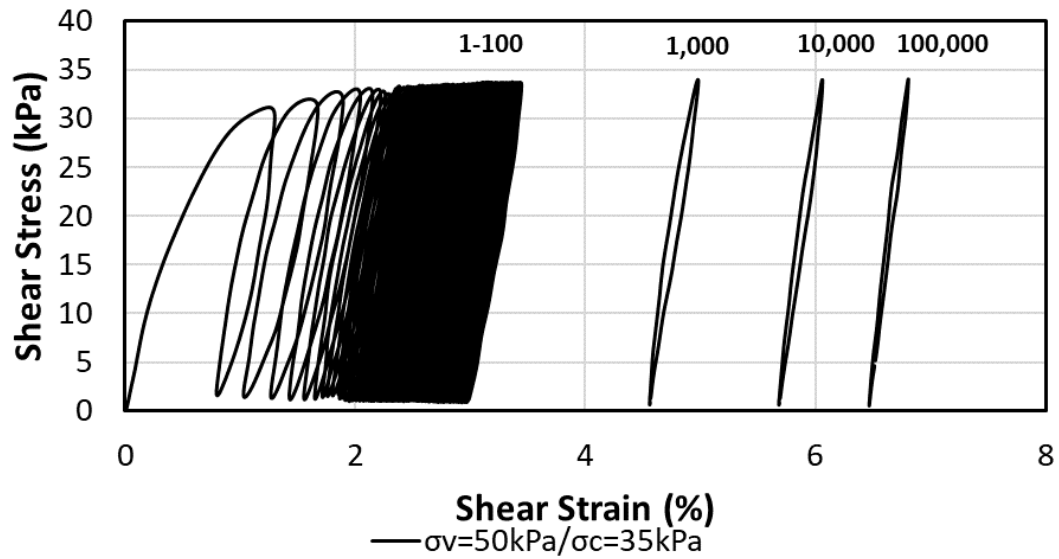
Figure 5.10. Influence of cyclic shear stress amplitude on the shear stress-shear strain of ballast #4 (10 kPa vertical stress). (a) 2.5 kPa cyclic shear stress; (b) 5 kPa cyclic shear stress; (c) 7 kPa cyclic shear stress



(a)

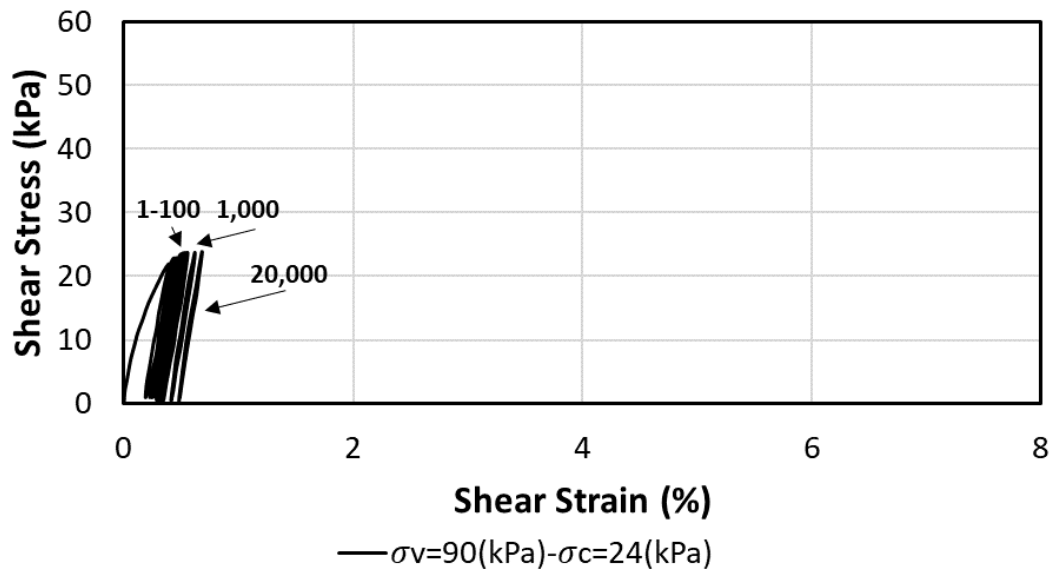


(b)

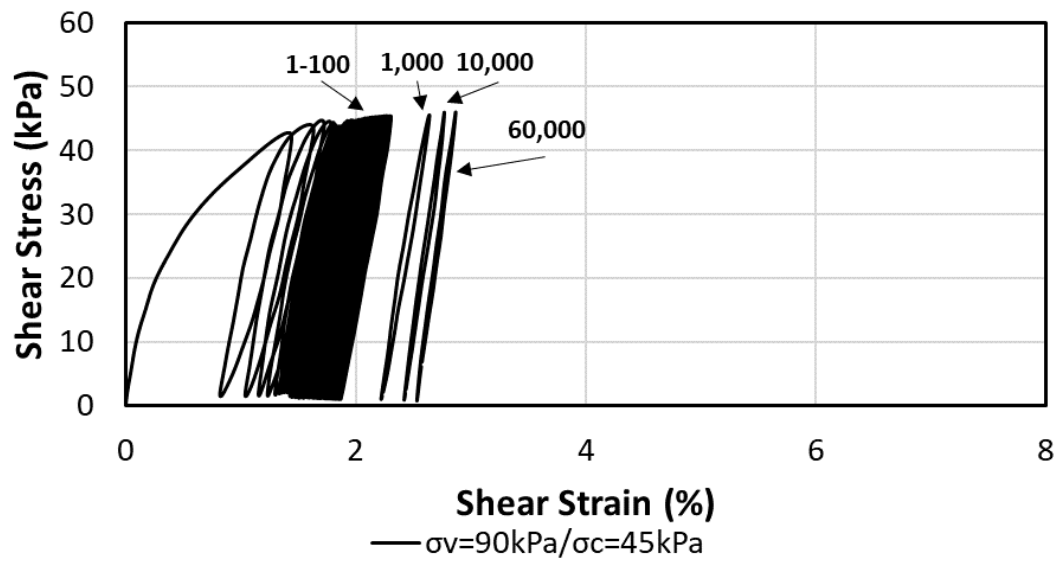


(c)

Figure 5.11. Influence of cyclic shear stress amplitude on the shear stress-shear strain of ballast #4 (50 kPa vertical stress). (a) 12.5 kPa cyclic shear stress; (b) 25 kPa cyclic shear stress; (c) 35 kPa cyclic shear stress



(a)



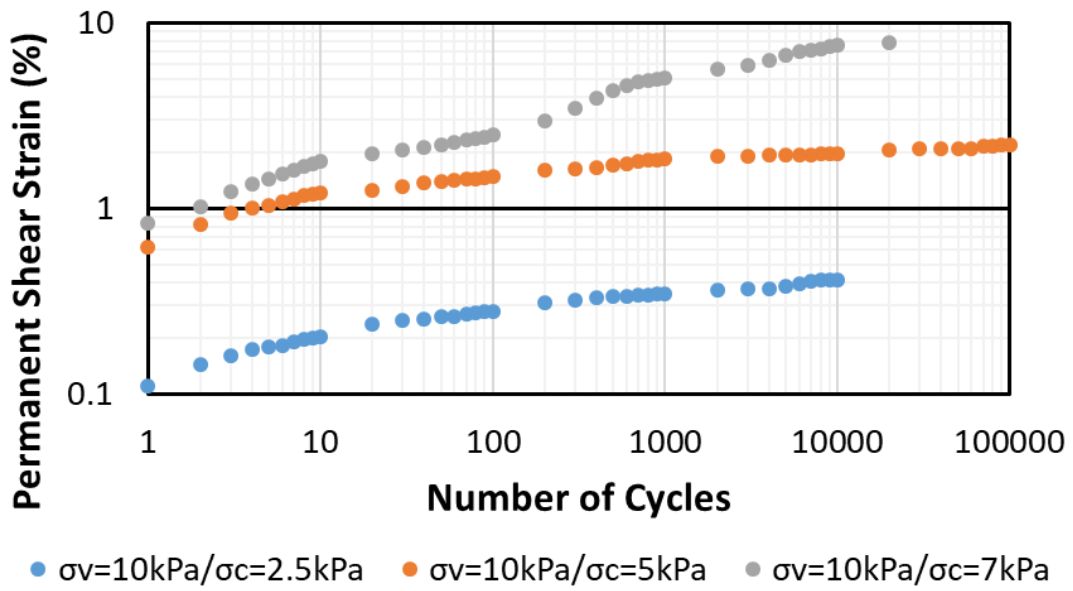
(b)

Figure 5.12. Influence of cyclic shear stress amplitude on the shear stress-shear strain of ballast #4 (90 kPa vertical stress). (a) 24 kPa cyclic shear stress; (b) 45 kPa cyclic shear stress

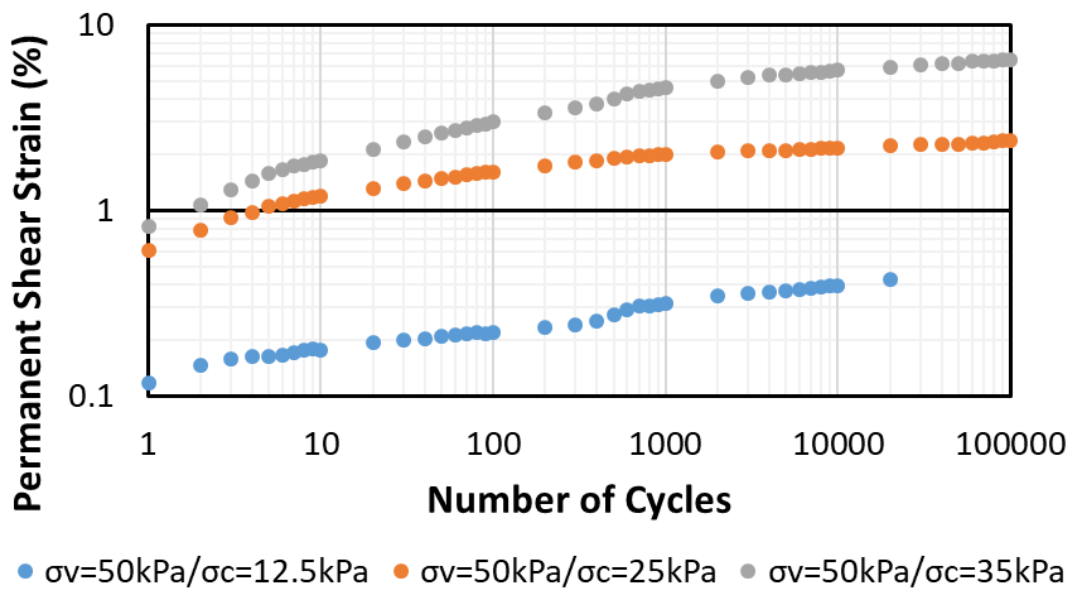
Figure 5.13 shows the impact of cyclic shear stress amplitude on the accumulation of the plastic shear strain with the number of cycles. The permanent deformation under cyclic loading is categorized to shakedown (defined as a zone that the ballast response under cyclic loading is completely elastic and recoverable), cyclic densification (defined as a zone that the ballast experiences the progressive plastic deformation), and frictional failure (defined as a zone that the frictional collapse happens, and it is for the case that the cyclic loading amplitude is higher than ballast shear strength) (Suiker and de Borst (2003)). According to the results, the permanent shear strain stabilized (shakedown) after 1,000 cycles for the tests with the cyclic stress ratio of less than 70%. However, the plastic shear strain continues to rise with the number of cycles up to 10,000 in a higher cyclic stress ratio.

The plastic shear strain accumulation is directly dependent on the cyclic stress amplitude. The results showed that increasing the magnitude of the cyclic stress (i.e., higher cyclic stress ratio) increases the plastic shear strain in all the tests. For example, for the test with 10 kPa vertical stress, the permanent shear strain after 10,000 is increased from 0.4% to 7.6% for increasing the cyclic stress ratio from 28% to 78%. The same trend was observed for the tests at 50 kPa vertical stress.

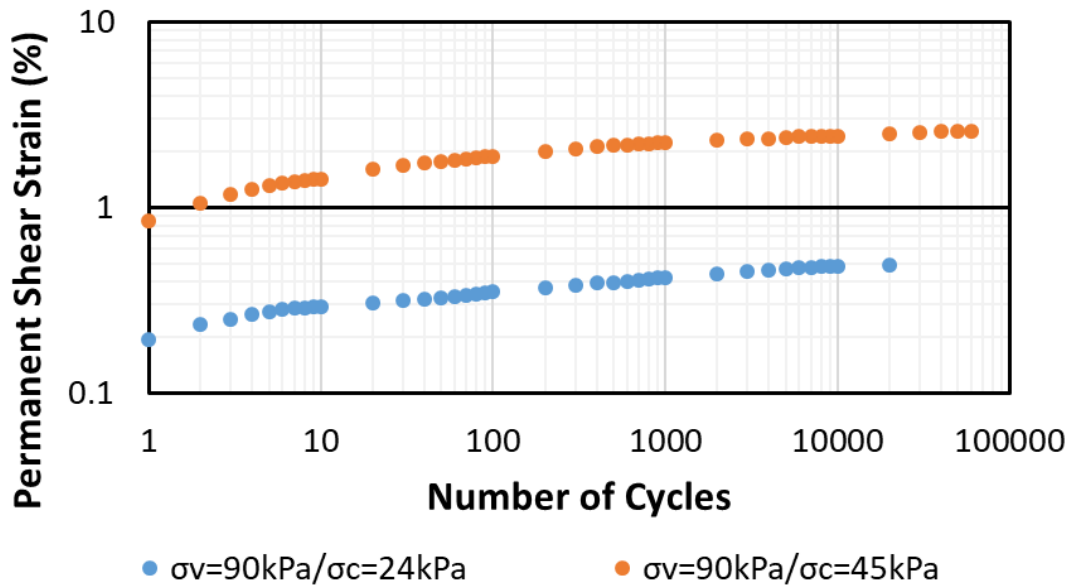
The plastic shear strain of the first cycle is also increased with the cyclic stress ratio. However, the rate of increment is lower in the higher cyclic stress ratio. For example, for series A tests, the γ_{p1} is increased from 0.11% to 0.62% for increasing the cyclic stress ratio from 28% to 55% while this value is 0.73% for the cyclic stress ratio from 78%. The test with 50 kPa vertical stress is also showed the same results.



(a)



(b)



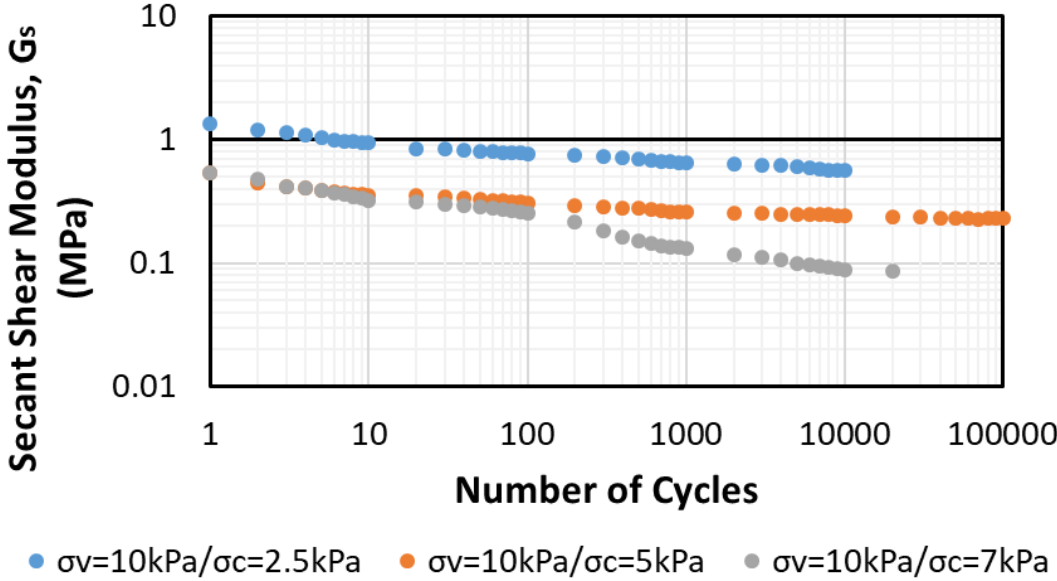
(c)

Figure 5.13. Influence of cyclic shear stress amplitude on the permanent shear strain of ballast #4 based on DSST. (a) 10 kPa vertical stress; (b) 50 kPa vertical stress; (c) 90 kPa vertical stress

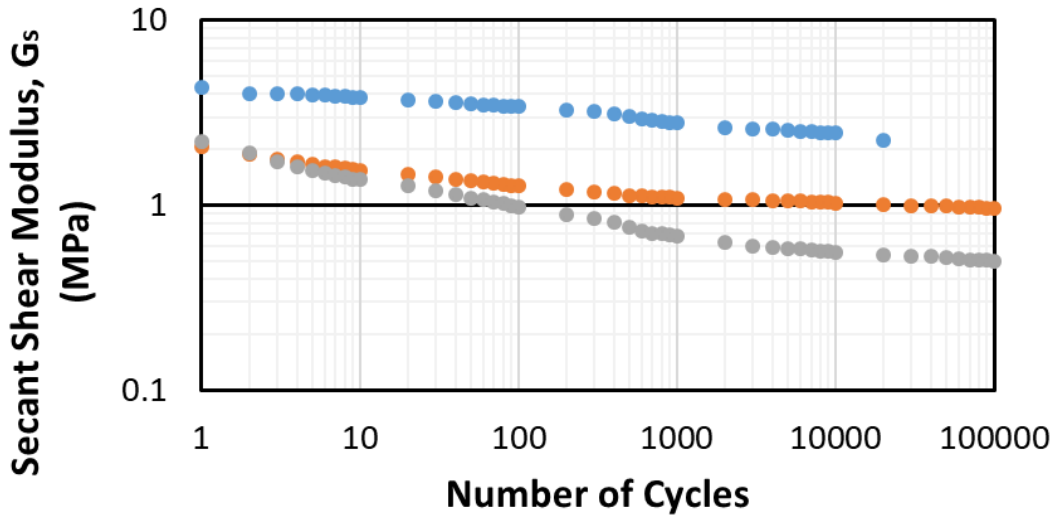
Figure 5.14 shows the influence of cyclic stress magnitude on the development of the secant shear modulus with the number of cycles. As was expected, a comparison of the secant shear modulus for the tests with different vertical stress showed that increasing the vertical stress increases the secant shear modulus.

The test results showed the dependency of the secant shear modulus to the cyclic shear stress amplitude. At the constant vertical stress level, increasing the cyclic shear stress up to a certain value decreases the secant shear modulus for the first cycle. But afterward, the secant shear modulus was not changing with the cyclic stress ratio anymore. For example, in the test series A, by increasing the cyclic stress ratio from 28% to 55%,

the G_{s1} decreased from 1.36 to 0.54 MPa while this value is still the same at the cyclic stress ratio of 78%. Moreover, the G_{s1} in the test series B is approximately the same for the tests at 70% and 94%.

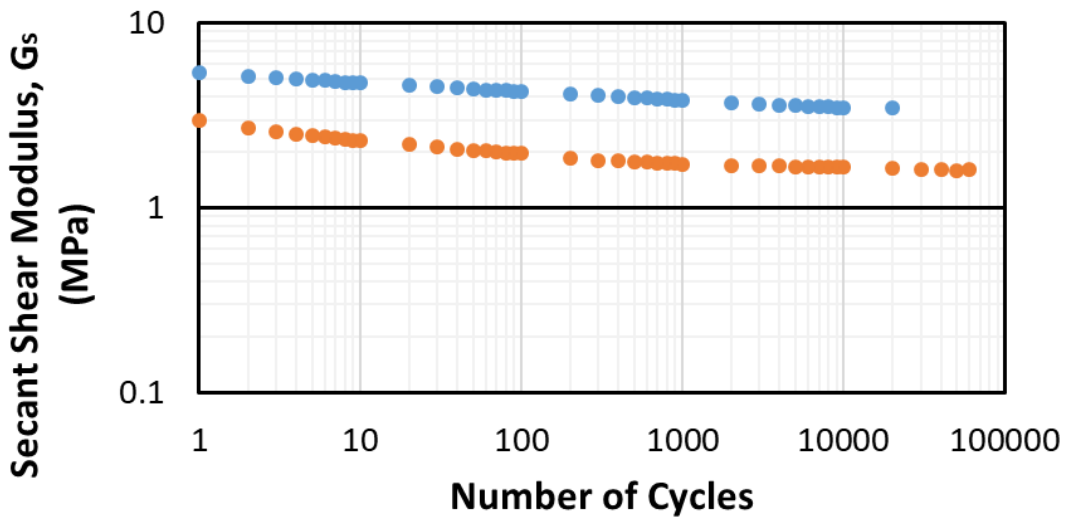


(a)



● $\sigma_v=50\text{kPa}/\sigma_c=12.5\text{kPa}$ ● $\sigma_v=50\text{kPa}/\sigma_c=25\text{kPa}$ ● $\sigma_v=50\text{kPa}/\sigma_c=35\text{kPa}$

(b)

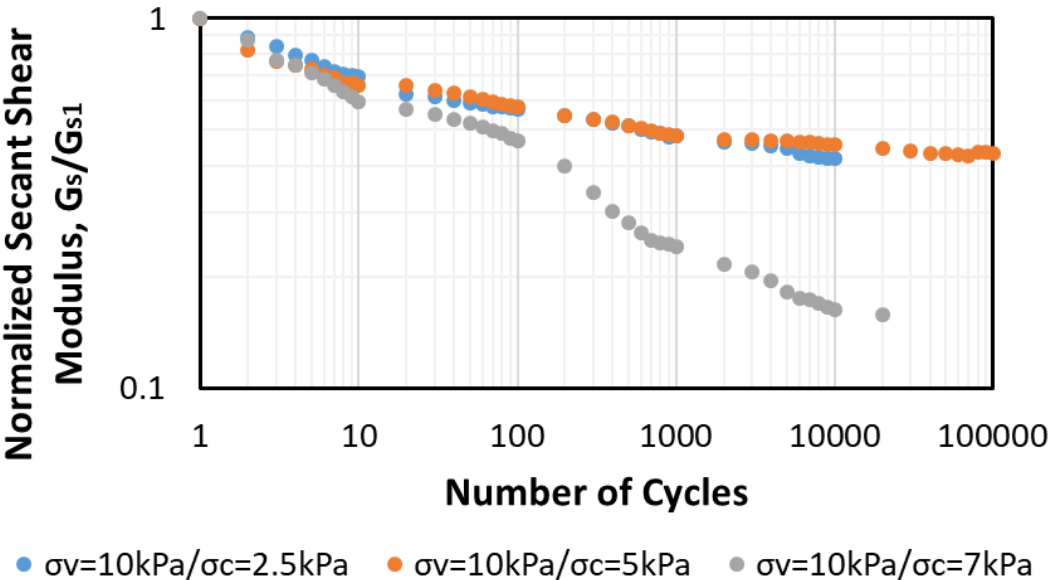


● $\sigma_v=90\text{kPa}/\sigma_c=24\text{kPa}$ ● $\sigma_v=90\text{kPa}/\sigma_c=45\text{kPa}$

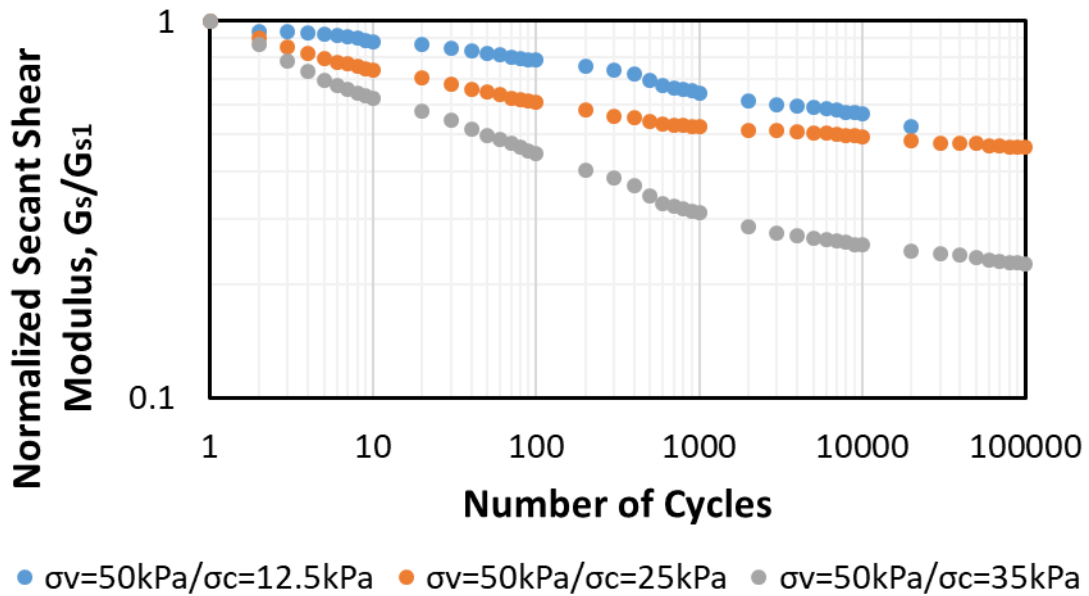
(c)

Figure 5.14. Influence of cyclic shear stress amplitude on the secant shear modulus of ballast #4 based on DSST. (a) 10 kPa vertical stress; (b) 50 kPa vertical stress; (c) 90 kPa vertical stress

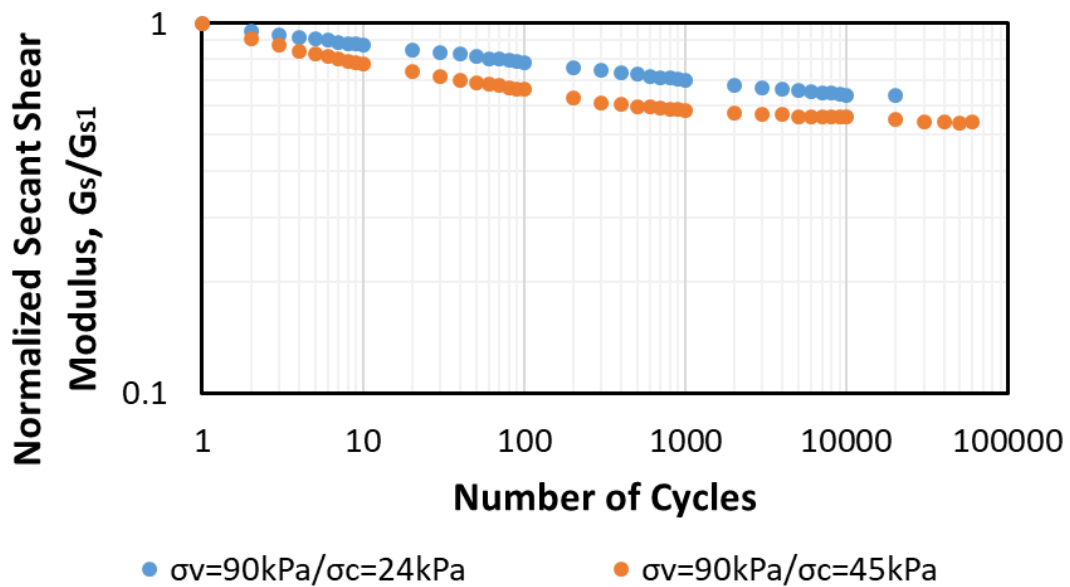
Figure 5.15 illustrates the normalized secant shear modulus degradation against the number of cycles. The reduction rate of the secant shear modulus is increasing with the cyclic stress ratio. However, the reduction rate is remarkable in high cyclic shear stress. This issue happened as a result of significant plastic shear strain accumulation observed in the test when the cyclic stress is approaching the monotonic shear strength of the ballast. For example, in the test series B the normalized secant shear modulus after 10,000 cycles reduced to 0.25 for the cyclic stress ratio of 94% while this value is 0.56 and 0.49 for the cyclic stress ratio of 36% and 70%, respectively.



(a)



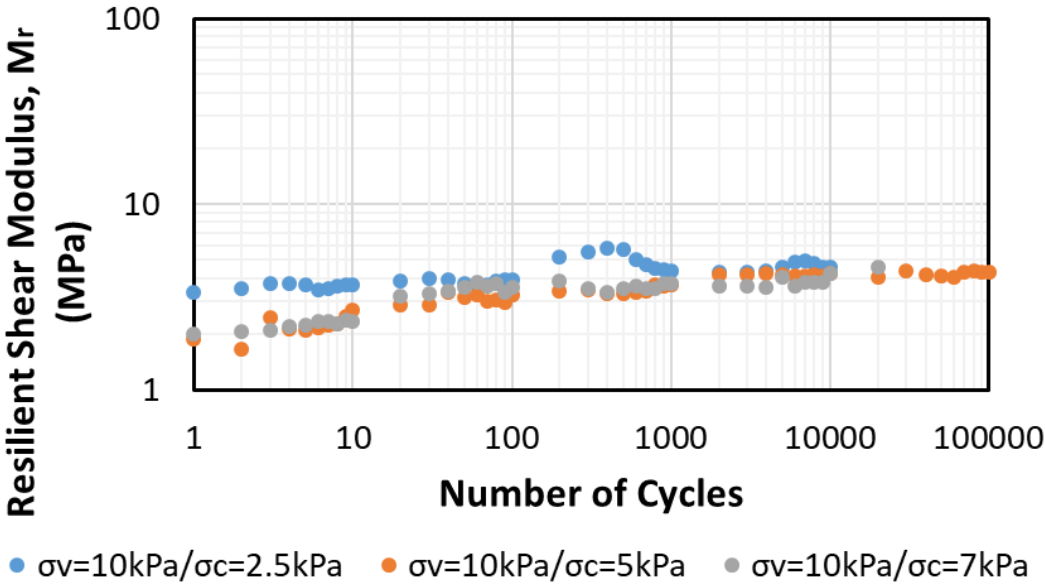
(b)



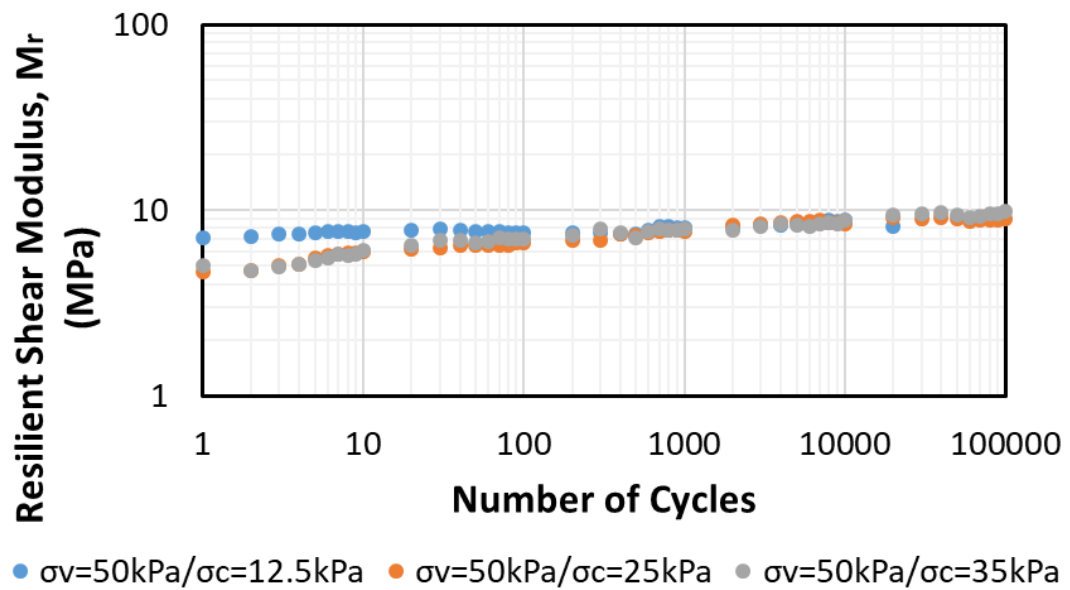
(c)

Figure 5.15. Influence of cyclic shear stress amplitude on the normalized secant shear modulus of ballast #4 based on DSST. (a) 10 kPa vertical stress; (b) 50 kPa vertical stress; (c) 90 kPa vertical stress

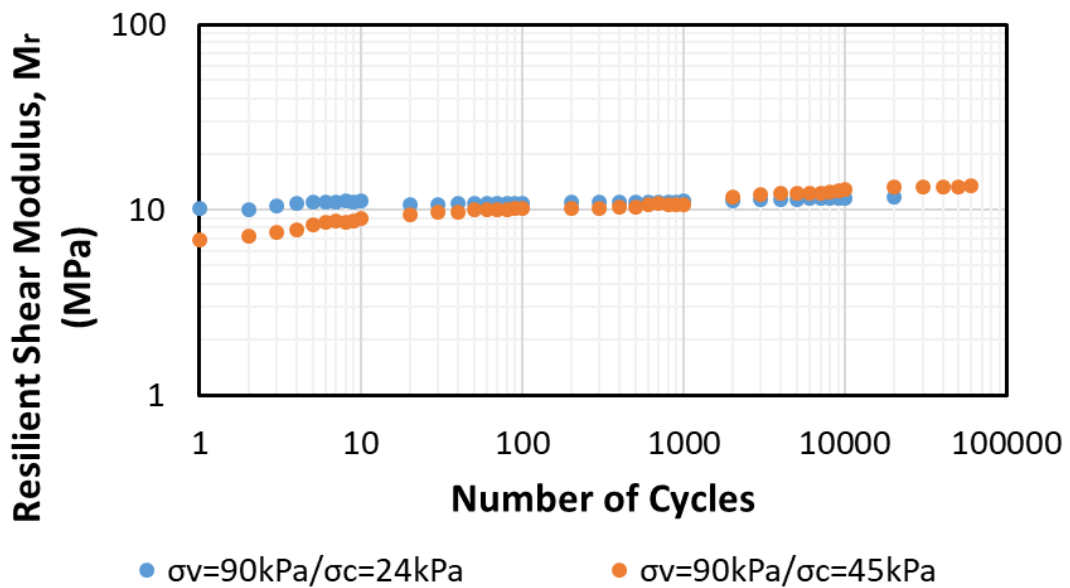
Figure 5.16 shows the impact of cyclic stress amplitude on the variation of the resilient shear modulus. According to the results, the value of the resilient shear modulus is reduced by increasing the cyclic shear stress magnitude in the initial stage of the test. For example, in the test series B, the resilient shear modulus of the first cycle is reduced from 11 and 11 MPa for increasing the cyclic stress ratio from 11% to 11%. But, the magnitude of the resilient shear modulus after 100 initial cycles is approximately the same irrespective of the cyclic stress ratio and increases with the low rate with the number of cycles. The reason that the resilient shear modulus is approached to approximately the same magnitude after 100 cycles are that the ballast is reaching its final density at the beginning of the test. The results also confirm that the resilient shear modulus is directly proportional to the magnitude of the applied vertical stress.



(a)



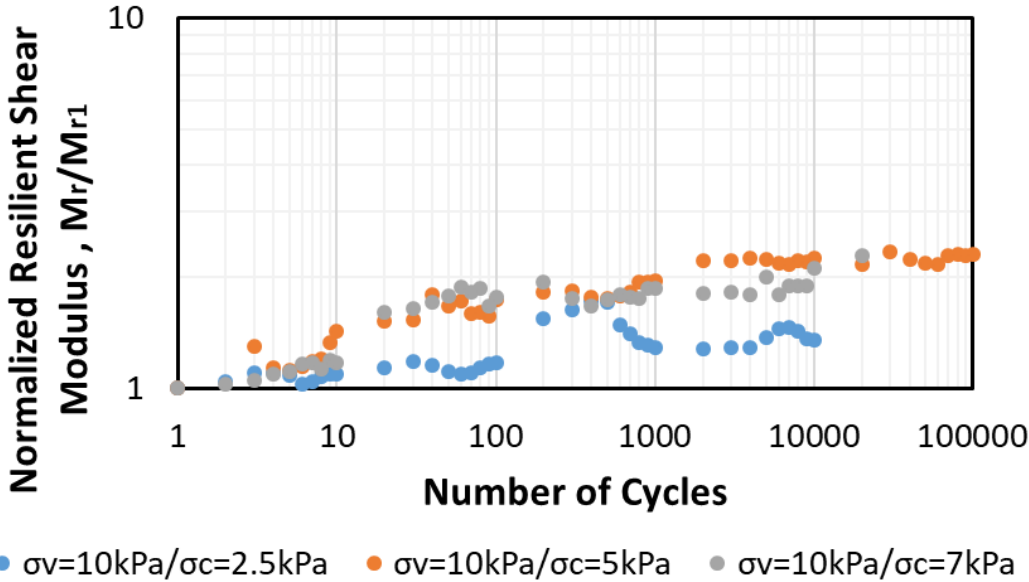
(b)



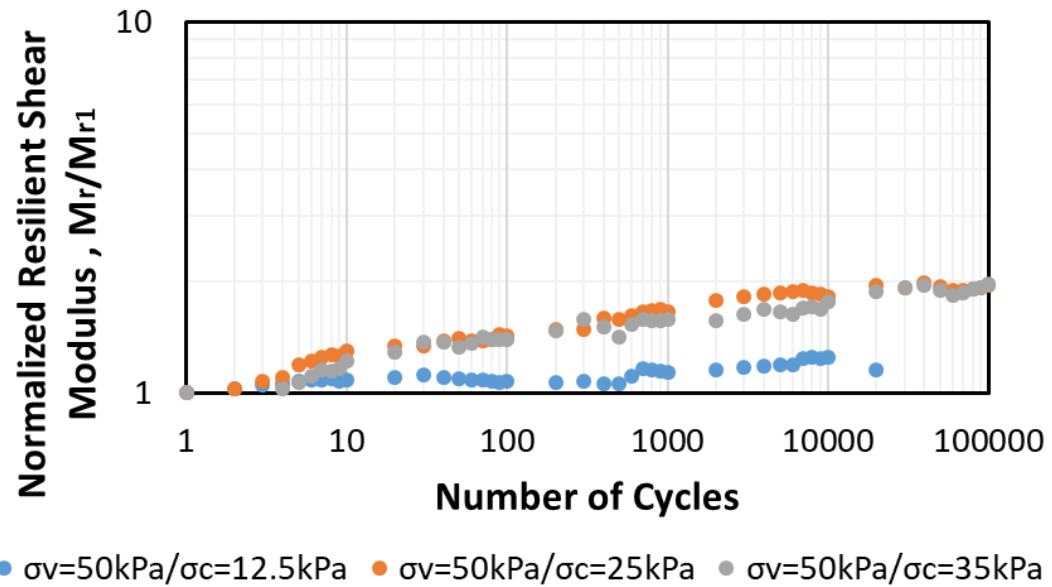
(c)

Figure 5.16. Influence of cyclic shear stress amplitude on the resilient shear modulus of ballast #4 based on DSST. (a) 10 kPa vertical stress; (b) 50 kPa vertical stress; (c) 90 kPa vertical stress

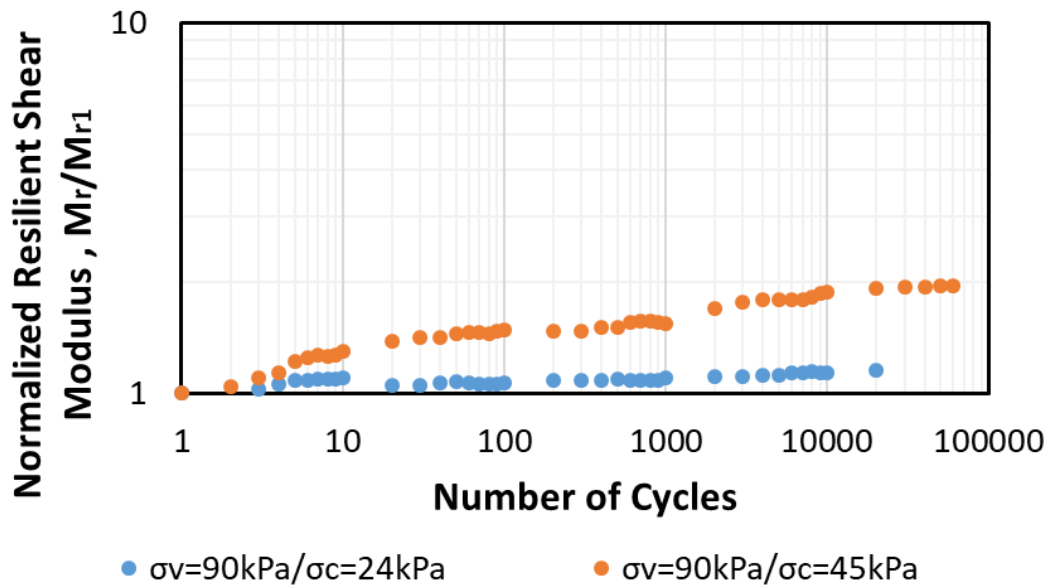
Figure 5.17 shows the variation of the normalized resilient shear modulus with the number of cycles. The overall increase in the normalized resilient shear modulus is observed with increasing the cyclic stress ratio. However, the increment is very low for the test with a low cyclic stress ratio (less than 35%). Moreover, the normalized resilient shear modulus is approximately the same for a high cyclic stress ratio. It is believed that it has happened because the sample reaches its maximum compaction. For instance, for the tests with 50 kPa vertical stress, the normalized resilient shear modulus after 10,000 cycles is nearly 1.8 for the experiments with 70% and 94% cyclic stress ratio. This value is 1.25 for the 36% cyclic stress ratio.



(a)



(b)



(c)

Figure 5.17. Influence of cyclic shear stress amplitude on the resilient shear modulus of ballast #4 based on DSST. (a) 10 kPa vertical stress; (b) 50 kPa vertical stress; (c) 90 kPa vertical stress

5.2.3. Empirical Models to Predict the Long-Term Behavior of the Railroad Ballast Based on Cyclic DSST Results

Experimental results of the cyclic DSST revealed that the behavior of the ballast under cyclic loading is affected by various factors, including soil physical state (dry density, material type), stress state, the amplitude of cyclic loading, and the number of cycles. Different empirical approaches were proposed in the literature to predict the long-term behavior of the granular materials under cyclic loading (Briaud (2013), Alva-Hurtado and Selig (1981), Jeffs and Marich (1987), Sato (1995), Indraratna and Nimbalkar (2013)). In this section, a series of models were proposed to predict the plastic shear strain, secant, and resilient shear modulus of the ballast under cyclic loading. These models include the effect of the number of cycles (number of train passage), stress state (field stress level), and the cyclic stress amplitude (train characteristics).

5.2.3.1. Permanent Shear Strain Prediction

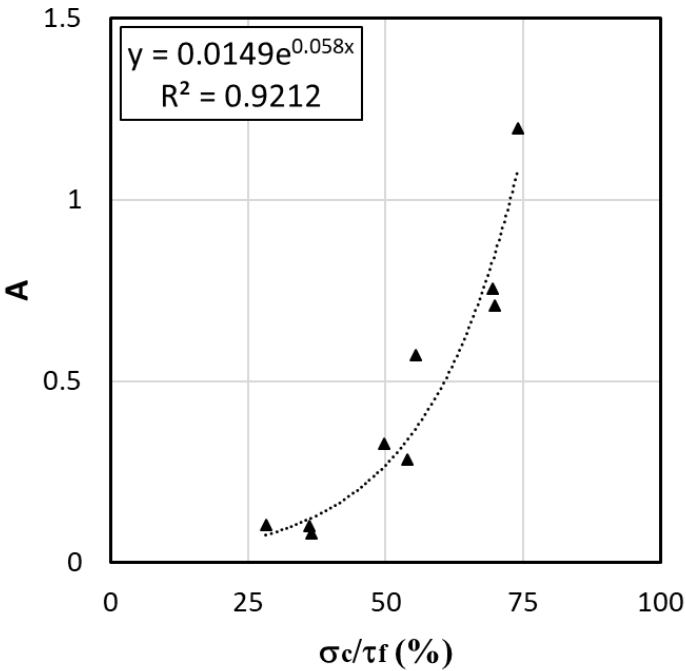
Based on the results obtained from cyclic DSST investigation on the ballast #4, the model proposed by Neidhart (2005) could describe the plastic shear strain development appropriately. The modified form of the model for the prediction of the plastic shear strain is given below:

$$\gamma_p = \gamma_{p1} + \frac{A \text{Log} N}{1 + B \text{Log} N} \quad (16)$$

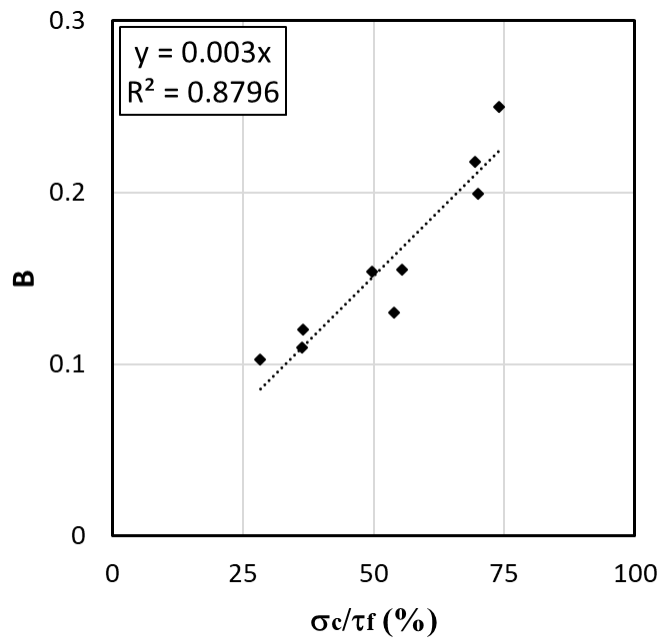
Where γ_{p1} is the plastic shear strain in the first cycle, N is the number of cycles, A and B are the constants influenced by the stress level and the cyclic loading condition. Comparison of the plastic shear strain in the first cycle (γ_{p1}) for all the tests revealed that

this parameter is proportional to the cyclic stress ratio (i.e., the ratio of cyclic shear stress amplitude over the monotonic shear strength). The parameters “A” and “B” in the Equation (16) are related to the applied cyclic shear stress and shear strength of the material.

Figure 5.18 shows the variation of the parameters A and B with the cyclic stress ratio. As can be seen, both parameters are increasing with the cyclic stress ratio. It should be noted that the model can only be used for the tests with the cyclic stress ratio of less than 70%. Therefore, the results of two tests with the cyclic stress ratio of more than 70% were not used to obtain the model parameters. The details about the calibration of the model based on the experimental results are provided in Table 5.3.



(a)



(b)

Figure 5.18. Variation of the plastic shear strain prediction equation (Equation (16)) constants with the cyclic stress ratio. (a) Parameter A; (b) Parameter B

Table 5.3. Calibration of the plastic shear strain model based on the experimental results

Test No.	Vertical Stress (kPa)	Shear Strength (kPa)	Cyclic Stress (kPa)	$\frac{\sigma_c}{\tau_f}$ (%)	γ_1 (%)	A	B
1	10	9.2	2.6	28.3	0.11	0.10	0.10
2	10	9.2	5.1	55.4	0.62	0.57	0.16
3	10	9.2	7.2	78.3	0.83	N/A	N/A
4	40	31.6	23.4	74.1	1.24	1.20	0.25
5	50	36.2	13.2	36.5	0.12	0.08	0.12
6	50	36.2	25.3	69.9	0.61	0.71	0.20
7	50	36.2	34	93.9	0.83	N/A	N/A
8	60	44.5	24	53.9	0.63	0.29	0.13
9	70	50.7	25.2	49.7	0.43	0.33	0.15
10	90	65.5	23.7	36.2	0.19	0.10	0.11
11	90	65.5	45.5	69.5	0.84	0.76	0.22

Figure 5.19 shows the variation of the plastic shear strain in the first cycle with the cyclic stress ratio. The black dots show the experimental measurement. The experimental data showed that the first cycle plastic shear strain could be well predicted ($R^2=0.79$) by modified Avrami equation as follow:

$$\gamma_{p1} = A(1 - \exp(-b(\frac{\sigma_c}{\tau_f})^n)) \quad (17)$$

where σ_c is the cyclic stress amplitude, τ_f is the monotonic shear strength, A, b, and n are the constant related to the ballast properties. The magnitude of the constants can be determined by fitting the proposed equation to the experimental results. As a result, for the crushed granite ballast #4 used in the current study, these constants are $A=1.0$, $b=2E-06$, and $n=3.18$.

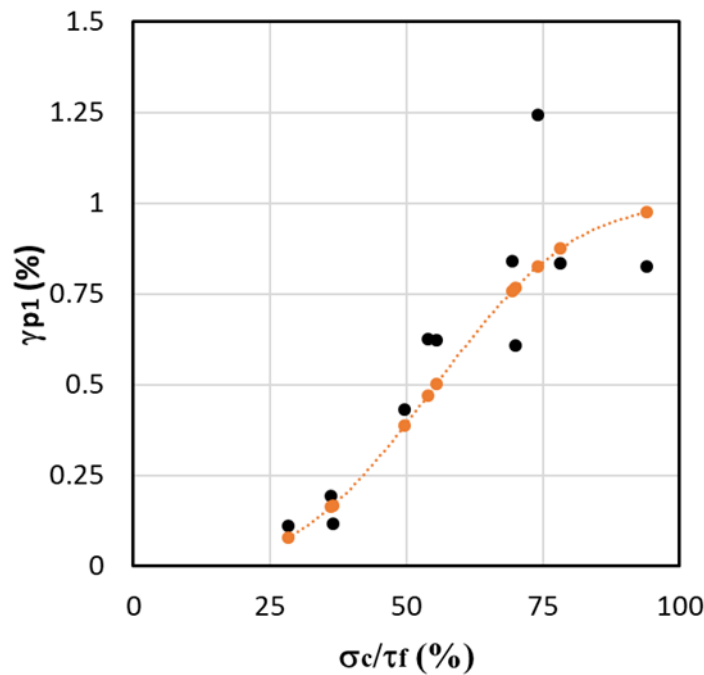
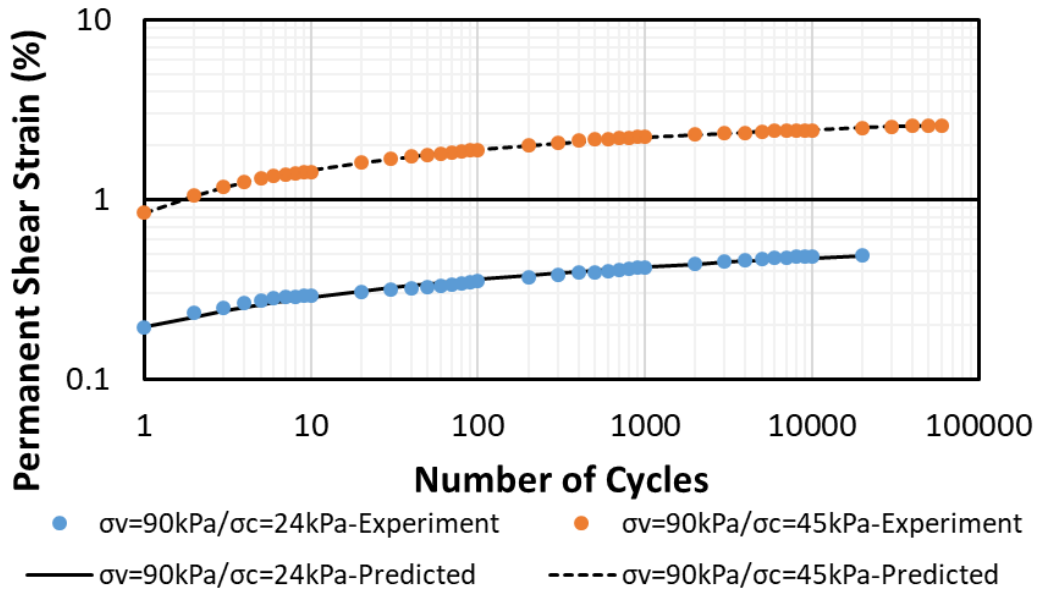


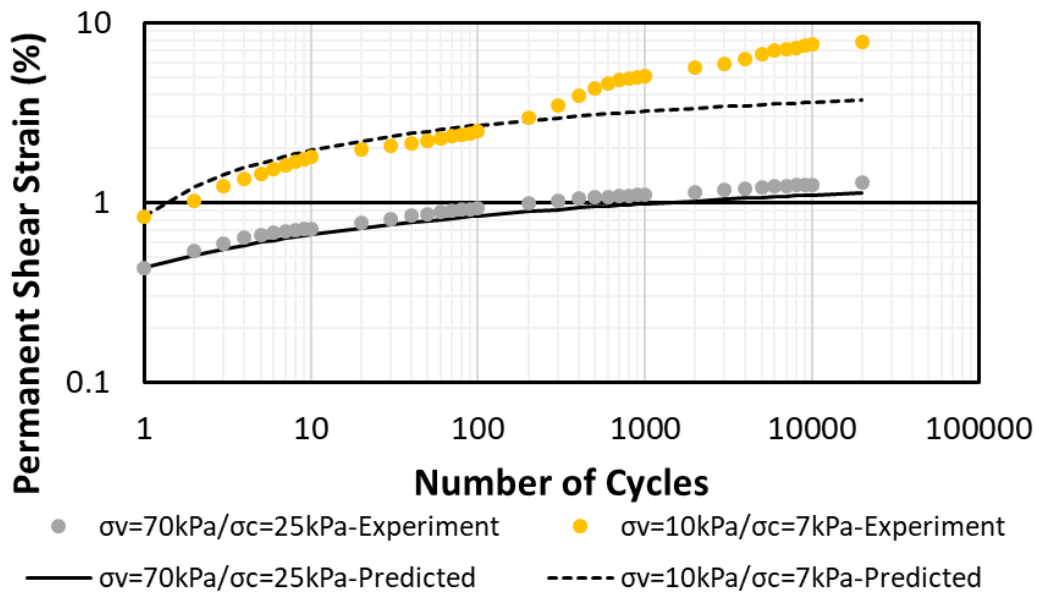
Figure 5.19. Variation of the plastic shear strain with the cyclic stress ratio

Figure 5.20(a) shows the example of fitting of the proposed model to the experimental results for two tests with 90 kPa vertical stress and the cyclic shear stress of 24 and 45 kPa. As can be seen, the model fits very well with the measured plastic shear strain. The same acceptancy of the model was observed for all the experimental data fitting. After the determination of the model parameters, the model was used to simulate two tests: (a) vertical stress of 70 kPa and the cyclic stress ratio of 50%, and (b) vertical stress of 10 kPa and the cyclic stress ratio of 78%. Figure 5.20(b) illustrates the comparison between the experimental data and the proposed model. As is evidenced, the model can satisfactorily simulate the results of the test with a 50% cyclic stress ratio. However, the model is unable to reproduce the results of the test with a 78% cyclic stress ratio.

The difference between the test results and the model prediction in a high cyclic stress ratio level could be interpreted by shakedown theory (Lackenby et al. (2007), Werkmeister et al. (2004), and Suiker and de Borst (2003)). There are three major regimes for the permanent deformation of the granular material under cyclic loading, including shakedown, plastic creep (cyclic densification), and the frictional failure. The proposed model can be employed for the tests in the shakedown categories (the permanent shear strain stabilized after 1,000 cycles for the tests with the cyclic stress ratio of less than 70%).



(a)



(b)

Figure 5.20. Plastic shear strain model prediction with the experimental data. (a) Example of determination of the model parameters by fitting the experimental results; (b) Verification of the proposed model

5.2.3.2. Secant Shear Modulus Prediction

The secant shear modulus of the ballast under the cyclic loading can be obtained from the Equation (18) as provided below:

$$\frac{G_s}{G_{s1}} = 1 - \frac{A \text{Log} N}{1 + B \text{Log} N} \quad (18)$$

where G_{s1} is the secant shear modulus of the first cycle, N is the number cycles, A , and B are the constants related to the material characteristics and controlling the non-linearity of the diagram. The variation of G_{s1} against the cyclic stress ratio is depicted in Figure 5.21. as illustrated, the secant shear modulus of the first cycle depends on both test stress state (vertical stress) and cyclic stress ratio (cyclic shear stress over monotonic shear strength). The secant shear modulus of the first cycle increasing with the vertical stress and decreasing with the cyclic stress ratio.

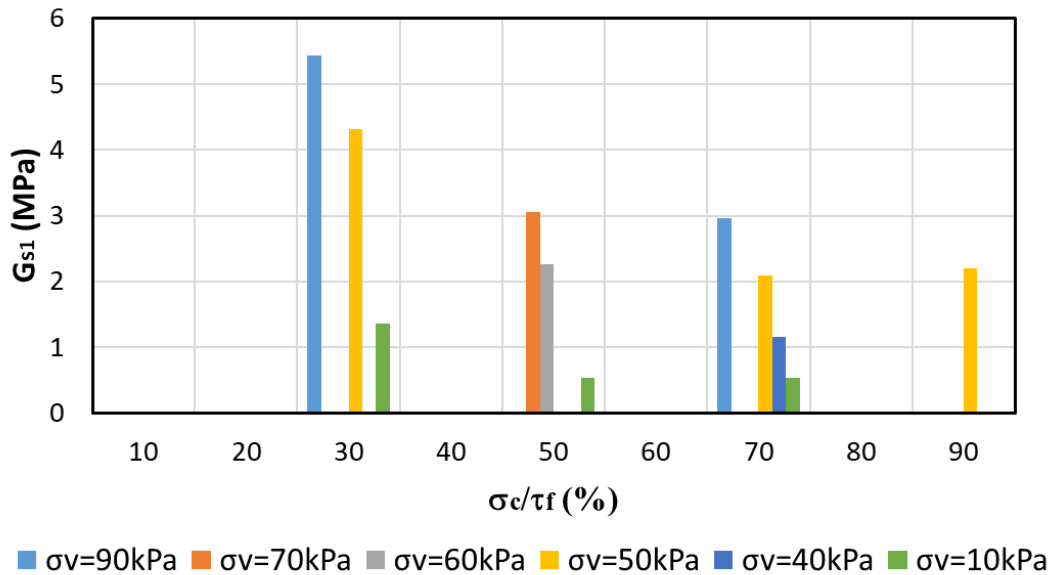
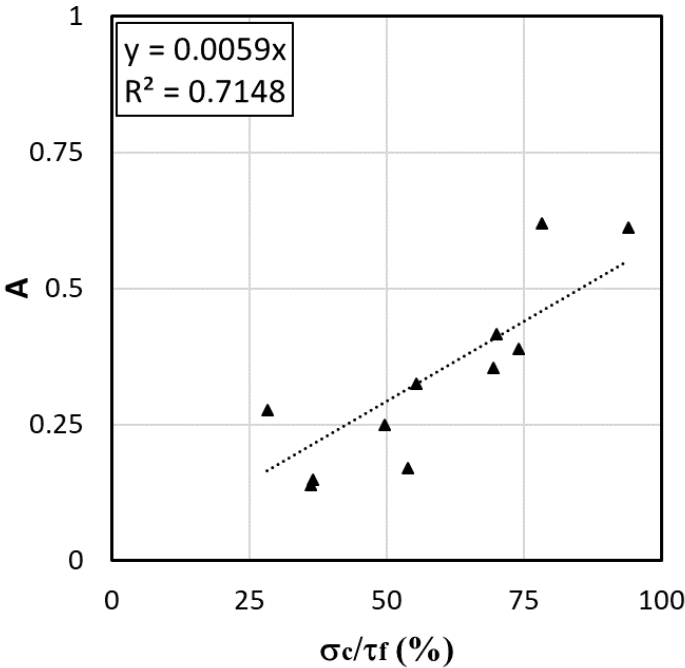
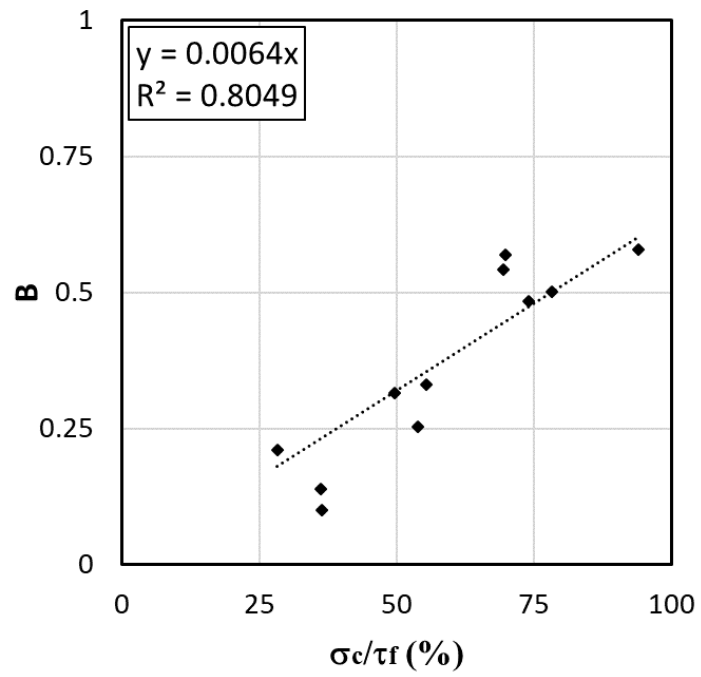


Figure 5.21. Variation of the secant shear modulus at the first cycle with the cyclic stress ratio

The constants of the Equation (18) are correlated with the magnitude of the cyclic stress ratio. Figure 5.22 shows the relationship between the parameter A and B with the cyclic stress ratio. It can be seen that the parameter A and B were increased nearly linearly with the cyclic stress ratio with the R^2 of 0.71 and 0.80, respectively. It should be pointed out that the values of these constants are based on the crushed granite ballast #4, which has been used in this study. The calibration of the secant shear modulus model with the cyclic DSST results is provided in Table 5.4. Similar to the proposed model for the permanent shear strain (Equation (17)), the secant shear modulus model can only be used for the cyclic stress ratio of less than 70% (shakedown category).



(a)



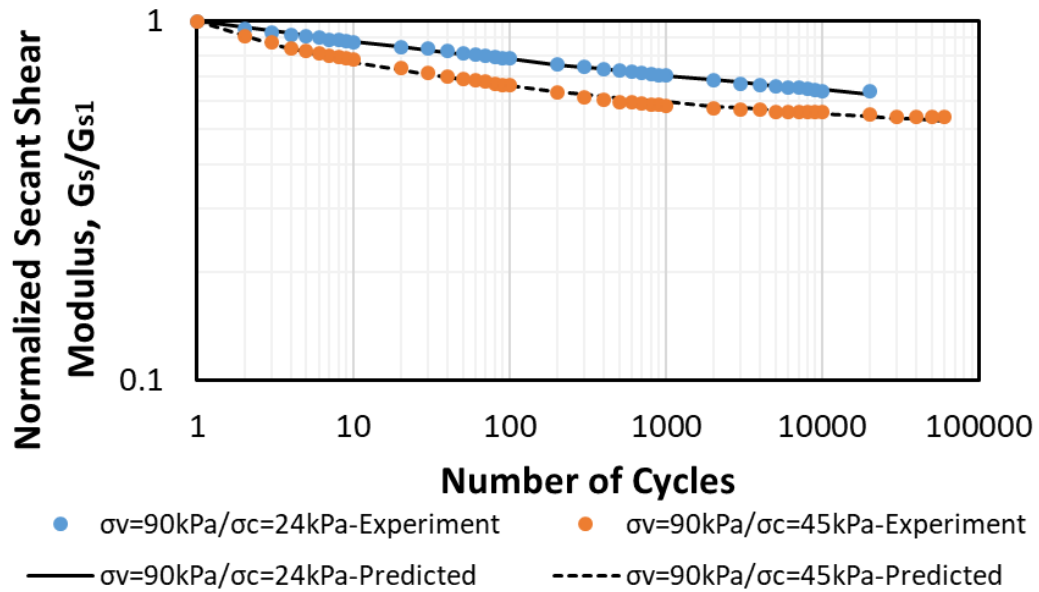
(b)

Figure 5.22. Variation of the secant shear modulus equation (Equation (18)) constants with the cyclic stress ratio. (a) Parameter A; (b) Parameter B

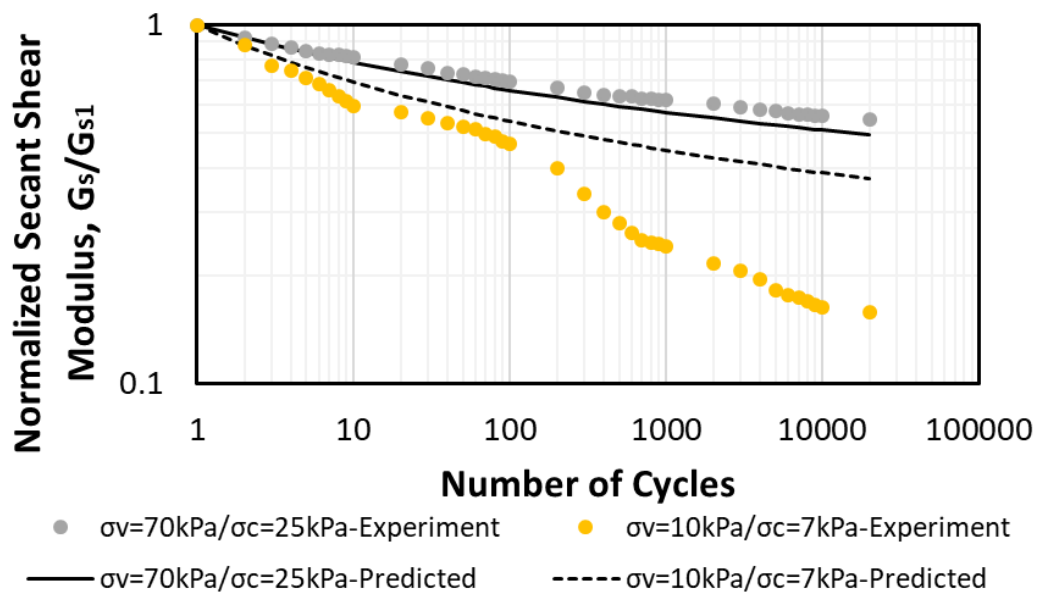
Table 5.4. Calibration of the secant shear modulus model based on the experimental results

Test No.	Vertical Stress (kPa)	Shear Strength (kPa)	Cyclic Stress (kPa)	$\frac{\sigma_c}{\tau_f}$ (%)	G_{s1} (MPa)	A	B	R ²
1	10	9.2	2.6	28.3	1.36	0.28	0.21	0.99
2	10	9.2	5.1	55.4	0.54	0.32	0.33	0.96
3	10	9.2	7.2	78.3	0.54	0.62	0.50	0.81
4	40	31.6	23.4	74.1	1.15	0.39	0.48	0.98
5	50	36.2	13.2	36.5	4.31	0.15	0.10	0.97
6	50	36.2	25.3	69.9	2.09	0.42	0.57	0.99
7	50	36.2	34	93.9	2.20	0.61	0.58	0.99
8	60	44.5	24	53.9	2.27	0.17	0.25	0.95
9	70	50.7	25.2	49.7	3.05	0.25	0.32	0.97
10	90	65.5	23.7	36.2	5.43	0.14	0.14	0.98
11	90	65.5	45.5	69.5	2.97	0.35	0.54	0.99

Figure 5.23(a) exemplifies how the proposed model fits the normalized secant shear modulus results. As it is evident, the model can reproduce the experimental results very well. It is noteworthy to mention that the same acceptancy of the model was observed for all the tests ($R^2 > 0.81$) (Table 5.4). Figure 5.23(b) shows how the model can simulate the experimental results. The close prediction was observed for the test, with a 50% cyclic stress ratio. As was indicated before, the model cannot be an appropriate representative for the test with the cyclic stress ratio of higher than 70%; consequently, as shown in the figure, the results of the test with 10 kPa vertical stress and the cyclic stress ratio was not simulated correctly.



(a)



(b)

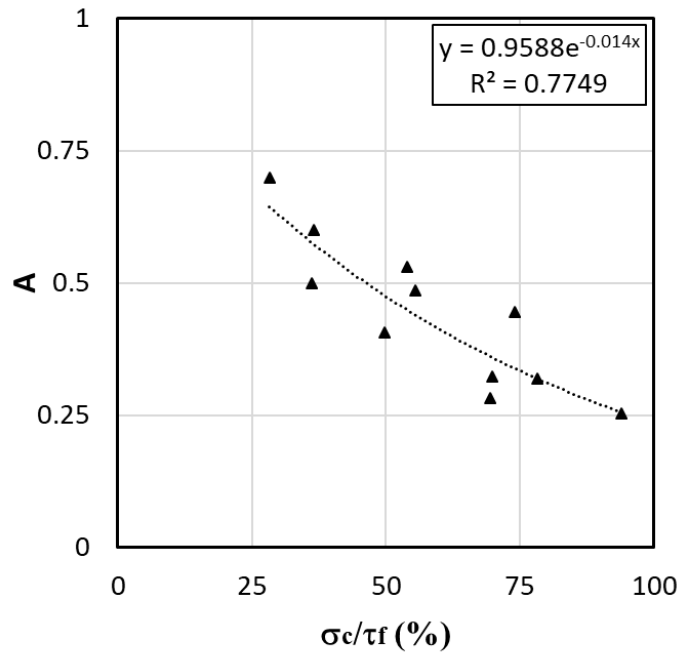
Figure 5.23. Secant shear modulus Model Prediction with the experimental data. (a) Example of determination of the model parameters by fitting the experimental results; (b) Verification of the proposed model

5.2.3.3. Resilient Shear Modulus Prediction

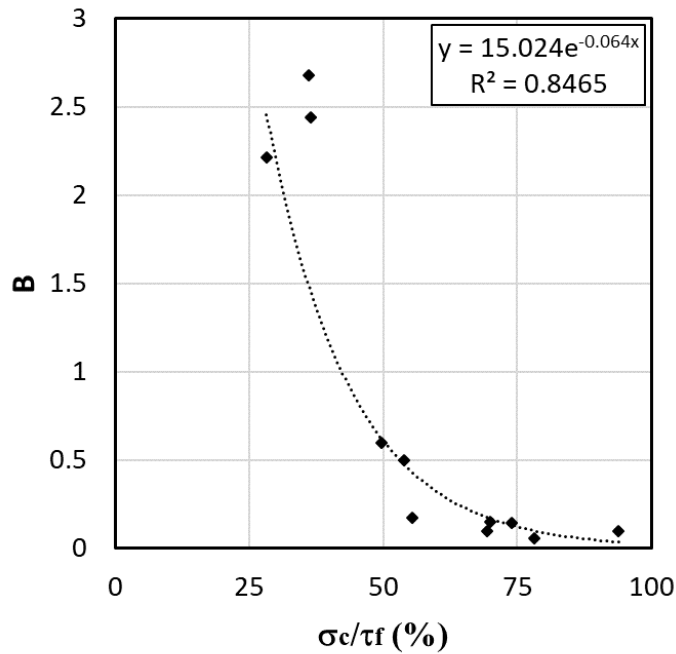
According to the cyclic DSST results, a function relating the resilient shear modulus of the ballast to the number of cycles and the stress states can be established as follow:

$$\frac{M_r}{M_{r1}} = 1 + \frac{A \text{Log} N}{1 + B \text{Log} N} \quad (19)$$

where M_{r1} is the resilient shear modulus of the first cycle, N is the number cycles, A , and B are the constants. The calibration of the abovementioned equation with the experimental results showed that the cyclic stress ratio influences the magnitude of the equation constants. Figure 5.24 shows the results of constant A and B versus the applied cyclic stress ratio. Both parameters are decreasing nonlinearly with increasing the cyclic stress ratio.



(a)



(b)

Figure 5.24. Variation of the resilient shear modulus equation (Equation (19)) constants with the cyclic stress ratio. (a) Parameter A; (b) Parameter B

Table 5.5 shows the magnitude of the parameter A and B for all the tests by fitting the model to the experimental data. The first difference between this model and the previous models (Equation (16) and (18)) is the acceptable prediction of this model for the test with high cyclic stress ratio (>70%). The reason is the magnitude of the resilient shear modulus did not increase drastically in the test with a high cyclic stress ratio. Because the resilient shear modulus is related to the elastic shear strain, which is stabilized after the initial stage of the test (mostly first 100 cycles).

The results showed that the R^2 of the proposed model for the experiments with low stress ratio (25% to 35%) is not satisfactory (0.36 to 0.52). It is noteworthy to mention that

in the test with a low cyclic stress ratio, the resilient shear modulus showed negligible growth with the number of cycles. For example, for the test with 90 kPa vertical stress and 36% cyclic stress ratio, the resilient shear modulus was increased only 12% after 20,000 cycles.

Table 5.5. Calibration of the resilient shear modulus model based on the experimental results

Test No.	Vertical Stress (kPa)	Shear Strength (kPa)	Cyclic Stress (kPa)	$\frac{\sigma_c}{\tau_f}$ (%)	M_{r1} (MPa)	A	B	R ²
1	10	9.2	2.6	28.3	3.37	0.70	2.21	0.36
2	10	9.2	5.1	55.4	1.88	0.49	0.18	0.91
3	10	9.2	7.2	78.3	2.03	0.32	0.06	0.78
4	40	31.6	23.4	74.1	3.34	0.45	0.14	0.95
5	50	36.2	13.2	36.5	7.06	0.60	2.44	0.45
6	50	36.2	25.3	69.9	4.64	0.32	0.15	0.92
7	50	36.2	34	93.9	4.99	0.25	0.10	0.93
8	60	44.5	24	53.9	5.87	0.53	0.50	0.92
9	70	50.7	25.2	49.7	6.68	0.41	0.60	0.95
10	90	65.5	23.7	36.2	10.16	0.50	2.68	0.52
11	90	65.5	45.5	69.5	6.87	0.28	0.10	0.95

It is previously shown that the resilient shear modulus of the first cycle depends on the test stress state and the applied cyclic stress. Figure 5.25 shows the variation of the resilient shear modulus of the first cycle with the cyclic stress ratio. The graph displays that M_{r1} is increasing in higher vertical stress. According to the results, at approximately 30% cyclic stress ratio, M_{r1} increases from 3.4 to 10.2 MPa for increasing the vertical stress from 10 to 90 kPa. The results also revealed that the resilient shear modulus of the first cycle decreases from 10.2 to 6.9 MPa for increasing the cyclic stress ratio from 36% to 70% for the constant vertical stress of 90 kPa.

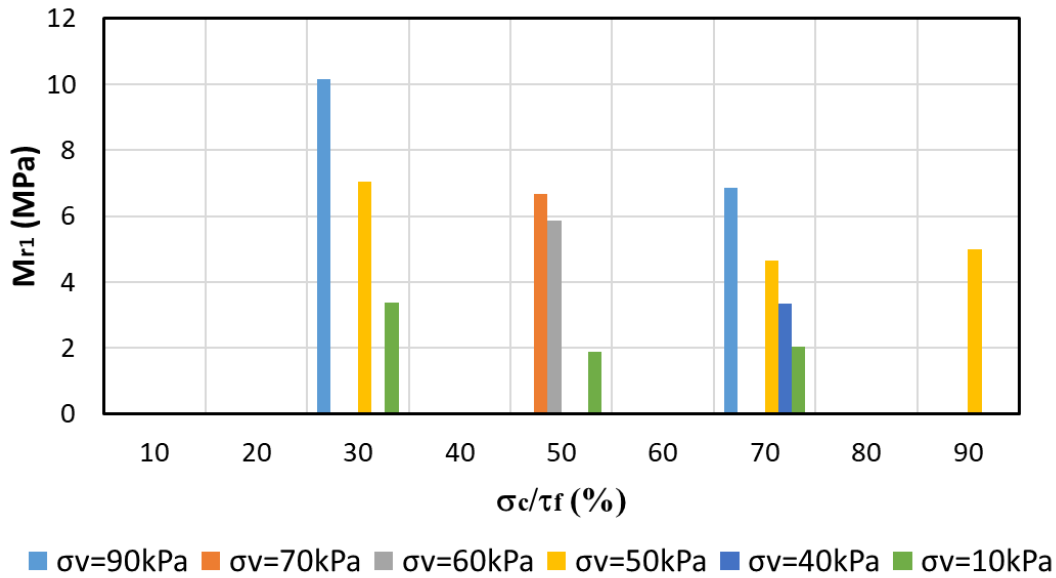
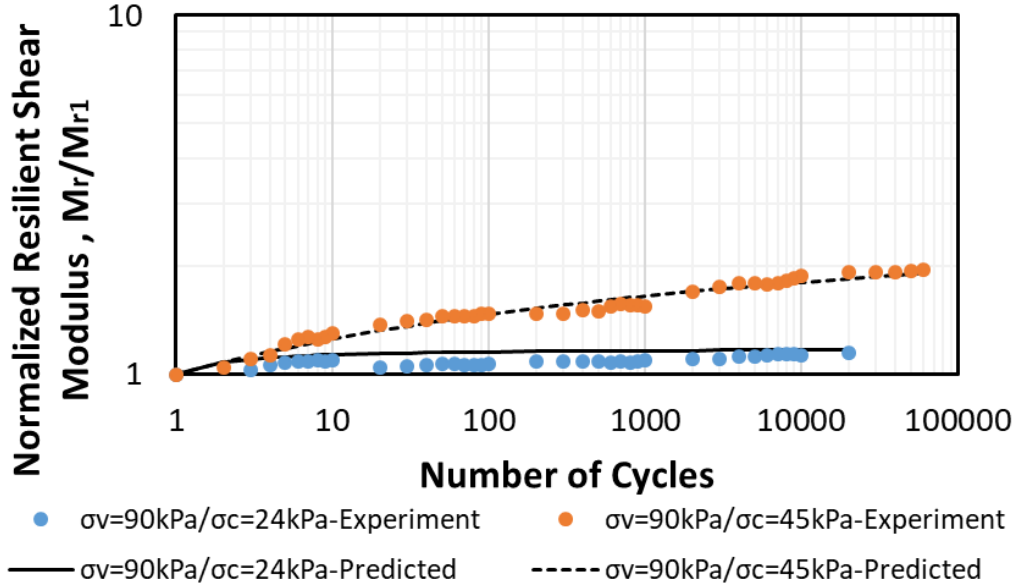


Figure 5.25. Variation of the resilient shear modulus at the first cycle with the cyclic stress ratio

The proposed model for the resilient shear modulus was calibrated with the results of all the cyclic DSST to obtain the model parameters. Figure 5.26(a) exemplifies the model fitting on the result of two tests with the vertical stress of 90 kPa and the cyclic shear stress of 24 and 45 kPa. The comparison showed that the model perfectly resembles the experimental data with the cyclic stress ratio of 70% (orange data points). In addition, the model slightly overpredicts the data of the test with a 36% cyclic stress ratio. This happens due to the negligible variation of the resilient shear modulus with the number of cycles in the low cyclic stress ratio.

Figure 5.26(b) demonstrates the verification of the model with the experimental data. It can be observed that the model shows the close prediction of the normalized resilient shear modulus against the number of cycles. It is important to be noted that

despite the proposed model for permanent shear strain and secant shear modulus, This model (resilient shear modulus) can be a good representative for the test with a high cyclic stress ratio (more than 70%).



(a)

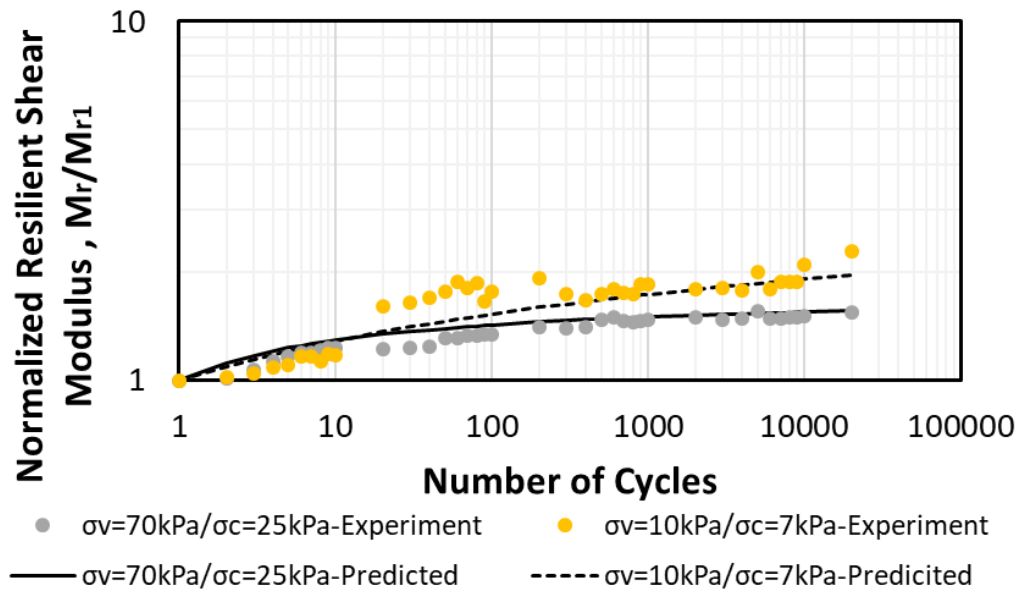


Figure 5.26. Resilient shear modulus Model Prediction with the experimental data. (a) Example of determination of the model parameters by fitting the experimental results; (b) Verification of the proposed model

5.3. Cyclic Triaxial Test (TT)

The results of the large-scale cyclic triaxial test will be presented and discussed in this section. The primary goals of this investigation are to develop an empirical formula to predict the permanent settlement and the elastic triaxial modulus of the ballast layer under the operation of a high-speed and heavy freight train. The sample preparation and the testing plan were explained thoroughly in chapter 3 and will not be repeated in this section. It is essential to mention that due to the limitation of the triaxial cell size, ballast #5 with the maximum particle size of 25 mm was used in all the TT investigations.

5.3.1. Experimental Results

5.3.1.1. Cyclic Deviatoric Stress-Axial Strain Response

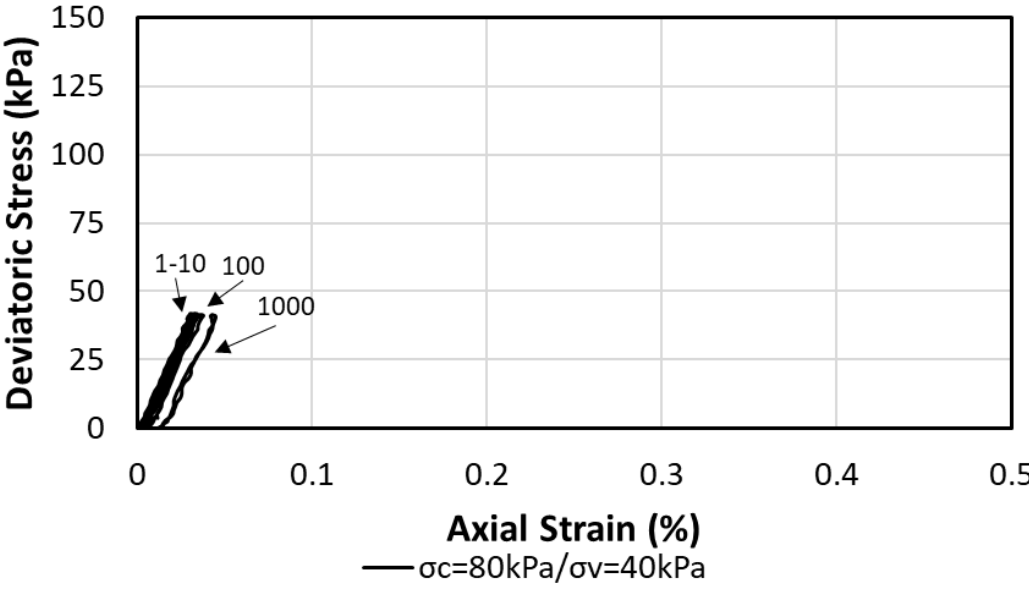
The deviatoric stress changes with the axial strain of the specimens under cyclic loading are presented in Figure 5.27. Experiments were performed at the constant confining pressure of 80 kPa and the cyclic deviatoric amplitude of 40, 80, and 125 kPa. In order to have a more transparent and understandable cyclic stress-strain diagram, only the results of the cycles 1st-10th, 100th, and 1,000th were depicted. It is shown that the axial strain is growing with the loading cycles. However, the rate of plastic axial strain growth is higher in the higher magnitude of the cyclic deviatoric stress. Similar to the cyclic DSST results, the best way to describe the stress dependency of the specimen is by the cyclic stress ratio.

The cyclic stress ratio for the triaxial test is defined as the ratio of cyclic deviatoric stress amplitude over the monotonic peak deviatoric stress, as shown in Equation :

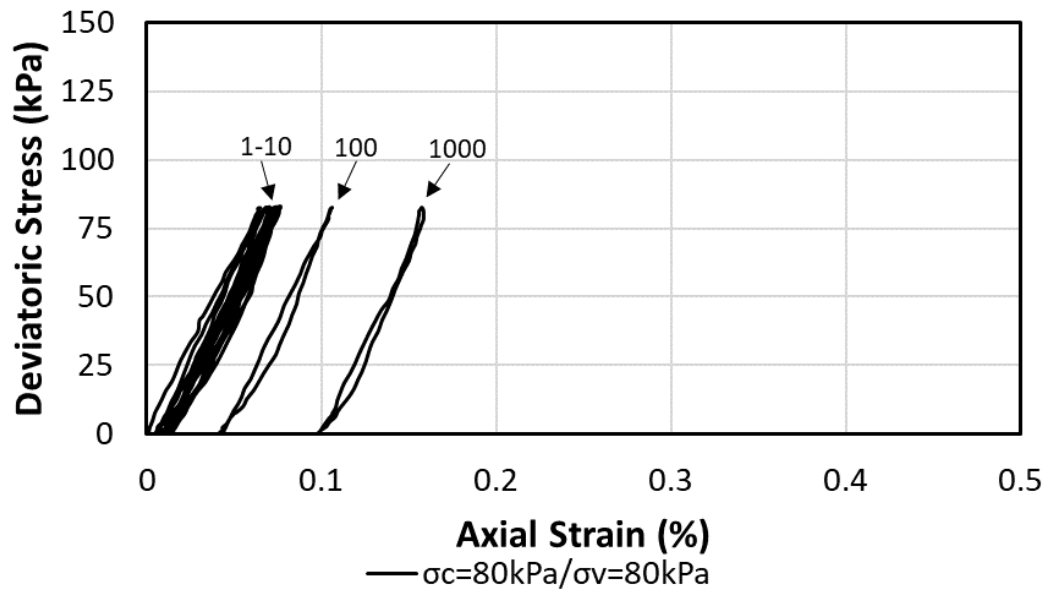
$$n = \frac{q_{max,cyclic} - q_{min,cyclic}}{q_{peak,static}} \quad (20)$$

where $q_{max,cyclic}$ is the maximum deviatoric stress magnitude, $q_{min,cyclic}$ is the minimum deviatoric stress magnitude, and $q_{peak,static}$ is the peak deviatoric stress in the monotonic test. According to the monotonic TT results provided in Table 4.7, the $q_{peak,static}$ of ballast #5 at the confining pressure of 80 kPa is 420 kPa. Details about the triaxial tests are provided in Table 4.6.

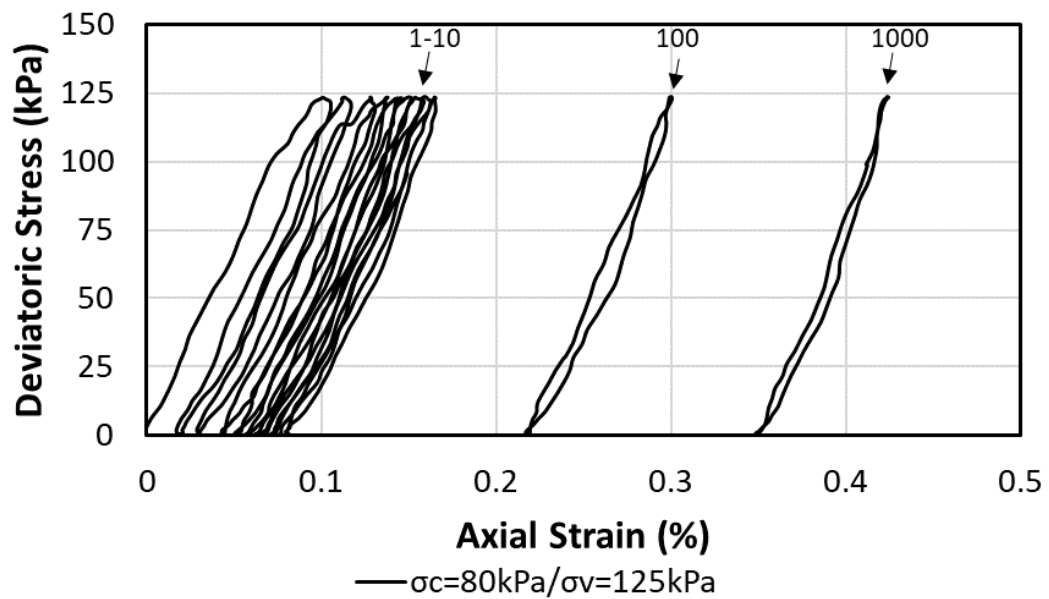
Figure 5.27(a) is related to the test with the cyclic stress ratio of 0.1. As can be seen, due to the low magnitude of the cyclic deviatoric stress, the most portion of the axial strain developed in this test is recoverable and only a negligible plastic axial strain growth after 1,000 cycles.



(a)



(b)



(c)

Figure 5.27. Cyclic deviatoric stress-axial strain response of railroad ballast based on TT results. (a) Deviatoric stress of 40 kPa; (c) Deviatoric stress of 80 kPa; (c) Deviatoric stress of 125 kPa

Table 5.6. Details of the cyclic TT

Test No.	σ_3 (kPa)	$q_{min,cyclic}$ (kPa)	$q_{max,cyclic}$ (kPa)	$q_{peak,static}$ (kPa)	n (%)	Frequency (Hz)	Number of Cycles
1	80	0	40	420	9.5	1	1000
2	80	0	80	420	19.0	1	1000
3	80	0	125	420	29.8	1	1000

5.3.1.2. Permanent Axial Strain

Figure 5.28 depicts the development of the plastic axial strain as a function of the number of cycles for three tests with different cyclic stress ratio. As expected, increasing the cyclic stress ratio increases the growth of the plastic axial strain. According to the results, the magnitude of the plastic axial strain after 1,000 cycles increases from 0.02% to 0.35% for increasing the cyclic stress ratio from approximately 10% to 30%. The trend of the permanent axial strain changes with the number of cycles showed that the accumulation rate is decreasing with the number of cycles.

The results of the test with the cyclic stress ratio of less than 10% showed nearly 0.02% permanent axial strain accumulation after 1,000 loading cycles. Therefore, It can be concluded that for the test with a low cyclic stress ratio (<10%), the permanent plastic strain is negligible, and the material stays in the elastic zone.

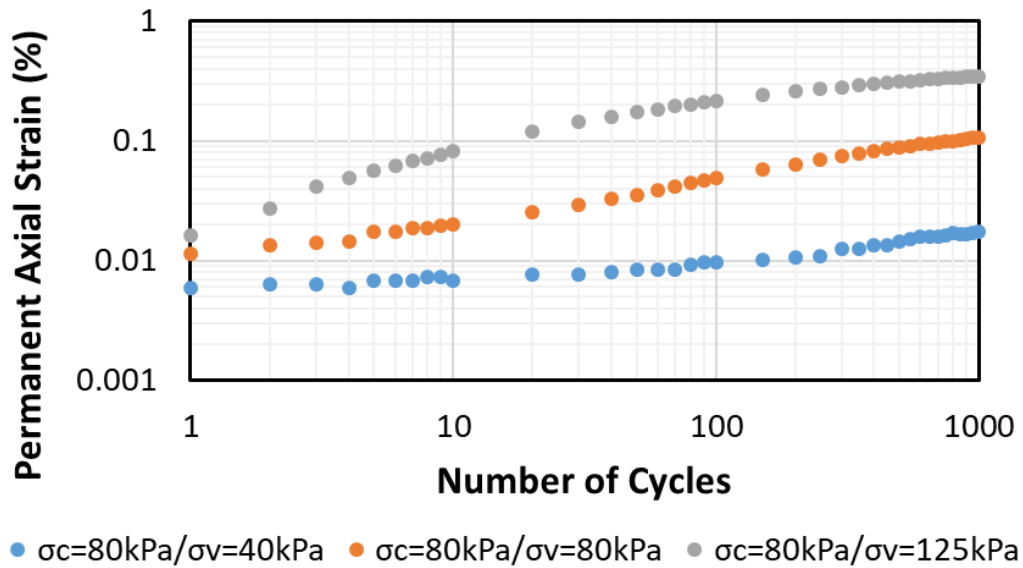


Figure 5.28. Development of the permanent axial strain of railroad ballast with the number of cycles

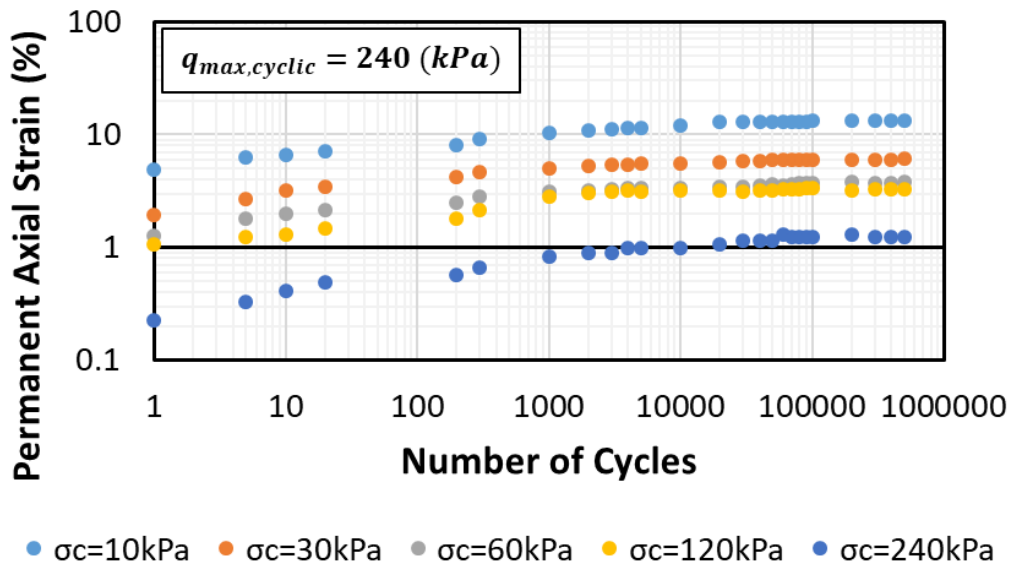
Due to the limitation of the cyclic triaxial test result in the current study (such as the number of cycles and the cyclic stress ratio), the data of the cyclic triaxial investigation performed by Lackenby et al. (2007) were used to simulate the long-term permanent settlement of the railroad ballast. They employed a large-scale triaxial cell with dimensions of 600 mm height and 300 mm in diameter. The material used in their study is a highly granular latite basalt with d_{max} , d_{min} , d_{50} of 53, 39.5, and 16 mm, respectively. The specimens were compacted to reach the initial density of 1560 kg/m³.

The data of eight tests with the confining pressure ranging from 10 to 240 kPa, the cyclic stress ratio ranging from 15% to 70%, and the number of cycles equal to 500,000 were used in this study. Further details about these tests are summarized in Table 5.7. Figure 5.29 shows the axial permanent strain accumulation with the number of cycles

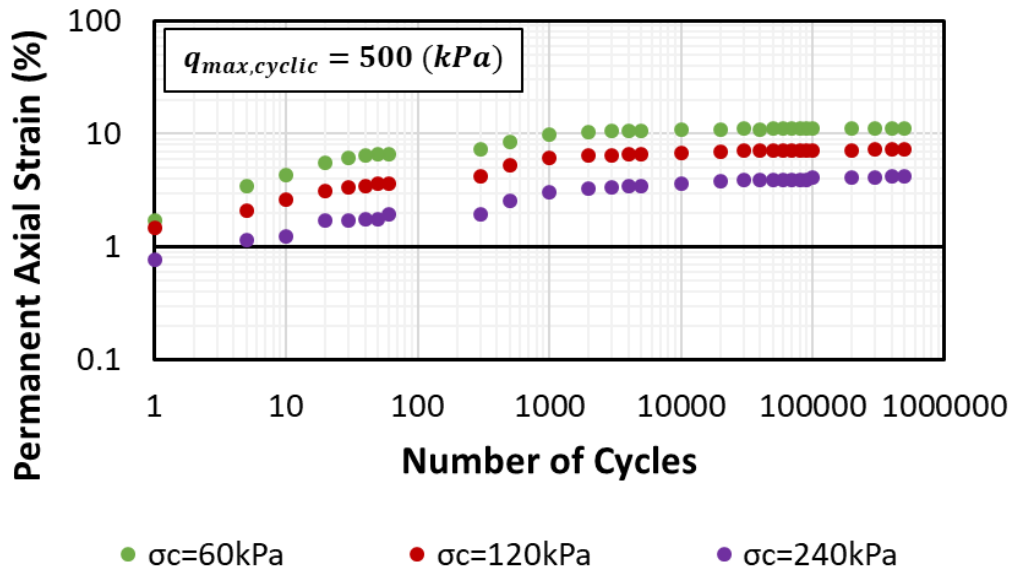
based on the Lackenby et al. (2007) experimental results. Similar to the results of the cyclic triaxial tests performed in the current study, the permanent axial strain influenced by the number of cycles, cyclic stress ratio, and the confining pressure.

Table 5.7. Summary of the cyclic triaxial testing program (data adopted from Lackenby et al. (2007))

Test No.	σ_3 (kPa)	$q_{min,cyclic}$ (kPa)	$q_{max,cyclic}$ (kPa)	$q_{peak,static}$ (kPa)	n (%)	Number of Cycles
1	10	45	230	270	68.5	500,000
2	30	45	230	385	48.1	500,000
3	60	45	230	665	27.8	500,000
4	120	45	230	801	23.1	500,000
5	240	45	230	1274	14.5	500,000
6	60	45	500	665	68.4	500,000
7	120	45	500	801	56.8	500,000
8	240	45	500	1274	35.7	500,000



(a)



(b)

Figure 5.29. Permanent axial strain versus the number of cycles. (a) For the tests with the maximum cyclic magnitude of 240 (kPa); (b) For the tests with the maximum cyclic magnitude of 500 (kPa) (data adopted from Lackenby et al. (2007))

5.3.1.3. Secant Triaxial Elastic Modulus

Secant triaxial elastic modulus is another critical property of the railroad ballast that can be evaluated from the cyclic triaxial test. The secant elastic modulus of each cycle was calculated based on Equation (12) stated previously. It should be noted that the secant elastic modulus of each cycle is corresponding to the peak axial strain value. Table 5.8 summarized the values of the secant elastic modulus derived from the cyclic TT results.

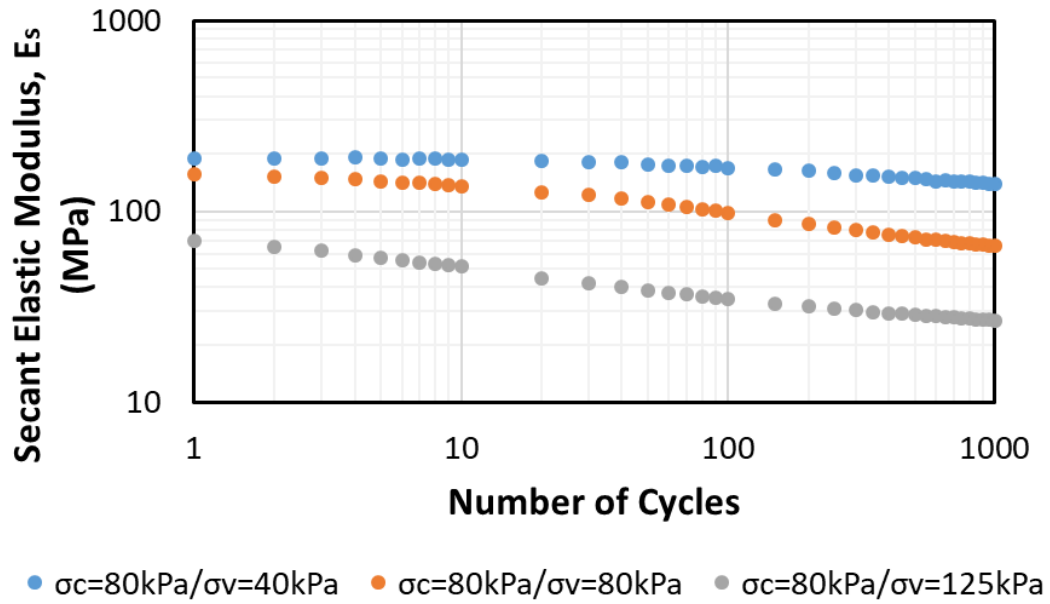
The variation of the secant elastic modulus with the number of cycles for three tests with similar confining stress and various cyclic stress ratio is depicted in Figure 5.30(a). It is observed that increasing the cyclic stress ratio decreases the magnitude of the

secant elastic modulus. For example, The secant elastic modulus at the first cycle decreased from 189 to 70 MPa for increasing the cyclic stress ratio from 9.5% to 29.8%. The reduction of the secant elastic modulus has occurred as a consequence of higher plastic axial strain in a higher cyclic stress ratio. The results also revealed the secant elastic modulus reduces with the number of cycles. This phenomenon happened as a result of the accumulation of the plastic axial strain with the number of cycles. For instance, for the test at confining pressure of 80 kPa and the cyclic stress ratio of 29.8%, the secant elastic modulus after 1000th cycles decreased from 70 to 27 MPa.

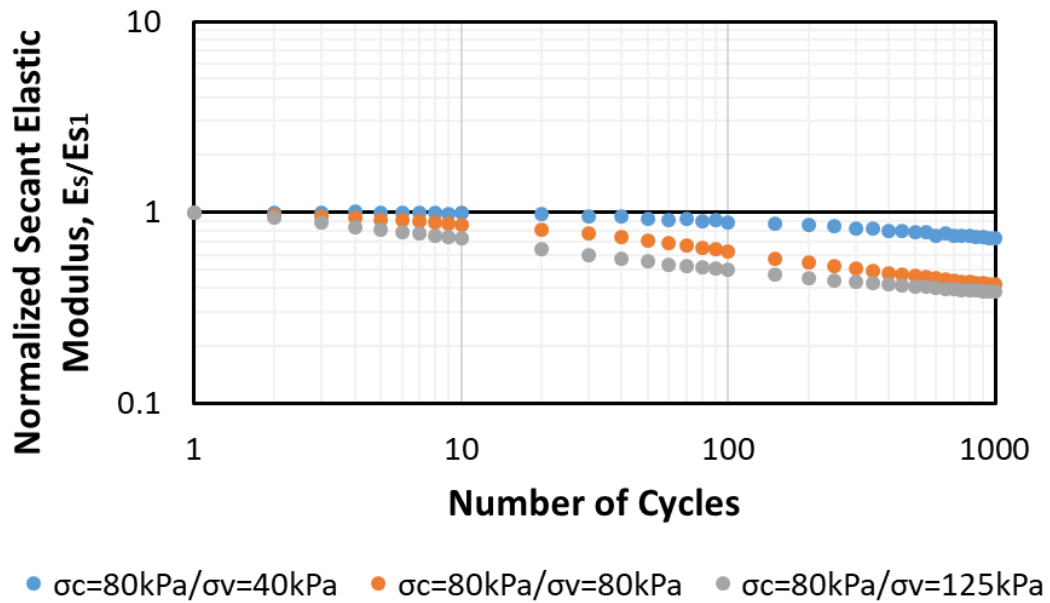
Figure 5.30(b) shows the variation of the normalized secant elastic modulus (E_s/E_{s1}) against the number of cycles. The results illustrate that the reduction rate of the secant elastic modulus was increased with the cyclic stress ratio. The reason is the plastic axial strain accumulation rate is higher in the higher cyclic stress ratio. According to the experimental results, the magnitude of the normalized after 1000th cycles are 0.73 and 0.38 for the cyclic stress ratio of 9.5% and 29.8%, consequently.

Table 5.8. Details of the TT modules

Test No.	σ_3 (kPa)	n (%)	E_{s1} (MPa)	E_{s1000} (MPa)
1	80	9.5	189	138
2	80	19.0	157	66
3	80	29.8	70	27



(a)



(b)

Figure 5.30. Development of the secant elastic modulus with the number of cycles based on cyclic TT results. (a) Secant elastic modulus; (b) Normalized secant elastic modulus

5.3.2. Empirical Models to Predict the Long-Term Behavior of the Railroad Ballast Based on Cyclic TT Results

5.3.2.1. Permanent Settlement Prediction

The main objective of the large-scale cyclic triaxial test is to develop an empirical model that can be used to predict the long term settlement of the ballast under cyclic load generated by the train passage. Analyzing the data reported by Lackenby et al. (2007) revealed that the modified version of the model proposed Neidhart (2005) can be a good representative of the experimental data. Therefore, by knowing the stress state and cyclic loading characteristics, the following equation can be used to predict the permanent shear strain of the ballast as a function of the number of cycles:

$$\varepsilon_p = \varepsilon_{p1} + \frac{A \text{Log} N}{1 + B \text{Log} N} \quad (21)$$

Where ε_{p1} is the plastic shear strain in the first cycle, N is the number of cycles, A and B are the constants influenced by the cyclic deviatoric stress characteristics, and the static peak deviatoric stress.

By knowing the axial permanent strain of ballast under cyclic loading, the settlement of the ballast layer can be measured as follow:

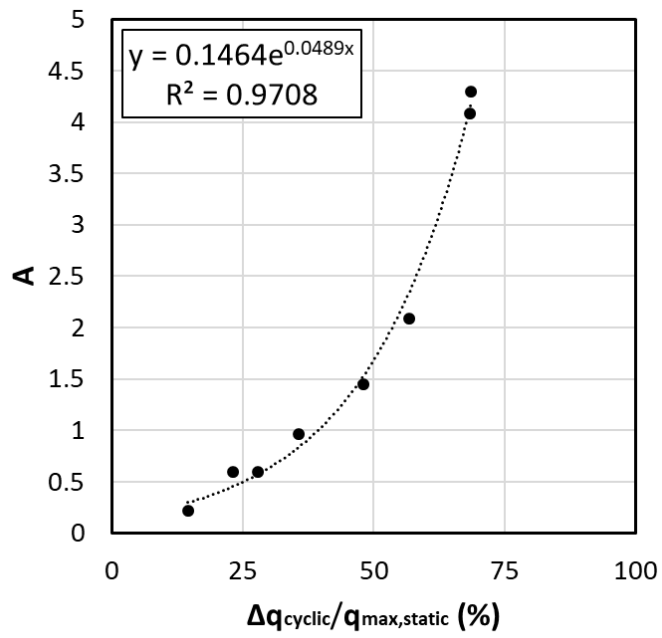
$$\delta_p = \varepsilon_p H \quad (22)$$

where ε_p is the plastic vertical strain, and H is the ballast thickness. Table 5.9 summarized the calibration of the plastic axial strain model and the values of the constants for each test. The $R^2 > 0.91$ for all the tests is indicated how accurately the proposed model can reproduce the permanent axial strain in the cyclic triaxial test. Figure 5.31 shows the

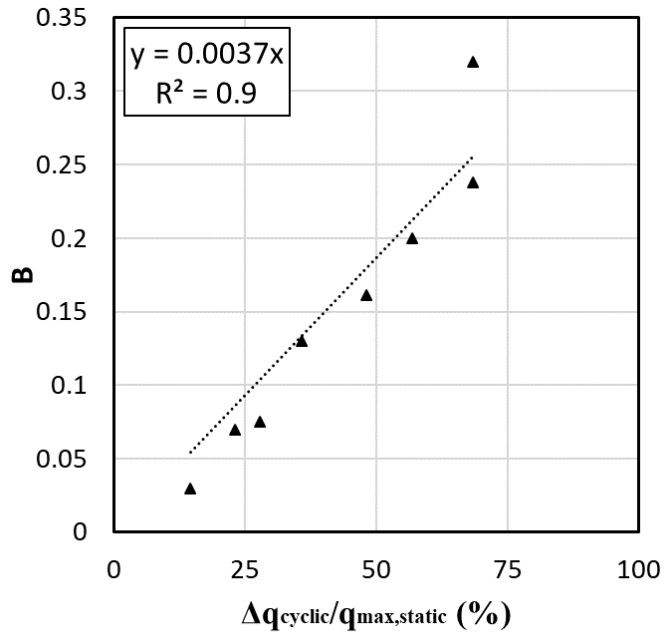
variation of the proposed model constants with the cyclic stress ratio. As is demonstrated, parameter “A” varies exponentially, and parameter “B” varies linearly with the cyclic stress ratio. These constants are based on the latite basalt material, which was used in Lackenby et al. (2007) study.

Table 5.9. Calibration of the permanent axial strain model based on the experimental results (Experimental data adopted from Lackenby et al. (2007))

Test No.	σ_3 (kPa)	Δq_{cyclic} (kPa)	$q_{peak,static}$ (kPa)	n (%)	A	B	R2
1	10	185	270	68.5	4.30	0.32	0.93
2	30	185	385	48.1	1.45	0.16	0.97
3	60	185	665	27.8	0.60	0.08	0.96
4	120	185	801	23.1	0.60	0.07	0.91
5	240	185	1274	14.5	0.22	0.03	0.92
6	60	455	665	68.4	4.08	0.24	0.96
7	120	455	801	56.8	2.09	0.20	0.97
8	240	455	1274	35.7	0.96	0.13	0.96



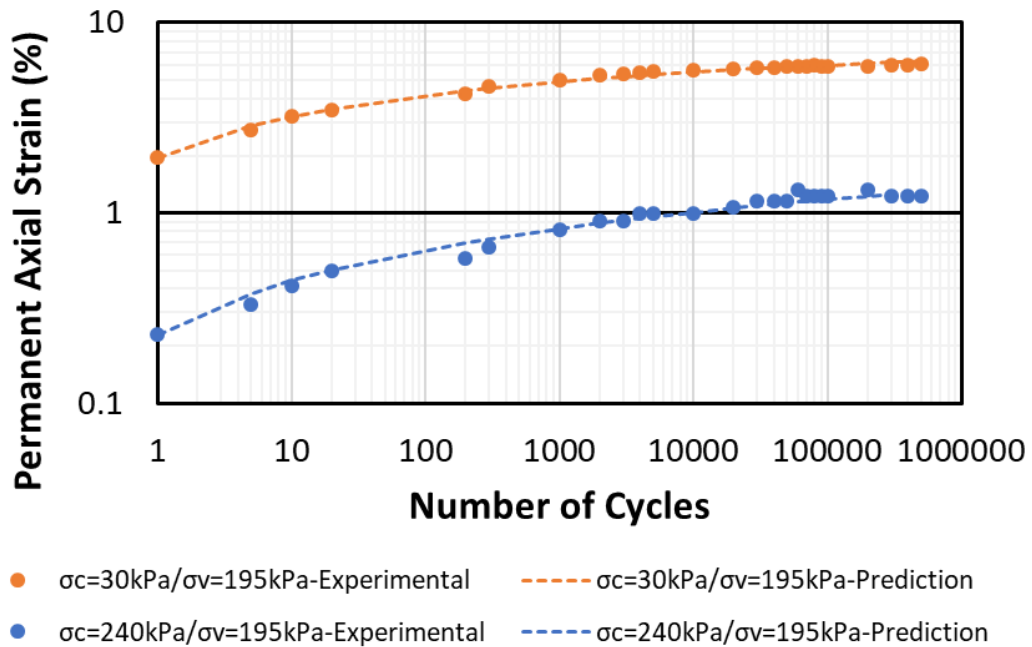
(a)



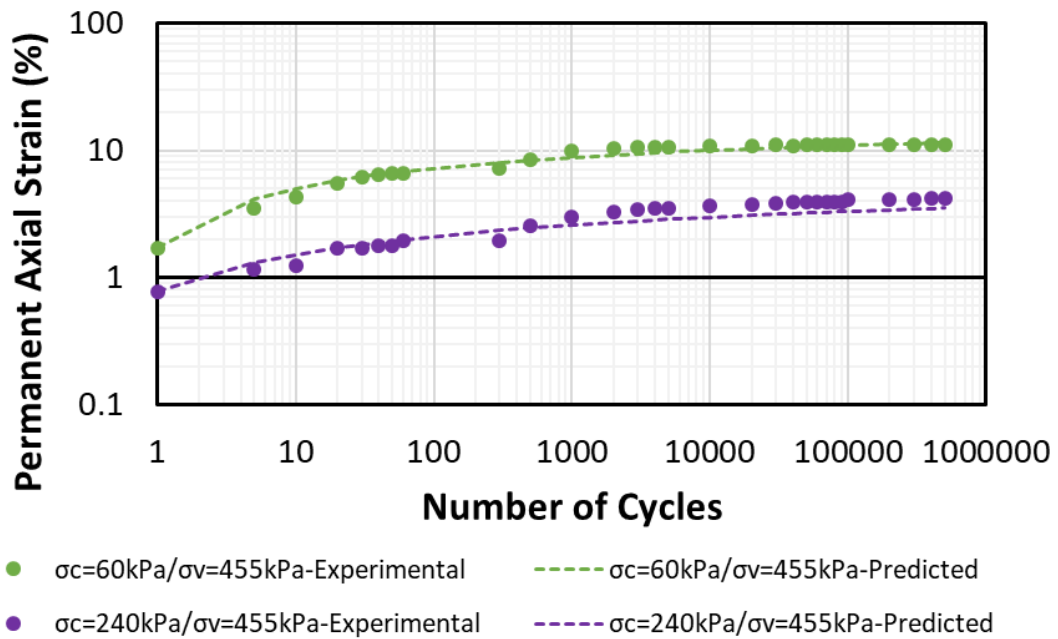
(b)

Figure 5.31. Variation of the permanent axial strain model (Equation (21)) constants with the cyclic stress ratio. (a) Parameter A; (b) Parameter B

As demonstrated by R^2 value in Table 5.9, the plastic axial strain equation can satisfactorily fit the experimental results. Figure 5.32(a) exemplifies the comparison of the model and the test results for up to 500,000 cycles. After the calculation of the model constants based on the results adopted from the Lackenby et al. (2007) study for the latite basalt, the accuracy of the model constants were checked by trying to reproduce the experimental data. Figure 5.32(b) shows the comparison between the experimental results and the model prediction. It can be observed from the results of both tests that the model can simulate the permanent axial strain very well.



(a)



(b)

Figure 5.32. Permanent axial strain prediction with the experimental data. ((a) Example of determination of the model parameters by fitting the experimental results; (b) Verification of the proposed model (Experimental data adopted from Lackenby et al. (2007))

The functionality of the permanent axial strain proposed model (Equation (22)) was further checked by trying to fit the model to the cyclic TT results performed in this study on the crushed granite ballast material. Figure 5.33 demonstrates the model verification with the experimental results. As can be seen, the model over predicts the axial strain at the beginning of the test, while the model works better in a larger number of cycles.

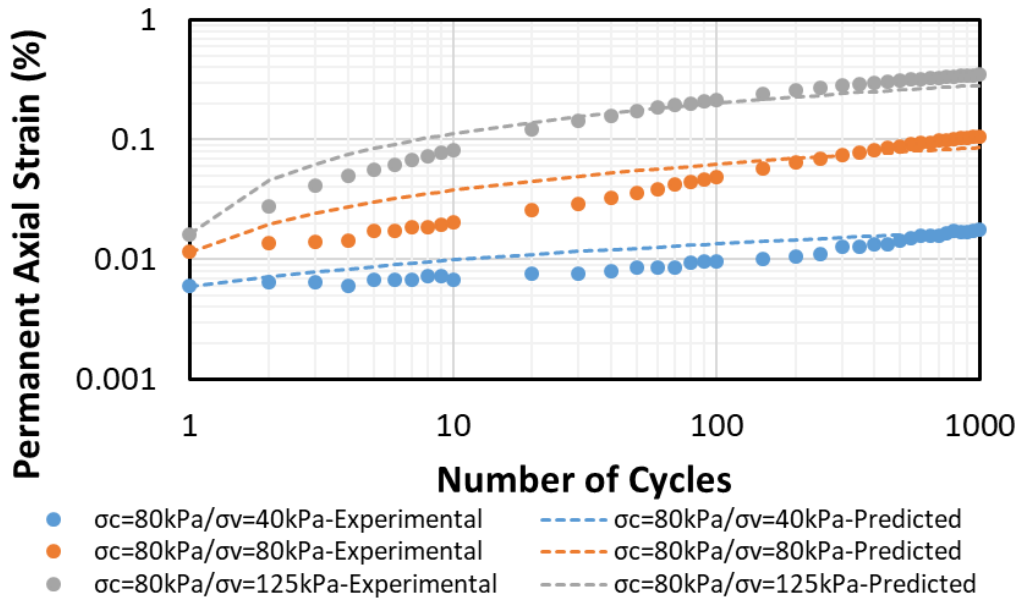


Figure 5.33. Verification of the proposed model for the axial permanent strain on the cyclic TT results on crushed granite ballast

5.3.2.2. Secant Elastic Modulus Prediction

The secant elastic modulus variation with the number of cycles is shown in equation (23) as indicated below:

$$\frac{E_s}{E_{s1}} = 1 - \frac{A \text{Log} N}{1 + B \text{Log} N} \quad (23)$$

where E_{s1} is the secant elastic modulus of the first cycle, N is the number of cycles, a , and b are the constants related to the cyclic stress ratio. The magnitude of the E_{s1} for all the three tests performed in this study was previously indicated in Table 5.8. The comparison of the secant elastic modulus model prediction with the experimental data is shown in Figure 5.34. It can be observed that the model can be a good representative of the experimental data. However, for increasing the accuracy of the model prediction, more

cyclic triaxial laboratory tests with a wider range of the cyclic stress ratio and more cycles are required.

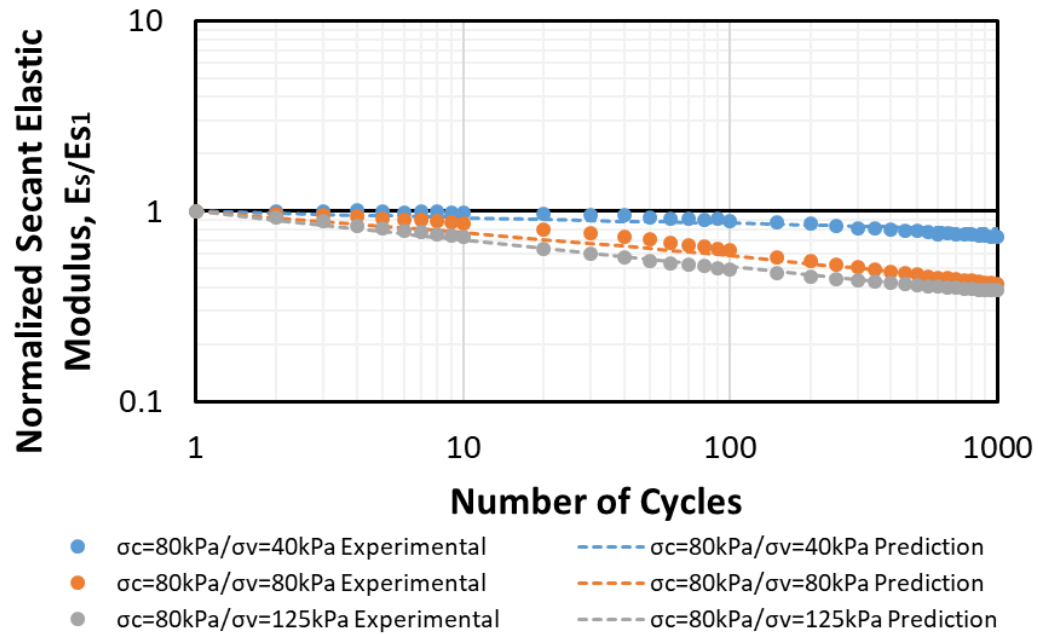
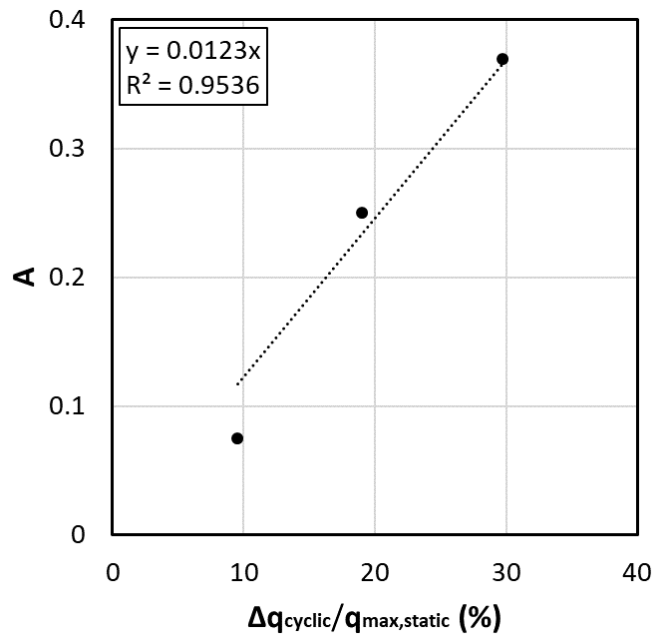
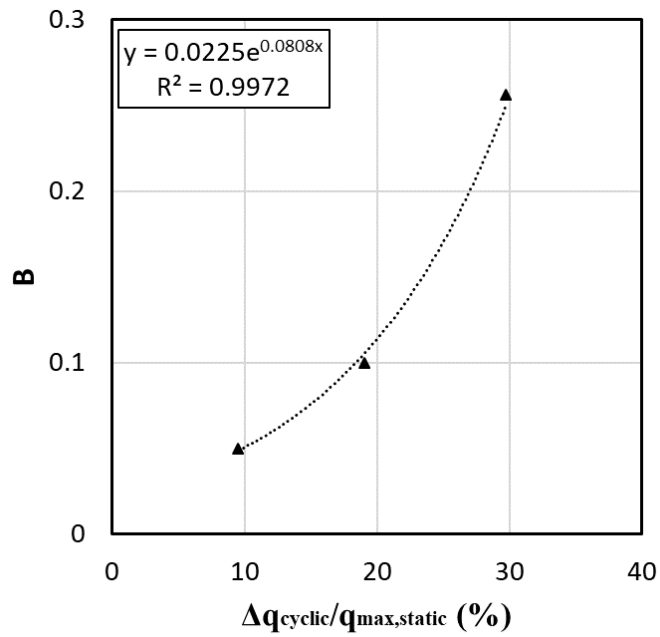


Figure 5.34. Comparison of the secant elastic modulus model prediction with the experimental data

After calibration of the proposed model for the secant shear modulus with the experimental data, it was observed that both constants a and b are proportional to the cyclic stress ratio. Figure 5.35 shows the variation of the constants a and b with the cyclic stress ratio. It is shown that the magnitude of both constants is increasing with the cyclic stress ratio.



(a)



(b)

Figure 5.35. Variation of the secant elastic modulus model (Equation (21)) constants with the cyclic stress ratio. (a) Parameter A; (b) Parameter B

6. FINITE ELEMENT ANALYSIS OF BALLASTED RAILWAY TRACK

6.1. Introduction

The long-term behavior of the ballasted track is highly dependent on cyclic stress generated in the track substructure under the operation of the high-speed and heavy freight train. Chapter 5 summarized the influence of cyclic stress magnitude on the long-term behavior of the ballast, such as permanent strain and modulus changes with the number of cycles. Therefore, a four-dimensional finite element model was developed to investigate the dynamic response of the ballasted track under the train passage. The 4D FEM model consists of a train, track, embankment, and natural subgrade. Field measurements of two different sites conducted in Sweden and Australia have been utilized to verify the reliability of the proposed numerical simulation. After verification of the numerical simulation results, the model was used for the parametric study.

This chapter starts with an introduction to the FEM software used for the numerical simulation. The methodology and model descriptions will be discussed afterward. In the next section, the FEM model verification with the field measurement in Sweden and Australia is presented. Finally, the results of the parametric study are provided. This part consists of the influence of the train characteristics (train weight and speed) and the sleeper's configuration (sleeper width and spacing).

6.2. Software Introduction (LS-DYNA)

LS-DYNA is a three-dimensional finite element method (FEM) software developed by Livermore Software Technology Corporation (LSTC). LS-DYNA is specialized in highly non-linear transient dynamic finite element analysis by using an explicit time integration method. LS-DYNA's potential application can be extended to many fields, including automobile, aerospace, manufacturing, mechanical, and civil engineering. Because of its capability in dynamic analysis, it is a suitable choice for the problems with moving vehicles and dynamic contact forces.

In the railway industry, LS-DYNA has been utilized for solving different problems such as modeling the crash impacts, dynamic analysis of the bridge, and the high-speed train critical speed (Nicks (2009), Rezaei Tafti (2018), Wilk (2017), and Lundqvist and Dahlberg (2005)). LS-DYNA is used in the current study to investigate the dynamic response of the ballasted track under the operation of a high-speed and heavy freight train. The software is chosen for the numerical simulation in this research because of the previous success of this package (Nicks (2009) and Rezaei Tafti (2018))

6.3. Finite Element Modeling of Ballasted Railway Track

In order to predict the long-term behavior of the railway ballasted track, a thorough understanding of the cyclic stress distribution due to train passage is necessary. Therefore, a four-dimensional finite element method (FEM) model with LS-DYNA was developed as a part of this study. This section describes the methodology, physical description, assumptions, and the verification of the numerical simulation.

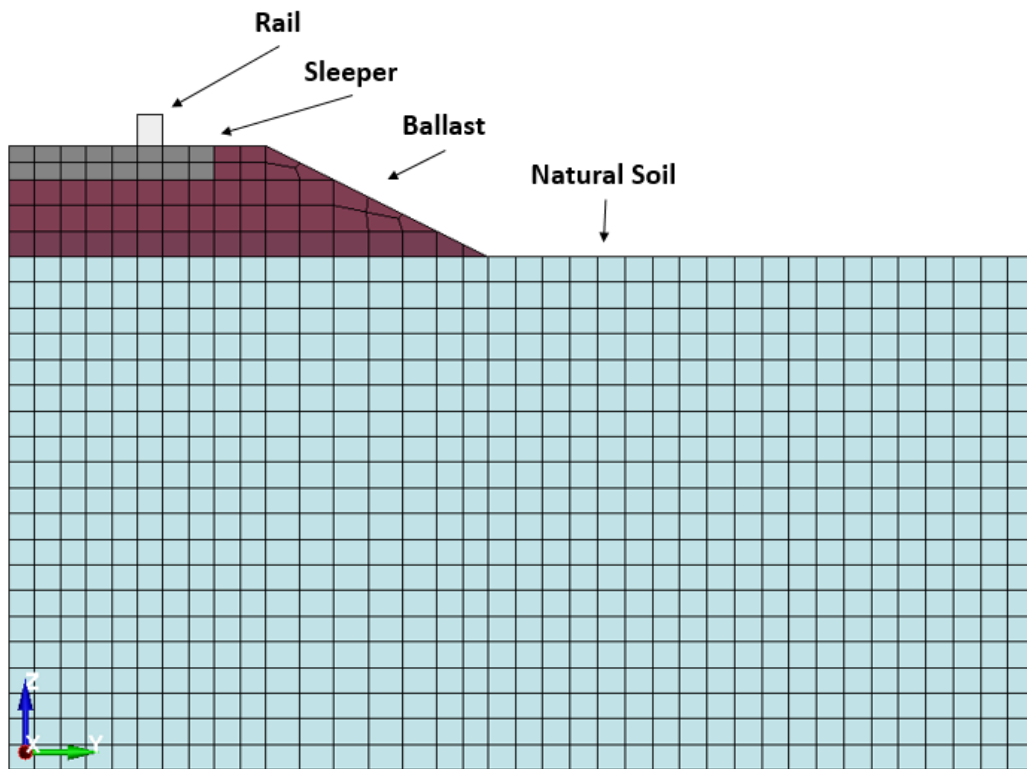
6.3.1. Railway Components Description

6.3.1.1. Track Components

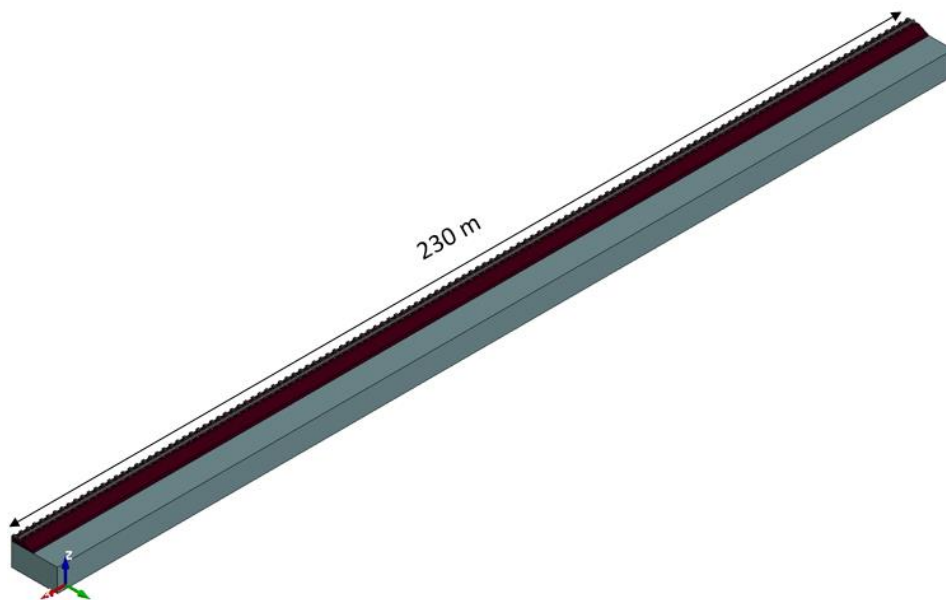
In a conventional ballasted railway track, the steel rail is placed on the concrete or wooden sleepers, which are typically spaced 600 to 800 mm intervals. The sleepers embedded into the ballast layer, which contains coarse grain material with a thickness of as low as 150 mm for the lightly trafficked lines. The ballast thickness usually increased to 500 mm for heavy traffic or high-speed trains. The ballast typically placed on the subballast layer with an average thickness of 150 mm. The slope of the embankment is 1:2.

Figure 6.1(a) depicts the perspective of the fundamental elements used for the FEM parametric study. It should be noted that the geometry of the models used for the calibration of the field results is different, which will be discussed in section 6.3.4. The subgrade dimensions are considered to be 3 m depth and 6 m wide to be sufficiently large to avoid any boundary conditions effects. The model was extended 230 m in length (Figure 6.1(b)) to ensure the convergence to the steady-state condition. It should be noted that because of the symmetrical condition of the railway track, only half of the model from the track centerline was simulated in the current research.

Figure 6.2 shows the configuration of the railroad ties. The sleepers modeled as a rectangular prism with dimensions of 300 mm \times 200 mm \times 1200 mm with a spacing of 600 mm. The rail is modeled as a continuously welded rectangle with dimensions of 150 mm \times 180 mm. The sleepers, rail, and substructures components (ballast, subballast, and subgrade) are modeled as solid elements.



(a)



(b)

Figure 6.1. Overview of the FEM model. (a) Cross-section; (b) Side view

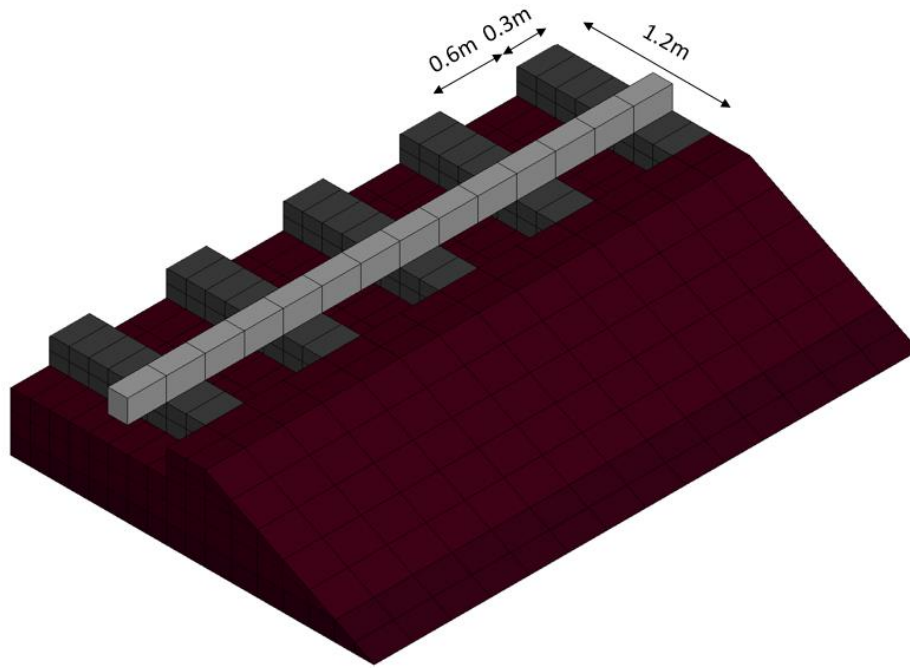


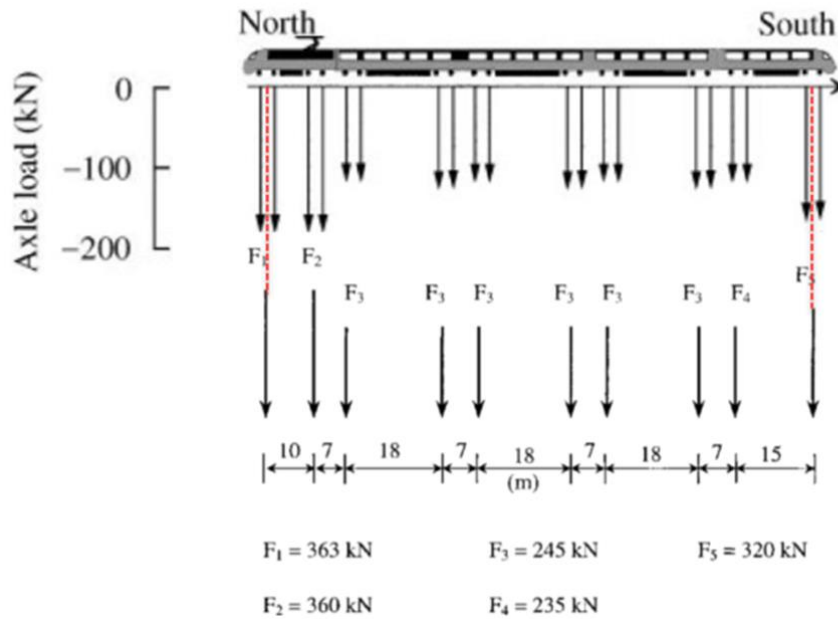
Figure 6.2. Sleeper's dimensions and spacing

6.3.1.2. Train

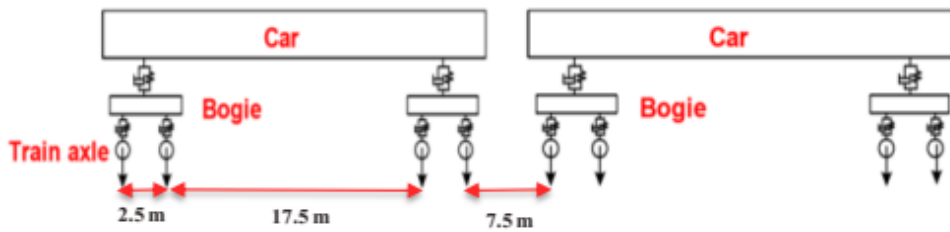
In the numerical simulation presented in this study, the train modeled as a series of wheels with rigid and solid elements moves along the rail. The wheels are moving with a constant velocity, which is representative of the train speed. A concentrated load applied at the center of the wheel that simulates the train axle load. As shown in Figure 6.3, two types of trains were modeled in this study. The first train model is X2000 that used for the validation of the field measurement in the Ledsgard site located in Sweden (Madshus and Kaynia (2000)).

The second train model was used for the calibration of the field measurement at Bulli, New South Wales, Australia, is shown in Figure 6.3(b). Because there is no information provided about the train wheels spacing operated in the abovementioned site,

the typical axle spacing of two train wagons (Rezaei Tafti (2018)) was used for this case study. However, the axle loads are based on the information provided in Indraratna et al. (2010) report. A similar train model was used for the parametric study.



(a)



(b)

Figure 6.3. Train specification used for model validation. (a) X2000 train (after Madshus and Kaynia (2000)); (b) Two wagons of a train (after Rezaei Tafti (2018))

6.3.2. Material Model and Properties

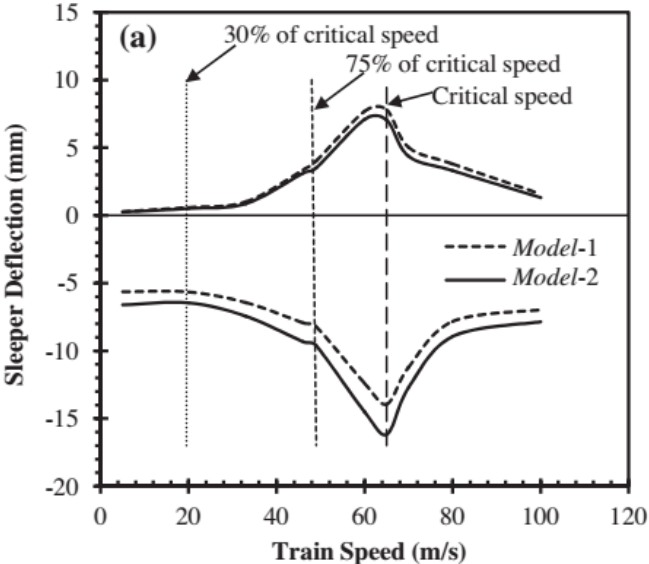
The constitutive model and the material parameters used for the wheel, rail, and sleeper materials are listed in Table 6.1. The wheels considered to be rigid material and rail and sleepers modeled as a linear elastic material. The material parameters of rail and wheels are considered to be a representative of steel material. The sleepers are modeled as reinforced concrete material. The properties of wheels, rail, and sleepers are similar for all the numerical models presented in this study.

Table 6.1. Superstructure components constitutive model and material properties used in the FEM models

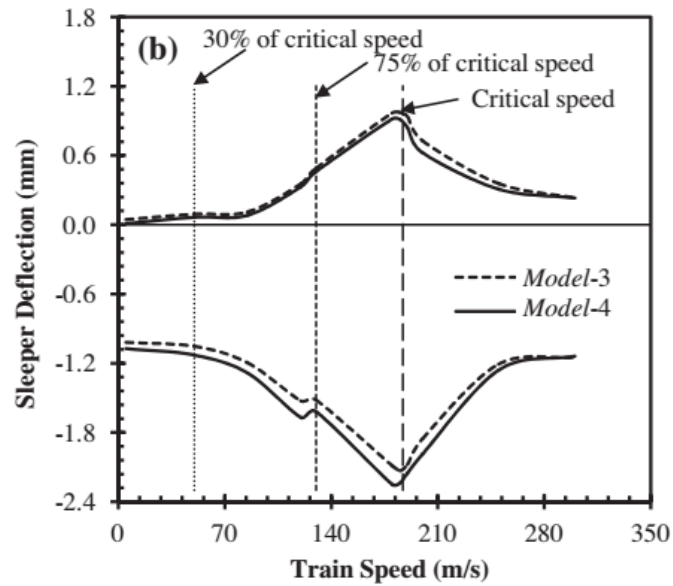
Component	Material Model	Elasticity Modulus, E (MPa)	Unit Weight, ρ (kg/m³)	Poisson's Ratio, ν
Wheel	Rigid	210,000	7950	0.25
Rail	Linear Elastic	210,000	7950	0.25
Sleeper	Linear Elastic	100,000	2440	0.15

The challenging part of the FEM modeling is to consider a constitutive model for the soil materials. Several studies can be found in the literature that investigates the influence of soil non-linearity on the railway track behavior. Sayeed and Shahin (2016) performed a 3D FEM numerical simulation to evaluate the impact of soil non-linearity on the dynamic response of high-speed rail. They modeled two different subgrades (soft soil and stiff soil) with two different material models (linear and non-linear). The elastoplastic Mohr-Coulomb (MC) and hyperbolic Duncan-Chang (DC) (Duncan and Chang (1970)) models were employed to show the non-linearity of the materials.

Figure 6.4 shows the influence of the soil non-linearity on the track deflection at different train speeds. It can be observed that the models with considering non-linear soil constitutive model show approximately the same upward movement and small higher downward movement. Comparing the subgrade stiffness revealed that the impact of soil non-linearity is more pronounced in the soft subgrade.



(a)



(b)

Figure 6.4. The influence of the soil non-linearity on the track deflection. (a) Soft subgrade; (b) stiff subgrade (after Sayeed and Shahin (2016))

Varandas et al. (2016) studied the influence of non-linearity of the ballast layer on the dynamic analysis of the railway under high-speed train loading. They used the linear elastic model for all the materials except the ballast that modeled with $k-\theta$ modeled developed by Brown and Pell (1967). Figure 6.5 shows the influence of ballast non-linearity on the track deflection in different train speeds (220, 320, 350 kph). They concluded that the influence of ballast non-linearity is only noticeable when the train speed approaches the track critical velocity. However, according to their results the downward displacement at 350 kph speed (86% of critical speed) is only 7% higher in the case of assuming non-linear behavior for the ballast.

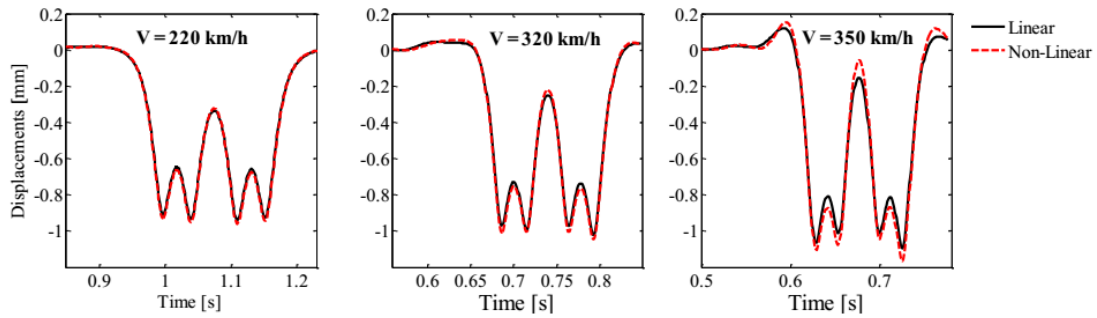


Figure 6.5. Comparison of the linear elastic and non-linear elastic behavior of ballast on the track deflection in different train speed (after Varandas et al. (2016))

Banimahd (2008) tried to study the influence of soil non-linearity on the track deflection and vertical stress acting on the ballast and subgrade at different train speeds. The comparison has been made for two train speeds equal to 108 and 252 kph. Figure 6.6 shows the influence of non-linearity at train speed of 108 kph. It is shown that both models respond similarly in terms of sleeper vertical displacement and vertical pressure acting on both subgrade and ballast due to the train passage. Figure 6.7 illustrates the similar results for the train velocity of 252 kph. Comparing the vertical stress acting on the ballast and subgrade showed that the magnitude of the dynamic vertical stress generated by the train is slightly altered by assuming the soil's non-linearity. However, the sleeper vertical displacement increased by approximately 15% in non-linear condition.

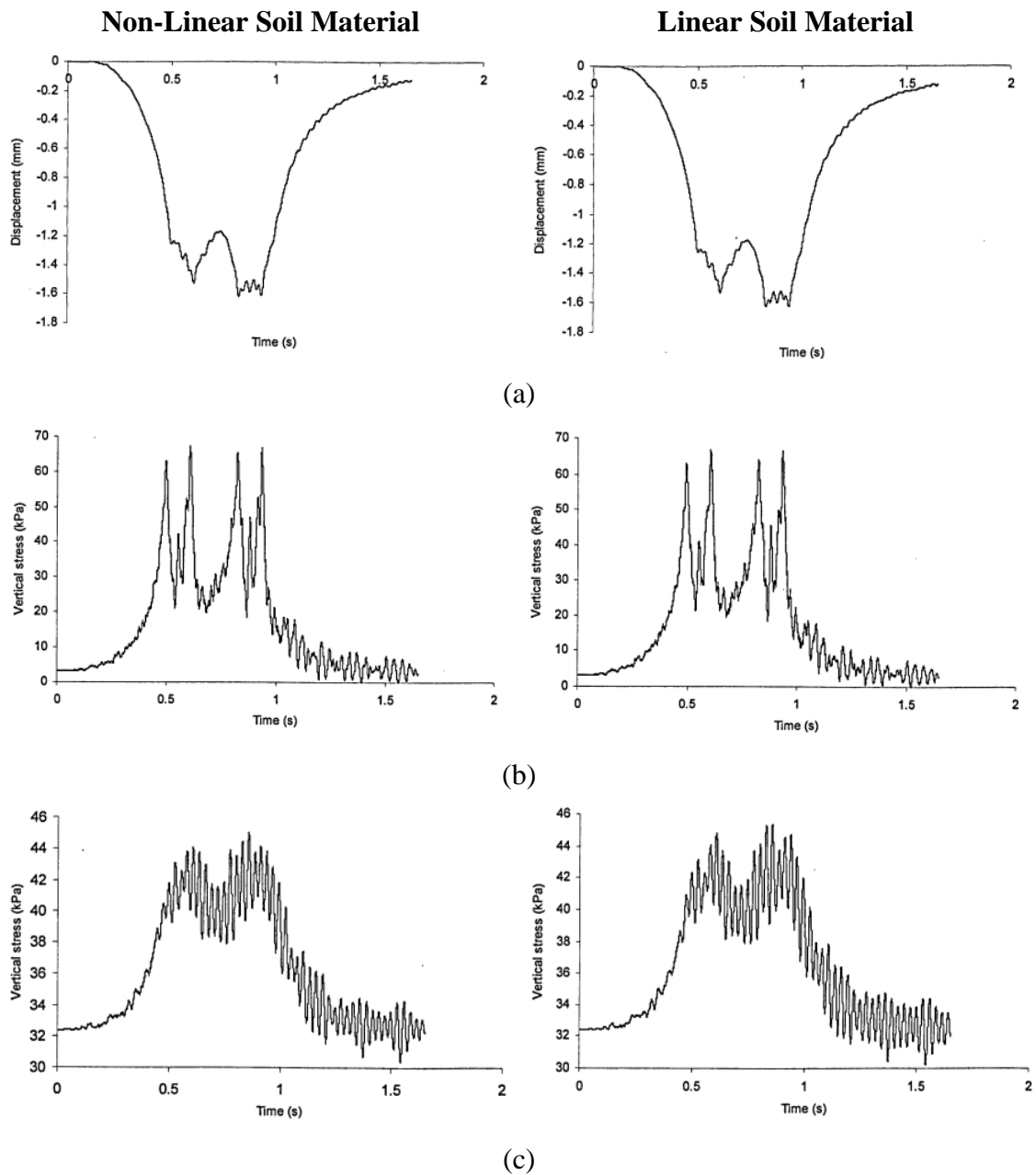


Figure 6.6. Influence of soil non-linearity on the response of railway track at train speed equal to 108 kph. (a) Sleeper displacement; (b) vertical stress on top of the ballast; (c) vertical stress on top of the subgrade (after Banimahd (2008))

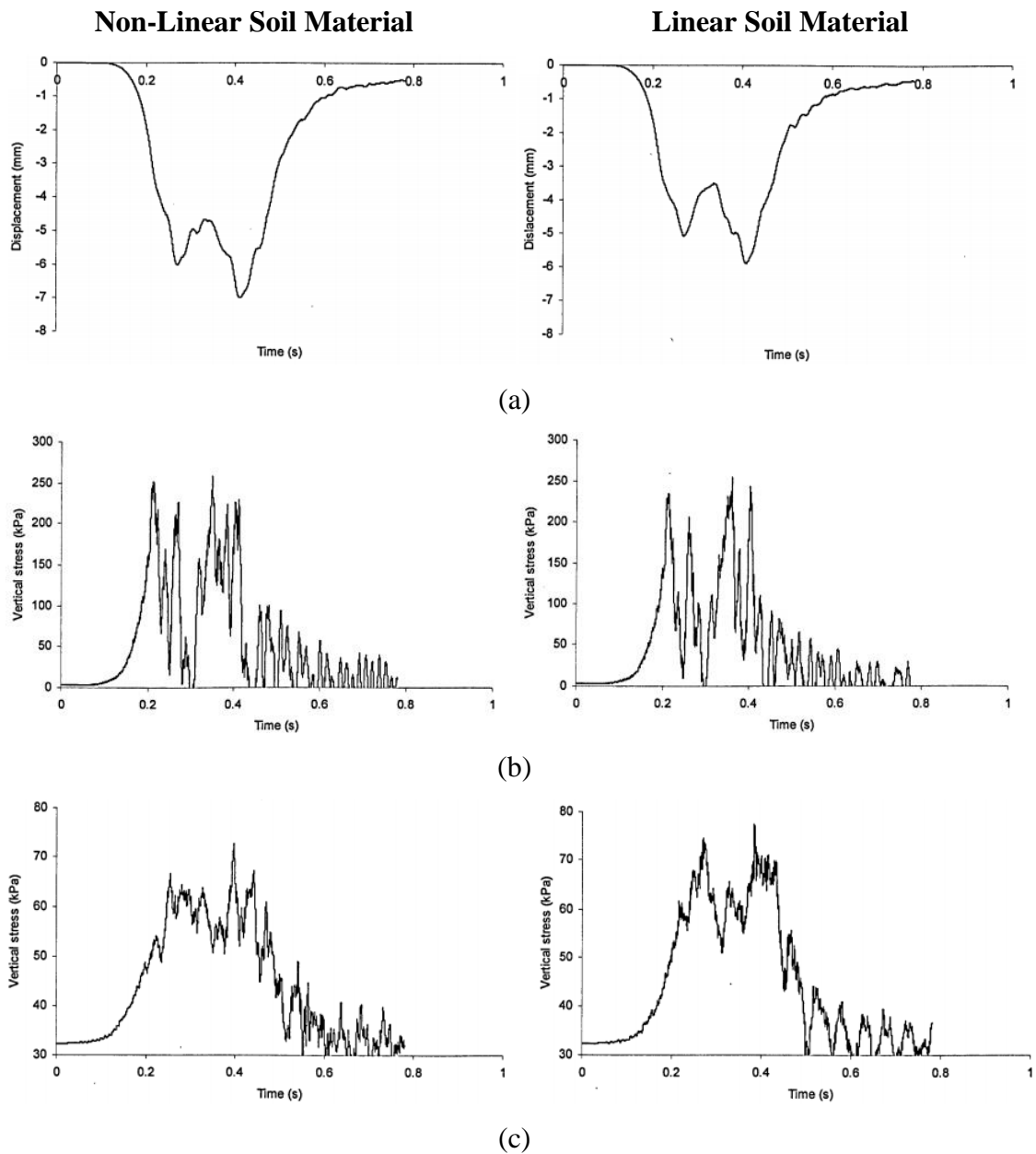


Figure 6.7. Influence of soil non-linearity on the response of railway track at train speed equal to 252 kph. (a) Sleeper displacement; (b) vertical stress on top of the ballast; (c) vertical stress on top of the subgrade (after Banimahd (2008))

In reality, soil material does not behave perfectly elastic, and the response of all different types of soil materials composed of elastic and plastic components. However, the

portion of the plasticity is different depending on the soil type and the loading conditions. As shown in chapter 5 for the cyclic laboratory tests, the strain is composed of elastic (recoverable) and plastic (irrecoverable) components. The same trend is expected in the field for the track settlement under the train passage. According to the results of the abovementioned study, it can be observed that although assuming the soil non-linearity can affect the results, the impact is not significant. In other words, although the soil material does not behave entirely elastic under the train passage, the magnitude of non-linearity is not substantial in short-term train operation. However, the accumulation of the plastic settlement in the long-term is considerable. Various finite FEM studies in modeling the railway tracks are available in the literature that assumed elastic properties for the soil material (Lundqvist and Dahlberg (2005), Wilk (2017), Rezaei Tafti (2018), Nicks (2009), Wang and Markine (2018), Connolly et al. (2013), Yang et al. (2009), and Powrie et al. (2007)).

A practical method to incorporate the effect of soil non-linearity is the “equivalent linear” approach. In this approach, the influence of the soil non-linearity is considered by reducing the modulus in a higher strain. This method was previously used for the application of the railway ballast by Madshus and Kaynia (2000), Kaynia et al. (2000), and Shih et al. (2017).

Therefore, in the current research with respect to the results of the previous study on the impact of soil non-linearity and to simplify the problem, the linear elastic model was assumed for the soil materials. The FEM study presented in this study includes the dynamic aspects of the train loading on the elastic soil. Moreover, in order to predict the

long-term settlement of ballast under the application of one million cycles, the elastic FEM results together with the secant modulus model with the number of cycles can be used.

6.3.3. Boundary Conditions

Applying the proper boundary conditions is an essential aspect of the FEM numerical simulation that has a significant impact on the results. Figure 6.8 illustrates the boundary conditions implemented in the FEM model. Pin supports are applied to the bottom of the model that restricts the movement in all three directions. The pin support is used to represent the bedrock location. The second type of boundary condition is roller support that applied to the sides of the model, which allows for the vertical movement and only restricts the horizontal movement in the y-direction.

To avoid the reflection of the generated wave due to the train passage back to the finite element mesh non-reflecting boundary condition (NRBC) was applied in all three directions. These type of boundary condition would absorb the energy of stress waves at the boundaries and prevent from re-entering to the model.

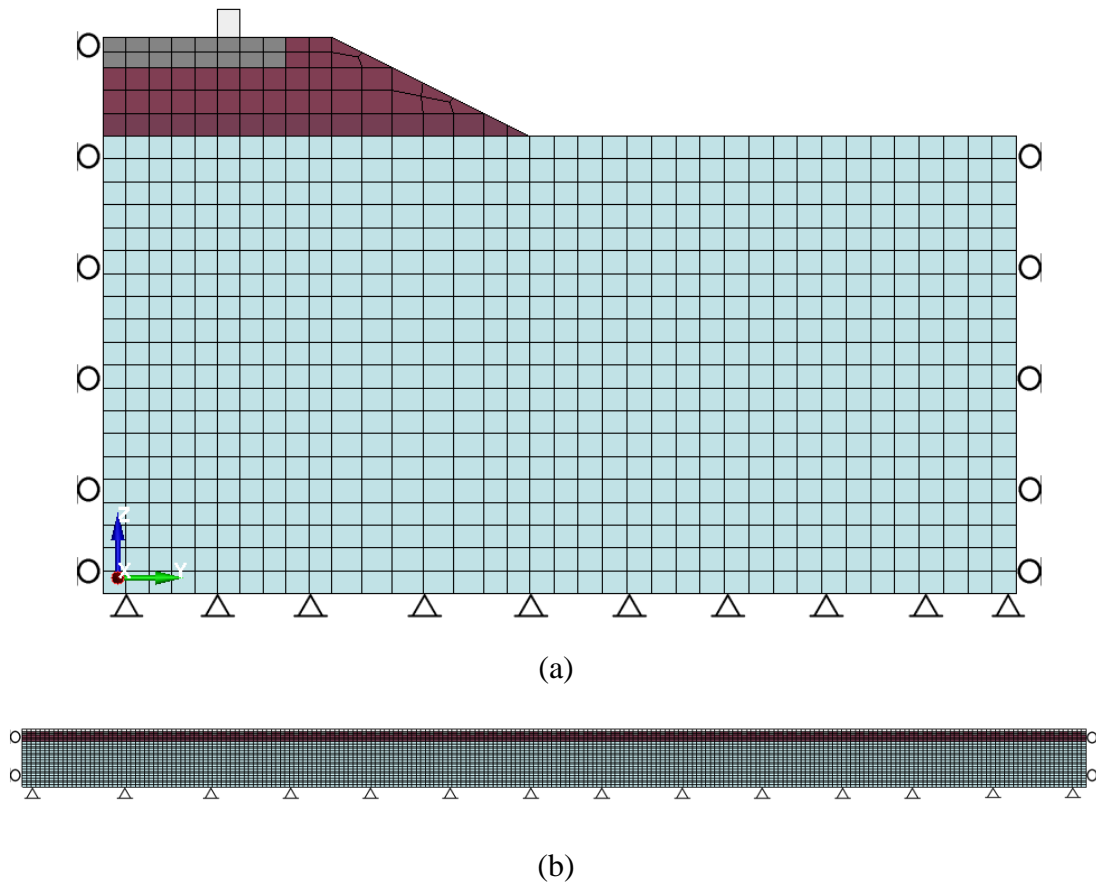


Figure 6.8. Boundary Conditions. (a) Transverse view; (b) Longitudinal view

6.3.4. Train-Track Interaction

The contact force between the two sliding elements during the train movement (e.g., the outer surface of the wheel and the rail) is calculated by the penalty method (Hallquist (2006)). This feature is defined as “Surface-To-Surface” contact in LS-DYNA. In this approach, the outer wheel surface is defined as the slave surface, and the top outer surface of the rail serves a master surface. In this type of contact, if the slave surface penetrates the mater surface, normal interface springs will be placed at the interface by the penalty algorithm and prevent the penetration (Hallquist (2006)).

The amount of static and dynamic coefficient of friction is 0.4 and 0.3, respectively. These assumptions are in line with the previous railway numerical simulation in LS-DYNA performed by Nicks (2009) and Rezaei Tafti (2018).

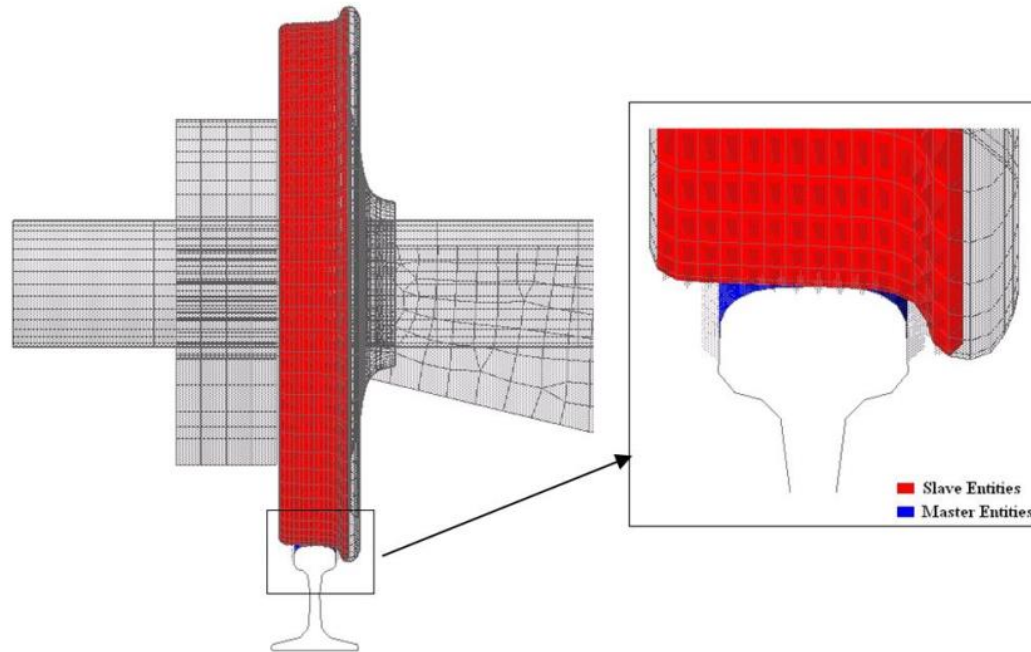


Figure 6.9. Wheel/rail contact surface (after Nicks (2009))

6.4. Model Verification

In order to evaluate the accuracy of the FEM modeling of this study by using LS-DYNA, the model was validated against the results of two well-established field measurements in the literature. The first case study is the high-speed rail on soft subgrade at the Ledsgard site in Sweden (Adolfsson et al. (1999)). The primary reason for using this site as a case study is the availability of the details about all the track and substructure components as well as track displacement measurements at different train speeds. The second case study used for the validation of the numerical simulation is the instrumented

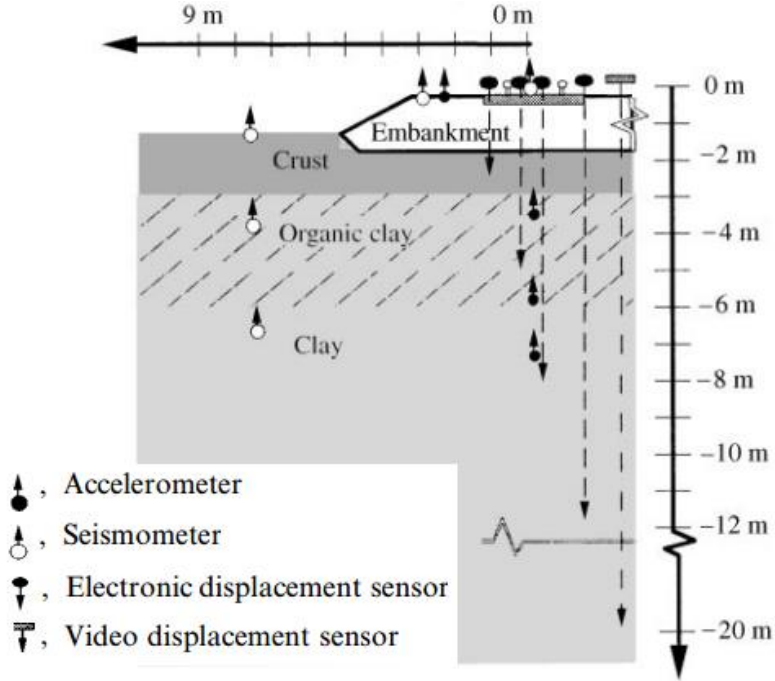
track at Bulli, New South Wales, Australia (Indraratna et al. (2010)). The importance of this case study is that it places between the very limited field trial that measured the cyclic stress generated in the track substructure due to the train passage. This field measurement also contains the data about the long-term settlement of the track with the number of cycles.

6.4.1. High-Speed Railway Track at Ledsgard, Sweden

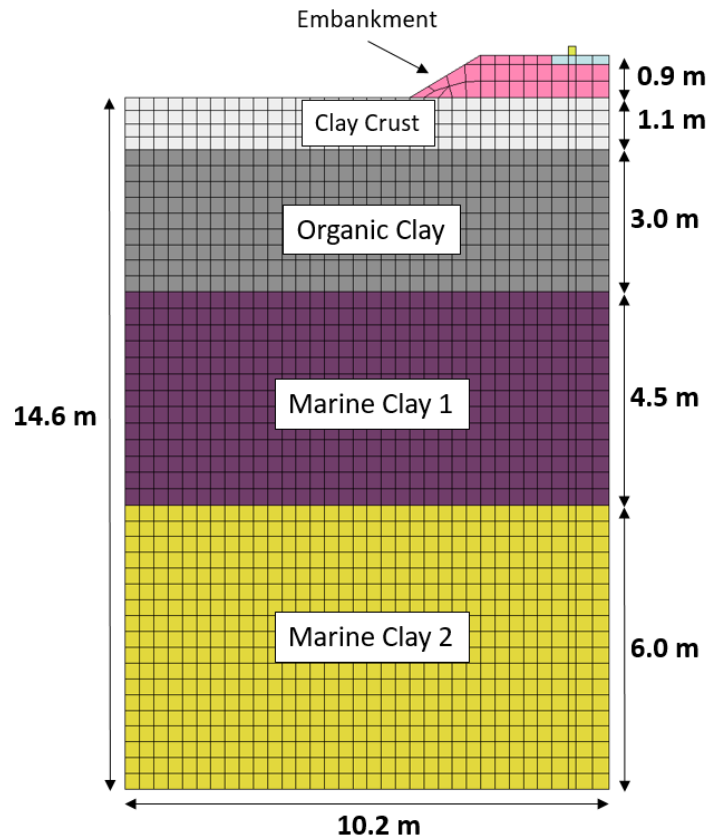
A significant dynamic amplification and the track settlement was recorded at the Ledsgard site due to the operation of the operation speed of the X2000 to 200 kph. The track was built on the layer of soft clay material. This phenomenon that is related to the approaching the train speed to the Rayleigh wave velocity the soil profile is known as “critical speed” (Woldringh and New (1999) and Madshus and Kaynia (2000)). As a result of extensive measurement of the train characteristics and the track response, this case study was used as a benchmark of various numerical simulation (Madshus and Kaynia (2000), Kaynia et al. (2000), Hall (2003), Holm et al. (2002), Banimahd (2008), Sayeed and Shahin (2016), Rezaei Tafti (2018)).

Figure 6.10(a) displays the cross-section of the track geometry and the location of the instrumentations that installed in the field. The embankment is placed on top of the natural ground with three main layers. These layers are including weathered crust with a thickness of 1.1 m placed over 3.0 m thick layer made of very soft organic clay over soft marine clays. Track superstructure components are including UIC60 steel rail placed over concrete sleepers with a spacing of 67 cm. A vehicle used in this study is an X-2000

passenger train with four wagons. Details about the train axle spacing and loads are provided in Figure 6.3(a).



(a)



(b)

Figure 6.10. The geometry of the HST railway track at the Ledsgard site. (a) Field cross-section (after Madshus and Kaynia (2000)); (b) FEM model

Thorough field investigations were performed to enable to soil classification and understand the essential soil parameters (Madshus and Kaynia (2000)). The testing program was included in different in situ tests (cross-hole, downhole, SASW (Spectral Analysis of Surface Waves)) and the laboratory test (cyclic triaxial test). Figure 6.11 shows the variation of the soil parameters with the depth underneath the rail. The solid line represents the initial soil properties at the site that measured from the soil in situ

testing. Therefore, the values corresponding to the solid line shows the small strain properties of the material.

On the other hand, the dashed line in Figure 6.11 represents the soil properties in larger strain induced by train. These values were approximated by the reduced secant shear modulus in comparison to the lower strain of the in situ tests. The reduced properties were estimated by using the cyclic triaxial test and the measured track displacement due to the train passage.

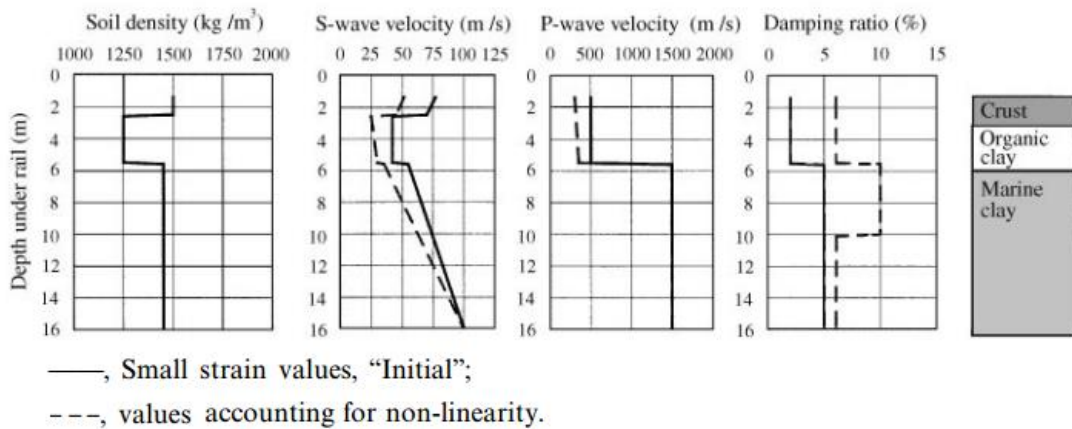


Figure 6.11. Dynamic soil properties at the Ledsgard site (after Madshus and Kaynia (2000))

Table 6.2 shows the detail of the soil properties used in the FEM study based on the information about the shear wave velocity and the density of the soil material provided in Kaynia et al. (2000) report. The Poisson's ratio of the soil materials was assumed to be 0.35. The shear modulus (G) and Elasticity modulus (E) were calculated according to the following equations:

$$V_s = \sqrt{\frac{G}{\rho}} \quad (24)$$

$$G = \frac{E}{2(1+\nu)} \quad (25)$$

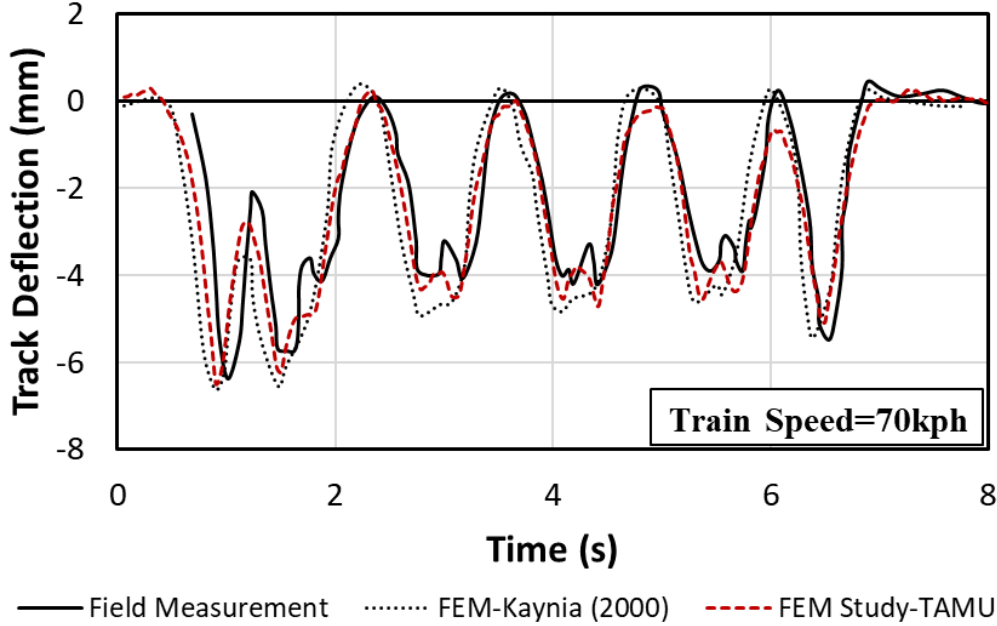
where V_s is shear wave velocity, ν is Poisson's ratio.

Table 6.2. Material properties of the Ledsgard site adopted in the FEM study (data adopted from Kaynia et al. (2000))

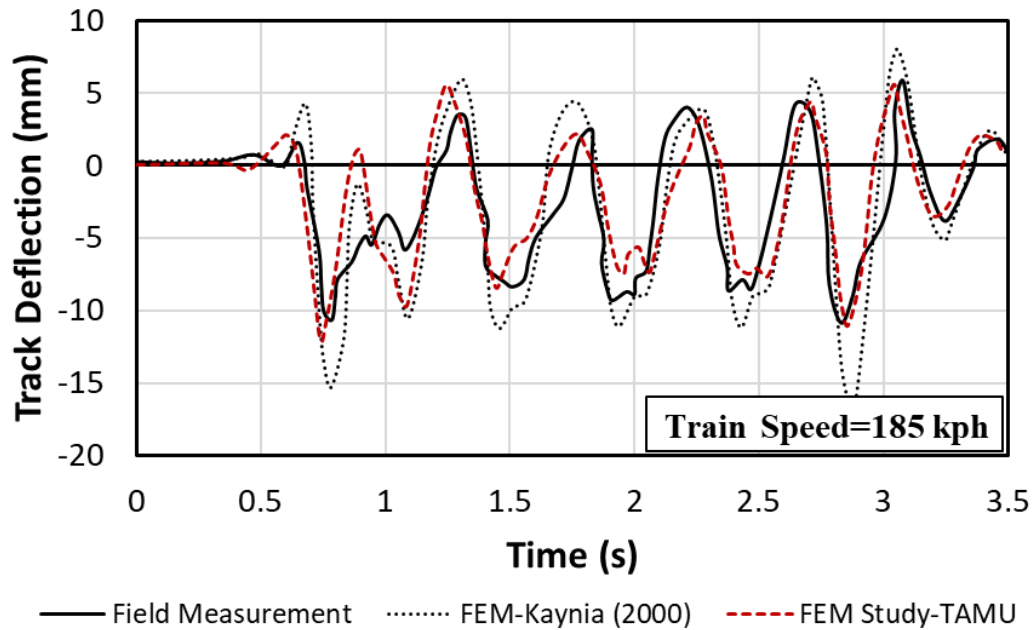
Components	Thickness (m)	ρ (kg/m ³)	ν	V_s (m/s)	G (MPa)	E (MPa)
Embankment	0.9	1800	0.35	160	44.0	120.0
Clay Crust	1.1	1500	0.35	63	6.0	16.2
Organic Clay	3	1250	0.35	33	1.3	3.6
Marine Clay 1	4.5	1475	0.35	58	5.0	13.4
Marine Clay 2	6	1475	0.35	84	10.5	28.4

Figure 6.12 shows the comparison of the field measurement of track deflection under the X-2000 train passage and the numerical simulation performed in this study and performed by Madshus and Kaynia (2000). The comparison has been made for the train velocity equal to 70 and 185 kph. The downward movement was presented in a negative sign, while the upward values are positive. As shown in Figure 6.12(a), for low train velocity (e.g., 70 kph), the track deflection is only downward (quasi-static deflection). However, in higher train velocity and approaching the critical speed (e.g., 185 kph), the track displacement is in both upward and downward directions (oscillatory response). As

depicted in Figure 6.12, the FEM simulation in the current study can simulate the field measurement with reasonable accuracy on both train speeds.



(a)



(b)

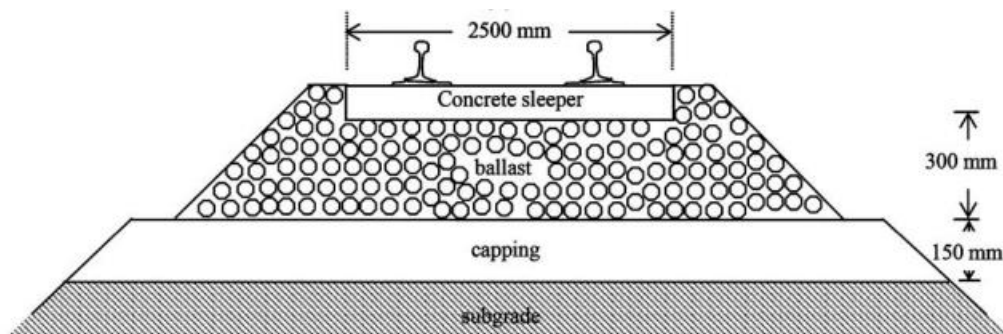
Figure 6.12. Comparison of the track vertical displacement (after Madshus and Kaynia (2000)) versus the FEM prediction. (a) train speed of 70 kph; (b) train speed of 185 kph

6.4.2. Ballasted Railway Track at Bulli, Australia

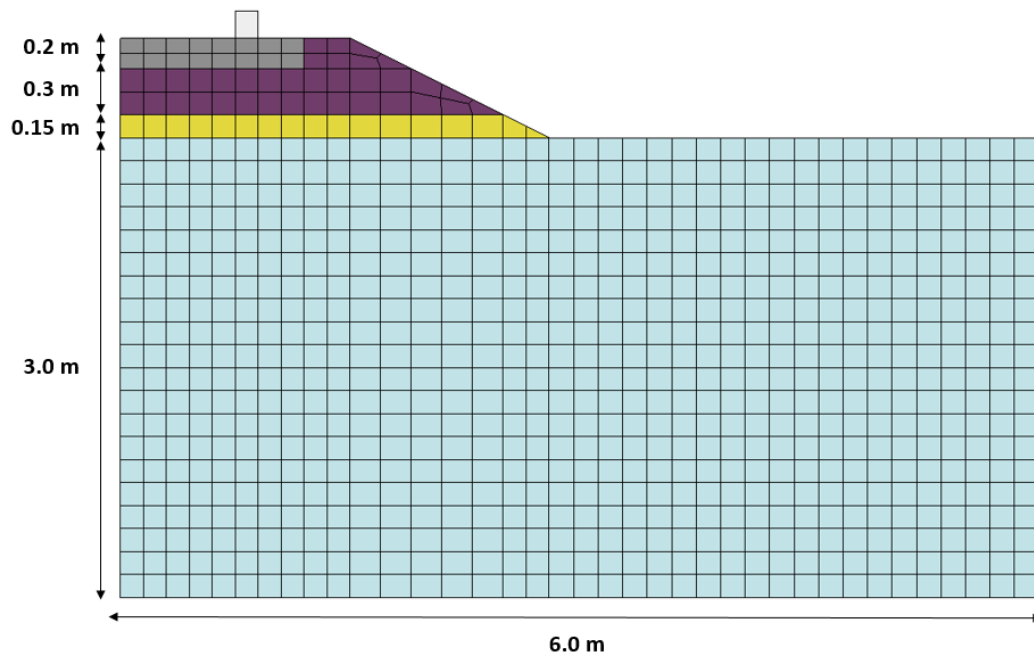
Understanding the mechanism of stress generation and transfer in the track substructure is a critical factor that affects the long-term behavior of the track. This case study has been chosen for the FEM model validation because it contains the measurement of the cyclic stress in the ballast and sub-ballast layers under passenger and freight train operation. The track is located in Bulli, New South Wales, Australia. The information presented in this section, which is used in the numerical simulation is related to measurement In the section with fresh ballast.

Figure 6.13(a) demonstrates the geometry of the track (Indraratna et al. (2010)). The embankment thickness is 450 mm, which contains a 300 mm ballast placed over a 150 mm sub-ballast layer. The ballast material is a coarse aggregate crushed latite basalt, and the sub-ballast material is a sand-gravel mixture. The embankment is constructed on top of a natural subgrade. Based on the results of a series of test peats and CPT tests performed at the site, the subgrade material classified as silty clay with shale cobbles and gravels. Regarding the high values of the electrical friction cone penetrometer test (EFCP), the subgrade was classified as a stiff, over consolidated material. The highly weathered sandstone bedrock found at approximately 2.3 m below the sub-ballast layer (Choudhury (2006)).

Figure 6.13(b) shows the geometry of the track that is used in the FEM study. Due to the symmetry of the track profile, only half of the track is simulated. The details about the model profile dimensions are in line with the Indraratna et al. (2012) 2D FEM study. The properties of each soil material are provided in Table 6.3. It should be noted that the elastic properties were driven from the data available about the Bulli site at Indraratna et al. (2012) and Jiang and Nimbalkar (2019) reports.



(a)



(b)

Figure 6.13. The geometry of the ballasted railway track at Bulli, Australia. (a) Cross-section (after Indraratna et al. (2010)); (b) FEM study

Table 6.3. Material properties of the Bulli site adopted in the FEM study (data adopted from Indraratna et al. (2012) and Jiang and Nimbalkar (2019))

Components	Thickness (m)	ρ (kg/m ³)	ν	G (MPa)	E (MPa)
Ballast	0.3	1590	0.35	37	100
Sub-ballast	0.15	1700	0.35	30	80
Subgrade	3	1250	0.35	12	31

Figure 6.14 shows the location of the instrumentations installed at the site. As shown in Figure 6.14(a), two series of displacement transducers and settlement peg were installed in the ballast layer to capture the permanent track deformation. In addition, a series of pressure cells were installed with vertical and horizontal orientation in different spots of both ballast and sub-ballast layer to capture the cyclic vertical and horizontal stress generated by the train passage. Therefore, the cyclic shear stress within the ballast and the cyclic vertical stress acting on the ballast, sub-ballast, and subgrade surface can be measured.

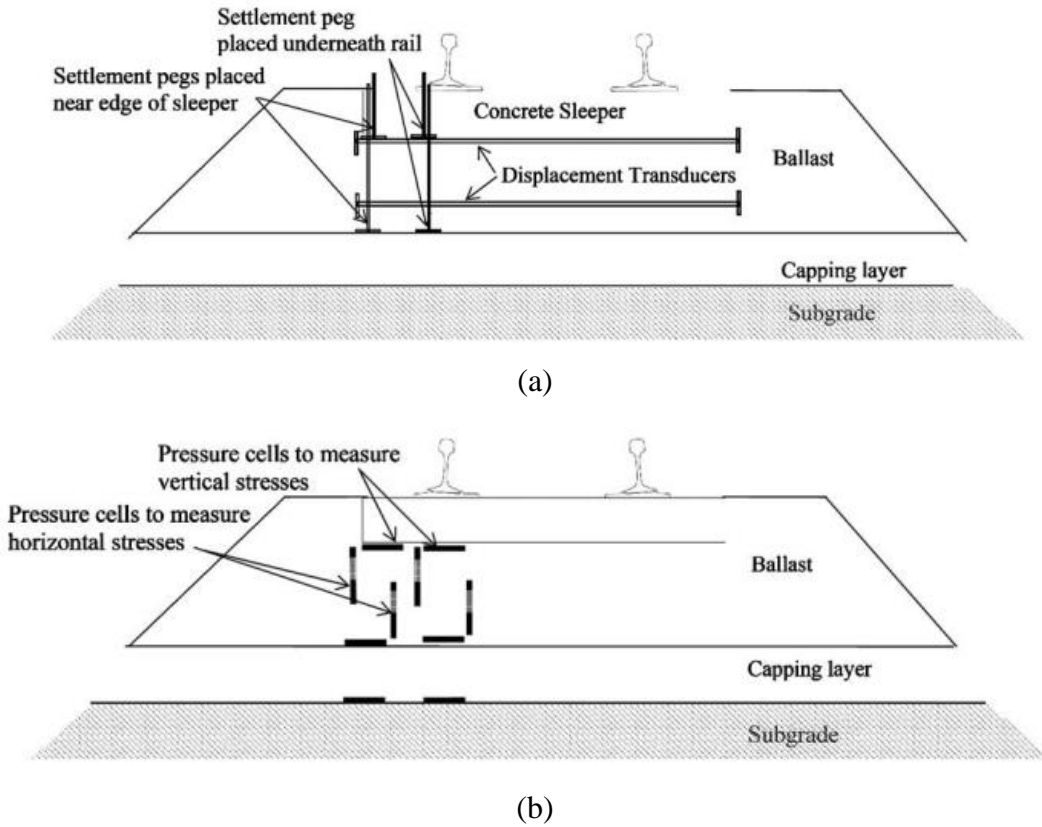


Figure 6.14. Schematic diagram of the location of the instrumentations. (a) Displacement transducers; (b) Pressure cells (after Indraratna et al. (2010))

Measurements were taken for the operation of a passenger and a freight train. However, only the data regarding the freight train operation was used for the purpose of the FEM model validation. The only information available about the freight train is that the weight of the wagons is 100 tons. For simplifying the numerical simulation, two wagons of the regular freight train with the axle load of 25 tons (100 tons wagon) were simulated. Figure 6.15 shows the spacing of train wheels used in the FEM model. It should be noted that each wheel loading is equal to 125 kN, which represents the wheel load of the freight train with 100 tons wagons. The freight train operated with a speed of 60 kph.

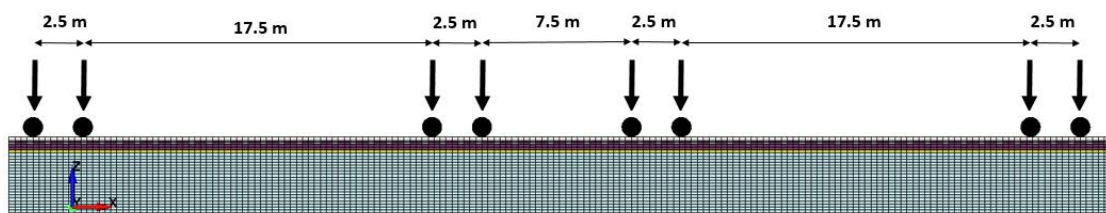


Figure 6.15. Schematic of the train axles spacing used in the FEM study

In order to validate the FEM numerical simulation, the distribution of the maximum cyclic stresses in the embankment (ballast and sub-ballast) were compared with field measurement by Indraratna et al. (2010). For increasing the accuracy of the FEM finding, the maximum cyclic vertical and shear stress is the average of the maximum cyclic stresses for at least 20 sleepers. In this approach, the values of the maximum dynamic stresses would be the best representative of the field values. Figure 6.16 depicts the comparison of the maximum cyclic vertical and shear stress bellow the base of sleepers for field measurements and the FEM model.

As can be observed, the FEM model is a good representative of the cyclic shear stress (dashed lines) in the ballast layer. However, the magnitude of the maximum cyclic vertical stress has a slight deviation in comparison with the field measurement. This discrepancy might have happened as a consequence of two main issues. First, the magnitude of the field measurement indicated in Figure 6.16 is corresponding to the number of cycles of $N=6.8 \times 10^5$. According to Indraratna et al. (2010), the magnitude of the cyclic stress increases with the number of cycles. Thus, the maximum vertical cyclic stress for the first train passage, which is simulated in the FEM model, is less than the magnitude presented in the figure. Unfortunately, there were no measurements of the stresses reported in their study. Second, all the soil layers in the FEM study were simulated as a linear elastic material, which may cause a slight under prediction of the dynamic stresses generated by the train passage. In conclusion, the FEM model is a good representative of the field response.

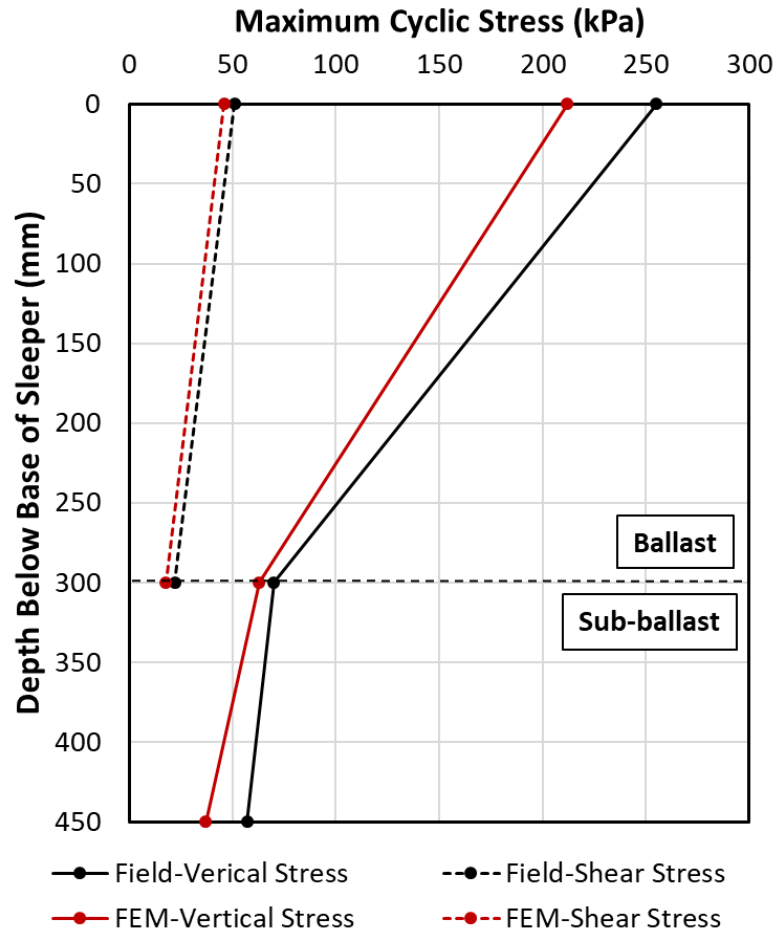


Figure 6.16. Comparison of the field measurement of the maximum cyclic vertical and shear stress underneath the rail (after Indraratna et al. (2010)) with the FEM study

The results of the maximum vertical cyclic stress distribution underneath the sleeper of the FEM study were further compared with the available measurements and the analytical studies in the literature. The model has the same geometry, as depicted in Figure 6.13(b). The magnitude of the wheel load in different studies was varying in the range of 125 kN to 200 kN. Therefore, in order to be consistent with the available data, two models with the axle loads of 125 kN and 200 kN were used for the comparison. Figure 6.17

shows the comparison of the FEM study with the different stress distribution measurements in the literature. Data is taken from the Indraratna et al. (2010) study.

Details about the geometry and axle load used in each study are as follow:

- Bulli track is a field measurement performed by Indraratna et al. (2010) on a 300 mm ballast overlying 150 mm sub-ballast layer with the axle load of 125 kN.
- Pueblo track is a field measurement performed by Rose et al. (2004) on 300 mm ballast overlying 100 asphalt layer with the axle load of 200 kN.
- KENTRACK is an analytical study performed by Rose and Konduri (2003) on the Pueblo track field measurements.
- MULTA, PSA, and ILLI-TRACK are analytical studies conducted by Adegoke et al. (1979) on a track with 380 mm ballast and 150 mm sub-ballast with the axle load of 145 kN.
- GEOTRACK is a modified version of MULTA performed by Selig and Waters (1994) on a 300 mm ballast with a 146 kN axle load.

It can be observed from Figure 6.17 that although the axle load and track substructure configuration is different in various case studies, the FEM results are in an acceptable agreement with the other results based on the applied axle loads.

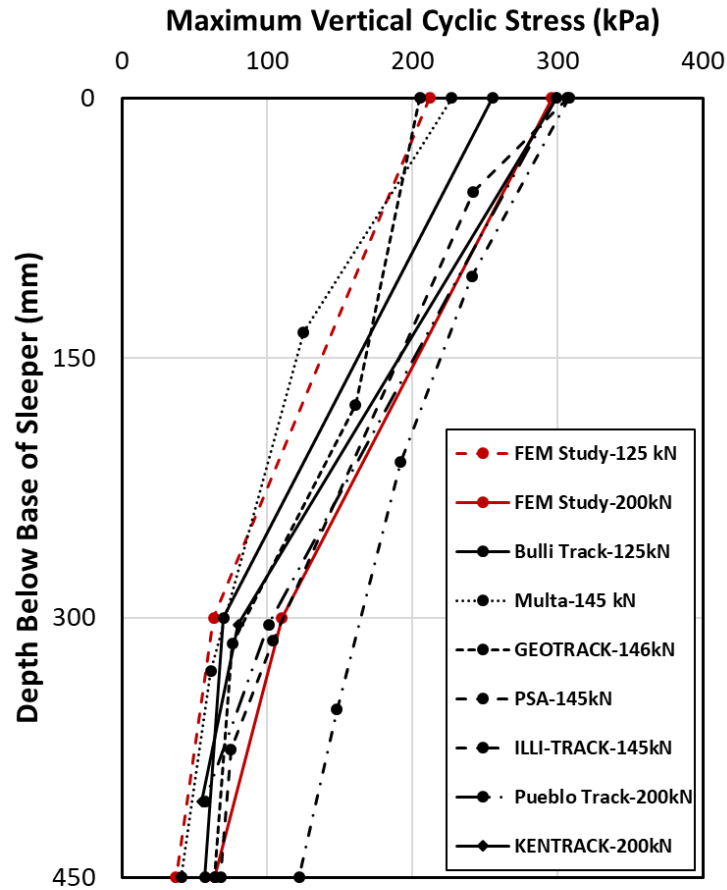


Figure 6.17. Comparison of the maximum cyclic vertical stress of the FEM study with the available measurement in the literature (data adopted from Indraratna et al. (2010))

6.5. Parametric Study

The parametric study was aimed to investigate the influence of train characteristics and sleepers configuration on the stress generated by train passage on substructure layers. The train characteristics are including train axle load, and speed and the sleepers configurations are including sleepers with and spacing. The verified FEM model was utilized for this investigation. The geometry of the model used for the parametric study is

similar to Figure 6.1. In order to simulate the train movement, two wagons of the train with axle spacing, as shown in Figure 6.15, were modeled in the parametric study. The material properties for the superstructure and substructure components are indicated in Table 6.1 and Table 6.3, respectively. It should be noted that the FEM parametric study model represents a track on the stiff subgrade. The parametric study illustrated the impact of each parameter on the dynamic response of the ballasted track.

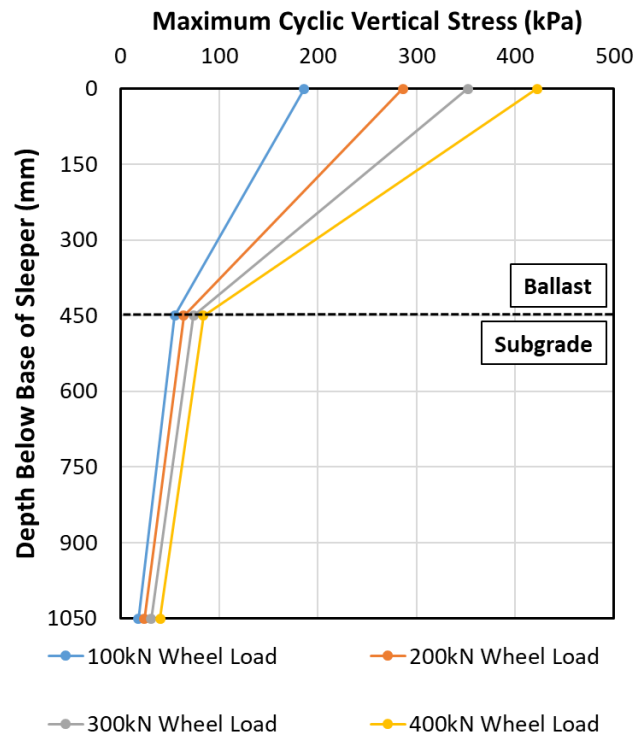
6.5.1. Influence of Train Weight

The first task of the parametric study is to analyze the influence of the train axle load on the cyclic stress growth in the substructure. Axle load is one of the most important factors in the railway design, which affects the performance of the track with heavy-haul train operation. For this purpose, four FEM models with identical conditions and varying wheel loads were simulated. The wheel loads are 100kN (22.5 tons axle load), 200kN (45 tons axle load), 300kN (67.5 tons axle load), and 400kN (90 tons axle load). The train speed is equal to 100 kph for all the models. As indicated in Figure 6.1, the track is placed on the ballast with 450 mm thickness overlying a stiff subgrade.

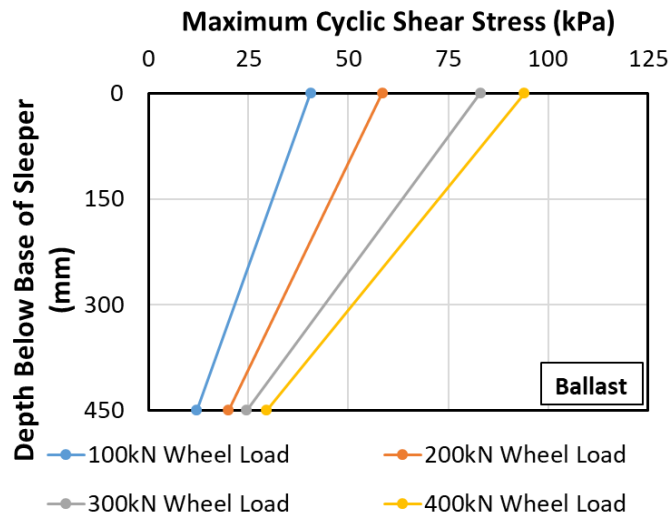
Figure 6.18 shows the influence of the wheel load on the distribution of the dynamic stress generated by train passage in the track substructure layers. The results are representative of the maximum values of the cyclic stress caused by train passage at the bottom of the sleeper and under the rail. All the stresses indicated in this section are the average of maximum cyclic stress for at least 20 sleepers.

Figure 6.18(a) shows the growth of the maximum cyclic vertical stress. As can be observed, the vertical stress generated by the train decreases significantly with depth. The results of all tests revealed the magnitude of the cyclic vertical stress acting on the subgrade (depth of 450 mm) is only approximately 25% of the stress at the bottom of the sleeper. It is illustrated that increasing the train wheel load from 100 to 400 kN increases the stress acting on the ballast from 186 to 422 kPa, respectively. This value is increasing from 55 to 84 kPa at a depth of 450 mm, which corresponds to the surface of the subgrade.

Figure 6.18(b) shows the growth of the maximum cyclic shear stress. Because of the low value of the maximum cyclic shear stress at the bottom of the ballast, only the distribution in the ballast is shown. Similar to the cyclic vertical stress, the cyclic shear stress in the ballast layer is increased for the heavier train. However, the magnitude of the shear stress is significantly lower than the vertical stress. This finding is in line with the field measurement performed by Indraratna et al. (2010). The cyclic shear stress is decreased with depth. The results showed that the maximum cyclic shear stress acting on the subgrade is reduced by 70% in comparison with the magnitude at the bottom of the sleeper. Increasing the wheel load from 100 to 400 kN increases the maximum cyclic shear stress from 40 to 94 kPa at the surface of the ballast and 12 to 30 kPa at the surface of the subgrade.



(a)



(b)

Figure 6.18. Influence of the train wheel load on the distribution of the maximum cyclic stress generated by train with depth below the sleeper. (a) Maximum cyclic vertical stress; (b) Maximum cyclic shear stress

Figure 6.19 shows the relationship of the maximum cyclic stresses at the base of the sleeper acting on the ballast layer with the train wheel load. As was anticipated, the cyclic vertical and shear stress is increasing with the train weight. Thus, increasing the weight of the freight train cause higher dynamic stress, which leads to higher deterioration in the ballast material and consequently shortens the track maintenance time. The same observation made by field instrumentation conducted by Indraratna et al. (2010). It is observed that the magnitude of the cyclic vertical stress in the ballast is significantly larger than the cyclic shear stress caused by train passage. Therefore as stated by Indraratna et al. (2010), this issue would cause a large shear strain in ballast, which is the main reason for the significant lateral movement of the ballast.

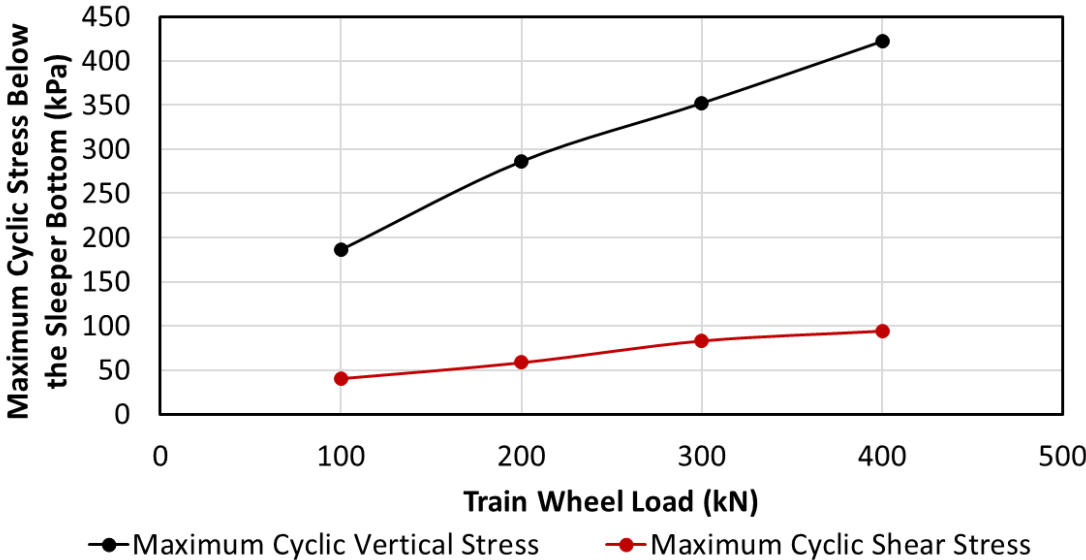


Figure 6.19. Relationship between the maximum cyclic stresses under the sleeper bottom with the train wheel load

Figure 6.20 illustrates the influence of the train wheel load on the maximum downward displacement of the track. The results showed that increasing the freight train

would increase track deformation. The nearly linear relationship between the load and the displacement happened as a result of assuming the elastic properties for the soil material. It is expected that, in reality, this relationship would be non-linear, and the track deflection will be higher in higher load magnitudes.



Figure 6.20. Relationship between the maximum track downward displacement with the train wheel load

6.5.2. Influence of Train Speed

Train speed is the second train characteristic that will be discussed in the parametric study. The influence of the train speed has been investigated extensively in the literature. Numerous research studied the impact of train speed on track deflection (Kaynia et al. (2000), Madshus and Kaynia (2000), Sheng et al. (2004), Bian and Chen (2006), Bian et al. (2016a), Costa et al. (2015), Tafti et al. (2017), and Rezaei Tafti (2018)). In contrast, to the author's knowledge, there are very limited studies that investigate the

impact of the train speed on the cyclic stress distribution caused by train passage in the track substructure.

In order to investigate the train speed on the dynamic response of the ballasted track, a wide range of train speeds were selected for the parametric study. Thirteen simulations performed with a train velocity increasing from 100 to 700 kph with an increment of 50 kph. The substructure layers consist of 450 mm ballast placed over a stiff subgrade (Figure 6.1). The superstructure and substructure material properties are constant for all the models and summarized in Table 6.1 and Table 6.3, respectively. The train configuration is shown in Figure 6.15 with a constant wheel load of 125 kN, which represents a 22.5 tons axle load.

An important issue for the high-speed trains that need to be considered is when the train speed approaches the critical speed of the railway system. The critical speed defines as a velocity of a moving load that creates an excessive dynamic amplification response (similar to resonance) (Costa et al. (2015)). This phenomenon was observed in Ledsgrad's case study when the train speed increased from 140 to 200 kph (Madshus and Kaynia (2000)). It is previously shown by Madshus and Kaynia (2000) that the critical speed is close to the equivalent Rayleigh wave speed of the ground profile. Mezher et al. (2016) showed that the critical speed is dominantly influenced by the stiffness of the track support system. The Rayleigh wave velocity can be calculated from the shear wave velocity by using the following equation:

$$V_R = \frac{0.87 + 1.12\nu}{1 + \nu} V_S \quad (26)$$

where V_s is shear wave velocity, and ν is the Poisson's ratio. The shear wave velocity can be obtained from the shear modulus and density based on the Equation (24). Table 6.4 summarized the shear and Rayleigh wave velocity of the soil materials used in this section.

Table 6.4. Rayleigh and shear wave velocity of the soil materials used in the parametric study

Components	ρ (kg/m ³)	ν	G (MPa)	E (MPa)	V_s (m/s)	V_R (m/s)
Ballast	1590	0.35	37	100	152	143
Subgrade	1250	0.35	12	31	98	92

Figure 6.21 shows the influence of the train speed on the maximum vertical deflection of the track. The red line shows the downward displacement, and the black line is corresponding to the upward movement of the track. It can be observed that for increasing the train speed from 100 to 250 kph, there is a negligible upward track motion observed, and the track settlement is not affected by the train speed. This zone is known as a quasi-static zone in which there is no dynamic amplification observed by the train passage (Madshus and Kaynia (2000)).

Beyond the train velocity of 250 kph, the track downward movement is increasing from approximately 2.2 mm to the peak value equal to 5.1 mm. This zone, known as the dynamic zone, contains both downward and upward displacement for the track. The corresponding train velocity to the maximum track displacement is the track critical velocity. Comparison of the track critical velocity with the substructure layers Reiligh wave speed showed that the critical speed (approximately 450 km/h) is between the

Reiligh wave speed of the subgrade (approximately 331 km/h) and the ballast (approximately 515 km/h). Above the critical velocity, the track vertical displacement is started to decrease with increasing the train speed. The same behavior reported previously in the literature (Kaynia et al. (2000), Banimahd (2008), Woodward et al. (2014), and Rezaei Tafti (2018)).

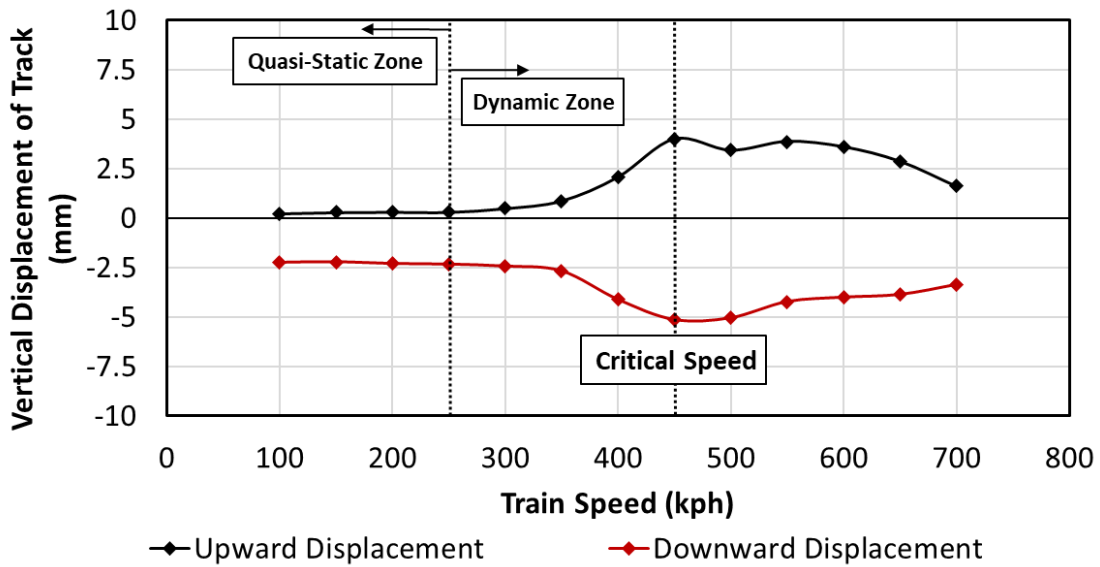


Figure 6.21. Influence of train speed on the vertical displacement of the track

Figure 6.22 shows the influence of the train speed on the maximum cyclic stresses developed at the sleeper-ballast contact cause by the train passage. The results showed that increasing the train speed up to 400 kph causes a very low increment in both maximum cyclic vertical and shear stresses at the sleeper-ballast interface (approximately 10%). However, a sudden increment at both stresses was observed at the train's critical speed. The magnitude of the maximum cyclic vertical and shear stresses at the sleeper-ballast interface in the crucial speed increased by approximately 25% and 30%, respectively.

Beyond the train velocity of nearly 550 kph, the magnitude of the cyclic stresses reduced slightly by increasing the train speed. It should be noted that the development of the cyclic stresses at the bottom of the sleeper follows the same trend as the track vertical movement by increasing the train speed. However, the extent of the dynamic amplification in stress is lower than the track displacement.

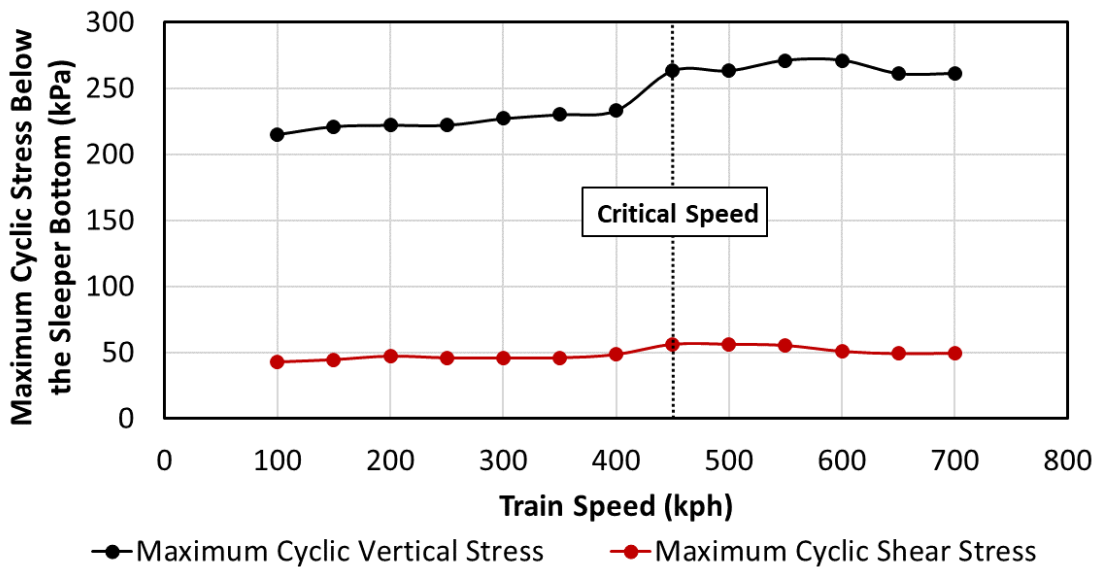
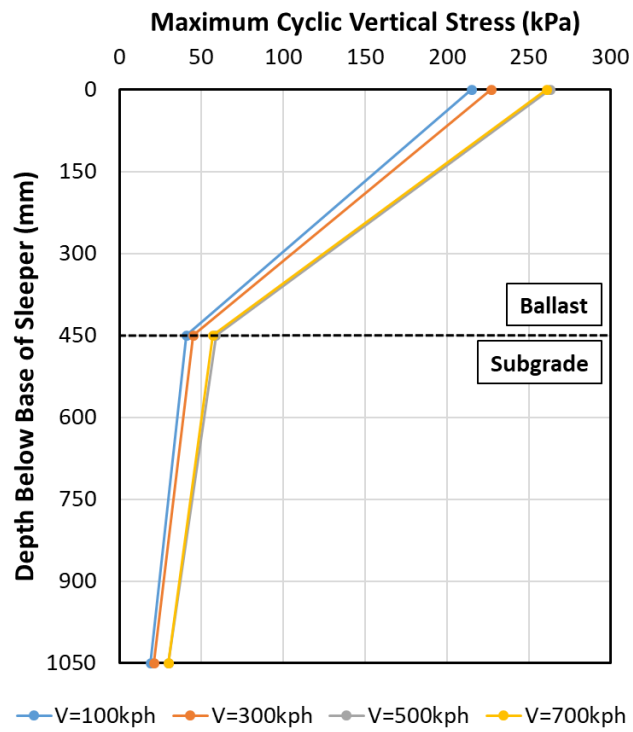
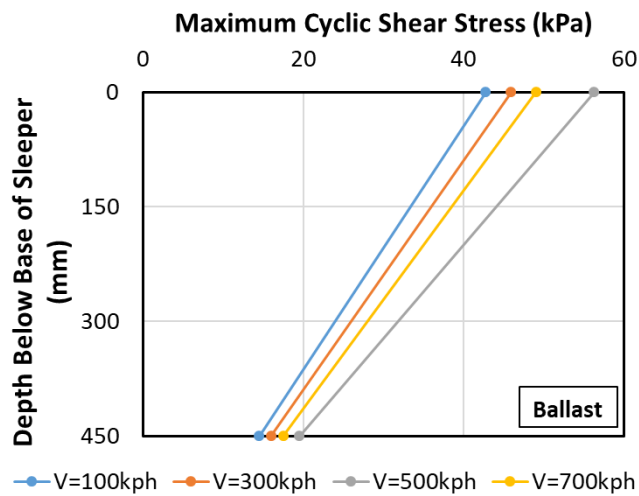


Figure 6.22. Influence of train speed on the maximum cyclic stresses under the sleeper bottom

Figure 6.23 shows the distribution of the maximum cyclic stresses with depth for train speed equal to 100, 300, 500, 700 kph. The results confirmed that most portion of the cyclic stresses generated by the train is damped in the ballast layer. It can be observed in Figure 6.23(a) that increasing the train speed to the train’s critical velocity increased the magnitude of the maximum cyclic vertical stress in the profile of the soil. Also, the cyclic vertical stress reduced slightly at the train speed equal to 700 kph. The same observations were made for the maximum cyclic shear stress in Figure 6.23(b).



(a)



(b)

Figure 6.23. Influence of the train speed on the distribution of the maximum cyclic stress generated by train with depth below the sleeper. (a) Maximum cyclic vertical stress; (b) Maximum cyclic shear stress

6.5.3. Influence of Sleeper's Width

The results of the FEM study shows considerably high cyclic stresses acting on the ballast layer due to the train passage. In addition, the cyclic laboratory tests on the ballast material revealed that with respect to the low confinement in the field, the large magnitude of the cyclic stresses acting on ballast could lead to a significant long-term settlement and consequently shorten the maintenance time. According to the cyclic laboratory tests on the ballast that discussed in Chapter 5, the long-term response of the ballast material is influenced by the cyclic stress ratio (ratio of cyclic stress amplitude over the monotonic shear strength of the ballast). Therefore, in order to lengthen the ballasted track maintenance time, either the ballast confinement should be increased, or the cyclic stresses generated by the train should be decreased.

In this section, the impact of increasing the sleeper's width on the cyclic stresses generated by train passage will be evaluated. For this purpose, four FEM models with sleeper's width equal to 150, 300, 450, and 600 mm were simulated. The track geometry has consisted of 450 mm ballast and 3000 mm subgrade (Figure 6.1). The sleeper's spacing is constant for all the models and equal to 600 mm. The superstructure and substructure material properties are consistent for all the models and summarized in Table 6.1 and Table 6.3, respectively. The train axle spacing is similar to Figure 6.15 with a constant wheel load of 125 kN, and the speed of 200 kph. The model boundary conditions are shown in Figure 6.8.

Figure 6.24 illustrates the influence of increasing the sleeper's width on the maximum cyclic stresses acting on the sleeper-ballast interface. The black line shows the

magnitude of the maximum cyclic vertical stress, and the red line shows the maximum cyclic shear stress. The results revealed that both the maximum cyclic vertical and the shear stresses are decreased with increasing the sleeper's width. For instance, By increasing the sleeper's width from 150 to 600 mm, the maximum cyclic vertical and shear stress acting at the surface of ballast decreased by 66% and 57%, respectively.

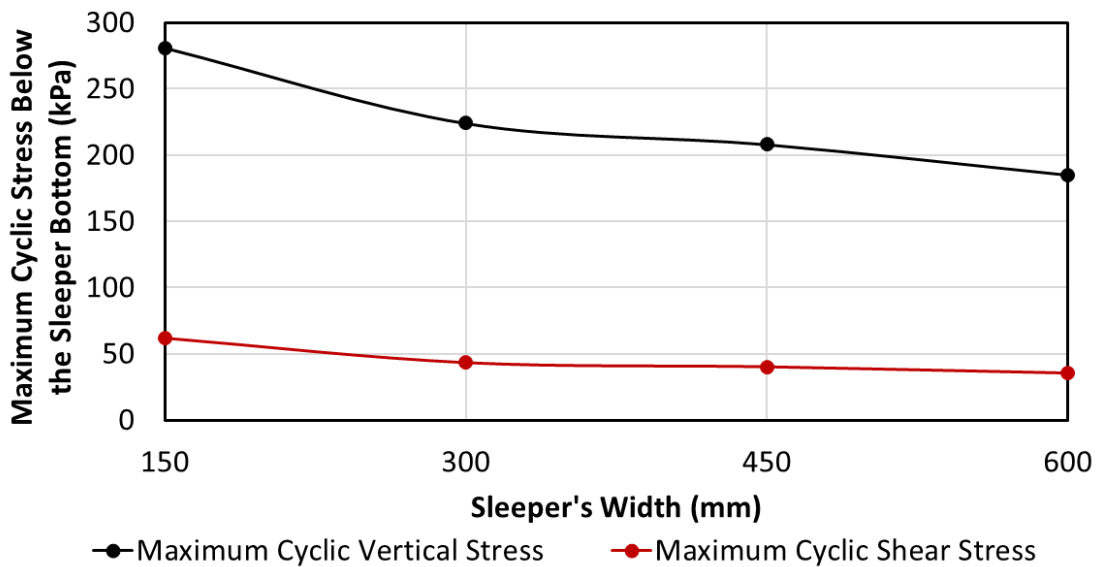


Figure 6.24. Influence of sleeper's width on the maximum cyclic stresses under the sleeper bottom

Figure 6.25 shows the impact of increasing the sleeper's width on the maximum downward deflection of the track. It should be noted that with regards to the train speed (200 kph), the track is in the quasi-static zone; therefore, there is negligible upward track deflection is observed. The results revealed that the short-term track settlement under train passage is decreased (approximately 10%) by increasing the sleeper's width. Although the short term settlement of the track is not significantly reduced, increasing the sleeper's

width causes a reduction in the cyclic stresses in the embankment, which creates a hugely beneficial impact on the permanent long-term settlement of the track.

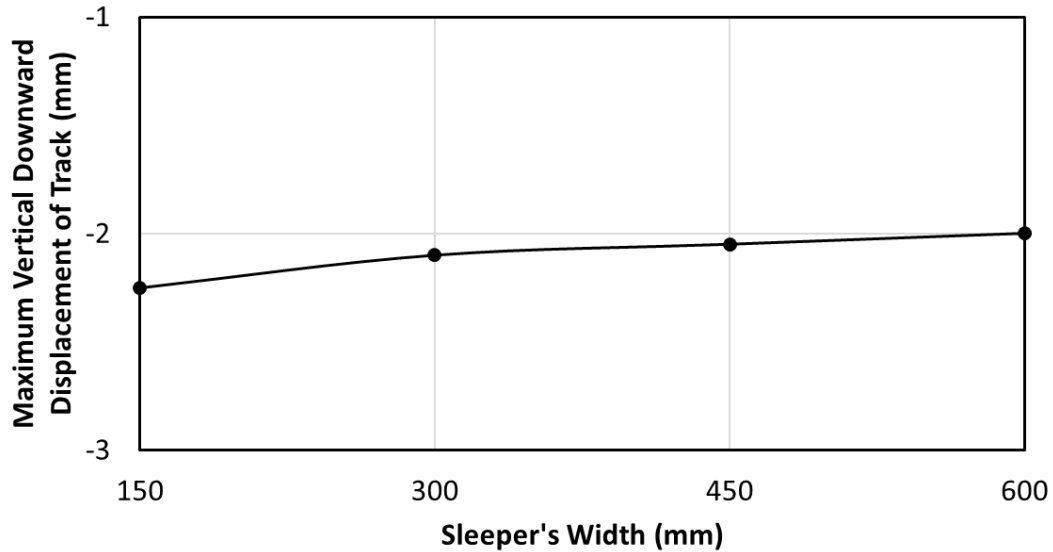
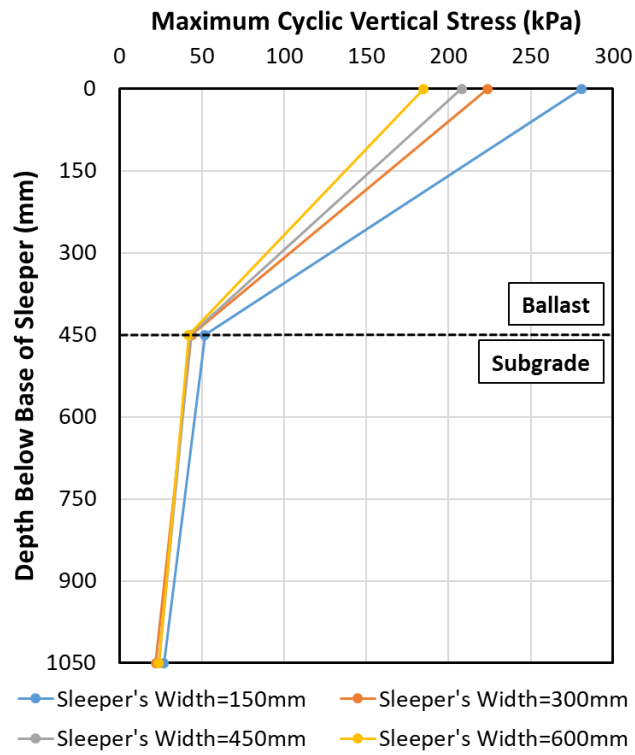
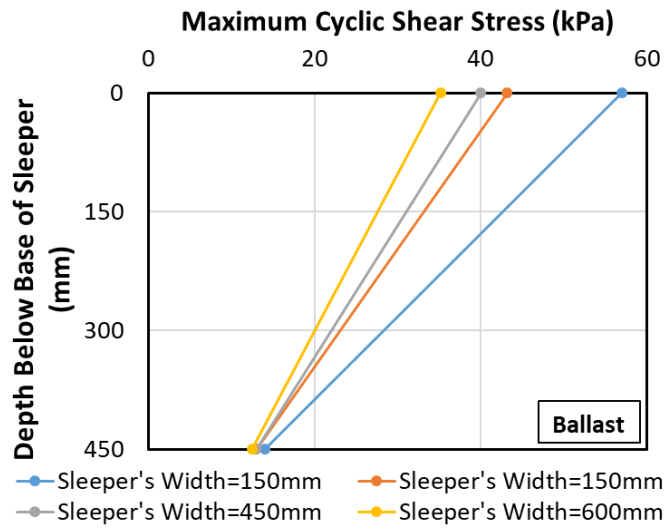


Figure 6.25. Influence of sleeper's width on the maximum downward displacement of the track

Figure 6.26 shows the development of the maximum cyclic stresses with the depth for the sleeper's width equal to 150, 300, 450, 600 mm. It is clearly evident that increasing the width of the sleepers reduces the cyclic stress magnitudes caused by train passage in the ballast layer. In contrast, Figure 6.26(a) shows that the value of the maximum cyclic vertical stress is not influenced by the sleeper's width in the subgrade layer.



(a)



(b)

Figure 6.26. Influence of the sleeper's width on the distribution of the maximum cyclic stress generated by train with depth below the sleeper. (a) Maximum cyclic vertical stress; (b) Maximum cyclic shear stress

6.5.4. Influence of Sleeper's Spacing

The second approach for reducing the cyclic stresses caused by train in the track substructure layers used in this study is to reduce the sleeper's spacing. For this purpose, four FEM models with identical conditions and different sleeper's spacing equal to 0, 300, 600, and 900 mm were simulated. The spacing in the current study is defined as an edge to edge distance between the two sleepers. Figure 6.2 depicts the sleeper's spacing in the FEM model. In this parametric study, the spacing of 0 mm is equivalent to the slap track with the same thickness, and the material properties of the regular sleepers.

The track geometry is shown in Figure 6.1, which consisted of 450 mm ballast and 3000 subgrade. The superstructure and substructure material properties are constant for all the models and summarized in Table 6.1 and Table 6.3, respectively. The train configuration is shown in Figure 6.15 with a constant wheel load of 125 kN and a speed of 200 km. It should be noted that the FEM properties except the sleeper's spacing are consistent with the previous section.

The variation of the maximum cyclic stresses generated by the train passage under the bottom of the sleepers acting on the ballast layer is shown in Figure 6.27. It can be observed that the magnitude of the cyclic stresses is in an approximately linear indirect relationship with the sleeper's spacing. According to the results decreasing the sleeper's spacing from 900 mm to 0 mm reduces the maximum cyclic vertical stress at the ballast-sleeper interface from 269 to 171 kPa. The same transition for the maximum cyclic shear stress is from 50 to 28.4 kPa.

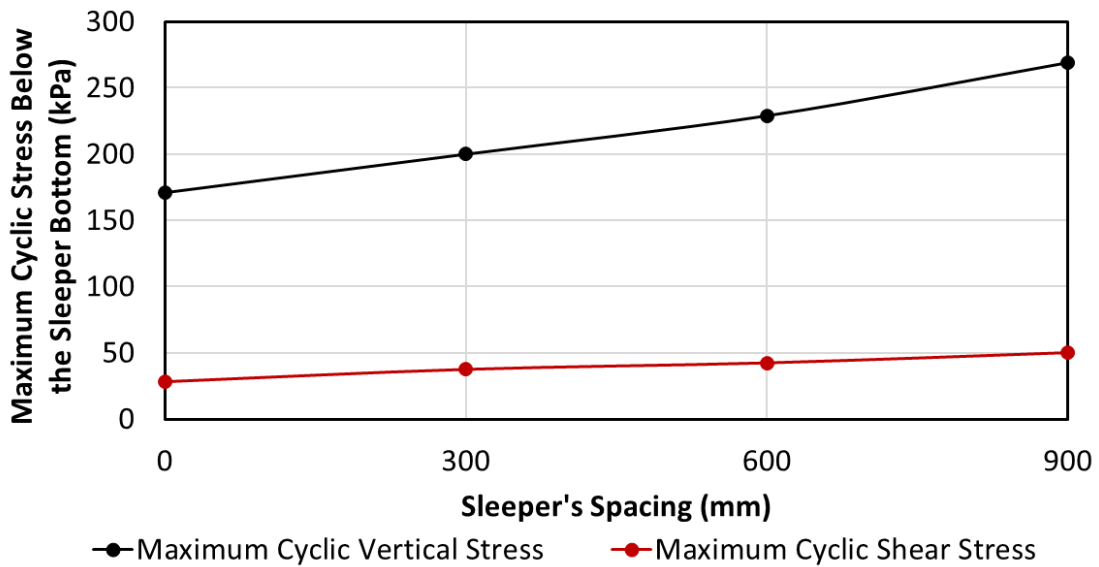


Figure 6.27. Influence of sleeper’s spacing on the maximum cyclic stresses under the sleeper bottom

Figure 6.28 shows the variation of the track maximum settlement with the sleeper’s spacing. As can be observed, decreasing the sleeper’s spacing reduces the track maximum deflection at the same train passage. For example, the track maximum downward deflection under train passage reduced from 2.47 to 1.86 mm for decreasing the sleeper's spacing from 900 mm to 0 mm. Similar to increasing the sleeper's width, reducing the spacing causes a reduction in the magnitude of the cyclic stresses. Thus, as a consequence, the long-term permanent settlement of the ballasted track would be decreased due to less cyclic stress ratio. The variation of the magnitude of the maximum cyclic vertical and shear stresses with the depth below the sleeper are shown in Figure 6.29.

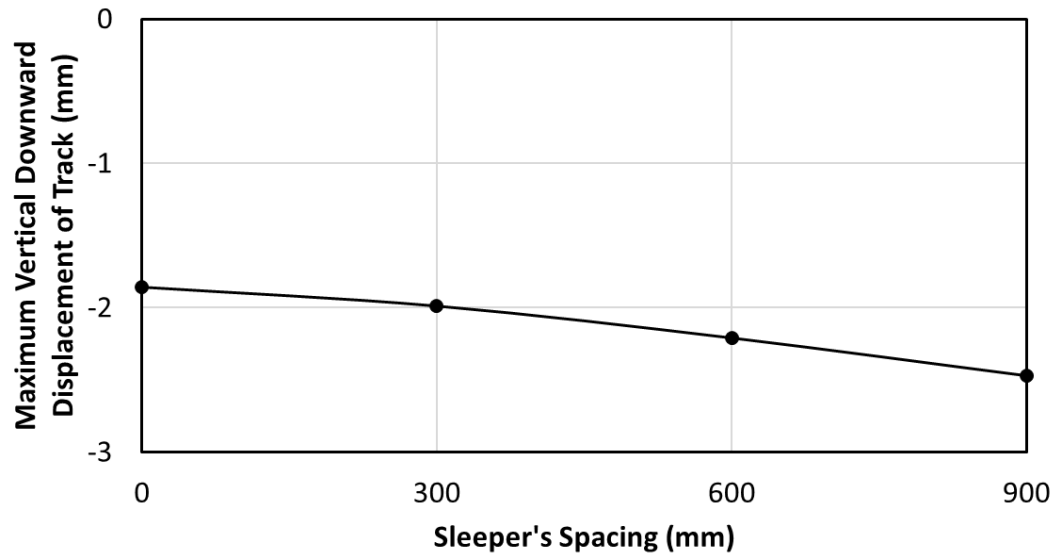
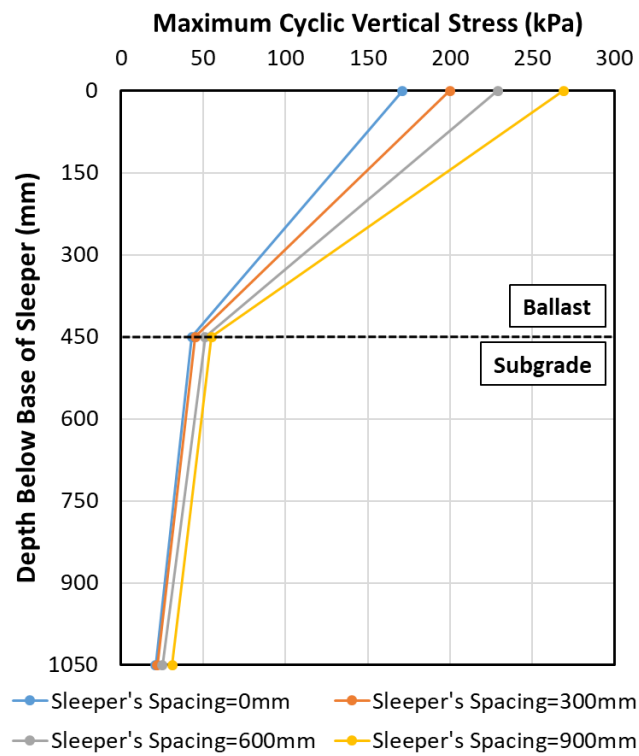


Figure 6.28. Influence of sleeper's width on the maximum downward displacement of the track



(a)

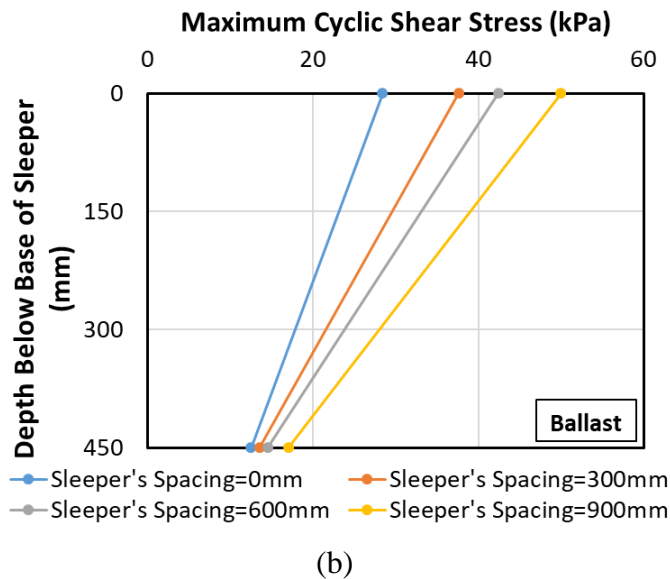


Figure 6.29. Influence of the sleeper’s spacing on the distribution of the maximum cyclic stress generated by train with depth below the sleeper. (a) Maximum cyclic vertical stress; (b) Maximum cyclic shear stress

6.6. Bearing Capacity of the Ballast Layer

The magnitude of cyclic vertical stress generated underneath the bottom of the sleeper due to the train passage was evaluated in the previous sections. As was measured in the FEM parametric study, the value of the maximum cyclic vertical stress was varying in the range of approximately 150 to 400 kPa depending on the train characteristics and the sleeper’s configuration. As a result of a large stress level, the maximum cyclic vertical stress acting on the ballast layer was compared with the ultimate bearing capacity of the ballast. In this analysis, a sleeper was considered as a strip footing on top of the ballast layer. The general bearing capacity equation for the strip footing is as follow:

$$P_u = c'N_c + \frac{1}{2}\gamma BN_\gamma + \gamma DN_q \quad (27)$$

where P_u is the ultimate capacity of the ballast layer, c' is the cohesion of the ballast material (equal to zero), γ is the ballast unity weight (approximately 17 kN/m³), B is the width of the sleeper (equal to 300 mm), D is the ballast thickness (equal to 450 mm), N_c , N_γ , and N_q are the bearing capacity factors which are a function of the friction angle. The values of parameters indicated before are assumed approximately for a typical ballast layer. By assuming the ballast friction angle in the range of 45 to 50 degrees, the ultimate bearing capacity of the ballast can be measured in the range of 1105 to 3145 kPa.

The magnitude of the bearing capacity of the ballast is considerably high and unrealistic. On the other hand, the magnitude of the ultimate deviatoric stress based on the large-scale monotonic triaxial test for ballast #5 for the confining stress of 40 kPa to 80 kPa (representing the field stress state) is 243 to 420 kPa. Therefore, with respect to the comparison of the ultimate bearing capacity from the equation above and the triaxial test, it can be concluded that the ultimate deviatoric stress of the TT can be a better representative of the ultimate capacity of the ballast layer.

7. CONCLUSION AND RECOMMENDATIONS

7.1. Conclusion

The primary objective of the current research was to predict the long-term behavior of the ballast layer under high-speed and heavy freight train loading. Figure 7.1 provides a step by step procedure to predict the long-term response of ballast in the railway embankment. This procedure contains four main steps toward the analysis of the ballast behavior under long-term train operation. It is important to mention that the same procedure can be employed to predict the long-term response of the other track substructure components.

The first step, as discussed thoroughly in Chapter 4, is the monotonic laboratory test of the ballast material. The main outcome of this step is to evaluate the ultimate capacity of the ballast material (i.e., shear strength in DSST or ultimate deviatoric stress in TT) based on the field stress state before the train loading. It is critically important to apply the appropriate stress condition that is representative of the field stress to the laboratory test. The other important outcome of this section is to evaluate the elastic modulus, shear modulus, friction angle, and dilation angle of the ballast materials.

The second step, as discussed in Chapter 6, is to evaluate the magnitude of the cyclic stress generated by the high-speed or heavy train passage acting on the ballast layer. The magnitude of the cyclic stress highly depends on the train characteristics (weight, and speed), the sleeper's configuration, and the track geometry. Therefore, by knowing the type of train weight, train velocity, sleeper's dimensions, sleeper's spacing, and the track

geometry, the magnitude of cyclic stresses due to train passage can be evaluated. The FEM simulation can also be utilized to estimate the critical velocity, stress distribution with depth, and the track maximum short-term deflection.

The third step is to perform a cyclic laboratory test (cyclic DSST or TT). A series of empirical equations have been developed to predict the long-term behavior of the railroad ballast. These equations are including, permanent shear strain, secant shear modulus, resilient shear modulus, permanent axial strain, and the secant elastic modulus. These equations are the function of the number of the cycles, monotonic ultimate strength (i.e., shear strength in DSST and ultimate deviatoric stress in TT), and the maximum cyclic stress amplitude (i.e., maximum cyclic shear stress in TT and maximum cyclic vertical stress in DSST). It should be noted that the constants of the empirical equation should be calculated based on the ballast material type.

The last step is to utilize the appropriate empirical equation and input the results of the monotonic test and the FEM study to predict the long-term behavior of the ballast material. The major findings of each section of the current research are summarized in the following sections.

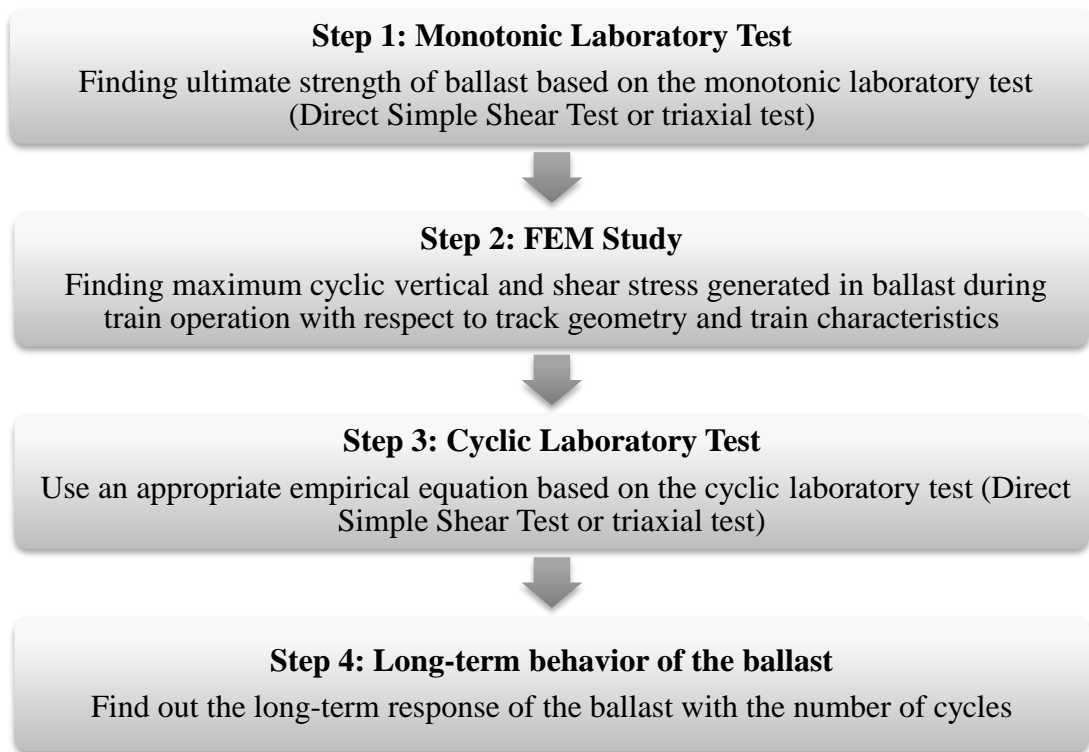


Figure 7.1. Step by step procedure to predict the long-term response of ballast in the railway embankment

7.1.1. Monotonic Behavior of the Railroad Ballast

The first phase of this study was aimed to investigate the shear behavior of the railroad ballast materials under monotonic loading. The primary objectives of this part are summarized below:

- Study the shear behavior of the ballast materials by using three different laboratory tests, including large-scale direct shear test (DST), direct simple shear test (DSST), and the triaxial test (TT).
- Compare the shear behavior properties of the railroad ballast based on large-scale DST, DSST, and TT.

- Study the influence of the maximum particle size (AREMA ballast #4 and #5) on the shear behavior of the railroad ballast under monotonic loading.
- Study the influence of the DST gap on the shear strength properties of the ballast materials.
- Provide empirical formula to calculate the shear strength properties of the ballast.

The primary conclusions of the monotonic behavior of the railroad ballast are summarized below:

- In all three tests, the shear stress increases when the shear strain/displacement or axial strain (in TT) increases until the peak shear stress is reached. However, there is a difference observed in the post-peak softening behavior of the material. The DST shear stress-shear displacement results show considerable strain-softening for the material while the DSST and the TT results show no or negligible post-peak strain-softening.
- All the tests revealed a fluctuating response of the stress-strain (displacement). This phenomenon is common for large aggregate angular materials and happened due to the deterioration of the particle edges, particle breakage, relocation, and rearrangement. However, DST shows more noise than DSST and TT because it forces the sample to fail in the narrow horizontal shear band.
- All the tests showed the dependency of the shear strength to the stress level. The peak shear strength increases with increasing normal/confining stress. But, the maximum shear strength measured in each test is different.

- The dilative response of the ballast material is different in DST and DSST. The DST results show a slight initial compression followed by significant dilation with increasing shear displacement. The results also showed that increasing the applied normal stress causes a reduction in dilatancy. On the other hand, the DSST results show significant compression at the beginning of the test. The behavior changed to dilation after a certain shear strain (approximately 3 to 5%). Most of the tests showed overall dilatancy at 15% shear strain. Similar to the DST results, increasing the applied normal stress in the DSST causes more compression at the beginning of the test and less dilatancy afterward. Although the volumetric behavior trend is similar to the DST results, the DSST shows higher compression at the beginning of the test, less overall dilation, and stays in the compression zone for a broad range of shear strain.
- The TT results give the complete Mohr circle while the DST and DSST give a single point on the Mohr circle, which corresponds to the stresses on the horizontal plane. Therefore, the interpretation of the results of the DST and DSST can only be achieved by making an assumption on the stress state in the specimen at failure. For the DST results, it is assumed that the specimen fails along the horizontal plane. Thus, the maximum horizontal stress and the vertical stress that were obtained from the test would be the shear and normal stress on the failure plane (β method). This assumption leads to conservative and low shear strength properties for DSST. Thus, for the DSST results, it is assumed that the horizontal plane

corresponds to the plane with the maximum shear stress but not to the failure plane (α method).

- The results of all three tests show a non-linear shear strength envelope, which is more pronounced in the lower stress level. This behavior can be attributed to the greater particle interlocking, more dilative behavior, and less particle breakage of the granular materials at lower stress levels. At higher stress levels, the dilation is restricted, the failure envelope becomes more linear, and the linear Mohr-Coulomb envelope is a good representation of the material behavior at failure.
- All three tests indicate that the friction angle of the ballast decreases nonlinearly with increasing stress levels. A comparison of the friction angle range for the tests shows that DST shows the highest magnitude of the friction angle while DSST shows the lowest. For the purpose of the comparison of the ballast #5 friction angle from all three tests, the magnitude of the friction angles at the vertical stress on the plane of failure equal to 1 kPa and 98.1 kPa (atmospheric pressure) are compared. The value of φ_1 for DST, TT, and DSST are 76.8, 68, and 67.3 degrees, respectively. Also the value of φ_{Pa} for DST, TT, and DSST are 55.8, 47.9, and 40.5 degrees, respectively.
- The results of DSST shows that the maximum shear modulus of the ballast (i.e., shear modulus at 0.01% shear strain) is increasing with the applied normal stress. For example, for ballast #5, the maximum shear modulus increased from 2.4 to 11.3 MPa for increasing the normal stress from 10 to 90 kPa. The same observations were made for variation of the initial triaxial elastic modulus ballast

(i.e., elastic modulus at 0.01% axial strain) with the confining pressure in TT results. For instance, the initial triaxial elastic modulus was risen from 49.1 to 169.9 MPa for increasing the confining pressure from 40 to 140 kPa.

- The results of DSST shows that the shear modulus is decreasing in higher shear strain. The results also revealed that the significant reduction in shear modulus happens in a low amount of the shear strain. For example, the ballast shear modulus in all the tests reduced to approximately 7 to 18% of their maximum shear modulus (i.e., at 0.01%) at shear strain equal to 1%. Moreover, it can be observed that although the magnitude of the shear modulus highly depends on the stress level, the normalized shear modulus (G/G_{\max}) trend is independent of the vertical stress level. In other words, the shear modulus degradation is independent of stress level.
- The influence of the maximum ballast particle size based on the comparison of the crushed granite ballast #4 ($D_{\max}=38$ mm) and ballast #5 ($D_{\max}=25$ mm) with using the DST and DSST are as follow: (1) Increasing the maximum particle size increases the shear strength of the ballast. (2) Samples with coarser particles show a higher friction angel. (3) The existence of larger grain in the ballast produces more dilation than the samples with smaller particles. (4) Comparing the normalized shear modulus of the tests revealed that the maximum shear modulus is increasing in larger specimen particle size.
- The influence of the gap in DST on the shear strength properties of crushed granite ballast #5 based on the regular gap (the gap dimension equal to D_{85} of the material, which is 21 mm) and the reduced gap (the gap dimension equal to D_{10} of the

material, which is 11 mm) are as follow: (1) Lowering the gap can significantly enhance the shear resistance of the material. The shear strength for the test with a reduced gap (11 mm) is up to 57% higher than the tests with the regular gap (21 mm). (2) The peak friction angle of the tests with a reduced gap is 2 to 8 degrees higher than the tests with a regular gap. (3) Decreasing the gap in the direct shear test would also cause higher dilatancy for the sample. Comparing the results of two series of experiments with 11 mm and 21 mm gap revealed that the tests with a lower gap show 5 to 8 degrees higher maximum dilation angle.

7.1.2. Cyclic Behavior of the Railroad Ballast:

The second phase of this study was investigating the behavior of the railroad ballast materials under cyclic loading. For this purpose, a series of cyclic large-scale laboratory tests have been performed on crushed granite ballast material. The primary objectives of this part are summarized below:

- Investigate the cyclic behavior of the crushed granite ballast material under large-scale cyclic direct simple shear (DSST) and triaxial tests (TT).
- Provide the appropriate empirical formulas for predicting the long-term cyclic permanent settlement, permanent shear strain, resilient shear modulus, secant shear modulus, and the secant elastic modulus of the ballast based on the laboratory data.

- Examine the effect of field stress states and various cyclic loading characteristics due to the train passage on the long-term behavior of the ballast.

The essential outcomes of the cyclic behavior of the railroad ballast are summarized as follow:

- Permanent (or plastic) shear strain is an important characteristic of the ballast material under cyclic loading that shows the unrecoverable portion of the shear strain. The plastic strain is occurring as a result of sliding between the particles or fracturing of the grains. The development of this parameter with the number of cycles can be used for two main reasons: (1) predict the long-term permanent shear strain of the ballast, and (2) calculate the cyclic secant shear modulus of the ballast material under cyclic train loading. The results of cyclic DSST show the rapid growth of the plastic strain in the early stage of the test (within the first 1,000 cycles) followed by increasing the plastic shear strain against the number of cycles with a lower rate up to 100,000 load cycles.
- The resilient shear modulus (M_R) is the ratio of cyclic loading amplitude over the recoverable portion of the shear strain. The results of cyclic DSST show the resilient shear modulus is increasing with the number of cycles, but the rate of changes is lower in a larger amount of cycles. This phenomenon happens because of increasing the specimen stiffness, which occurs as a result of specimen compaction during the cyclic loading.

- The secant shear modulus (G_s) is another important characteristic of the ballast under cyclic loading, which is defined as the slope of a straight line drawn from the origin to the maximum shear stress in a given cycle. The results of the cyclic DSST illustrate that the secant shear modulus decreased with the number of cycles, while the rate of the changes is lower in higher cycles.
- The cyclic behavior of the ballast material is highly influenced by the cyclic stress ratio, which defines as the ratio of the cyclic shear stress amplitude over the monotonic shear strength of the material. The cyclic shear stress amplitude is corresponding to the maximum cyclic shear stress acting on the ballast layer generated by the train passage. The monotonic shear strength of the ballast material in the DSST is directly influenced by the applied normal stress, which is the representative of the field's initial stress. The cyclic stress ratio can be altered in two ways: (1) variation of the cyclic shear stress amplitude which is the function of train dynamic loading, and (2) variation of the monotonic shear strength of the material which is a function ballast material type, compaction, field initial state.
- In order to investigate the influence of the cyclic stress ratio on the cyclic response of the railroad ballast, two series of parametric studies have been performed using cyclic DSST. First, the cyclic stress amplitude kept constant (i.e., the same cyclic stress generated by train) while the vertical stress applied in the test was varied (i.e., increasing the shear strength of the ballast). Second, the same vertical stress applied in the test, which represents the field stress state while the cyclic stress amplitude was varied (i.e., different possible cyclic stress generated the operation

of various trains). The observations of the influence of the cyclic stress ratio on the cyclic response of the ballast are as follow:

1. The permanent shear strain is in a direct relationship with the cyclic stress ratio. Higher unrecoverable shear strain accumulation was observed in the tests with a higher cyclic stress ratio. The results of two tests with the cyclic stress ratio of 78% (vertical stress of 10 kPa and cyclic shear stress of 7 kPa) and 94% (vertical stress of 50 kPa and cyclic shear stress of 34 kPa) show a remarkably higher plastic strain in comparison with other tests. It was observed that the permanent shear strain stabilized (shakedown) after 1,000 cycles for the tests with the cyclic stress ratio of less than 70%. However, the plastic shear strain continues to rise with the number of cycles up to 10,000 in a higher cyclic stress ratio.
2. The secant shear modulus of the first cycle depends on both test stress state (vertical stress) and cyclic stress ratio (cyclic shear stress amplitude over the monotonic shear strength). The secant shear modulus of the first cycle increasing with the vertical stress and decreasing with the cyclic stress ratio. The main reason for the reduction in the secant shear modulus is the higher magnitude of the plastic shear strain in a larger cyclic stress ratio. The results of the cyclic DSST revealed that At the constant vertical stress level, increasing the cyclic shear stress up to a certain value (the cyclic stress ratio equal to approximately 0.7) decreases the secant shear modulus for the first cycle. But afterward, the secant shear modulus was not

changing with the cyclic stress ratio anymore. For example, at the constant vertical stress equal to 50 kPa, by increasing the cyclic stress ratio from 36% to 70%, the G_{s1} decreased from 4.3 to 2.1 MPa while this value is still the same at the cyclic stress ratio of 94%.

3. The secant shear modulus is decreasing with the number of cycles. The results of the normalized secant shear modulus (G_s/G_{s1}) against the number of cycles illustrates that the reduction rate is remarkable in high cyclic shear stress. This issue happened as a result of significant plastic shear strain accumulation observed in the test when the cyclic stress is approaching the monotonic shear strength of the ballast.
4. The resilient shear modulus is highly influenced by the stress state, and it is increasing in higher magnitude if the vertical stress. This behavior can be explained by more densification of the ballast at higher stress levels. The results also revealed that this parameter is reduced by increasing the cyclic shear stress amplitude in the initial stage of the test. But, the magnitude of the resilient shear modulus after 100 initial cycles is approximately the same irrespective of the cyclic stress ratio and increases with the low rate with the number of cycles. The reason that the resilient shear modulus is approached to approximately the same magnitude after 100 cycles are that the ballast is reaching its final density at the beginning of the test. The results also confirm that the resilient shear modulus is directly proportional to the magnitude of the applied vertical stress.

- In addition to the cyclic DSST investigations, a series of cyclic TT have been performed to study long-term settlement and the secant elastic modulus of the railroad ballast. The observations about both parameters are summarized below:
 1. The plastic axial strain is a function of the number of cycles and cyclic stress ratio. The results revealed that the permanent axial strain is increasing with the number of cycles. As expected, increasing the cyclic stress ratio increases the growth of the plastic axial strain. According to the results, the magnitude of the plastic axial strain after 1,000 cycles increases from 0.02% to 0.35% for increasing the cyclic stress ratio from approximately 10% to 30%. The trend of the permanent axial strain changes with the number of cycles showed that the accumulation rate is decreasing with the number of cycles. The results of the test with the cyclic stress ratio of less than 10% showed nearly 0.02% permanent axial strain accumulation after 1,000 loading cycles. Therefore, It can be concluded that for the test with a low cyclic stress ratio (<10%), the permanent plastic strain is negligible, and the material stays in the elastic zone.
 2. Secant elastic modulus (E_s) is a crucial property of the railroad ballast the can be used to illustrates the degradation of the ballast materials under cyclic loading. The results of the cyclic TT showed that increasing the cyclic stress ratio decreases the magnitude of the secant elastic modulus. For example, the secant elastic modulus at the first cycle decreased from 189 to 70 MPa for increasing the cyclic stress ratio from 9.5% to 29.8%.

The reduction of the secant elastic modulus has occurred as a consequence of higher plastic axial strain in a higher cyclic stress ratio. The results also revealed the secant elastic modulus reduces with the number of cycles. This phenomenon happened as a result of the accumulation of the plastic axial strain with the number of cycles. For instance, for the test at confining pressure of 80 kPa and the cyclic stress ratio of 29.8%, the secant elastic modulus after 1000th cycles decreased from 70 to 27 MPa.

7.1.3. FEM Numerical Simulation of the Ballasted Railway Track:

The third phase of this dissertation was to study the dynamic response of the ballasted railway track under the operation of the high-speed passenger and heavy freight trains. For this purpose, a four-dimensional finite element model was developed to investigate the dynamic response of the conventional ballasted track. The main objectives of the 4D FEM model investigations are indicated below:

- Study the track deflection and the cyclic stresses development in the track substructure due to the high-speed passenger and heavy freight trains.
- Evaluate the influence of train characteristics (weight and speed) on the dynamic response of the ballasted track.
- Study the influence of the sleeper's characteristics (width and spacing) on reducing the magnitude of the cyclic stresses generated by the train operation.

The reliability of the FEM model developed in the current study was validated by two field case studies, including; (1) high-speed railway track at Ledsgard, Sweden, and (2) ballasted railway track at Bulli, Australia. The primary conclusions of this section are summarized below:

- The results of the FEM numerical simulation presented in this study confirm that when the train speed approaches the critical speed of the railway system, it creates an excessive dynamic amplification response (similar to resonance). The results also revealed that the critical speed is close to the equivalent Rayleigh wave speed of the ground profile, which is dominantly influenced by the stiffness of the track support system.
- The track vertical displacement time histories obtained from the simulation and the measurement of the high-speed railway track at Ledsgard, Sweden, shows that when the train operates at low speed ($V_T < 0.5V_c$), there is a negligible upward track motion observed, and the track settlement is not affected by the train speed. This zone is known as a quasi-static zone in which there is no dynamic amplification observed by the train passage. Beyond the quasi-static zone and by approaching the train speed to the profile critical velocity, the track displacement is in both upward and downward directions and increased to its maximum values (oscillatory response). This zone, known as the dynamic zone, contains both downward and upward displacement for the track.
- The comparison of the maximum cyclic stresses generated by the train passage shows that the magnitude of the maximum vertical cyclic stress is significantly

higher than maximum cyclic shear stress. Therefore, this issue would cause a large shear strain in ballast, which is the main reason for the significant lateral movement of the ballast. For example, the field measurement and the numerical simulation of the passage of passenger train (axle load of 20.5 ton) with the speed of 60 km/h at Bulli, Australia, creates an approximately 230 kPa maximum cyclic vertical stress and 50 kPa maximum cyclic shear stress acting on the ballast layer. The results also revealed that the maximum cyclic stresses are decreased significantly with depth. For example, the maximum cyclic vertical and shear stress decreased to approximately 30% and 40% at the bottom of the ballast layer with a thickness of 300 mm.

- The first task of the parametric study was to analyze the influence of the train axle load on the cyclic stress growth in the track substructure. Axle load is one of the most important factors in the railway design, which affects the performance of the track with heavy-haul train operation. The results of the FEM study showed that the magnitude of the cyclic stresses generated in the track substructure layers is directly influenced by the train axle load. For example, increasing the train wheel load from 100 to 400 kN, which represents the axle load of 22.5 to 90 tons, increases the stress acting on the ballast from 186 to 422 kPa, respectively. This value is increasing from 55 to 84 kPa at the bottom of the ballast with a thickness of 450mm (surface of the subgrade). Similar to the cyclic vertical stress, the cyclic shear stress in the ballast layer is increased for the heavier train. However, the magnitude of the shear stress is significantly lower than the vertical stress.

Increasing the wheel load from 100 to 400 kN increases the maximum cyclic shear stress from 40 to 94 kPa at the surface of the ballast and 12 to 30 kPa at the surface of the subgrade. Thus, increasing the weight of the freight train cause higher dynamic stress, which leads to higher deterioration in the ballast material and consequently shortens the track maintenance time.

- The influence of the passenger train speed on the dynamic response of the ballasted track is studied through the FEM parametric study. Thirteen simulations performed with a train velocity increasing from 100 to 700 kph with an increment of 50 kph. The substructure layers consist of 450 mm ballast placed over a stiff subgrade. The train axle load for this section was chosen to be 22.5 tons that represent a regular passenger train weight. The time history of the track vertical deflection shows that for increasing the train speed from 100 to 250 kph, there is a negligible upward track motion observed, and the track settlement is not affected by the train speed (quasi-static zone). Beyond the train velocity of 250 kph, the track downward movement is increasing from approximately 2.2 mm to the peak value equal to 5.1 mm (dynamic zone). The critical velocity of the ballasted track profile is estimated to be 450 kPh from the FEM study that is corresponding to the peak downward settlement of the tack. Comparison of the track critical velocity with the substructure layers Reiligh wave speed showed that the critical speed (approximately 450 km/h) is between the Reiligh wave speed of the subgrade (approximately 331 km/h) and the ballast (approximately 515 km/h). Above the critical velocity, the track vertical displacement is started to decrease with

increasing the train speed. The variation of the maximum cyclic stresses developed at the sleeper-ballast contact with the train speed showed that increasing the train speed up to 400 kph causes a very low increment in both maximum cyclic vertical and shear stresses at the sleeper-ballast interface (approximately 10%). However, a sudden increment at the maximum cyclic vertical and shear stresses was observed at the train's critical speed. The magnitude of the maximum cyclic vertical and shear stresses at the sleeper-ballast interface in the crucial speed increased by approximately 25% and 30%, respectively. Beyond the train velocity of nearly 550 kph (above the critical velocity), the magnitude of the cyclic stresses reduced slightly by increasing the train speed.

- The results of the FEM study shows considerably high cyclic stresses acting on the ballast layer due to the train passage. In addition, the cyclic laboratory tests on the ballast material revealed that with respect to the low confinement in the field, the large magnitude of the cyclic stresses acting on ballast could lead to a significant long-term settlement and consequently shorten the maintenance time. Therefore, in order to lengthen the ballasted track maintenance time, either the ballast confinement should be increased, or the cyclic stresses generated by the train should be decreased. In this study, two approaches were evaluated to decrease the magnitude of the cyclic stresses, including (1) increasing the sleeper's width and (2) reducing the sleeper's spacing. The impact of each approach is discussed in the following:

1. For the first method, four identical FEM models with sleeper's width equal to 150, 300, 450, and 600 mm were simulated. The train wheel load was assumed to be 125 kN moving with a constant speed of 200 kph. The results revealed that both the vertical and the shear stresses are decreased with increasing the sleeper's width. For instance, by increasing the sleeper's width from 150 to 600 mm, the maximum cyclic vertical and shear stress acting at the surface of ballast decreased by 66% and 57%, respectively. The results revealed that the short-term track settlement under train passage is decreased (approximately 10%) by increasing the sleeper's width. Although the short term settlement of the track is not significantly reduced, increasing the sleeper's width causes a reduction in the cyclic stresses in the embankment, which creates a hugely beneficial impact on the permanent long-term settlement of the track.
2. For the second approach, four FEM models with identical conditions and different sleeper's clear spacing equal to 0, 300, 600, and 900 mm were simulated. The spacing of 0 mm is equivalent to the slap track with the same thickness and the material properties of the regular sleepers. It was observed that the magnitude of the cyclic stresses is in an approximately linear indirect relationship with the sleeper's spacing. According to the results decreasing the sleeper's spacing from 900 mm to 0 mm reduces the maximum cyclic vertical stress at the ballast-sleeper interface from 269 to 171 kPa. The same transition for the maximum cyclic shear stress is from

50 to 28.4 kPa. The results of the variation of the track maximum settlement with the sleeper's spacing showed that reducing the sleeper's spacing decreases the track maximum deflection at the same train passage. For example, the track maximum downward deflection under train passage reduced from 2.47 to 1.86 mm for decreasing the sleeper's spacing from 900 mm to 0 mm.

7.2. Future Related Research

There are several possible areas for further investigations in the field of this research. The recommendation of future studies are indicated below:

- Study the influence existence of the fouling material and water content on the monotonic and cyclic behavior of the ballast material.
- Perform more large-scale triaxial tests with a wider cyclic stress ratio and more number of cycles to further investigate the cyclic behavior of the ballast material.
- Perform in situ plate test in cyclic condition on the ballast material to evaluate the ultimate bearing capacity of the ballast under cyclic loading condition.
- Conduct a numerical simulation of the ballasted track with assuming the non-linear behavior for the soil material to investigate the impact of soil non-linearity on the FEM results.
- Conduct a field investigation to monitor the long-term settlement of the track.

REFERENCES

- ABU-FARSAKH, M., SOUCI, G., VOYIADJIS, G. Z. & CHEN, Q. 2011. Evaluation of factors affecting the performance of geogrid-reinforced granular base material using repeated load triaxial tests. *Journal of Materials in Civil Engineering*, 24, 72-83.
- ADEGOKE, C. W., CHANG, C. S. & SELIG, E. T. 1979. Study of analytical models for track support systems. *Transportation research record*, 733, 12-20.
- ADOLFSSON, K., ANDREASSON, B., BENGTSSON, P. & ZACHRISSON, P. High speed train X2000 on soft organic clay-measurements in Sweden. Twelfth European Conference on Soil Mechanics and Geotechnical Engineering (Proceedings) The Netherlands Society of Soil Mechanics and Geotechnical Engineering; Ministry of Transport, Public Works and Water Management; AP van den Berg Machinefabriek; Fugro NV; GeoDelft; Holland Railconsult, 1999.
- AGARWAL, M. 1984. *Indian Railway Track: Design, Construction, Maintenance and Modernisation*, Prabha.
- AIREY, D. W. 1985. Some aspect of the behaviour of soils in simple shear. *Developments in Soil Mechanics and Foundation Engineering-2, Stress-strain Modeling of Soils*, 185-213.
- ALLEN, J. J. & THOMPSON, M. R. 1974. Resilient response of granular materials subjected to time-dependent lateral stresses. *Transportation Research Record*.

- ALVA-HURTADO, J. & SELIG, E. Permanent strain behavior of railroad ballast. Proceedings of The International Conference on Soil Mechanics and Foundation Engineering, 10th., 1981.
- ANDERSON, W. F. & FAIR, P. 2008. Behavior of railroad ballast under monotonic and cyclic loading. *Journal of Geotechnical and Geoenvironmental Engineering*, 134, 316-327.
- AREA (American Railway Engineering Association). (1996). Manual for railway engineering, Washington, DC.
- AREMA (American Railway Engineering and Maintenance-of-Way Association). (2008). Manual for Railway Engineering. Washington, DC.
- ARULRAJAH, A., RAHMAN, M., PIRATHEEPAN, J., BO, M. & IMTEAZ, M. 2013. Evaluation of interface shear strength properties of geogrid-reinforced construction and demolition materials using a modified large-scale direct shear testing apparatus. *Journal of Materials in Civil Engineering*, 26, 974-982.
- ASADZADEH, M. & SOROUSH, A. 2009. Direct shear testing on a rockfill material. *Arabian Journal for Science and Engineering*, 34, 379.
- ASTM International. C29/C29M-17a Standard Test Method for Bulk Density (“Unit Weight”) and Voids in Aggregate. West Conshohocken, PA; ASTM International, 2017.
- ASTM International. C88/C88M-18 Standard Test Method for Soundness of Aggregates by Use of Sodium Sulfate or Magnesium Sulfate. West Conshohocken, PA; ASTM International, 2018.

ASTM International. C117-17 Standard Test Method for Materials Finer than 75- μm (No. 200) Sieve in Mineral Aggregates by Washing. West Conshohocken, PA; ASTM International, 2017.

ASTM International. C127-15 Standard Test Method for Relative Density (Specific Gravity) and Absorption of Coarse Aggregate. West Conshohocken, PA; ASTM International, 2015.

ASTM International. C131/C131M-14 Standard Test Method for Resistance to Degradation of Small-Size Coarse Aggregate by Abrasion and Impact in the Los Angeles Machine. West Conshohocken, PA; ASTM International, 2006.

ASTM International. C136/C136M-14 Standard Test Method for Sieve Analysis of Fine and Coarse Aggregates. West Conshohocken, PA; ASTM International, 2014.

ASTM International. C142/C142M-17 Standard Test Method for Clay Lumps and Friable Particles in Aggregates. West Conshohocken, PA; ASTM International, 2017.

ASTM International. C535-16 Standard Test Method for Resistance to Degradation of Large-Size Coarse Aggregate by Abrasion and Impact in the Los Angeles Machine. West Conshohocken, PA; ASTM International, 2016.

ASTM International. C702/C702M-18 Standard Practice for Reducing Samples of Aggregate to Testing Size. West Conshohocken, PA; ASTM International, 2018.

ASTM International. D5321/D5321M-20 Standard Test Method for Determining the Shear Strength of Soil-Geosynthetic and Geosynthetic-Geosynthetic Interfaces by Direct Shear. West Conshohocken, PA.

- AURSUDKIJ, B. 2007. *A laboratory study of railway ballast behaviour under traffic loading and tamping maintenance*. University of Nottingham.
- BANIMAHD, M. 2008. *Advanced finite element modelling of coupled train-track systems: a geotechnical perspective*. Heriot-Watt University.
- BARKSDALE, R. D. Laboratory evaluation of rutting in base course materials.
Presented at the Third International Conference on the Structural Design of Asphalt Pavements, Grosvenor House, Park Lane, London, England, Sept. 11-15, 1972., 1972.
- BARSKALE, R. D. & ITANI, S. Y. 1989. Influence of aggregate shape on base behavior. *Transportation research record*.
- BATHURST, R. J. & KARPURAPU, R. 1993. Large-scale triaxial compression testing of geocell-reinforced granular soils. *Geotechnical Testing Journal*, 16, 296-303.
- BAUER, G. E. & ZHAO, Y. 1993. Shear strength tests for coarse granular backfill and reinforced soils. *Geotechnical Testing Journal*, 16, 115-121.
- BIAN, X. & CHEN, Y. 2006. An explicit time domain solution for ground stratum response to harmonic moving load. *Acta Mechanica Sinica*, 22, 469-478.
- BIAN, X., CHENG, C., JIANG, J., CHEN, R. & CHEN, Y. 2016a. Numerical analysis of soil vibrations due to trains moving at critical speed. *Acta Geotechnica*, 11, 281-294.
- BIAN, X., JIANG, J., JIN, W., SUN, D., LI, W. & LI, X. 2016b. Cyclic and postcyclic triaxial testing of ballast and subballast. *Journal of Materials in Civil Engineering*, 28, 04016032.

- BISHOP, A. W. & HENKEL, D. J. 1962. The measurement of soil properties in the triaxial test.
- BOLER, H., QIAN, Y. & TUTUMLUER, E. 2014. Influence of Size and Shape Properties of Railroad Ballast on Aggregate Packing: Statistical Analysis. *Transportation Research Record*, 2448, 94-104.
- BOSSERMAN, B. 1982. Ballast experiments at FAST.
- BOWNESS, D., LOCK, A., POWRIE, W., PRIEST, J. & RICHARDS, D. 2007. Monitoring the dynamic displacements of railway track. *Proceedings of the Institution of Mechanical Engineers, Part F: Journal of Rail and Rapid Transit*, 221, 13-22.
- BOYCE, J. R. 1976. *The behaviour of a granular material under repeated loading*. University of Nottingham.
- BRIAUD, J.-L. 2013. *Geotechnical engineering: unsaturated and saturated soils*, John Wiley & Sons.
- BROWN, S. & PELL, P. An experimental investigation of the stresses, strains and deflections in a layered pavement structure subjected to dynamic loads. Intl Conf Struct Design Asphalt Pvmnts, 1967.
- BROWN, S. & SELIG, E. 1991. The design of pavement and rail track foundations. *Cyclic loading of soils*, 249-305.
- CAO, Z., CHEN, J., CAI, Y., ZHAO, L., GU, C. & WANG, J. 2018. Long-term behavior of clay-fouled unbound granular materials subjected to cyclic loadings with different frequencies. *Engineering geology*, 243, 118-127.

- CASAGRANDE, A. & POULOS, S. 1964. Fourth Report on Investigation of Stress-Deformation Characteristics of Compacted Clays. *US Army Waterways Experiment Station, Harvard Soil Mechanics Series.*
- CASTELLANOS, B. & BRANDON, T. A comparison between the shear strength measured with direct shear and triaxial devices on undisturbed and remolded soils. Proceedings of the 18th international conference on soil mechanics and geotechnical engineering, Paris, 2013. 317-320.
- CHARLES, J. & WATTS, K. 1980. The influence of confining pressure on the shear strength of compacted rockfill. *Geotechnique*, 30, 353-367.
- CHARLES, J. A. 1973. Correlation between laboratory behaviour of rockfill and field performance with particular reference to Scammonden Dam.
- CHOUDHURY, J. 2006. Geotechnical investigation report for proposed Bulli track upgrading between 311 and 312 turnouts: Dn track 71.660–71.810 km, up track, 71.700–71.780 km. *Memorandum, Engineering Standards & Services Division, Geotechnical Services, NSW, Australia.*
- CHRISMER, S. 1986. Considerations of factors affecting ballast performance. *American Railway Engineering Association*, 87.
- CLARK, C. 1957. Track Loading Fundamentals–Parts 1-7. *Railway Gazette*, 106.
- CONNOLLY, D., GIANNOPOULOS, A. & FORDE, M. 2013. Numerical modelling of ground borne vibrations from high speed rail lines on embankments. *Soil Dynamics and Earthquake Engineering*, 46, 13-19.

- CORNFORTH, D. H. 1964. Some experiments on the influence of strain conditions on the strength of sand. *Geotechnique*, 14, 143-167.
- COSTA, P. A., COLAÇO, A., CALÇADA, R. & CARDOSO, A. S. 2015. Critical speed of railway tracks. Detailed and simplified approaches. *Transportation Geotechnics*, 2, 30-46.
- CUI, Y.-J. 2018. Mechanical behaviour of coarse grains/fines mixture under monotonic and cyclic loadings. *Transportation Geotechnics*.
- DAHLBERG, T. 2001. Some railroad settlement models—a critical review. *Proceedings of the Institution of Mechanical Engineers, Part F: Journal of Rail and Rapid Transit*, 215, 289-300.
- DAI, B. B., YANG, J. & ZHOU, C. Y. 2015. Observed effects of interparticle friction and particle size on shear behavior of granular materials. *International Journal of Geomechanics*, 16, 04015011.
- DAWSON, A. & GOMES CORREIA, A. The effects of stress and pore water pressure states on the resilient properties of granular materials. International Conference on Soil Mechanics and Foundation Engineering, 12th, 1989, Rio de Janeiro, Brazil, 1989.
- DE MELLO, V. F. 1977. Reflections on design decisions of practical significance to embankment dams. *Géotechnique*, 27, 281-355.
- DEGROOT, D. J., LADD, C. C. & GERMAINE, J. T. 1992. *Direct simple shear testing of cohesive soils*, [Ralph M. Parsons Laboratory], Department of Civil Engineering

- DISSANAYAKE, D., KURUKULASURIYA, L. & DISSANAYAKE, P. 2016. Evaluation of shear strength parameters of rail track ballast in Sri Lanka. *Journal of the National Science Foundation of Sri Lanka*, 44.
- DONAGHE, R. T. & COHEN, M. W. 1978. Strength and Deformation Properties of Rock Fill. ARMY ENGINEER WATERWAYS EXPERIMENT STATION VICKSBURG MISS.
- DOUGLAS, K. 2002. The shear strength of rock masses [PhD thesis]. *School of Civil and Environmental Engineering. The University of New South Wales.*
- DOUNIAS, G. T. & POTTS, D. M. 1993. Numerical analysis of drained direct and simple shear tests. *Journal of Geotechnical Engineering*, 119, 1870-1891.
- DOYLE, N. F. 1980. Railway track design: a review of current practice.
- DRUCKER, D. C. 1957. Soil mechanics and work-hardening theories of plasticity. *Trans. ASCE*, 122, 338-346.
- DUNCAN, J. M. & CHANG, C.-Y. 1970. Nonlinear analysis of stress and strain in soils. *Journal of Soil Mechanics & Foundations Div.*
- DYVIK, R. & KAYNIA, A. 2018. Large-Scale Triaxial Tests on Railway Embankment Material. *Railroad Ballast Testing and Properties*. ASTM International.
- EBRAHIMI, A., TINJUM, J. M. & EDIL, T. B. 2014. Deformational behavior of fouled railway ballast. *Canadian Geotechnical Journal*, 52, 344-355.
- EISENMANN, J. 1970. Stress distribution in the permanent way due to heavy axle loads and high speeds. *Proceedings of AREA*, 71, 24-59.

- ESTAIRE, J. & SANTANA, M. 2018. Large direct shear tests performed with fresh ballast. *Railroad Ballast Testing and Properties*. ASTM International.
- ESVELD, C.-A. 1989. Modern Railway Track, Germany. *Hakan Guler, Murat Akad and Murat Ergun TS20*, 3.
- FEI, X. & ZEKKOS, D. 2018. Comparison of direct shear and simple shear responses of municipal solid waste in USA. *Environmental Geotechnics*, 5, 158-167.
- FERREIRA, J. N. V. D. S. 2013. Long-term behaviour of railway transitions under dynamic loading application to soft soil sites.
- FORD, R. 1995. Differential ballast settlement, and consequent undulations in track, caused by vehicle-track interaction. *Vehicle System Dynamics*, 24, 222-233.
- FU, W., ZHENG, X., LEI, X. & DENG, J. 2015. Using a modified direct shear apparatus to explore gap and size effects on shear resistance of coarse-grained soil. *Particuology*, 23, 82-89.
- FUMAGALLI, E. 1969. Tests on cohesionless materials for rockfill dams. *Journal of Soil Mechanics & Foundations Div*, 92.
- GEOCOMPCO. 2015. Control and Report Software for Fully Automated Direct Shear Tests on ShearTrac-III DSS Systems using Windows®XP/Vista/7, Cyclic Direct Simple Shear- User's Manual.
- GHARAVY, M. 1996. *Experimental and numerical investigations into the mechanical characteristics of rockfill materials*. University of Newcastle upon Tyne.
- GOUDARZI, A. 2019. *Steel and Geosynthetic Reinforcement-Soil Interaction*.

- HALL, L. 2003. Simulations and analyses of train-induced ground vibrations in finite element models. *Soil Dynamics and Earthquake Engineering*, 23, 403-413.
- HALLQUIST, J. O. 2006. LS-DYNA theory manual. *Livermore software Technology corporation*, 3, 25-31.
- HANZAWA, H., NUTT, N., LUNNE, T., TANG, Y. & LONG, M. 2007. A comparative study between the NGI direct simple shear apparatus and the Mikasa direct shear apparatus. *Soils and foundations*, 47, 47-58.
- HARDIN, B. O. 1985. Crushing of soil particles. *Journal of geotechnical engineering*, 111, 1177-1192.
- HAYNES, J. & YODER, E. 1963. Effect of Repeated Loading on Gravel and Crushed Stone Base Course Materials Used in the AASHO (American Association of State Highway Officials) Road Test. *Highway Research Record*, 39, 422.
- HEYDINGER, A. G., XIE, Q., RANDOLPH, B. W. & GUPTA, J. D. 1996. Analysis of resilient modulus of dense-and open-graded aggregates. *Transportation research record*, 1547, 1-6.
- HICKS, R. G. & MONISMITH, C. L. 1971. Factors influencing the resilient response of granular materials. *Highway research record*, 345, 15-31.
- HOLM, G., ANDRÉASSON, B., BENGTSSON, P.-E., BODARE, A. & ERIKSSON, H. 2002. Mitigation of track and ground vibrations by high speed trains at Ledsgard, Sweden. *Swedish Deep Stabilization Research Centre, Report*, 10, 58-67.
- HOLTZ, W. G. & GIBBS, H. 1956. Triaxial shear tests on pervious gravelly soils. *Journal of the Soil Mechanics and Foundations Division*, 82, 1-22.

- INDRARATNA, B., HUSSAINI, S. K. K. & VINOD, J. S. 2011a. On the shear behavior of ballast-geosynthetic interfaces. *Geotechnical Testing Journal*, 35, 305-312.
- INDRARATNA, B. & IONESCU, D. 2000. State of the art large scale testing of ballast.
- INDRARATNA, B., IONESCU, D., CHRISTIE, D. & CHOWDHURY, R. 1997. Compression and degradation of railway ballast under one-dimensional loading.
- INDRARATNA, B., IONESCU, D. & CHRISTIE, H. 1998. Shear behavior of railway ballast based on large-scale triaxial tests. *Journal of geotechnical and geoenvironmental Engineering*, 124, 439-449.
- INDRARATNA, B., NGO, N. T. & RUJIKIATKAMJORN, C. 2011b. Behavior of geogrid-reinforced ballast under various levels of fouling. *Geotextiles and Geomembranes*, 29, 313-322.
- INDRARATNA, B. & NGO, T. 2018. *Ballast railroad design: smart-uow approach*, CRC Press.
- INDRARATNA, B. & NIMBALKAR, S. 2013. Stress-strain degradation response of railway ballast stabilized with geosynthetics. *Journal of geotechnical and geoenvironmental engineering*, 139, 684-700.
- INDRARATNA, B., NIMBALKAR, S., CHRISTIE, D., RUJIKIATKAMJORN, C. & VINOD, J. 2010. Field assessment of the performance of a ballasted rail track with and without geosynthetics. *Journal of Geotechnical and Geoenvironmental Engineering*, 136, 907-917.

- INDRARATNA, B., NIMBALKAR, S. & RUJIKIATKAMJORN, C. 2012. Track stabilisation with geosynthetics and geodrains, and performance verification through field monitoring and numerical modelling.
- INDRARATNA, B., NIMBALKAR, S. S., NGO, N. T. & NEVILLE, T. 2016. Performance improvement of rail track substructure using artificial inclusions—Experimental and numerical studies. *Transportation Geotechnics*, 8, 69-85.
- INDRARATNA, B. & SALIM, W. 2002. Modelling of particle breakage of coarse aggregates incorporating strength and dilatancy.
- INDRARATNA, B. & SALIM, W. 2005. *Mechanics of ballasted rail tracks: a geotechnical perspective*, CRC Press.
- INDRARATNA, B., WIJewardena, L. & BALASUBRAMANIAM, A. 1993. Large-scale triaxial testing of greywacke rockfill. *Geotechnique*, 43, 37-51.
- IONESCU, D. 2004. Evaluation of the engineering behaviour of railway ballast.
- IONESCU, D., INDRARATNA, B. & CHRISTIE, H. D. Deformation of railway ballast under dynamic loads. Conference on Railway Engineering Proceedings: Engineering Innovation for a Competitive Edge, 1998. Central Queensland University, 111.
- JANARDHANAM, R. & DESAI, C. 1983. Three-dimensional testing and modeling of ballast. *Journal of Geotechnical Engineering*, 109, 783-796.
- JEFFS, T. Towards ballast life cycle costing. Fourth International Heavy Haul Railway Conference 1989: Railways in Action; Preprints of Papers, The, 1989. Institution of Engineers, Australia, 439.

- JEFFS, T. & MARICH, S. Ballast characteristics in the laboratory. Conference on railway engineering 1987: preprints of papers, 1987. Institution of Engineers, Australia, 141.
- JEFFS, T. & TEW, G. 1991. A review of track design procedures: Sleepers and ballast. *Railways of Australia*, 2.
- JENKINS, H., STEPHENSON, J., CLAYTON, G., MORLAND, G. & LYON, D. 1974. The effect of track and vehicle parameters on wheel/rail vertical dynamic forces. *Railway Engineering Journal*, 3.
- JIANG, Y. & NIMBALKAR, S. S. 2019. Finite Element Modelling of Ballasted Rail Track Capturing Effects of Geosynthetic Inclusions. *Frontiers in Built Environment*, 5, 69.
- KATZENBACH, R. & FESTAG, G. 2004. Material behaviour of dry sand under cyclic loading. *Cyclic Behaviour of Soils and Liquefaction Phenomena*, 153-158.
- KAYNIA, A. M., MADSHUS, C. & ZACKRISSON, P. 2000. Ground vibration from high-speed trains: prediction and countermeasure. *Journal of Geotechnical and Geoenvironmental Engineering*, 126, 531-537.
- KEMPFERT, H. & HU, Y. Measured dynamic loading of railway underground. Proc., 11th Pan-American Conf. on Soil Mechanics and Geotechnical Engineering, 1999. International Society for Soil Mechanics Brazil, 843-847.
- KEY, A. J. 1999. *Behaviour of two layer railway track ballast under cyclic and monotonic loading*. University of Sheffield.

- KHARANAGHI, M. M. & BRIAUD, J.-L. Large-Scale Direct Shear Test on Railroad Ballast. *Geo-Congress 2020: Modeling, Geomaterials, and Site Characterization*, 2020. American Society of Civil Engineers Reston, VA, 123-131.
- KHEDR, S. 1985. Deformation characteristics of granular base course in flexible pavements. *Transportation Research Record*, 1043, 131-138.
- KHOGALI, W. E. & ZEGHAL, M. 2000. On the resilient behaviour of unbound aggregates. *Unbound Aggregates in Road Construction, Nottingham, England*, 29-34.
- KIM, Y.-S. 2009. Static simple shear characteristics of Nak-dong River clean sand. *KSCE Journal of Civil Engineering*, 13, 389-401.
- KNUTSON, R. M. 1977. FACTORS INFLUENCING THE REPEATED LOAD BEHAVIOR OF RAILWAY BALLAST.
- KOERNER, R. M. 1970. Effect of particle characteristics on soil strength. *Journal of Soil Mechanics & Foundations Div.*
- KOFFMAN, J. & FAIRWEATHER, D. 1975. Some problems of railway operation at high axleloads. *Rail Engineering International*, 5.
- KOLBUSZEWSKI, J. & FREDERICK, M. The significance of particle shape and size on the mechanical behaviour of granular materials. *Proceedings of European conference on the soil mechanics and foundation engineering, 1963*. 253-263.
- KOLISOJA, P. Factors affecting deformation properties of coarse grained granular materials. *PROCEEDINGS OF THE INTERNATIONAL CONFERENCE ON SOIL MECHANICS AND FOUNDATION ENGINEERING-*

INTERNATIONAL SOCIETY FOR SOIL MECHANICS AND FOUNDATION
ENGINEERING, 1997. AA BALKEMA, 337-342.

LACKENBY, J., INDRARATNA, B., MCDOWELL, G. & CHRISTIE, D. 2007. Effect
of confining pressure on ballast degradation and deformation under cyclic triaxial
loading.

LADD, R. 1978. Preparing test specimens using undercompaction. *Geotechnical Testing
Journal*, 1, 16-23.

LAMBE, T. W. & WHITMAN, R. V. 1969. Soil mechanics. John Willey & Sons. *Inc.*,
New York, 553.

LEE, K. L. 1970. Comparison of plane strain and triaxial tests on sand. *Journal of the
Soil Mechanics and Foundations Division*, 96, 901-923.

LEE, K. L. & SEED, H. B. 1967. Drained strength characteristics of sands. *Journal of
Soil Mechanics & Foundations Div.*

LEE, K. L. & VERNESE, F. J. 1978. End restraint effects on cyclic triaxial strength of
sand. *Journal of Geotechnical and Geoenvironmental Engineering*, 104.

LEKARP, F., ISACSSON, U. & DAWSON, A. 2000. State of the art. I: Resilient
response of unbound aggregates. *Journal of transportation engineering*, 126, 66-
75.

LIGHT, T. J., HO, C. L. & LAMBERT, R. S. 2014. Effect of Moisture on the
Engineering Characteristics of Fouled Ballast.

- LINI DEV, K., PILLAI, R. J. & ROBINSON, R. G. 2016. Drained angle of internal friction from direct shear and triaxial compression tests. *International Journal of Geotechnical Engineering*, 10, 283-287.
- LIU, J., WANG, P. & LIU, J. 2015. Macro-and micro-mechanical characteristics of crushed rock aggregate subjected to direct shearing. *Transportation Geotechnics*, 2, 10-19.
- LUNDQVIST, A. & DAHLBERG, T. 2005. Load impact on railway track due to unsupported sleepers. *Proceedings of the Institution of Mechanical Engineers, Part F: Journal of Rail and Rapid Transit*, 219, 67-77.
- LUO, Y., YIN, H. & HUA, C. 1996. The dynamic response of railway ballast to the action of trains moving at different speeds. *Proceedings of the Institution of Mechanical Engineers, Part F: Journal of Rail and Rapid Transit*, 210, 95-101.
- MADSHUS, C., LACASSE, S., KAYNIA, A. & HÅRVIK, L. 2004. Geodynamic challenges in high speed railway projects. *Geotechnical Engineering for Transportation Projects*.
- MADSHUS, C. C. & KAYNIA, A. 2000. High-speed railway lines on soft ground: dynamic behaviour at critical train speed. *Journal of Sound and Vibration*, 231, 689-701.
- MARSAL, R. J. 1967. Large-scale testing of rockfill materials. *Journal of the Soil Mechanics and Foundations Division*, 93, 27-43.

- MARSCHI, N. D., CHAN, C. K. & SEED, H. B. 1972. Evaluation of properties of rockfill materials. *Journal of the Soil Mechanics and Foundations Division*, 98, 95-114.
- MCDOWELL, G., BOLTON, M. & ROBERTSON, D. 1996. The fractal crushing of granular materials. *Journal of the Mechanics and Physics of Solids*, 44, 2079-2101.
- MEZHER, S. B., CONNOLLY, D. P., WOODWARD, P. K., LAGHROUCHE, O., POMBO, J. & COSTA, P. A. 2016. Railway critical velocity—Analytical prediction and analysis. *Transportation Geotechnics*, 6, 84-96.
- MISHRA, D., KAZMEE, H., TUTUMLUER, E., PFORR, J., READ, D. & GEHRINGER, E. 2013. Characterization of railroad ballast behavior under repeated loading: results from new large triaxial test setup. *Transportation Research Record*, 2374, 169-179.
- MISHRA, D. & MAHMUD, S. N. Effect of Particle Size and Shape Characteristics on Ballast Shear Strength: A Numerical Study Using the Direct Shear Test. 2017 Joint Rail Conference, 2017. American Society of Mechanical Engineers, V001T01A014-V001T01A014.
- MOGHADDAS-NEJAD, F. & SMALL, J. C. 2003. Resilient and permanent characteristics of reinforced granular materials by repeated load triaxial tests. *Geotechnical testing journal*, 26, 152-166.
- MOORE, W. M., BRITTON, S. C. & SCRIVNER, F. H. 1970. A laboratory study of the relation of stress to strain for a crushed limestone base material.

- NAKAO, T. & FITYUS, S. 2008. Direct shear testing of a marginal material using a large shear box. *Geotechnical Testing Journal*, 31, 393-403.
- NÅLSUND, R. 2010. Effect of grading on degradation of crushed-rock railway ballast and on permanent axial deformation. *Transportation Research Record*, 2154, 149-155.
- NEIDHART, T. 2005. True-to-scale in situ tests determining dynamic performance of earthworks under high speed train loading.
- NGO, N. T. 2012. Performance of geogrids stabilised fouled ballast in rail tracks.
- NICKS, J. & ADAMS, M. Large-scale direct shear testing of common open-graded aggregates. Geo-Congress 2014: Geo-characterization and Modeling for Sustainability, 2014. 47-53.
- NICKS, J. E. 2009. *The bump at the end of the railway bridge*.
- OLOWOKERE, D. O. 1975. *Strength and deformation of railway ballast subject to triaxial loading*. Thesis (M. Sc.(Eng.))--Queen's University.
- ORE 1965. Stresses in Rails, Question 017, Stresses in the Rails, the Ballast and the Formation Resulting from Traffic Loads, Report D71/RPI/E, Utrecht.
- PIKE, D. 1973. Shear-box tests on graded aggregates.
- PING, W. V. & YANG, Z. 1998. Experimental verification of resilient deformation for granular subgrades. *Transportation research record*, 1639, 12-22.
- PONCE, V. M. & BELL, J. M. 1971. Shear strength of sand at extremely low pressures. *Journal of Soil Mechanics & Foundations Div.*

- POWRIE, W., YANG, L. & CLAYTON, C. R. 2007. Stress changes in the ground below ballasted railway track during train passage. *Proceedings of the Institution of Mechanical Engineers, Part F: Journal of Rail and Rapid Transit*, 221, 247-262.
- PROFILLIDIS, V. 2016. *Railway management and engineering*, Routledge.
- QIAN, Y., MISHRA, D., TUTUMLUER, E., HASHASH, Y. M. & GHABOUSSI, J. Moisture effects on degraded ballast shear strength behavior. 2016 Joint Rail Conference, 2016. American Society of Mechanical Engineers, V001T01A034-V001T01A034.
- RADA, G. & WITCZAK, M. W. 1981. *Comprehensive evaluation of laboratory resilient moduli results for granular material*.
- RAYMOND, G. P. 1985. Research on railroad ballast specification and evaluation. *Transportation Research Record*, 1006, 1-8.
- RAYMOND, G. P. & DAVIES, J. R. 1978. Triaxial tests on dolomite railroad ballast. *Journal of the Geotechnical Engineering Division*, 104, 737-751.
- RAYMOND, G. P. & DIYALJEE, V. A. 1979. Railroad ballast sizing and grading. *Journal of Geotechnical and Geoenvironmental Engineering*, 105.
- RAYMOND, G. P., GASKIN, P. N. & SVEC, O. 1978. Selection and performance of railroad ballast. *Railroad track mechanics and technology*. Elsevier.
- RAYMOND, G. P., LAMSON, S. T. AND LAW, J. E. 1983. *A review of current track structure design and future track research requirements*, Kingston, Ont.: Canadian Institute of Guided Ground Transport.

- REZAEI TAFTI, S. 2018. *High Speed Train Geotechnics: Numerical and Experimental Simulation of Some Embankment Problems*.
- RONER, C. J. 1985. Some effects of shape, gradation and size on the performance of railroad ballast. *MS degree project report, Report No. AAR85-324P, Department of Civil Engineering, University of Massachusetts, Amherst, June*.
- ROSCOE, K. An apparatus for the application of simple shear to soil samples. Proc. 3rd ICSMFE, 1953. 186-191.
- ROSE, J., SU, B. & TWEHUES, F. Comparisons of railroad track and substructure computer model predictive stress values and in-situ stress measurements. Proceedings of the AREMA 2004 Annual Conference & Exposition, Nashville, TN, September, 2004.
- ROSE, J. G. & KONDURI, K. C. 2003. KENTRACK: A Railway trackbed structural design and analysis program.
- SAADA, A. & TOWNSEND, F. 1981. State of the art: laboratory strength testing of soils. *Laboratory shear strength of soil*. ASTM International.
- SALIM, W. 2004. Deformation and degradation aspects of ballast and constitutive modelling under cyclic loading.
- SATO, Y. 1995. Japanese studies on deterioration of ballasted track. *Vehicle system dynamics*, 24, 197-208.
- SAYEED, M. A. & SHAHIN, M. A. 2016. Three-dimensional numerical modelling of ballasted railway track foundations for high-speed trains with special reference to critical speed. *Transportation Geotechnics*, 6, 55-65.

- SEED, H., MITRY, F., MONISMITH, C. & CHAN, C. 1965. Prediction of Pavement Deflections from Laboratory Repeated Load Tests, Report No. TE 65-6, Soil Mechanics and Bituminous Materials Research Laboratory. *University of California, Berkeley*.
- SEED, H., MITRY, F., MONISMITH, C. & CHAN, C. 1967. Factors influencing the resilient deformations of untreated aggregate base in two-layer pavements subjected to repeated loading. *Highway Research Record*, 190, 19-57.
- SELIG, E. 1985. Ballast for heavy duty track. *Track Technology*. Thomas Telford Publishing.
- SELIG, E. 1987. Tensile zone effects on performance of layered systems. *Geotechnique*, 37, 247-254.
- SELIG, E. 1998. Ballast deformation: its causes and cures. *Railway Track And Structures*, 94.
- SELIG, E. & ALVA-HURTADO, J. Predicting effects of repeated wheel loading on track settlement. Proc. 2nd Int. Heavy Haul Railway Conf., Colorado Springs, 1982. 476-487.
- SELIG, E. T. & WATERS, J. M. 1994. *Track geotechnology and substructure management*, Thomas Telford.
- SEVI, A. F., GE, L. & TAKE, W. A. 2009. A large-scale triaxial apparatus for prototype railroad ballast testing. *Geotechnical testing journal*, 32, 297-304.

- SHENG, X., JONES, C. & THOMPSON, D. 2004. A theoretical study on the influence of the track on train-induced ground vibration. *Journal of Sound and Vibration*, 272, 909-936.
- SHENTON, M. 1974. Deformation of railway ballast under repeated loading conditions. Rapport RP5, British Railways Research and Development Division. Pergamon, Oxford.
- SHIH, J.-Y., THOMPSON, D. J. & ZERVOS, A. 2017. The influence of soil nonlinear properties on the track/ground vibration induced by trains running on soft ground. *Transportation Geotechnics*, 11, 1-16.
- SITHARAM, T. G. 1999. Micromechanical modeling of granular materials: effect of confining pressure on mechanical behavior. *Mechanics of materials*, 31, 653-665.
- SKEMPTON, A. 1964. Long-term stability of clay slopes. *Geotechnique*, 14, 77-102.
- SOWERS, G. Compressibility of broken rock and the settlement of rockfills. Proceedings of the 6th International Conference on Soil Mechanics and Foundation Engineering, Montreal, Canada, 1965. 561-565.
- STARK, T., WILK, S. & SWAN, R. 2018. Review of Size and Loading Conditions for Large-Scale Triaxial Testing. *Railroad Ballast Testing and Properties*. ASTM International.
- STARK, T. D., HUVAJ-SARIHAN, N. & LI, G. 2009. Shear strength of municipal solid waste for stability analyses. *Environmental geology*, 57, 1911-1923.

- STARK, T. D., SWAN, R. H. & YUAN, Z. Ballast direct shear testing. 2014 Joint Rail Conference, 2014. American Society of Mechanical Engineers, V001T01A003-V001T01A003.
- SUIKER, A. S. & DE BORST, R. 2003. A numerical model for the cyclic deterioration of railway tracks. *International journal for numerical methods in engineering*, 57, 441-470.
- SUIKER, A. S., SELIG, E. T. & FRENKEL, R. 2005. Static and cyclic triaxial testing of ballast and subballast. *Journal of geotechnical and geoenvironmental engineering*, 131, 771-782.
- SUN, Q., INDRARATNA, B. & NIMBALKAR, S. 2014. Effect of cyclic loading frequency on the permanent deformation and degradation of railway ballast. *Géotechnique*.
- SWEERE, G. T. 1992. Unbound granular bases for roads.
- TALBOT, A. N. 1980. *Stresses in railroad track: the Talbot reports*, AREA.
- TANG, A. M., CUI, Y.-J., DUPLA, J.-C., CANOU, J., CALON, N., LAMBERT, L., ROBINET, A. & SCHOEN, O. 2012. Mechanical characterisation of the fouled ballast in ancient railway track substructure by large-scale triaxial tests. *Soils and foundations*, 52, 511-523.
- TEJCHMAN, J. & BAUER, E. 2005. Fe-simulations of a direct and a true simple shear test within a polar hypoplasticity. *Computers and Geotechnics*, 32, 1-16.
- TERZAGHI, K., PECK, R. B. & MESRI, G. 1996. *Soil mechanics in engineering practice*, John Wiley & Sons.

- THAKUR, P. K. 2011. Cyclic densification of ballast and associated deformation and degradation.
- THORN, N. & BROWN, S. 1989. The mechanical properties of unbound aggregates from various sources. *Unbound aggregates in roads*. Elsevier.
- TOLOUKIAN, A. R., SADEGHI, J. & ZAKERI, J.-A. 2018. Large-scale direct shear tests on sand-contaminated ballast. *Proceedings of the Institution of Civil Engineers-Geotechnical Engineering*, 171, 451-461.
- TROLLOPE, D., LEE, I. & MORRIS, J. Stresses and deformation in two layer pavement structures under slow repeated loading. Australian Road Research Board (ARRB) Conference, 1st, 1962, Canberra, 1962.
- VALLERGA, B., SEED, H., MONISMITH, C. & COOPER, R. 1957. Effect of shape, size, and surface roughness of aggregate particles on the strength of granular materials. *Road and Paving Materials*. ASTM International.
- VARANDAS, J. N., PAIXÃO, A., FORTUNATO, E. & HÖLSCHER, P. 2016. A numerical study on the stress changes in the ballast due to train passages. *Procedia engineering*, 143, 1169-1176.
- VESIC, A. S. & CLOUGH, G. W. 1968. Behavior of granular materials under high stresses. *Journal of Soil Mechanics & Foundations Div.*
- VILAR, O. M. & CARVALHOD, M. 2004. Mechanical properties of municipal solid waste. *Journal of Testing and Evaluation*, 32, 438-449.
- WANG, H. & MARKINE, V. 2018. Modelling of the long-term behaviour of transition zones: Prediction of track settlement. *Engineering structures*, 156, 294-304.

- WANG, J. & GUTIERREZ, M. 2010. Discrete element simulations of direct shear specimen scale effects. *Géotechnique*, 60, 395.
- WERKMEISTER, S., DAWSON, A. & WELLNER, F. 2004. Pavement design model for unbound granular materials. *Journal of Transportation Engineering*, 130, 665-674.
- WILK, S. T. 2017. *Mitigation of differential movements at railroad bridge transition zones*. University of Illinois at Urbana-Champaign.
- WNEK, M. A., TUTUMLUER, E., MOAVENI, M. & GEHRINGER, E. 2013. Investigation of aggregate properties influencing railroad ballast performance. *Transportation Research Record*, 2374, 180-189.
- WOLDRINGH, R. & NEW, B. Embankment design for high speed trains on soft soils. Twelfth European Conference on Soil Mechanics and Geotechnical Engineering (Proceedings) The Netherlands Society of Soil Mechanics and Geotechnical Engineering; Ministry of Transport, Public Works and Water Management; AP van den Berg Machinefabriek; Fugro NV; GeoDelft; Holland Railconsult, 1999.
- WOODWARD, P., KENNEDY, J., LAGHROUCHE, O., CONNOLLY, D. & MEDERO, G. 2014. Study of railway track stiffness modification by polyurethane reinforcement of the ballast. *Transportation Geotechnics*, 1, 214-224.
- XIAO, Y., LIU, H., CHEN, Y. & JIANG, J. 2014. Strength and deformation of rockfill material based on large-scale triaxial compression tests. I: Influences of density

- and pressure. *Journal of Geotechnical and Geoenvironmental Engineering*, 140, 04014070.
- YANG, L., POWRIE, W. & PRIEST, J. 2009. Dynamic stress analysis of a ballasted railway track bed during train passage. *Journal of Geotechnical and Geoenvironmental Engineering*, 135, 680-689.
- ZAMAN, M., CHEN, D.-H. & LAGUROS, J. 1994. Resilient moduli of granular materials. *Journal of Transportation Engineering*, 120, 967-988.
- ZEGHAL, M. 2004. Discrete-element method investigation of the resilient behavior of granular materials. *Journal of Transportation Engineering*, 130, 503-509.
- ZEKKOS, D., ATHANASOPOULOS-ZEKKOS, A., HUBLER, J., FEI, X., ZEHTAB, K. H. & MARR, W. A. 2018. Development of a large-size cyclic direct simple shear device for characterization of ground materials with oversized particles. *Geotechnical Testing Journal*, 41, 263-279.
- ZEKKOS, D., ATHANASOPOULOS, G. A., BRAY, J. D., GRIZI, A. & THEODORATOS, A. 2010. Large-scale direct shear testing of municipal solid waste. *Waste management*, 30, 1544-1555.
- ZEKKOS, D., BRAY, J. D. & RIEMER, M. F. 2008. Shear modulus and material damping of municipal solid waste based on large-scale cyclic triaxial testing. *Canadian Geotechnical Journal*, 45, 45-58.